Influence of concrete cracking on ingress and reinforcement corrosion

Pease, Bradley Justin; Geiker, Mette Rica; Stang, Henrik; Weiss, Jason

Publication date:
2011

Document Version
Publisher's PDF, also known as Version of record

Influence of concrete cracking on ingress and reinforcement corrosion

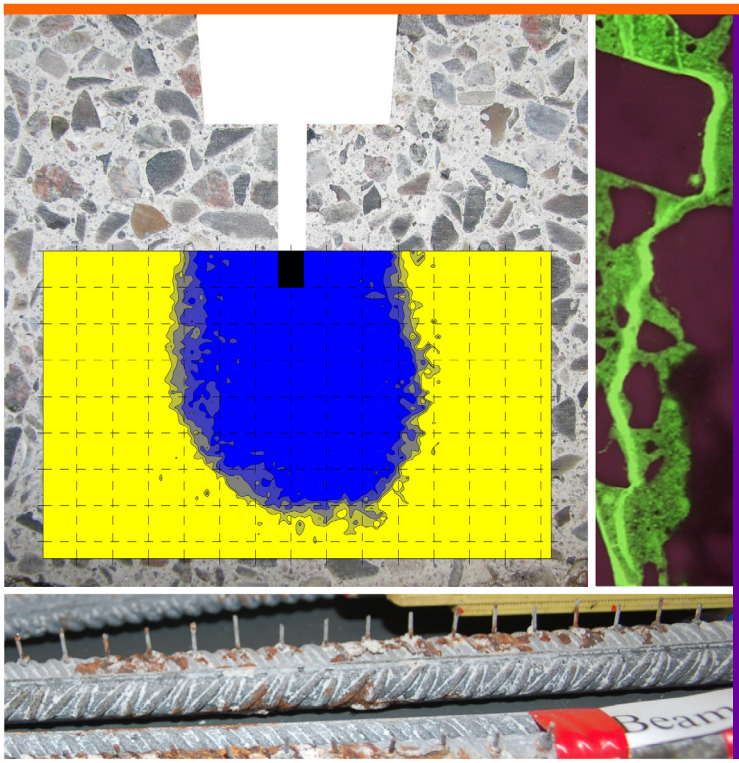

Brad J. Pease

PhD Thesis

Department of Civil Engineering

2010

DTU Civil Engineering Report R-233 (UK)
December 2010

DTU Civil Engineering
Department of Civil Engineering

Influence of concrete cracking on ingress and reinforcement corrosion

Brad J. Pease

Ph.D. Thesis

Department of Civil Engineering
Technical University of Denmark

2010

Influence of concrete cracking on ingress and reinforcement corrosion

Printed by DTU Tryk
Department of Civil Engineering
Technical University of Denmark
ISBN: 9788778773128
ISSN: 1601-2917
Report: BYG R-233

Preface

This thesis is submitted as a partial fulfillment of the requirements for the Danish Ph.D. degree. The thesis is based on experimental investigations conducted as part of the Ph.D. project "Transport and corrosion in cracked reinforced concrete," undertaken at the Department of Civil Engineering at the Technical University of Denmark (DTU Byg), Lyngby, Denmark between August 2005 and July 2009. The thesis consists of the following three parts:

I Introduction and summary
II Appended papers
III Appendix

Part **I** is the main thesis, which includes reviews of previous research, descriptions and results of all experiments carried out, discussion of results, and conclusions. Part **II** is a collection of four papers completed as part of the Ph.D. project. Part **III** is a collection of four appendices which were developed through the Ph.D. project. Appendix A includes a questionnaire and the resulting report which were used to help focus Ph.D. study based on the views of numerous experts with industrial/in-field experience. Appendix B provides additional details concerning the concrete constituent materials, while Appendices C and D are practical user guides on the photogrammetry and x-ray equipments, respectively, prepared for future researchers at the Technical University of Denmark.

The principal supervisor of the Ph.D. project was Associate Professor Mette Geiker from DTU Byg with co-supervisors Henrik Stang, also from DTU Byg, and Jason Weiss from the Purdue University School of Civil Engineering. Experimental works were carried out at DTU Byg and in the Charles Pankow Concrete Materials Laboratory at the Purdue University School of Civil Engineering.

Lyngby the 6^{th} of September 2010

Brad J. Pease

Acknowledgements

I would like to express my deepest gratitude to my supervisors, Mette Geiker and Henrik Stang at the Technical University of Denmark and Jason Weiss at Purdue University for their guidance, support, advice, and teaching throughout the course of my Ph.D. study. I have gained immeasurable experience and knowledge, not only scientific in nature, during the span of my Ph.D. research. I would like to thank all of my supervisors for their contributions to that.

Furthermore, I would like again to thank Jason Weiss and his group at Purdue University for welcoming me back to my alma mater during two external stays from the Technical University of Denmark. During that time, the assistance of Jon Couch was vital for the completion of x-ray attenuation testing completed there.

I also appreciate the support of all the laboratory assistants at the Technical University of Denmark where the majority of experimental works were completed.

Financial contributions, which supported travel including external research stays and attendance of conferences, provided by the Otto Mønsted's Fund and the DTU Byg Rejselegat were very much appreciated.

I would also like to acknowledge the continuous support of my family, albeit from a distance, including my mother, Lynn Pease; my siblings, Jason Pease, Rebecca Brown, and Jennifer Brabb; and my cousin, Marvin Matteson. I must acknowledge the assistance and friendship of several of my graduate student colleagues at the Technical University of Denmark that I had the pleasure to work with directly during my studies, including André Küter, Peter Nygaard, Alexander Michel, Anders Solgaard, Jan Skoček, and Lennart Østergaard. The assistance of Kim Beck Hansen in the preparation of the corrosion experimental setup was also greatly appreciated. And finally, I would like to extend my gratitude to all of my friends here in Denmark and back in the United States who have been a continuous support.

Abstract

Reinforced concrete is known to crack due to restrained hygral/thermal shrinkage, various expansive reactions, and the application of mechanical load. In particular, load-induced cracks are unavoidable in reinforced concrete structures as concrete cracking is required to engage the tensile capacity of the embedded steel. Cracks provide a path of least resistance for transport of moisture, chlorides, and various other deleterious substances, which may affect durability and structural performance. Cracks, reaching the depth of the steel reinforcement in reinforced concrete structures, have been shown to allow rapid depassivation of reinforcement and corrosion initiation in some cases. The goal of this work is to investigate the possibility of a link between cracking behavior of concrete and subsequent transport of moisture and chloride ions through the cracked material. Furthermore, the influence cracking has on the initiation of reinforcement corrosion was investigated as part of this Ph.D. study.

The cracking behavior was investigated using several experimental methods applied to the wedge splitting test specimen geometry. Two mixture designs were utilized, one ordinary concrete and one steel fiber reinforced concrete, in order to have mixtures with distinctly different fracture properties and cracking behaviors. Fracture properties were determined using the wedge splitting test specimen by performing inverse analysis of measured load-crack opening displacement response. Cracking behavior was investigated by impregnating cracked specimens with a fluorescent epoxy and making plane and thin sections. Moisture ingress was measured for the cracked specimens using non-destructive x-ray equipment, which detects variations in density caused by moisture entering concrete pores and cracks. By repeating measurements over time, the moisture front was tracked in cracked wedge splitting test specimens. Chloride ingress was measured through destructive testing after exposing several similarly mechanically loaded specimens to chloride contaminated water for various periods of time. The samples were split after exposure and the ingress front of chloride ions was detected by spraying the surface with silver nitrate. Comparisons of the cracking and ingress behaviors indicate only a portion of the crack length readily allows ingress of water. A portion of the crack, near the crack tip, restricts ingress of water.

To assess the influence of cracking on corrosion of reinforcement, an instrumented rebar was developed as part of the Ph.D. project. The instrumented rebar, which were cast into three point bending beam specimens, assess the aggressivity of the local environment towards corrosion of the steel reinforcement. Results indicated the length along the instrumented rebar where active corrosion was thermodynamically favored increased with

exposure time. Through this investigation, it was hypothesized that the extent of debonding along the concrete-reinforcement interface is more important than simple surface crack width measurements in terms of depassivation and corrosion of reinforcement.

Resumé

Revner opstår i armeret beton på grund af fugt- og temperaturbetinget svind, ekspansive reaktioner og mekanisk belastning. Revner forårsaget af mekaniske belastninger er en forudsætning for, at trækstyrken af den indstøbte stålarmering udnyttes og således en naturlig del af trækbelastede konstruktionsdele. Revner giver mindre modstand mod transport af fx fugt og chloridioner, som kan påvirke holdbarhed og funktion af konstruktionen. Revner med kontakt til armeringen kan således forårsage depassivering og korrosion af denne.

Formålet med det her rapporterede arbejde var at undersøge a) sammenhængen mellem revnedannelse i beton og transport af fugt og chloridioner gennem det revnede materiale og b) indflydelse af revnedannelse på initiering af armeringskorrosion.

Revnedannelse og transport af fugt- og chloridioner blev undersøgt ved hjælp af flere eksperimentelle metoder. Disse undersøgelser blev udført på betonprøver til "wedge splitting test". To betontyper blev anvendt for at variere revneformen, en traditionel beton og en stålfiberarmeret beton. Brudegenskaberne blev bestemt ved invers analyse af last-deformationskurver. Revnedannelsen blev beskrevet på basis af plan- og tyndslib af prøver imprægneret med fluorescerende epoxy. Fugtindtrængning blev målt ved hjælp af røntgenabsorption, hvorved variationer i massefylde registreres. Fugtfrontens position som funktion af tiden blev bestemt ved gentagne røntgenabsorptionsmålinger. Chloridindtrængning blev bestemt til udvalgte tidspunkter ved at flække prøverne og påsprøjte sølvnitrat, som reagerer med chloridioner. Sammenligning af revner og indtrængning viste, at en del af revnen gav direkte adgang for indtrængende væske, mens indtrængning skete langsommere i en afstand optil 16 mm eller mere fra revnespidsen.

En instrumenteret armeringsstang med sytten individuelle sensorer blev udviklet for at undersøge indflydelsen af revner langs armeringen på initieringen af armeringskorrosion blev. Den instrumenterede armeringsstang blev indstøbt i betonbjælker, som blev belastet ved tre-punkt-bøjning, og en chloridopløsning blev tilført fra en beholder monteret over revnen. Det elektrokemiske potentiale af sensorerne blev bestemt løbende gennem flere uger, og armeringen blev efterfølgende frilagt, så korrosionsomfang og chloridindtrængning kunne bestemmes. Målingerne indikerer, at revnedannelse i grænsefladen mellem beton og armeringen har større indflydelse på armeringens elektrokemiske tilstand end revnevidden på betonens overflade.

Table of Contents

List of Symbols

Abbreviations

CCD	charged couple device
CHM	cracked hinge model
CMOD	crack mouth opening displacement [mm]
CSE	copper/copper sulfate electrode [mV_{SHE}]
CSH	calcium silicate hydrate
C_2S	dicalcium silicate, $(CaO)_2 \cdot Si0_2$
C_3A	tricalcium aluminate, $(CaO)_3 \cdot Al_2O_3$
C_3S	tricalcium silicate, $(CaO)_3 \cdot Si0_2$
C_4AF	tetracalcium aluminoferrite, $(CaO)_4 \cdot Al_2O_3 \cdot Fe_2O_3$
DOF	degree of freedom
LEFM	linear elastic fracture mechanics
LPR	linear polarization resistance
MMO-Ti	mixed metal oxide activated titanium
NaI(Tl)	thallium doped sodium iodide
NDT	non-destructive test
NLEFM	non-linear elastic fracture mechanics
OCP	open circuit corrosion potential [mV_{SHE}]
RC	reinforced concrete
SCE	standard calomel electrode [mV_{SHE}]
SF	silica fume
SFRC	steel fiber reinforced concrete
SHE	standard hydrogen electrode [mV]
SSCE	silver/silver chloride electrode [mV_{SHE}]
TPBT	three point bending test
UV	ultraviolet
w/c	water-to-cement ratio
WST	wedge splitting test

Standard and derived units used

A	ampere
C	Coulomb $[A \cdot s]$

°C	degree Celsius
g	gram
kg	kilogram
J	Joule $[kg \cdot m^2/s]$
K	Kelvin
L	liter
m	meter
cm	centimeter
μm	micron or micrometer
mol	mole
Pa	Pascal $[kg/(m \cdot s^2)]$
MPa	megapascal
s	second
V	volt $[kg \cdot m^2/(A \cdot s^3)]$
mV	millivolt
mV_{SHE}	millivolt versus standard hydrogen electrode
Ω	Ohm $[kg \cdot m^2/(s^3 \cdot A^2)]$

Latin letters

(See also Δ's in Greek letters section)

a	initial crack length $[mm]$
a_i	slope of the cohesive law
a_m	WST dimension $[mm]$
a_0	WST dimension $[mm]$
a_X^x	activity of substance X raised to the stoichiometric coefficient x
b	crack length $[mm]$
b	WST dimension $[mm]$
b_a	anodic Tafel constant $[mV/A]$
b_c	cathodic Tafel constant $[mV/A]$
b_i	y-axis intersect of the cohesive law
b_m	WST dimension $[mm]$
c_i	concentration of substance, i $[g/g$ or $kg/m^3]$
$c_{i,0}$	surface concentration of substance, i $[g/g$ or $kg/m^3]$
c_b	bound chloride ion concentration $[g/g$ or $kg/m^3]$
c_f	free chloride ion concentration $[g/g$ or $kg/m^3]$
c_t	total chloride ion concentration $[g/g$ or $kg/m^3]$
$\frac{ds}{dt}$	rate of cross-sectional reduction $[cm/s]$
d	depth of crack in CHM $[mm]$
d	length of flow path $[mm]$
d_0	unit crack depth $[mm]$
d_1	WST dimension $[mm]$
d_2	WST dimension $[mm]$
e	eccentricity $[mm]$

f_t	tensile strength $[MPa]$
g	gravitational acceleration $[m/s^2]$
$g(w)$	dimensionless softening curve
h	height of cracked hinge $[mm]$
h	pressure head $[mm]$
i_{corr}	corrosion current density $[A/cm^2]$
k	intrinsic permeability $[m^2]$
k_p	permeability coefficient $[m^2/s]$
m	WST specimen mass $[kg]$
p_j	partial vapor pressure of a substance j $[Pa]$
$p_{0,j}$	saturated partial vapor pressure of a substance j $[Pa]$
q	flow rate $[m^3/s]$
q_0	flow rate through smooth parallel crack $[m^3/s]$
q_r	flow rate through rough parallel crack $[m^3/s]$
r	pore radius $[mm]$
s	cracked hinge width $[mm]$
t	specimen thickness $[mm]$
t	time $[s]$
u	deformation $[mm]$
$u(y)$	deformation of incremental strip of CHM $[mm]$
w	crack width $[mm]$
w_c	critical crack width $[mm]$
w_i	intersection of two consecutive line in cohesive law $[mm]$
w_0	unit crack width $[mm]$
$w(y)$	crack width at location, y $[mm]$
x	depth $[mm]$
y	vertical location in CHM $[mm]$
z	valence
z_i	valence of ion, i
A	absorption coefficient $[m^2/s]$
A	area $[m^2]$
A_a	area of the anode $[cm^2]$
B	absorption coefficient
B	Stern-Geary coefficient
$CMOD_{exp,Hinge}$	crack mouth opening displacement from experimental data and cracked hinge model $[mm]$
D	diffusion coefficient $[m/s^2]$
D_i	diffusion coefficient of ion, i $[m/s^2]$
D_{RH}	diffusion coefficient at given RH, i $[m/s^2]$
D_{REF}	reference diffusion coefficient $[m/s^2]$
D_{100}	diffusion coefficient at 100% RH, i $[m/s^2]$
E	elastic modulus $[GPa]$
E	electrical potential $[mV]$
E_0	equilibrium potential $[mV]$
E_0^0	standard equilibrium potential $[mV]$

I_{corr}	corrosion current $[A]$
F	Faraday's constant = 96,485 $C/mol\ e^-$
F_e	convection ion flow $[mol/m^2 \cdot s]$
F_i	total ion flow $[mol/m^2 \cdot s]$
G_c	critical energy release rate $[J/m^2]$
G_F	fracture energy $[J/m^2]$
$K_{I,II,III}$	stress intensity factors modes I-III $[MPa\sqrt{mm}]$
K_{I_c,II_c,III_c}	critical stress intensity factors modes I-III $[MPa\sqrt{mm}]$
L	WST dimension $[mm]$
L_{char}	characteristic length $[mm]$
$M_{exp,Hinge}$	experimental and cracked hinge bending moment $[kN \cdot mm]$
M	molecular weight $[g/mol]$
P	load $[N]$
P	pore pressure $[MPa]$
P_{exp}	load from experimental results $[N]$
P_{Hinge}	load predicted by CHM $[N]$
P_{sp}	splitting load $[N]$
P_v	vertical load $[N]$
$Q_{cl}(t)$	time-dependent chloride ions ingress $[kg/m^3]$
R	ideal gas constant = 8.314 $J/(K \cdot mol)$
R_p	polarization resistance $[\Omega]$
RH	relative humidity [%]
S	sorptivity $[mm^2/s]$
S_i	sorptivity at uniform moisture content, θ_i $[mm^2/s]$
S_0	sorptivity of dry specimen $[mm^2/s]$
T	temperature $[K]$
V_m	molar volume $[m^3/mol]$

Greek letters

α	coefficient in Equation 3.8
α_w	wedge angle [°]
β_i	dimensionless factor
γ	surface tension $[dyne/cm]$
δ_e	elastic deformation $[mm]$
δ_g	geometrically amplified deformation $[mm]$
δ_w	deformation from crack $[mm]$
ε	elastic strain [mm/mm]
$\varepsilon^*(y)$	mean longitudinal strain [mm/mm]
ζ_i	dimensionless factor
η	absolute viscosity $[Pa \cdot s]$
θ	contact angle between liquid and solid phases [°]
θ_i	uniform moisture content
$\lambda_{Ca,Cl}$	crack influence factor for carbonation and chloride ions

μ	linear attenuation coefficient $[cm^{-1}]$
μ	viscosity $[kg/(m \cdot s)]$
μ_c	roller bearings frictional coefficient
ξ	roughness factor
ρ	density $[g/cm^3]$
ρ_w	water density $[g/cm^3]$
σ	normal stress $[MPa]$
σ_c	critical stress level $[MPa]$
$\sigma_w(w)$	cohesive stress $[MPa]$
υ_1	geometric function
υ_2	geometric function
ϕ	material porosity
φ	angular rotation [radians]
Δi_p	measured change in current density $[A/cm^2]$
Δp	change in water pressure $[Pa]$
ΔE_p	potential applied during LPR $[mV]$
ΔG	Gibbs free energy $[J]$

Part I

Introduction and summary

Chapter 1

Introduction

1.1 Background

1.1.1 Basics of reinforced concrete

Reinforced concrete (RC) is a versatile and widely used composite building material consisting of concrete and embedded reinforcement, which is typically steel. Figure 1.1 shows several applications of RC, which can be shaped, textured, and colored for architectural and aesthetic considerations. Structural designers utilize RC as a composite material, where concrete is relied upon to resist compressive load and steel resists tensile loads as concrete is relatively weak in tension. Concrete cracking is required in the composite material in order to fully engage the tensile capacity of the reinforcement and to ensure a safe (i.e. non-brittle) structural response of the structure to load.

Concrete, in an uncracked condition, provides an effective cover to protect reinforcement from corrosion. The high alkalinity of concrete pore solution, as discussed further in Chapter 4, places reinforcing steel in a thermodynamically passive corrosion region where corrosion rates are practically negligible. Additionally, concrete (especially concretes with low water-to-cement ratios, supplementary cementitious materials, etc.) provides a dense covering material over reinforcement. As described in Chapter 3, this slows the ingress of various aggressive substances (e.g., chloride ions, carbon dioxide, moisture, oxygen), which contribute to reinforcement corrosion.

Reinforcement is typically provided by high strength steel reinforcing bar (rebar). While other rebar materials such as stainless steel and fiber reinforced polymers provide additional corrosion resistance, the associated cost increase limits the use of these materials. Reinforcement corrosion can present a danger to structural stability (through loss of tensile load capacity, concrete spalling, etc.) and durability. Deterioration of RC structures through reinforcement corrosion may lead to costly repairs, need for replacement, or potentially dangerous conditions where sudden structural failures may occur.

1.1.2 Concrete cracking

Cracking of concrete and reinforced concrete may occur, as illustrated in Figure 1.2, due to a multitude of potential mechanisms. Types of cracks include the following, with symbols

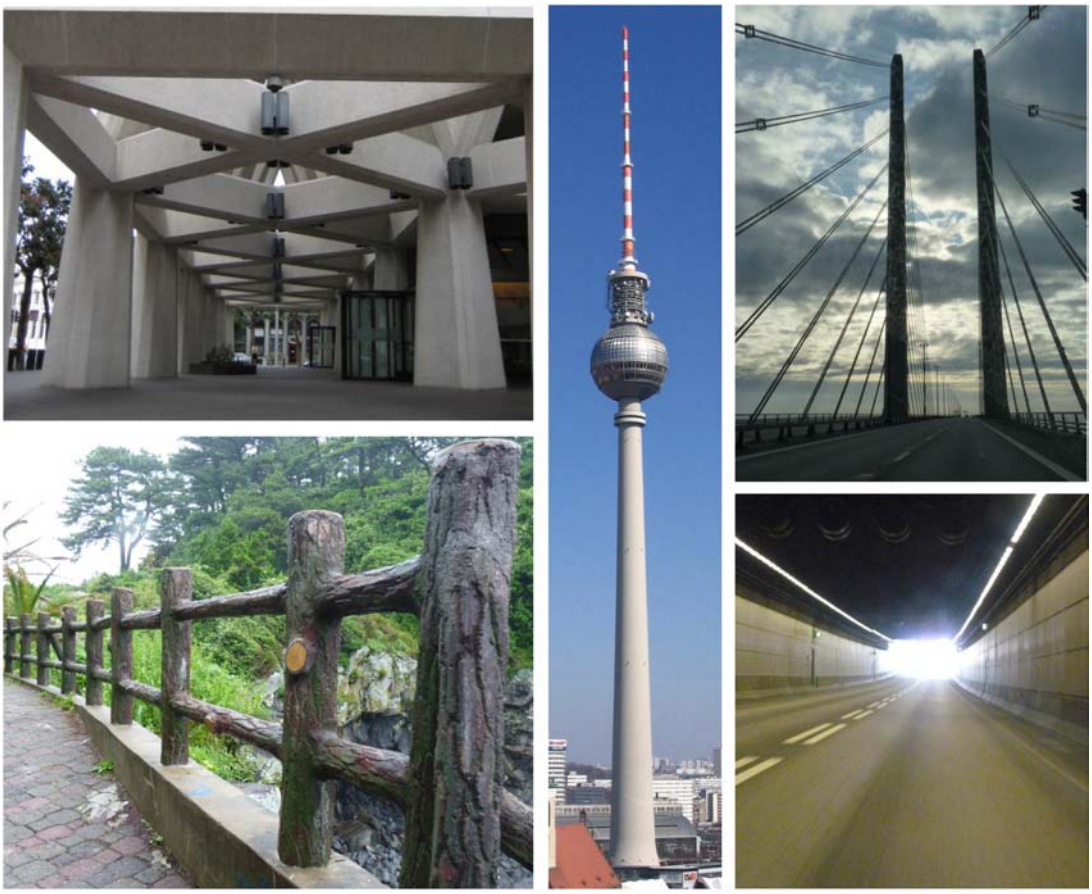

Figure 1.1 *Various structural and architectural applications of RC, including (clockwise from top left) the atrium of the Transamerica Pyramid in San Francisco, California; Fernsehturm 'television tower' in Berlin, Germany; Øresund Bridge and tunnel between Denmark and Sweden; and faux-wood concrete railing on Jeju Island, S. Korea. (Author's photos)*

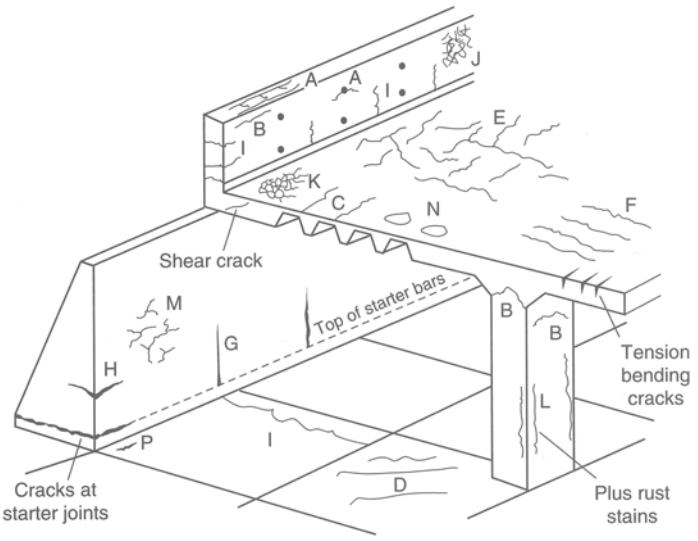

Figure 1.2 *Examples of intrinsic cracks in hypothetical concrete structure, from [Concrete Society Report, 1992; Neville, 1996].*

corresponding to those in Figure 1.2:

- Plastic settlement cracking:
  - A – Over reinforcement in deep sections
  - B – Arching at column tops
  - C – Changes in cross-sectional depth
- Plastic shrinkage cracking:
  - D – Diagonal cracking of slabs
  - E – Random cracking
  - F – Over slab reinforcement
- Thermal shrinkage cracking due to:
  - G – External restraint
  - H – Internal restraint
- I – Shrinkage cracking
- Crazing:
  - J – Against the formwork
  - K – Over troweling
- L – Corrosion induced cracking
- M – Alkali-aggregate reaction induced cracking
- N – Blistering of slabs cause by trapped bleed water
- P – D-cracking due to freeze-thaw damage
- Load-induced cracking:
  - Tension and bending cracking
  - Shear cracking

The majority of these cracks can be largely avoided through proper mixture design, placement, compacting, finishing, and curing techniques. However, load-induced cracking is inevitable in RC structures as described above.

1.1.3 Predicting service life of reinforced concrete structures

Service life models, such as DuraCrete [*DuraCrete*, 2000], *fib* [*fib Bulletin 34*, 2006], Life-365 [*Ehlen et al.*, 2009; *Life-365 Consortium II*, 2010], 4sight [*Synder*, 2001], Hetek [*Nilsson et al.*, 1996, 1997; *Frederiksen and Poulsen*, 1997], Stadium [SIMCO, 2009], etc., have been developed to provide tools to estimate the length of time during which a RC structure maintains a desired level of functionality. Figure 1.3 illustrates the basic approach of these service life models. Two phases exist in the service life of a RC structure – initiation and propagation phases. A limit state is set as the end of service life of a given RC structure, at which time either maintenance/repair or demolition is required. In some cases the propagation phase is considered as part of the service life [*Life-365 Consortium II*, 2010]. However, uncertainties during the propagation phase typically lead to the end of the initiation phase also indicating the end of the predicted service life.

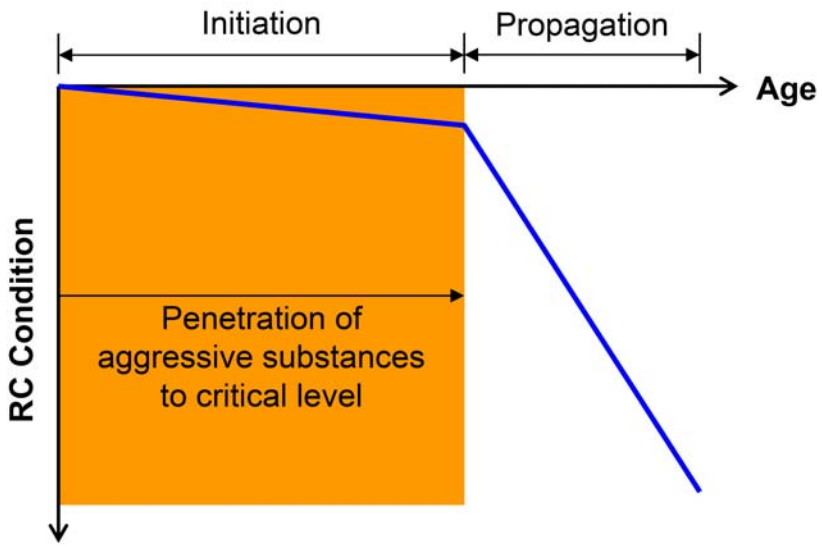

Figure 1.3 *Schematic of a service life model for RC, after [Tuutti, 1982a].*

During the initiation phase, the RC structure is exposed to environmental and mechanical loading. Substances that may lead to the initiation of corrosion, such as chloride ions or carbon dioxide, penetrate into the concrete cover during the initiation phase. Service life models for reinforcement corrosion estimate the time required for a critical amount of these aggressive substances to reach the level of the reinforcement. At that time, corrosion of the reinforcement is probable and the initiation phase of the service life ends.

During the corrosion propagation phase, the reinforcement cross-section reduces and corrosion products are deposited within the concrete. Reduction in reinforcement cross-section affects load carrying capacity and may lead to structural failure, while the expanded volume of corrosion products may cause cracking and spalling of covering concrete. The rate of concrete deterioration increases greatly during the corrosion propagation phase, compared to the initiation phase. Extensive research work has been conducted on modeling the effects of corrosion propagation, including reinforcement cross-section reduction [*Hasegawa et al.*, 2004; *Isgor and Razaqpur*, 2006] and damage to the concrete cover [*Alonso et al.*, 1998; *Liu and Weyers*, 1998; *Li*, 2003; *Vu et al.*, 2005; *Ahmed et al.*, 2007; *Li et al.*, 2008; *Hwan Oh et al.*, 2009]. However, numerous factors, including environmental conditions (temperature and relative humidity), loading of the structure (dynamic or static), material properties of the concrete after years of service, etc., influence the propagation phase, causing uncertainties with such predictions.

The potential benefits of service life modeling has become more recognized in the civil engineering community as owners' service life requirements continue to increase, while little information on reaching such requirements is provided in structural design codes. For example, service life's of 100 to 200 years are becoming more common in Denmark and internationally (e.g., Great Belt and Øresunds Links in Denmark were designed for a 100 year service life and the proposed Messina bridge between Sicily and Italy will have a 200 year service life); however, the concrete cover thicknesses specified in [EuroCode2, 2003] assume a service life of 50 years. American design codes do not provide estimated service life's from the specified concrete cover thicknesses [*ACI Committee 318*, 2008; *AASHTO*, 2007]. Service life models therefore aid designers in determining adequate concrete diffusion coefficients and cover thicknesses to ensure these requirements are met by the uncracked concrete.

While the benefits of existing service life models are clear, improvements are still needed to more accurately portray actual as-built RC structures. One area in which further scientific knowledge is needed to improve service life models is the role of cracking on durability of RC structures. As discussed above, concrete cracks form through various physical and chemical processes (Figure 1.2) and at varying periods of the lifetime of a structure. In particular, mechanical load-induced cracking is unavoidable in RC. As discussed in Chapters 3 and 4, respectively, cracking can enable rapid ingress of aggressive substances and an accelerated depassivation of reinforcing steel. This may reduce the initiation phase of the service life (Figure 1.3) and cause accelerated deterioration of RC structures compared to model predictions.

1.2 Scope and objectives

The general objective of this Ph.D. study was to investigate the effect cracking has on the ingress and corrosion behavior of RC. To narrow the scope of the study it was decided to focus on partially saturated concretes and mechanical load-induced V-shaped cracks, as mechanical load-induced cracks are unavoidable in practice. In a series of experimental specimens the fracture mechanics properties, ingress behavior of water and chloride con-

taminated water, and corrosion initiation behavior was investigated.

The main objectives of this research were:

- To quantify the effect cracks, of varying dimension, have on ingress of liquid water through concrete,
- To assess the effect changing fracture properties have on cracking and ingress behaviors,
- To link these ingress behaviors to a mechanical model which describes the cracking behavior of concrete, and
- To study the effect cracks have on the thermodynamic state of steel reinforcement as a function of distance from a crack in RC.

1.3 Testing paradigm

Table 1.1 lists all test completed and presented throughout this thesis. Additional details and descriptions of each test method are provided in the following chapters. As shown, two mixtures were used for some testing. Details of the mixture designs are presented in Chapter 2.

Table 1.1 *Overview of test methods/purpose and the number of individual samples used for each test.*

Test method	**Test purpose**	**Number of specimen used**	
		Mixture 1	**Mixture 2**
Wedge split testing	Fracture parameter determination	3	3
	Assessment of effect of plastic shims	-	2
	Assessment of cracking behavior	3	1
	Water ingress testing	7	7*
	Chloride ion ingress testing	12	12
Three point bending beam†	Assessment of cracking behavior	1	-
	Corrosion testing	6	-

* Water ingress results not presented in thesis
† Beams cast with an instrumented rebar

1.4 Organization of contents

This thesis is divided into three parts, including:

I Introduction and summary
II Appended papers
III Appendices

Part **I**, which is the main thesis, includes reviews of previous research, descriptions and results of all experiments carried out, discussion of results, and conclusions. The contents

of the chapters comprising Part **I** are summarized in the following paragraphs. Part **II** is a collection of four papers completed as part of the Ph.D. project. These papers were utilized during the writing of, and are referenced within, this thesis. However, the thesis is a stand-alone document containing information not yet published in the appended papers or elsewhere. Part **III** is a collection of four appendices which were developed through the Ph.D. project. Appendix A includes a questionnaire and the resulting report which were used to help focus Ph.D. study based on the views of numerous experts with industrial/in-field experience. Appendix B provides additional details concerning the concrete constituent materials. Appendix C is a quick guide for the setup, use, and analysis of data from the photogrammetric equipment used (called Aramis). The author was one of the initial user of the equipment at DTU Byg and the guide was created after his experience to assist future users. Similarly, Appendix D is a practical guide to the use of the x-ray attenuation system located at DTU Byg. During the term of the presented Ph.D. study a major update of the equipment was completed, namely, installation of an 'x-ray camera' (see Chapter 4). The author was the first user after the update and a practical guide was developed based on his experience to assist future users with the basic and advanced operations of the system and analysis of x-ray attenuation images. Part **I** is organized as follows.

Chapters 2 to 4 present detailed descriptions of the experimental works completed. Each chapter consists of an introduction section, an experimental procedures section, a results section, and a summary and conclusions section. The introduction sections present a background of knowledge including basic principles and a literature study. The experimental procedures sections present details of the testing completed as parts of this Ph.D. study. The result sections present and discuss the results of experiments completed, while all major findings are listed in the summary and conclusions sections.

Chapter 2 introduces the wedge splitting test specimen, which was utilized extensively through this research, as well as the mixture proportions used throughout this work. Fracture properties were determined for each mixture through inverse analysis of the experimental data by applying a cracked hinge model to the wedge splitting test specimen geometry. Optimization and sensitivity analysis of the inverse analysis results indicate a 3–slope cohesive law provides the optimal number of degrees of freedom to both accurately and repeatedly fit experimental data. Cracked specimens, impregnated by a fluorescent epoxy, indicated cracking occurred at locations in the wedge splitting test specimen which violate assumptions of the applied cracked hinge model; therefore, photogrammetry measurements were also used to determine fracture properties. Additionally, comparison of measured and estimated crack profiles show that cracks in the wedge splitting test specimen consist of a coalesced crack which follows a region of non-coalesced cracking that has a relatively consistent length. Finally, it was found that inserting plastic shims into the cracked wedge splitting specimens drastically reduced crack width recovery, which was an important observation for the work presented in Chapter 3.

Chapter 3 describes the use of cracked wedge splitting test specimens to assess the influence cracking has on ingress of moisture and chloride ions. Cracked specimens were

exposed to liquid water and the ingress behavior was monitored using x-ray attenuation measurements. Chloride ingress was observed by splitting specimen and spraying with silver chloride. It was found that as the crack mouth opening displacement increases moisture and chloride ions reached deeper into the WST specimens. X-ray attenuation measurements indicated that only a portion of the crack length has a free surface sorption behavior, while a consistent length of the total crack inhibits water sorption. This relates to the observation from Chapter 2 that a portion of the crack is not coalesced.

In Chapter 4 a new type of instrumented rebar is described, which was designed to measure local environmental condition along the length of the rebar, to assess how cracking influences reinforcement corrosion. The instrumented rebars were cast along with a standard rebar into three point bending beams, which were loaded to induce cracks of varying width and were exposed to a chloride solutions. It was found that the instrumented rebar had a similar mechanical behavior as standard rebar, carrying tensile loads and inducing similar cracking at the concrete/steel interface and in the concrete. Measurements from the instrumented rebar indicated that increased crack width allowed the local environment to changed more rapidly, favoring depassivation of the reinforcement. However, results indicated the length along the instrumented rebar where depassivation of the steel was favored due to the environment was significantly larger than the length where active corrosion was actually observed. This was explained as the formation of anodic site 'protects' other regions of the reinforcement where the environment favored depassivation. One beam was impregnated with fluorescent epoxy to highlight the cracks. Comparison of the cracking behavior to other measurements seems to indicate the slip and separation between the reinforcement and concrete more fundamentally affects reinforcement corrosion in cracked concrete, rather than the surface crack width.

Chapter 5 compares and discusses selected results presented in the preceding chapters and from the appended papers in **Part II**. Data from the multiple experiments is compared to construct an argument for a model which combines fracture and ingress behavior. Additionally, the effect damage along the interface of concrete and steel reinforcement has on reinforcement corrosion is discussed. The chapter also provides a listing of the conclusions based on the observations made in this research.

Chapter 2

Determination of fracture properties of unreinforced concrete

2.1 Introduction

This chapter presents investigations using wedge splitting test (WST) specimen to determine fracture properties and cracking behavior of the concrete and steel fiber reinforced concrete (SFRC) mixtures used throughout the presented Ph.D. project. Section 2.1 introduces important terms and principles of fracture mechanics and properties and describes the application of fracture mechanics to cementitious materials. Details of the experimental investigation completed as part of this project are presented in Section 2.2. Results and discussion of results are presented in Section 2.3. Conclusions of these investigations are presented in Section 2.4.

The following sections provide a brief review of the development of fracture mechanics over the past century including testing and analysis procedures for determination of fracture mechanics properties in cementitious materials. The intent of this section is to introduce terms and concepts important to the work completed as part of this Ph.D. study. This is not intended to be a complete review of the field as such information is available elsewhere (e.g., [*Shah et al.*, 1995; *Karihaloo*, 1995; *van Mier*, 1997; *ACI Committee 446*, 1991; *Anderson*, 2005]).

2.1.1 Fracture mechanics of concrete

Linear elastic fracture mechanics

Fracture mechanics was first introduced, in the form of linear elastic fracture mechanics (LEFM), by A. A. Griffith to describe the fracture behavior and size effect of glass and other brittle materials [*Griffith*, 1920]. Griffith determined that a remote stress applied to a brittle material causes stresses near a crack tip to approach infinity, as shown in Figure 2.1. Based on this observation, Griffith and later Irwin [*Irwin*, 1957] showed the process of crack propagation can be idealized as a energy balance in which one side of the balance holds the energy required to create a new surface and the other holds a change in potential energy. Equation 2.1 expresses this energy balance, according to Griffith (first

part) and Irwin (second part):

$$\sigma_c = \sqrt{\frac{EG_c}{\pi a}} = \frac{K_{Ic}}{\sqrt{\pi a}} \tag{2.1}$$

where σ_c is the critical stress level, E is elastic modulus, a is the initial crack length, and G_c is the critical energy release rate (Griffith formulation) and K_{Ic} is the critical stress intensity factor (Irwin formulation). G_c and K_{Ic} are both material properties. In both formulations, if $\sigma < \sigma_c$ the material is capable of carrying such load without further cracking, while if the critical stress is reached uncontrolled cracking and failure occurs.

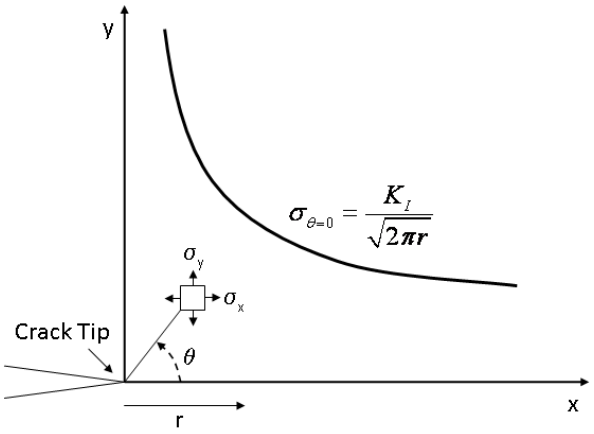

Figure 2.1 *Stress distribution near crack tip according to linear elastic fracture mechanics*

Griffith used Equation 2.1 to explain experimental results indicating that reducing cross-section of a piece of glass increased its strength. The initial crack length, a represents defects intrinsic to the material, surface defects and scratches in the case of glass. Other examples of intrinsic material defects include point or dislocation defects in metals and pores, cracks, etc. in the cementitious materials.

The experimental foundation of Griffith's work [*Griffith*, 1920] was tensile testing, resulting in Mode I, or opening mode, fracture. Figure 2.2 shows the possible crack tip deformation modes including Mode I – opening mode, Mode II – sliding or shearing mode, and Mode III – tearing mode. Irwin [*Irwin*, 1957] determined the order of the stress singularity near crack tip shown in Figure 2.1 holds for all fracture modes; however, the critical stress intensity factor is a function of the fracture mode. Therefore K_{Ic}, K_{IIc}, and K_{IIIc} correspond to the critical stress intensity factor for mode I, II, and III, respectively, and all are material properties.

Attempts to apply LEFM to cementitious materials determined a size-dependency in values of G_c and K_{Ic} [*Karihaloo*, 1995; *ACI Committee 446*, 1991]. A critical assumption of LEFM concerns the size of the fracture process and non-linear zones. As shown in Figure 2.3(a), LEFM assumes a minute region of non-linear behavior. This assumption is largely correct for brittle materials. Ductile and quasi-brittle fracture however have

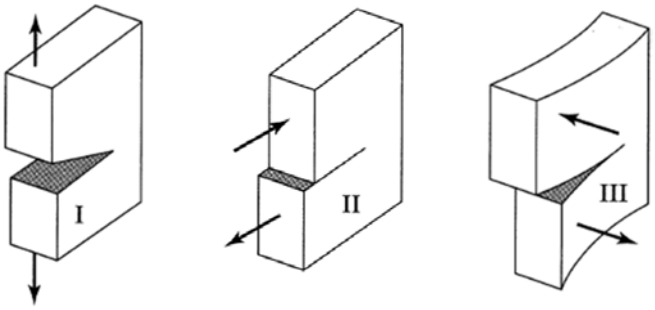

(a) (b) (c)

Figure 2.2 *Fracture modes include (a) mode I opening, (b) mode II sliding, and (c) mode III tearing [Mindess et al., 2003].*

much larger non-linear regions as shown in Figure 2.3(b) and (c), respectively. Therefore, non-linear elastic fracture mechanics (NLEFM) approaches have been developed and have emerged as powerful and increasingly accepted techniques to describe the load response of cementitious and other quasi-brittle materials. The development of NLEFM is shortly described below.

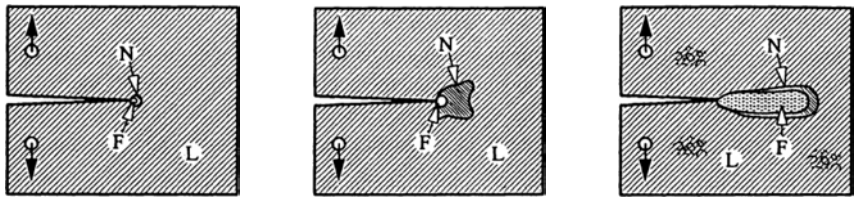

(a) (b) (c)

Figure 2.3 *Conceptualistic schematic of (a) linear elastic fracture mechanics, (b) non-linear plastic fracture mechanics, and (c) non-linear quasi-brittle fracture mechanics. Regions in the schematics include the linear zone (L), non-linear zone (N), and fracture process zone (F) [Bazant, 1985; ACI Committee 446, 1991; Karihaloo, 1995].*

Non-linear elastic fracture mechanics

Cohesive crack models, introduced in [*Barenblatt*, 1959] and [*Dugdale*, 1960] for metals, consider the energy required to initiate and propagate a crack and the ability of stresses to be transferred across a crack up to a particular, critical width. Based on these principles Hillerborg's fictitious crack model [*Hillerborg et al.*, 1976] was initially developed for concrete and later shown to be applicable to fiber reinforced concrete [*Hillerborg*, 1980].

Hillerborg's fictitious crack model assumes a linear-elastic response until the tensile strength has been reached. Crack propagation commences when the tensile strength is exceeded; however, stresses still transfer across the crack in a fracture process zone which consists of microcracking, aggregate and fiber bridging, and other toughening mechanisms as shown

in Figure 2.4. In the Hillerborg approach fracture energy is consumed in the fracture-process zone, which in theory causes a smooth crack closure, a zero stress intensity factor at the crack tip, and transfer of stress controlled by the crack width opening. The stress distribution and transfer of stress across the fracture process zone in cracked concrete is illustrated in Figure 2.5. Figure 2.6 shows the material responses used in the fictitious crack model (i.e., fracture properties), starting with a linear-elastic response (Figure 2.6(a)) up to a critical stress level, σ_c, causing cracking followed by a cohesive laws which describes the post-crack material response. Two generic exemplary cohesive laws are shown in Figures 2.6(b) and (c). The stress transferred across the fracture process zone is controlled by the cohesive laws and as seen the cohesive stress tends to decrease with increasing crack width. Depending on the method used to estimate the cohesive law the cohesive stress may increase and decrease until a critical crack width, w_c is reached, where stresses are no longer transferred.

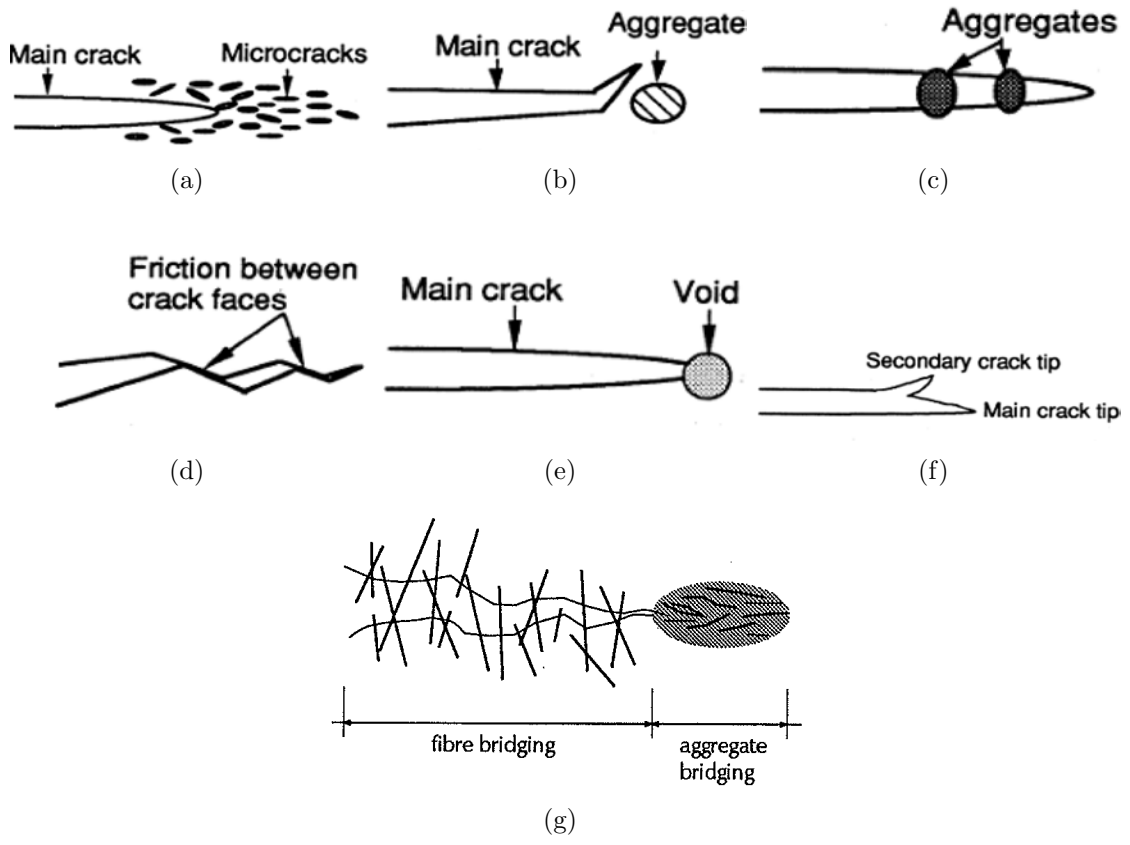

Figure 2.4 *Fracture toughening mechanisms in cementitious systems (a)–(f) [Shah et al., 1995] and (g) the fiber bridging mechanisms in fiber reinforced cementitious systems [van Mier, 1997].*

2.1.2 Methods for determining fracture properties of concrete

The simplest technique for determining fracture properties (i.e., material responses shown in Figure 2.6) of concrete is, in theory, a direct measurement using the uniaxial tensile

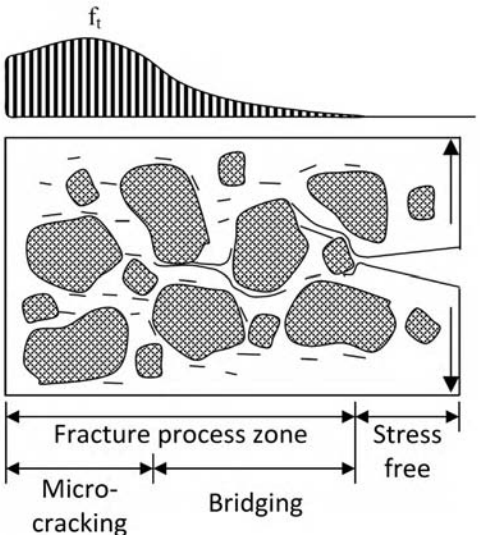

Figure 2.5 *Stress distribution assumed in Hillerborg's fictitous crack model and the corresponding details of the fracture process zone [Østergaard, 2003].*

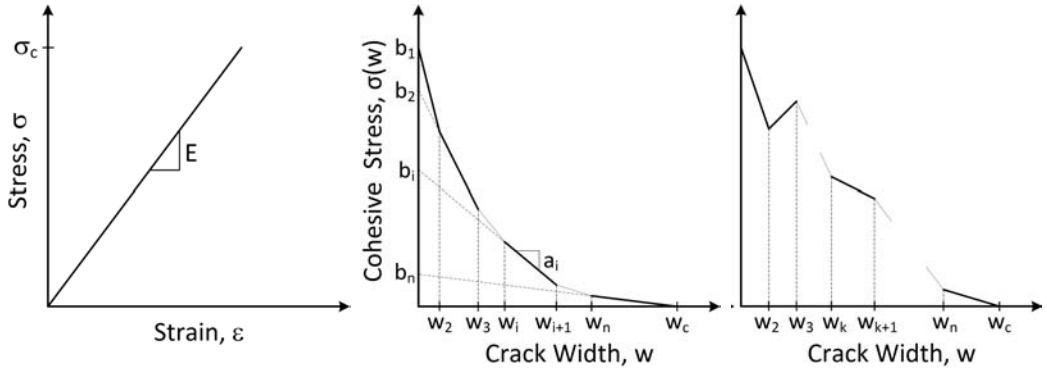

(a) (b) (c)

Figure 2.6 *Material response assumed in the Hillerborg's fictitous crack model including (a) linear-elastic response prior to cracking and (b) and (c) two possible generalized cohesive laws describing the post-cracking response, after [Østergaard, 2003; Skoček, 2010].*

test. However, in practice, results from the uniaxial tensile test are heavily dependent upon load eccentricities, complications from multiple cracking, stiffness of the loading machine, and other issues as discussed in [*van Mier and van Vliet*, 2002; *Østergaard*, 2003]. Other specimen geometries may however be used to indirectly determine the cohesive law of concrete. These indirect techniques use more stable loading configurations to measure the post-peak load response by inducing and stably propagating a single crack in a controlled manner. Fracture properties may then be estimated through an inverse analysis of an applicable analytical or numerical model, as discussed below.

The three-point bending test (TPBT) (cf., Figure 4.16) is one such indirect test which

may be used to determine fracture properties of concrete. The large elastic energy storage capacity of the TPBT specimen requires careful control to avoid snapback behavior or uncontrolled failure particularly in very brittle materials (i.e., cement paste). An additional drawback of the TPBT is the relatively large size and weight of the specimen, which limits its versatility (e.g., early-age testing) [*Østergaard*, 2003].

The wedge splitting test (WST) shown in Figure 2.8 provides an alternative, simple method to stably propagate a single crack in relatively small specimen (cf. Figure 2.7, 100 mm^3 commonly used). The WST, developed in [*Linsbauer and Tschegg*, 1986] and its predecessor the wedge loaded compact tension test [*Hillemeier and Hilsdorf*, 1977], utilize a wedge to induce a splitting load (Figure 2.8). Therefore, splitting displacements applied to the specimen are only a fraction of vertical load actuator displacements, easing control of crack propagation. In addition, analysis and secondary experimental procedures, described in the following paragraphs, have been developed for use with the WST specimen.

As previously mentioned the cohesive law is not directly measured by the WST and TPBT. Therefore, inverse analysis of an analytical or numerical model is required. Inverse analysis techniques estimate the cohesive law by minimizing differences between experimental and model results. Most inverse analysis techniques work in one of two ways: i) the cohesive law has a predefined shape, as shown in Figure 2.6(b), and through inverse analysis the slopes and intercepts are determined, or ii) the cohesive law is determined in an incremental analysis to determine the slopes and intercepts without a predefined shape, as shown in Figure 2.6(c). While the latter technique, described in [*Nanakorn and Horii*, 1996; *Kitsutaka*, 1997], allows for any shape of the cohesive law, problems have been found in the estimation of the tensile strength [*Uchida and Barr*, 1998]. In addition due to the incremental approach used, estimate error from previous steps in the inverse analysis effect estimates of later steps, causing an accumulation of errors. A technique described in [*Østergaard*, 2003] utilizes a cracked hinge model (CHM) developed in [*Olesen*, 2001] with a predefined bi-linear cohesive law. This technique has been implemented with success to the WST geometry for concrete [*Østergaard*, 2003], fiber reinforced concrete [*Löfgren et al.*, 2005], and even interfaces of cementitious materials and steel [*Walter et al.*, 2005]. In [*Skoček and Stang*, 2008] this technique was expanded to allow additional slope changes in the predefined cohesive law (as shown in Figure 2.6(b)), improving the results of the inverse analysis in the post-peak load region. Additional details on the WST specimen and procedure, application of the CHM to the WST geometry, and the inverse analysis technique from [*Skoček and Stang*, 2008] are provided in Section 2.2.

2.2 Experimental procedures

The following sections describe the experimental investigations completed as part of this study using the WST to ascertain the fracture behavior of the concrete mixtures used throughout this work. The goal of this section of the work is to determine the cohesive laws and other material properties of the concrete mixtures for use in future modeling. The materials and concrete mixtures are introduced in Section 2.2.1, followed by descriptions

of the test methods and inverse analysis in Sections 2.2.2 and 2.2.3, respectively. Results are presented in Section 2.3.

2.2.1 Materials and specimen preparation

Two different concrete mixture designs were used for the testing described here, one with steel fibers and one without. In addition, Mixture 1 was used for all testing described in Chapters 3 and 4. Table 2.1 provides details on each mixture (see Appendix B for additional details on the constituent materials). Aalborg white portland cement was used with an estimated Bouge composition of 78.8% C_3S, 10.5% C_2S, 4.9% C_3A, 1.0% C_4AF, 0.6% MgO, 2.1% SO_3, and an Na_2O equivalent alkali content of 0.19%. Class E 0-4 mm sea-sand was used along with washed Class A 4-8 mm sea-gravel (classifications in accordance with [*DS-2426*, 2004]). Mixture 1 was a typical concrete, developed in a previous project [*Nygaard*, 2008]. Mixture 2 was a SFRC mixture with the same type and relative proportion of sand and coarse aggregate as Mixture 1 with 1% of the aggregates replaced with steel fiber. The steel fibers had a length of 12.5 mm and diameter of 0.4 mm. The fibers used for were steel with an elastic modulus of 200 GPa and tensile strength of 1300 MPa. All constituent materials are shown in Figure B.1 in Appendix B.

Table 2.1 *Mixture proportions.*

Mixture I.D.	**1**	**2**
w/c	0.50	0.50
Cement Content (kg/m^3)	330	330
Sand Content (kg/m^3)	766	764
Coarse Aggregate (kg/m^3)	1103	1099
Fiber Content (kg/m^3)	—	19

The concrete was mixed using a standard pan mixer with a 120 L capacity. The fine and coarse aggregate were first mixed dry for 1 minute, followed by 3 minutes mixing with one third of the mixing water. Mixing was stopped for 2 minutes prior to adding and mixing the cement for 1 minute. The remaining water was then added and mixing continued for 3 minutes after addition of water. The mixer was then opened and the pan and blades were scraped, followed by 1 additional minute of mixing. Compressive cylinders with a 100 mm diameter and 200 mm height were cast for all batches to assess quality. The concrete was placed into forms and consolidated using an external vibrator.

After casting and vibrating, the specimens were stored in laboratory conditions (i.e., 18°C ±2°C) overnight covered with wet burlap and plastic sheet. The samples were demolded after 24 hours and were sealed using multiple layers of thick plastic sheet and packaging tape. Once the samples were sealed they were placed in a environmental chamber at 20°C ±2°C and 85% ±2% relative humidity (RH) for 6 additional days. After this time the samples were placed in an large-capacity oven at 45°C ±2°C to accelerate curing. A large bucket was kept filled with water at the bottom of the oven in order to increase RH to limit the risk of drying. Once the samples reached the desired maturity age (at least 12

months) they were removed from the plastic and placed in chambers at 50% ±3% RH and 20°C ±2°C (RH controlled by salt solution). These procedure and mixture designs presented in Table 2.1 were used throughout this entire thesis, unless otherwise noted.

2.2.2 Wedge splitting test (WST) method

Figure 2.7 illustrates the WST specimen geometry. The specimen consists of a 100 mm x 100 mm x 100 mm concrete prism, with a 30 mm x 32 mm x 100 mm recess centered on the top of the specimen. The void is cast-in using a specialty mold particularly for WST specimens. After casting and curing of the WST specimen (but prior to conditioning) a notch is cut a further 28 mm from the bottom of the void using a water-cooled concrete saw. The notch has been cut into the specimens rather than cast as to eliminate edge effects. In addition to cutting the notch, all specimen were cut in half (perpendicular to the notch) resulting in two separate specimen of thickness 50 mm. Halving the specimens was necessary for moisture ingress testing described in Chapter 3.

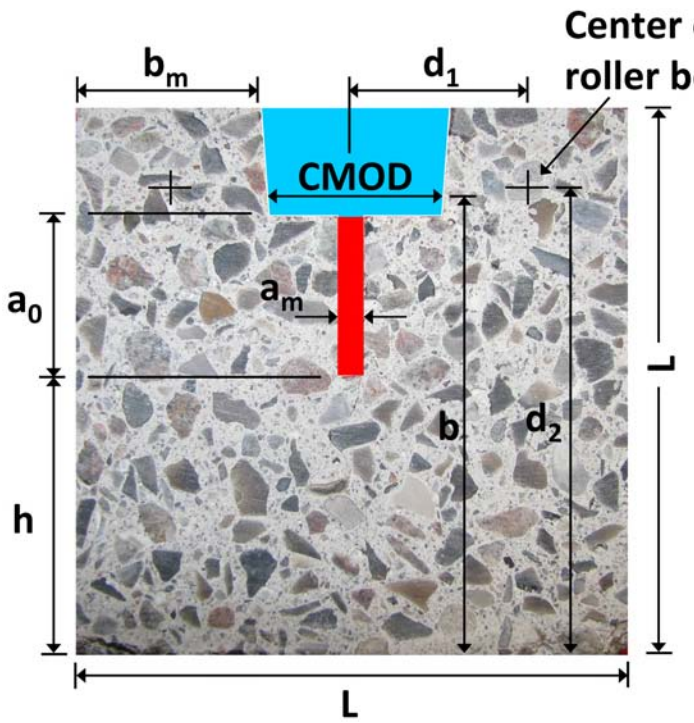

Label	Length (mm)
a_0	28
a_m	4.5
b	83.5
b_m	35
d_1	39.5
d_2	85.4
h	50
L	100

Figure 2.7 *WST specimen geometry with the blue region indicating the cast-in recess and the red region indicating the 4.5 mm notch cut using a wet-saw.*

The WST method applies a splitting load using a rigid steel wedge and roller bearings as pictured in Figure 2.8(a). Loading is controlled by displacement measurements from a clip gage inserted into the recess (see Figure 2.7) of the WST specimen to measure the crack mouth opening displacement (CMOD). The clip gage was modified by using brass feet that contact the side of the recess, as shown in Figure 2.8(b). Vertical load is recorded by the testing machine, and used for calculation of the splitting load. The

wedge angle, from vertical, used for testing was 15°. The rate of CMOD increases was initially 0.05 mm/min to a CMOD of 0.4 mm. After reaching 0.40 mm CMOD the rate was increased to 0.10 mm/min, which minimized testing time while still providing a stable crack growth. Extensive details on the WST procedure is available in the literature [*Linsbauer and Tschegg*, 1986; *Brühwiler and Wittman*, 1990; *Østergaard*, 2003].

Testing completed for this work included loading three WST specimens from both mixtures (concrete and SFRC) to a CMOD of 1.8 mm for determination of fracture properties using the inverse analysis technique described in Section 2.2.3. Additional WST specimen were loaded to varying loads and CMOD's (peak load and 0.10 mm, 0.15 mm, 0.20 mm, and 0.40 mm CMOD). As discussed in Section 2.3.2, crack width recovery was minimized for the cracked specimens (i.e., 0.10 mm, 0.15 mm, and 0.20 mm CMOD specimens) by pausing the loading machine at the desired crack width, inserting hard plastic shims, and then unloading the specimen. Immediately after removing a specimen from the loading apparatus aluminum tape was used to seal all sides of the specimen except for the top. This procedure was completed to create a pond, which was used for water sorption testing via x-ray attenuation measurements discussed in Chapter 3. It is vital to note that during water sorption testing the specimens were exposed to liquid water for 24 hours. After exposure to water the samples were allowed to dry at 50% RH ±2% for a minimum of a week prior to epoxy impregnation described in Section 2.2.4.

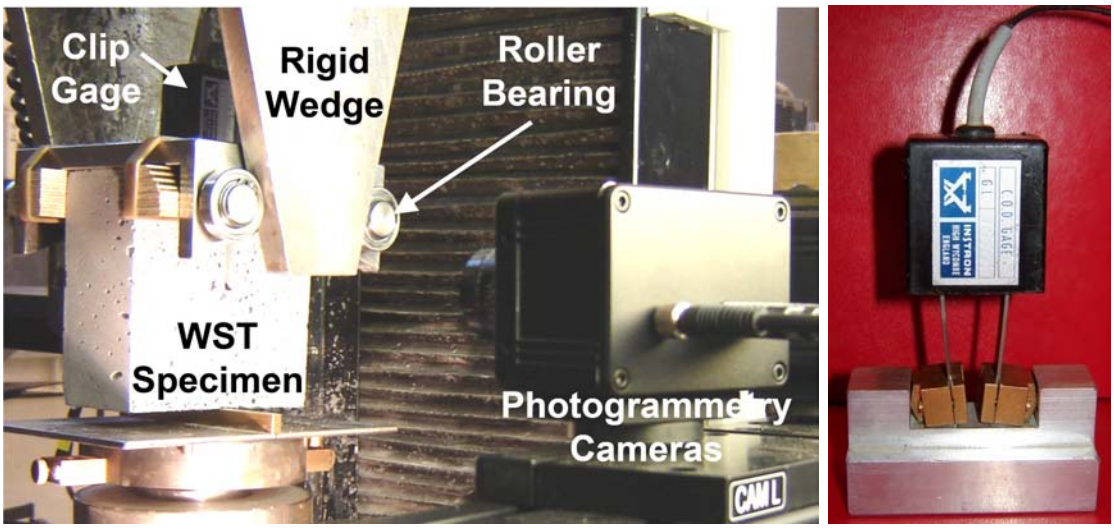

(a) (b)

Figure 2.8 *(a) Wedge splitting test experimental setup includes a rigid steel wedge which applies load via roller bearings to the specimen, photogrammetry equipment, and a modified clip gage for CMOD measurements as shown in (b). (Author's photos)*

2.2.3 Inverse analysis of the cracked hinge model

Crack hinge model

Figure 2.9 shows the implementation of the crack hinge model (CHM), developed in [*Ulfkjaer et al.*, 1995; *Olesen*, 2001], to the WST geometry. The CHM simulates the area directly surrounding a propagating crack as an array of springs, which are attached to rigid boundaries. The rigid boundaries of the cracked hinge are allowed to translate and rotate as indicated in Figure 2.9(b). The cracked hinge behavior is controlled by the stress profile shown in Figure 2.9(c). The rigid boundaries join the bulk specimen, where the behavior is controlled by the classical elastic theory (i.e. Figure 2.6(a)).

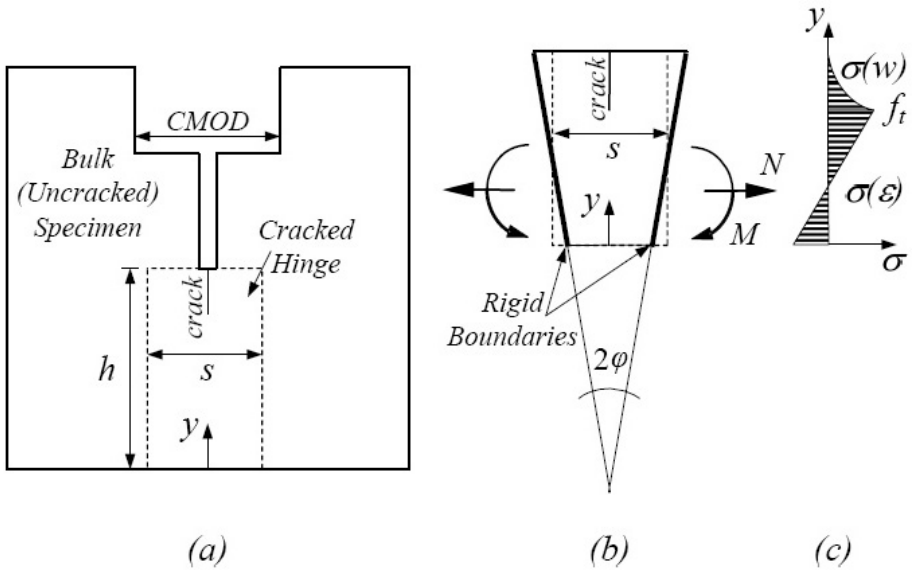

Figure 2.9 *(a) The wedge split testing specimen with the cracked hinge model applied (after [Østergaard, 2003]), (b) Loading and deformation of the hinge (after [Olesen, 2001]), and (c) The assumed stress distribution (after [Olesen, 2001]).*

The stresses transferred by the springs are controlled by Equation 2.2

$$\sigma = \begin{cases} \sigma(\varepsilon) = E\varepsilon & \text{Precracked State} \\ \sigma_w(w) = g(w)f_t & \text{Cracked State} \end{cases} \tag{2.2}$$

where E denotes elastic modulus, ε denotes elastic strain, $\sigma_w(w)$ represents the cohesive law, and f_t denotes uniaxial tensile strength. Figure 2.6(b) illustrates a general $g(w)$ curve, which mathematically is given by:

$$g(w) = b_i - a_i w \text{ where } w_{i-1} < w < w_i \text{ and } i = 1 \ldots N \tag{2.3}$$

The term w_i is the intersection of two consecutive lines and is computed by:

$$w_i = \frac{b_i - b_{i+1}}{a_i - a_{i+1}} \text{ where } i < N \tag{2.4}$$

The critical crack width (width at which $g(w) = 0$) is calculated by:

$$w_c = w_N = \frac{b_N}{a_N} \tag{2.5}$$

where N is equal to the number of lines in the cohesive law. The deformation of the hinge is determined by the angular rotation, φ and the location of the neutral axis, y_0 (See Figure 2.6(b)). The mean value of longitudinal strains, $\varepsilon^*(y)$ is then calculated by:

$$\varepsilon^*(y) = (y - y_0)2\varphi/s \tag{2.6}$$

The deformation of an incremental strip of the hinge is then given by $u(y) = s\varepsilon^*(y)$, where s is the length of the hinge ($s = 0.5h$). Once cracking occurs, $u(y)$ can be computed as the sum of the elastic deformation and the crack opening, as shown in Equation 2.7.

$$u(y) = s\varepsilon^*(y) = s\frac{\sigma_w(w(y))}{E} + w(y) \tag{2.7}$$

By combining 2.6 and 2.7 the stress distribution (Figure 2.9c) equation appears as follows

$$\sigma_w(w(y)) = (2(y - y_0)\varphi - w(y))\frac{E}{s} \tag{2.8}$$

and by introducing the cohesive law (Equation 2.2) and solving with respect to $w(y)$ and $\sigma_w(w(y))$ the following solutions are obtained:

$$\sigma_w(w(y)) = \frac{\zeta_i - 2\varphi(y - y_0)\beta_i}{1 - \beta_i}\frac{E}{s} \tag{2.9}$$

$$w(y) = \frac{2\varphi(y - y_0) - \zeta_i}{1 - \beta_i} \tag{2.10}$$

where the dimensionless factors β_i and ζ_i are defined by

$$\beta_i = \frac{f_t a_i s}{E} \text{ and } \zeta_i = \frac{f_t b_i s}{E} \tag{2.11}$$

Additional information on the development and implementation of the CHM can be found in [*Olesen*, 2001] and [*Østergaard*, 2003; *Löfgren et al.*, 2005; *Skoček and Stang*, 2008], respectively.

Inverse analysis approach

In [*Østergaard*, 2003] the CHM was applied to the WST geometry and an analytical solution was utilized to determine a bilinear cohesive law. An iterative approach was developed in [*Skoček and Stang*, 2008] which allows for determination of N-linear cohesive laws. The following section provides details on the necessary computations for the iterative inverse analysis for determination of N-linear cohesive laws. Additional information on this approach is available in the literature [*Skoček and Stang*, 2008].

In order to determine the material properties from the CHM the following two equations must be fulfilled:

$$M_{exp} - M_{Hinge} = 0 \text{ and } CMOD_{exp} - CMOD_{Hinge} = 0 \tag{2.12}$$

where M_{exp} is the bending moment applied during experimental testing, M_{Hinge} is the bending moment applied in the hinge model approach, $CMOD_{exp}$ is the experimental CMOD measured by the clip gage, and $CMOD_{Hinge}$ is the CMOD computed from the CHM. The experimental bending moment, M_{exp} is calculated based upon the specimen geometry, splitting load (P_{sp}) and vertical load (P_v), as

$$M_{exp} = P_{sp}(d_2 - y_0) + \frac{1}{2}P_v d_1 + \frac{1}{2}mge \tag{2.13}$$

where

$$P_v = P_{sp}\frac{2\tan\alpha_w + \mu_c}{1 - \mu_c \tan\alpha_w} \tag{2.14}$$

which accounts for the wedge angle, α_w and the friction in the roller bearings, μ_c; m is the mass of the specimen, g is the acceleration of gravity, and e is the eccentricity of the gravity load. The bending moment applied in the CHM, M_{Hinge} is computed by:

$$M_{Hinge} = \int_0^h \sigma(y)(y - y_0)dy \tag{2.15}$$

where σ is the cohesive law from Equation 2.2. The CMOD calculated by the CHM, $CMOD_{Hinge}$ is a sum of the elastic deformation, δ_e; the deformation caused by the crack, δ_w; and the deformation caused by geometrical amplification, δ_g. The $CMOD_{Hinge}$ is therefore given by Equation 2.16.

$$CMOD_{Hinge} = \delta_e + \delta_w + \delta_g \tag{2.16}$$

The calculation of the elastic deformation, δ_e is found in [*Tada et al.*, 1985] as

$$\delta_e = \frac{P}{Et}\upsilon_1 \tag{2.17}$$

from the measurement of the crack opening displacement at the crack edge, and as

$$\delta_e = \frac{P}{Et}\upsilon_2 \tag{2.18}$$

for measurement of CMOD at the loading line. Here t = specimen thickness and equations for υ_1 and υ_2 are:

$$\upsilon_1 = \frac{1}{(1-x)^2}[8.89 + 19.3x - 34.1x^2 + 25.6x^3] \tag{2.19}$$

$$\upsilon_2 = \frac{x}{(1-x)^2}[38.2 - 55.4x + 33.0x^2] \tag{2.20}$$

as determined from [*Roberts*, 1969; *Tada et al.*, 1985], where $x = b/d$. As discussed in a following section, photogrammetry measurements were taken which allowed for measurement of crack opening displacement at, among other locations, the edge of the crack.

In the case these measurements, it is therefore necessary to use v_1 when computing the elastic deformations.

The deformation caused by the crack, δ_w can be directly calculated from Equation 2.10 at $y = h$. Finally, the deformation caused by geometrical amplification, δ_w is computed by:

$$\delta_g = 2(b-h)\left(\frac{\delta_w}{2d} - \frac{\varphi_e}{1-\beta_i}\right) \tag{2.21}$$

where φ_e is defined as the maximum elastic angular deformation of the hinge and d is the depth to which the crack has propagated through the hinge.

The inverse analysis is an iterative process used to minimize the difference between model calculations and experimental results by fitting mechanical behaviors. Utilizing an inverse analysis of the CHM (Figure 2.9(b)) developed in [*Ulfkjaer et al.*, 1995; *Olesen*, 2001], experiment results from the WST can be used to determine the properties for cementitious composites. This technique has been successfully applied to WST results for cement paste, mortar, concrete [*Østergaard*, 2003], and fiber reinforced concrete [*Löfgren et al.*, 2005]. The iterative process minimizes the difference between the observed load applied in experiments, P_{exp} and the load predicted by the CHM, P_{Hinge} according to the following error normalization function:

$$\|P_{exp} - P_{Hinge}\| = \sqrt{1 + \frac{(P_{exp} - P_{Hinge})^2}{2}} - 1 \tag{2.22}$$

This normalization function is applied to various stages of the load response curves, including the elastic portion for determination of E, the peak load for determination of f_t, and the softening branch for determination of a_i and b_i through the step-by-step scheme shown below:

$$\begin{aligned}
&\text{while (convergence is not achieved)}\\
&\quad \min_{E} \sum_{j=1}^{K^{el}} \| P_{j,exp} - P_{j,Hinge} \|\\
&\quad \min_{f_t,a_1} \sum_{j=1}^{K} \| P_{j,exp} - P_{j,Hinge} \|\\
&\text{for i=2:N}\\
&\quad \min_{a_i,b_i} \sum_{j=1}^{K} \| P_{j,exp} - P_{j,Hinge} \|\\
&\text{check convergence}
\end{aligned} \tag{2.23}$$

where $P_{j,exp}$ and $P_{j,Hinge}$ are the experimentally observed and CHM calculated load at a given data point, j. The points from the experimental load-CMOD data used by the

inverse analysis program to determine the cohesive law were selected equidistantly in regard to the arc length in the normalized coordinate system. Linear interpolation is used for points selected between measured data. The arc length increment used for analysis was 0.05.

2.2.4 Visual assessments of WST specimen cracking behavior

Plane and thin section

Thin and plane sections were prepared for Mixture 1 (concrete) WST specimens loaded peak load and various crack widths. Only plane sections were prepared for Mixture 2 (SFRC) as the steel fibers can damage the grinding equipment used for preparation of thin sections. Table 2.2 lists all sections prepared as part of this work. These sections are discussed in Section 2.3.2.

Table 2.2 *Number of plane and thin sections prepared from WST specimens.*

Mixture I.D.	**1**		**2**	
Load level / Crack width	**Section type**			
	Plane	Thin	Plane	Thin
Peak Load	3	1	-	-
0.15 mm CMOD	3	1	-	-
0.20 mm CMOD	3	1	3	-

As described above, the WST specimens used plane and thin sections were mechanically loaded, exposed to liquid water for 24 hours, and then allowed to dry at 50% ±2% RH for a minimum of a week. The specimens were then impregnated with a fluorescent epoxy, to prepare plane and thin sections, at Pelcon Materials & Testing ApS, Søborg, Denmark. Epoxy impregnation was completed using specialized vacuum chambers equipped with ports which allow epoxy to pass into the evacuated chamber. The chamber was evacuated to 10 mBar for 60 minutes, during which the resin (resin premixed with Hudson Yellow fluorescent dye) and hardener are mixed. Epoxy enters the evacuated chamber, removing any air from the epoxy, until the impregnated area is fully covered with epoxy. After 5-10 minutes the vacuum is gently released to create an overpressure which pulls the epoxy into any connected voids. To avoid excessive heating of the epoxy during hardening, the specimen is wrapped in plastic and placed in a water bath (avoiding contact between epoxy and water). The epoxy hardens for 16-24 hours at ∼23°C prior to additional handling. Additional information on the fluorescent epoxy impregnation technique used here can be found in [*Laugesen*, 2005].

WST specimens were impregnated in two steps. First, the cast-in void (see Figure 2.7) was filled with epoxy to impregnating the coalesced crack extending from the notch. After allowing the epoxy to harden for ∼24 hours, the specimens were cut (perpendicular to the crack) in to three slices as shown in Figure 2.10(a). Images were acquired from all cut faces using a digital camera under natural and ultraviolet (UV) lighting conditions

and the specimens underwent the second impregnation step. The second impregnation step involved impregnating the cut faces to impregnate any cracks which were isolated from the coalesced crack. The outer slices were then ground using a water-cooled grinding apparatus (Figure 2.10(b)) to remove excess epoxy and to identify isolated cracks. The middle slice was used to prepare a thin section, in accordance with [*DSF 423.40*, 1998], as outlined by the following steps (shown in Figures 2.11 and 2.12):

(a) (b)

Figure 2.10 *(a) WST specimen were sliced in 3 pieces after fluorescent epoxy impregnation. The outer slices were impregnated again from the cut surface to highlight isolated microcracks and (b) were ground to remove excess epoxy. (Author's photos, taken at Pelcon Materials & Testing ApS)*

Step 1 A secondary impregnation was completed on one face of the middle slice to impregnate isolated cracks.

Step 2 After 24 hours (allowing the epoxy to harden) a 45 mm x 35 mm wafer containing the crack tip was cut from the middle slice.

Step 3 The wafer was mounted to a piece of glass (Figure 2.11(a)).

Step 4 The opposite surface was ground to both remove excess hardened epoxy and to create a flat surface (Figure 2.11(b)).

Step 5 The flat surface was then fixed to a second piece of glass and the concrete wafer was sliced as close as safely possible to the second glass surface as shown in Figure 2.11(c).

Step 6 As shown in Figure 2.12 automated grinding equipment was used to plane the section to a thickness of $\sim$20 μm.

Step 7 The final thin section was covered for protection with micro-cover glass and labeled as shown in Figure 2.11(d).

Images of plane and thin sections were captured using a digital camera as well as through stereo and polarizing microscopes. As shown in Figure 2.13, thin section images were

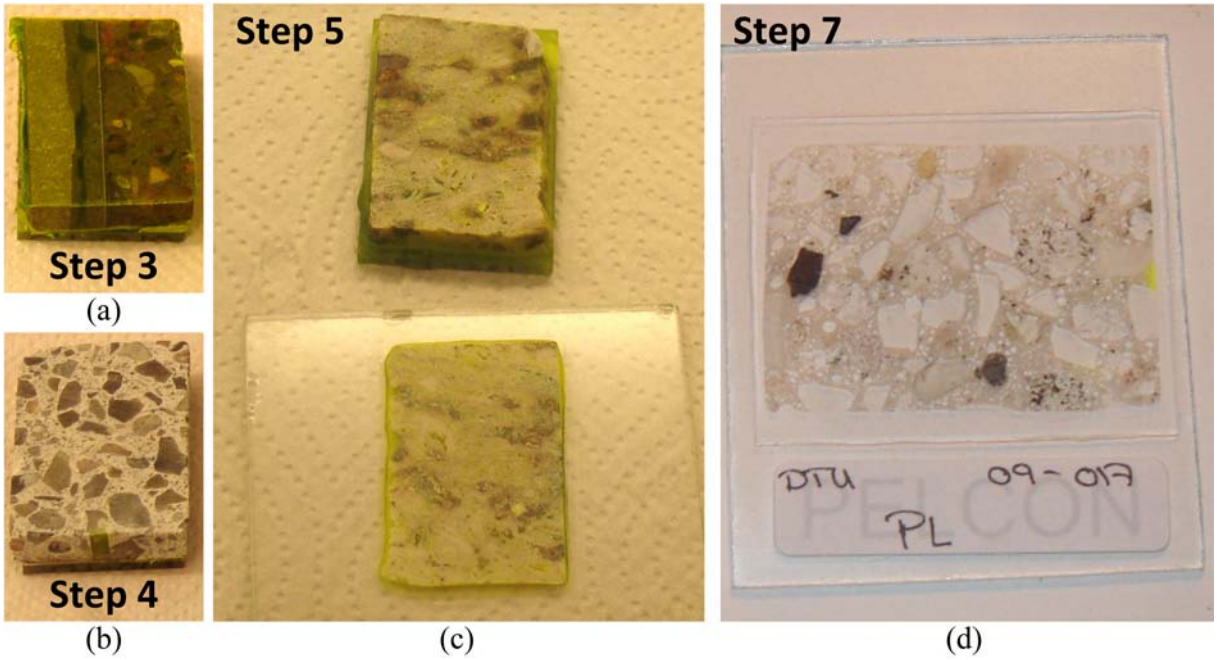

Figure 2.11 *Steps 3–5 and 7 in the preparation of thin sections. (Author's photos, taken at Pelcon Materials & Testing ApS)*

captured under natural, ultraviolet, and polarized light. While ultraviolet light clearly highlights cracks, natural and polarized light are also useful to identify other constituents of the concrete as well as identifying ettringite forming on the crack surface, as discussed further in Section 2.3.2.

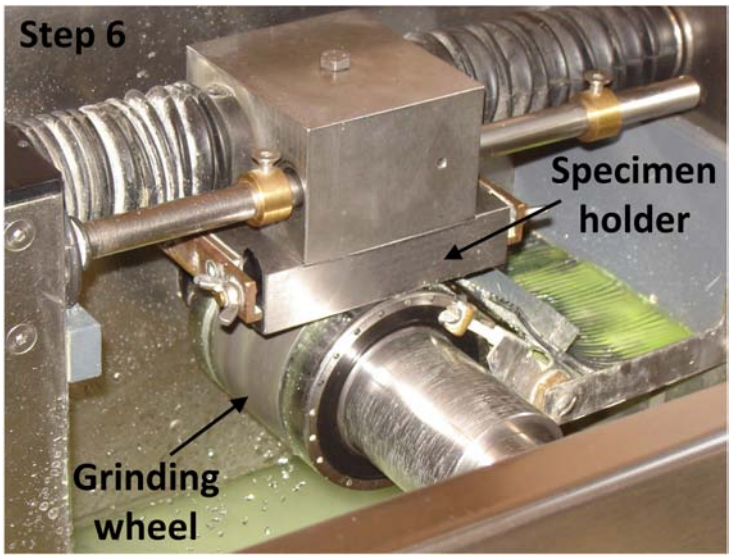

Figure 2.12 *Specialized automated grinding equipment for Step 6 griding. (Author's photos, taken at Pelcon Materials & Testing ApS)*

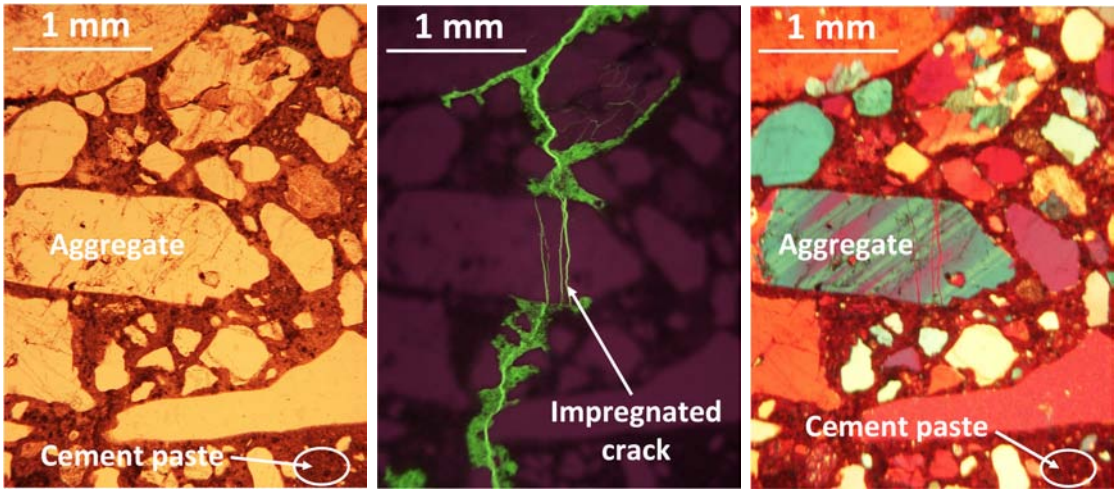

(a) (b) (c)

Figure 2.13 *Thin section images from the 0.15 mm CMOD WST under (a) natural, (b) ultraviolet, and (c) polarized light with various artifacts identified. (Author's photos)*

Using image analysis software [*ImageJ*, 2008] crack widths and depths can be measured from images captured under UV-light as shown in Figure 2.14. First, the color channels (red, blue, and green) were split (Figure 2.14(b)). Using the green channel, a threshold was applied to isolate the impregnated crack as shown in Figure 2.14(b) and a binary image was created (Figure 2.14(c)). A grid mask, consisting of 1 pixel thick horizontal lines spaced every other pixel, was then subtracted from the crack image. As shown in Figure 2.14(e) the resulting line segments were identified and their lengths and vertical locations were measured using built-in *ImageJ* macros. Using the extracted data output crack width and depth was measured. Further details on this procedure are available in the literature [*Qi et al.*, 2003].

3-D photogrammetry setup

A commercially available 3-D photogrammetry system [*Aramis*, 2005] was utilized to capture full field deformation measurements on the surface of the WST and other specimens (see Paper II). In order to facilitate photogrammetry measurements, adequate contrast in the grayscale of individual objects is required. This was achieved by applying a black and white stochastic speckle pattern using spray paint to the cut surface of the WST specimen as seen in Figure 2.15(a) and (b). The individual aggregates remained clearly visible through the black and white speckles.

The photogrammetry system, which consists of two black and white CCD (charged couple device) cameras and a data acquisition computer, captures and processes images at a preset interval (1 hertz used here). Figure 2.8 shows one of the two cameras used in this system positioned adjacent to the WST specimen. The photogrammetry system, using the speckle pattern, identifies unique areas of greyscale variations called facets. Figure

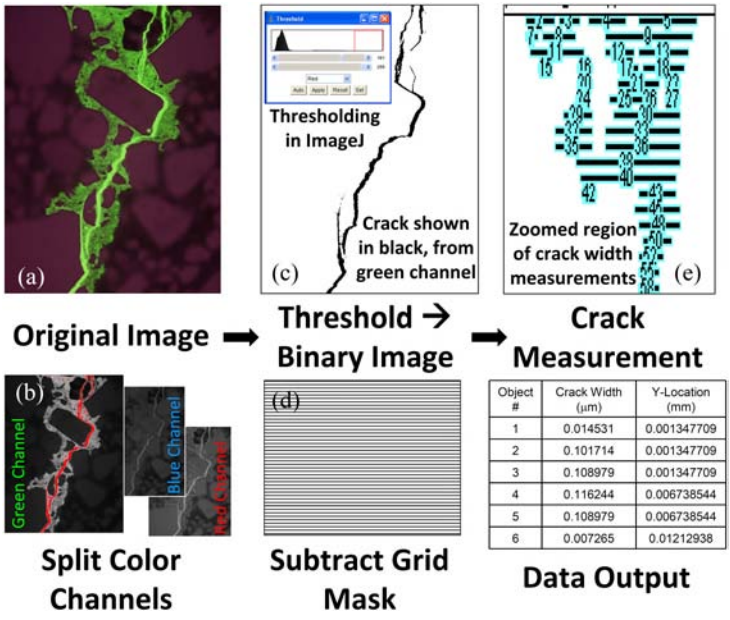

Figure 2.14 *Image analysis technique used to extract crack width and depth information from images of cracked specimen under UV-light, after [Qi et al., 2003].*

2.15(c) shows many individual facets, which overlap by 2 pixels, prior to application of load. Figure 2.15(d) shows the facets after cracking of the specimen. The system tracks movements of the facets during application of load. For example, the red facet shown in Figures 2.15(c) and (d) highlight the process of identifying and tracking the movement of a single facet (identifiable by the two black dots on the top half of the facet).

The photogrammetry measurement process consist of i) proper placement of the camera with respect to the specimen (according to system manual [*Aramis*, 2005]), ii) calibration of the measurement volume using a calibration panel provided by the manufacturer, iii) record images from both cameras simultaneously during loading, and iv) computation of facet deformations. After computation of the facet deformation, 'virtual clip-gages' can be installed using the photogrammetry system to measure the crack opening displacement at any location in the calibrated measurement volume. These virtual clip gages were utilized to extract crack profiles and the crack opening displacement at the crack edge. Additional details on the use of the Aramis 2M photogrammetry system is available in **Paper II**, Appendix C, and elsewhere in the literature [*Aramis*, 2005; *Skoček and Stang*, 2008].

2.3 Results and discussion

2.3.1 Clip gage measurements

Figures 2.16, 2.18(a), and 2.19(a) show typical splitting load versus CMOD responses measured using the clip gage (Figure 2.8(b)) for both mixtures. For both mixtures, the splitting load initially increases rapidly as CMOD increases, until the peak load is reached. After peak load, a softening branch of the response is observed as the splitting load contin-

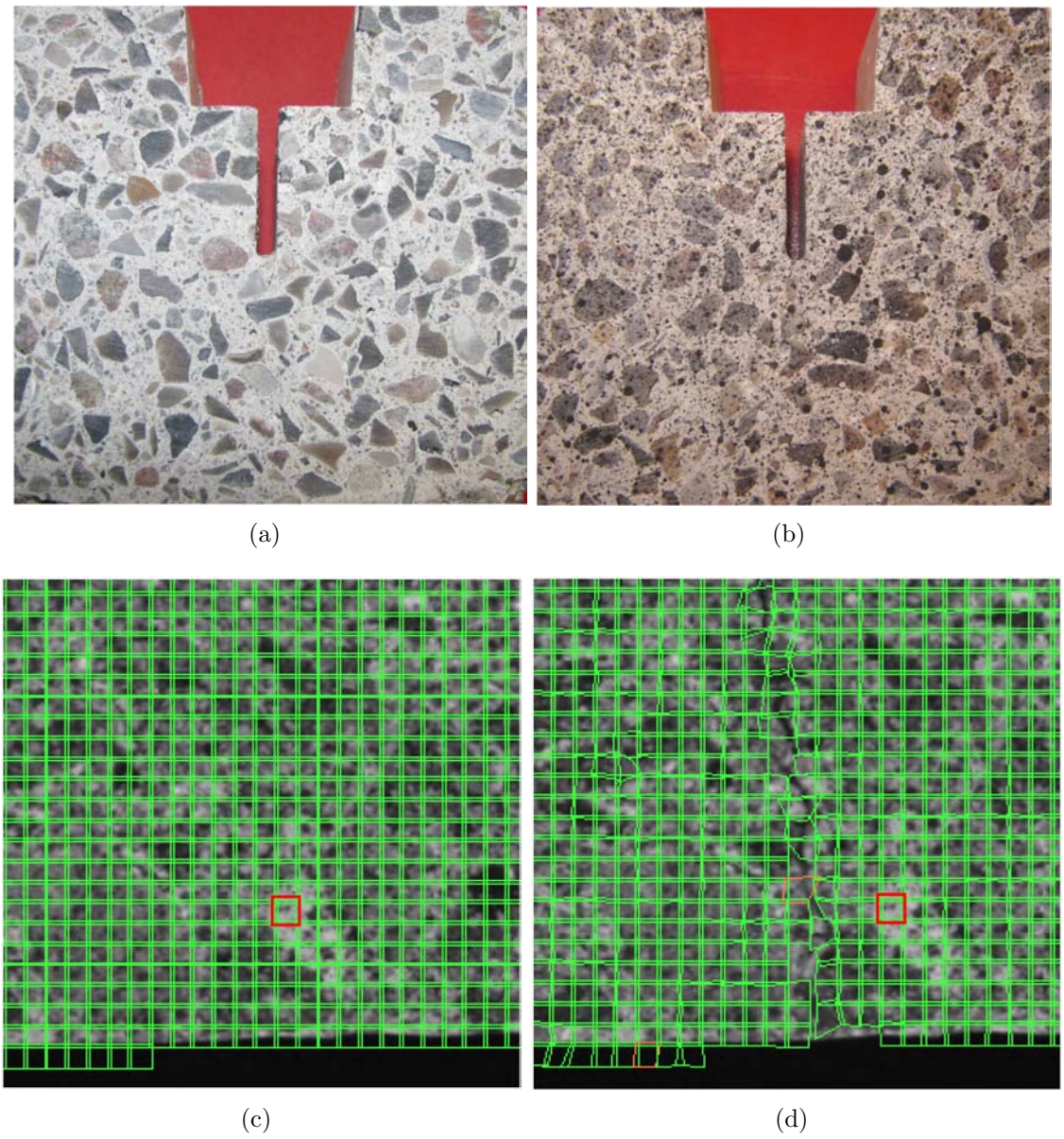

(a) (b)

(c) (d)

Figure 2.15 *A WST specimen with (a) a cut surface exposed of a WST specimen, (b) WST with speckle pattern applied. The photogrammetry system identifies the original location of unique areas as shown in (c) prior to application of load, and re-identifies locations after movements occur (d) (images (c) and (d) are zoomed).*

ually decreases in with increased CMOD. As shown in Figures 2.16 and 2.19(a), Mixture 2 (SFRC) WST specimen continue to hold appreciable splitting loads (∼100 N) up to 1.8 mm CMOD, when the tests were terminated. Mixture 1 (concrete) WST specimen, however, held only minute splitting loads at 1.8 mm CMOD as shown in Figure 2.18(a). Additional effects of the fibers in Mixture 2 are evident by the increased peak load and increased splitting loads throughout the entire softening branch of the load-CMOD curves.

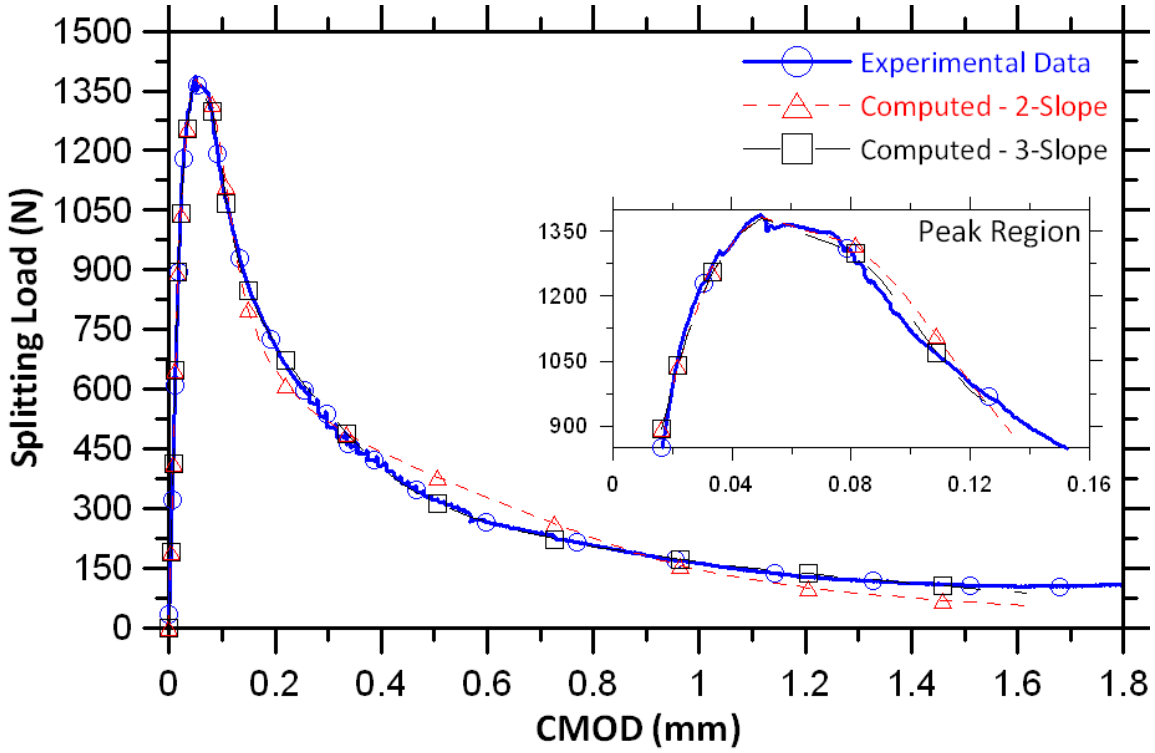

Figure 2.16 *Splitting load-CMOD response curves for experimental and CHM data from Mixture 2. CHM data has been computed from 2- and 3-slope cohesive laws. The inset figure shows a close-up of the peak region.*

Differences in the materials can be further quantified using the inverse analysis of the CHM approach described earlier. Figure 2.16 shows computed responses using 2– and 3–slope cohesive laws applied to the CHM. The inset figure, zooming in on the peak region, shows an accurate estimate of the pre-peak and peak load response is provided by both the 2– and 3–slope cohesive laws. However, the figure indicates the 3–slope cohesive law more accurately estimates the experimental data compared to the 2–slope response, which alternates between under- and over-estimating the splitting load in the post-peak load region. The error between the measured and computed load-CMOD, which is calculated by Equation 2.24, is shown in Tables 2.3 and 2.4 for concrete and SFRC, respectively.

$$L_1 - L_2 = \|P_{exp} - P_{Hinge}\| = \sum_{i=1}^{M} \left(\sqrt{1 + \frac{(P_{exp}^i - P_{Hinge}^i)^2}{2}} - 1 \right) \tag{2.24}$$

where M denotes the number of equidistantly (in terms of arc length method) placed points on the load-CMOD curve. The values indicate the 3-slope cohesive laws provide improved fitting of experimental data. Similar results were observed for Mixture 1 concerning the accuracy of the fits provided by the 2 and 3-slope cohesive laws, as shown in Table 2.3. The following sections describe the optimization and sensitivity of the inverse analysis of the CHM as well as the fracture properties determined from clip gage

measurements of the two mixtures.

Optimization and Sensitivity of Inverse Analysis

An additional slope in the cohesive law applied to the CHM corresponds to 2 additional degrees of freedom (DOF's) in the inverse analysis, an intersection point and a slope. As shown in Figure 2.16, the addition of 2 DOF's lead to an improved fitting of experimental data in this case. However, as discussed in the this section, too many DOF's may lead several issues with the inverse analysis, including non-unique solutions and lengthy computation times. In addition, previous work has shown inverse analysis results may be sensitive to the initially estimated material properties applied to the CHM [*Skoček and Stang*, 2008]. Therefore, in order to optimize the number of DOF's in the cohesive law and ascertain the sensitivity of the inverse analysis, two *Property Sets* were applied to 2–, 3–, and 4–slope cohesive laws and inverse analysis was performed on WST results from both mixtures.

Table 2.3 *Elastic modulus, E, tensile strength, f_t, error of the fit provided by the inverse analysis (Equation 2.24), critical crack width, w_c, fracture energy, G_F, and characteristic length, L_{char} from inverse analyses using property sets 1 and 2 for concrete. The number of slopes in the cohesive law are indicated.*

Mixture 1 – Concrete						
	E (GPa)		f_t (MPa)		Error	
Property Set	*1*	*2*	*1*	*2*	*1*	*2*
2–slope	31.678	31.678	3.264	3.266	2.75	2.75
3–slope	31.678	31.678	3.378	3.347	1.57	1.69
4–slope	31.767	31.678	3.076	3.380	2.50	1.46
	w_c (mm)		G_F (J/m^2)		L_{char} (mm)	
Property Set	*1*	*2*	*1*	*2*	*1*	*2*
2–slope	0.294	0.293	177.4	177.3	527.6	526.7
3–slope	0.407	0.415	176.7	177.2	490.8	501.3
4–slope	0.417	0.418	175.7	176.7	589.7	490.2

Two initial sets of estimated material properties were used to assess the sensitivity of the inverse analysis. As [*Skoček and Stang*, 2008] indicated inverse analysis results are relatively insensitive to the initial shape of the cohesive law, both initial estimates use equidistance spacing of the slope changes in the cohesive law. Initial estimates for elastic modulus, E, tensile strength, f_t, and critical crack width, w_c were 20 GPa, 3.0 MPa, and 0.8 mm for *Property Set 1*; and 40 GPa, 4.5 MPa, and 1.5 mm for *Property Set 2*. The number of DOF's in the cohesive law was optimized to account for the total error of the fit, the computation time, and the ability to provide a unique solution from the two *Property Sets*. For this analysis cohesive laws with 2–, 3–, and 4–slopes were investigated. Additional slopes in the cohesive law were found to not reach the inverse analysis convergence criteria. A similar observation was made in [*Skoček and Stang*, 2008].

Table 2.4 *Elastic modulus E, tensile strength, f_t, error of the fit provided by the inverse analysis (Equation 2.24), critical crack width, w_c, fracture energy, G_F, and characteristic length, L_{char} from inverse analyses using property sets 1 and 2 for SFRC. The number of slopes in the cohesive law are indicated.*

Mixture 2 – Steel fiber reinforced concrete (SFRC)						
	E (GPa)		**f_t (MPa)**		**Error**	
Property Set	*1*	*2*	*1*	*2*	*1*	*2*
2–slope	34.489	34.560	3.574	3.490	2.48	3.04
3–slope	35.740	34.560	3.427	3.590	1.42	1.60
4–slope	34.560	34.560	3.593	3.589	1.56	1.57
	w_c (mm)		**G_F (J/m^2)**		**L_{char} (mm)**	
Property Set	*1*	*2*	*1*	*2*	*1*	*2*
2–slope	1.189	1.193	450.1	448.8	1215	1273
3–slope	2.090	2.453	556.4	595.7	1693	1598
4–slope	4.560	741.1	838.1	84877	2243	2.2e5

Tables 2.3 and 2.4 shows the results of inverse analysis using *Property set 1* and *2* as initial estimates and varying DOF's in the inverse analysis for the Mixture 1 and Mixture 2, respectively. It should be noted the results of inverse analysis are not expected to be accurate to the number of significant digits shown; however, the additional digits are provided to better describe variations in inverse analysis outputs. Values for elastic modulus, E, tensile strength, f_t, total error, critical crack width, w_c, fracture energy, G_F, and characteristic length, L_{char} are given. Varying DOF's and initial estimates have little effect on E and f_t estimates, which vary by a maximum of 3.6% and 9.9%, respectively. Similar robustness in E and f_t estimates have previously been observed [*Østergaard*, 2003; *Skoček and Stang*, 2008]. The total error indicates the overall accuracy of the fit provided by the cracked hinge model to the experimental data. For example, the 2– and 3–slope curves shown in Figure 2.16 have a total error of 3.04 and 1.60, respectively. Optimization of the inverse analysis according to the percentage error indicates using a 3–slope cohesive law typically provides the best overall fit of the experimental data for both materials; while maintaining a relatively consistent w_c, G_F, and L_{char}. Additionally, the computation time for a 3–slope cohesive law was ∼40 minutes while 2– and 4–slope computations took ∼15 and >120 minutes, respectively to reach convergence.

Tables 2.3 and 2.4 also indicate the sensitivity of inverse analysis results to initial estimates and DOF's in the cohesive law. This is most clearly seen in the SFRC results in Table 2.4 for the 4–slopes results where w_c, G_F, and L_{char} estimates vary by over two orders of magnitude. It is also important to point out that the total error varied only by 0.01 between the two inverse analysis results. This indicates the inverse analysis was able to determine two solutions which both accurate fit experimental data. Figures 2.17(c) and (d) provide two examples of how this occurred by showing 4–slope cohesive laws resulting from inverse analyses using *Property Set 1* and *2*. In Figure 2.17(c) the 'kink' points (points of changing slope) and the critical crack widths vary; however, total error

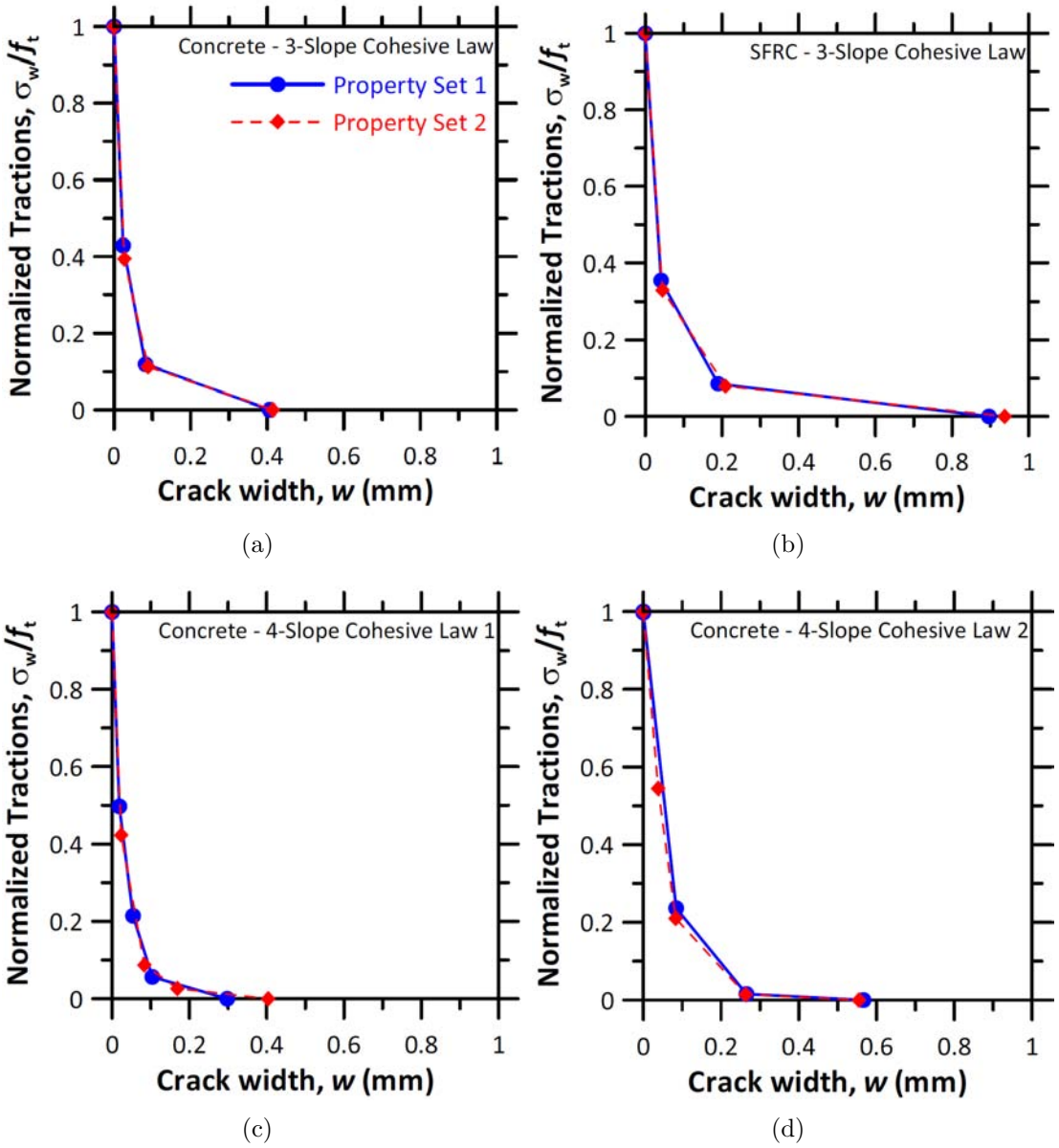

Figure 2.17 *Cohesive laws determined via inverse analysis using initial property set 1 and 2: (a) 3-slope cohesive law for concrete, (b) 3-slope cohesive law for SFRC, (c) and (d) 4-slope cohesive laws for two different concrete specimen. Legend in (a) is common to all plots.*

values (0.69 and 0.75 for *Property Set 1* and *2*, respectively) indicated accurate fitting. In Figure 2.17(d) results from *Property Set* 1 gave only a 3–slope cohesive law after inverse analysis, which was caused by the analysis placing two points at a normalized traction of 1. These variations indicate 4–slopes in the cohesive law provide excessive DOF's, resulting in multiple acceptable solutions for the materials used here. Figure 2.17(a) and (b) show that unique and repeatable 3–slope cohesive laws were determine by the inverse analysis for Mixture 1 (concrete) and 2 (SFRC), respectively. Based on the optimization

and sensitivity results, the 3–slope cohesive laws is recommended as the maximum number of DOF's in the cohesive law.

Fracture properties from clip gage measurements

Based upon the result discussed above, 3-slope cohesive laws are provide the most accurate, unique, and repeatable representation of the materials used here. However, some modeling programs are only capable of implementing 2-slope cohesive laws. Therefore, both 2- and 3-slope cohesive laws are presented here to assist in future use of this data. All results shown here were determined using *Property Set 2* as the initial estimates of the materials properties.

Table 2.5 *Average fracture and material properties from clip gage measurements for Mixtures 1 and 2 using a 2-slope cohesive law*

Property	**Mixture 1**	**Mixture 2**
E(GPa)	31400	30100
f_t (MPa)	3.1	3.1
a_1	18.095	10.783
a_2	1.874	0.646
b_2	0.350	0.300

Tables 2.5 and 2.6 show the average material properties (elastic modulus plus fracture properties) for both mixtures using 2- and 3-slope cohesive laws applied to the CHM, respectively. To determine these values, individual inverse analyses were performed for three different experimental data sets and values were average. Figures 2.18(a) and 2.19(a) show experimental and calculated load-CMOD responses for Mixtures 1 and 2, respectively. Figures 2.18(b) and (c) show individual cohesive laws measured for Mixture 1 along with the averaged cohesive laws with 2– and 3–slope cohesive laws, respectively. Figures 2.19(b) and (c) shows the same for Mixture 2.

Table 2.6 *Average fracture and material properties from clip gage measurements for Mixtures 1 and 2 using a 3-slope cohesive law*

Property	**Mixture 1**	**Mixture 2**
E(GPa)	31400	32400
f_t (MPa)	3.1	3.04
a_1	19.482	10.682
a_2	3.93	1.447
b_2	0.477	0.424
a_3	0.282	0.128
b_3	0.098	0.108

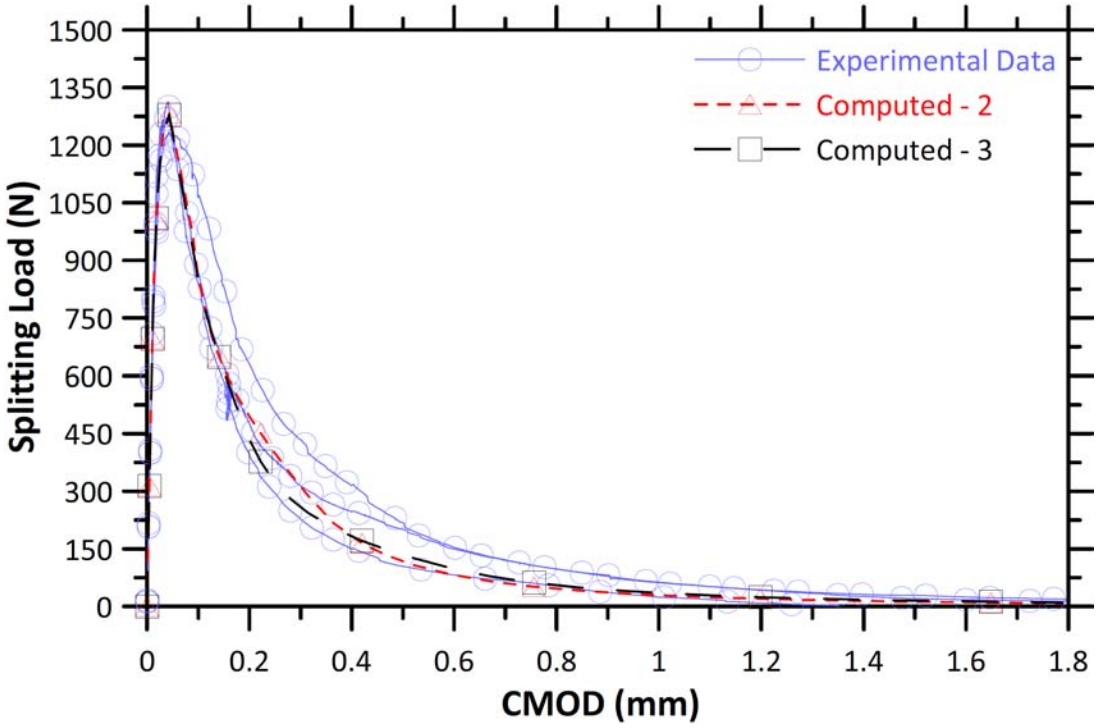

(a)

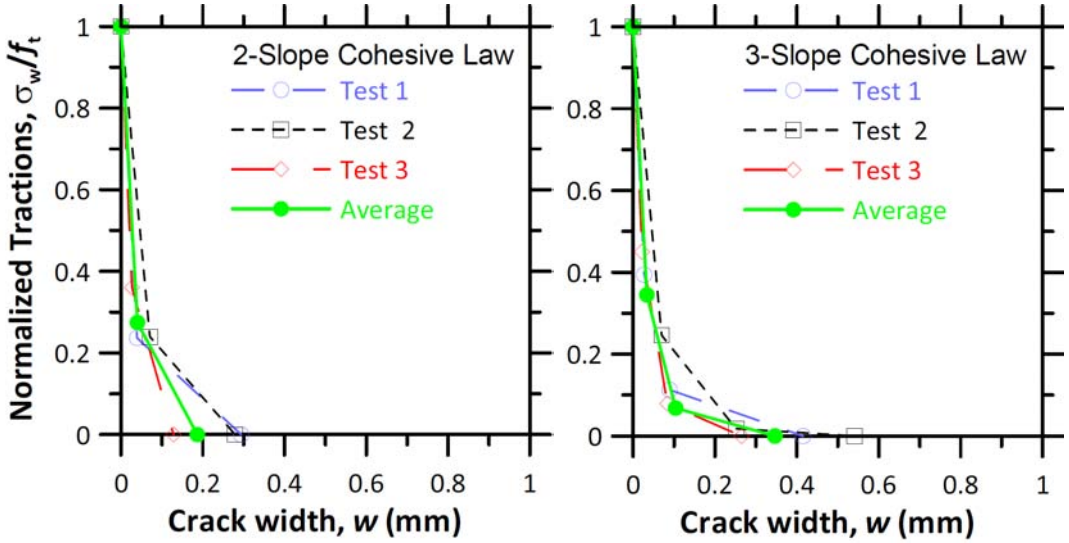

(b) (c)

Figure 2.18 *(a) Experimental and computed splitting load versus CMOD for Mixture 1, (b) 2–slope cohesive laws for individual tests and the averaged response, and (c) 3–slope cohesive laws for individual tests and the averaged response.*

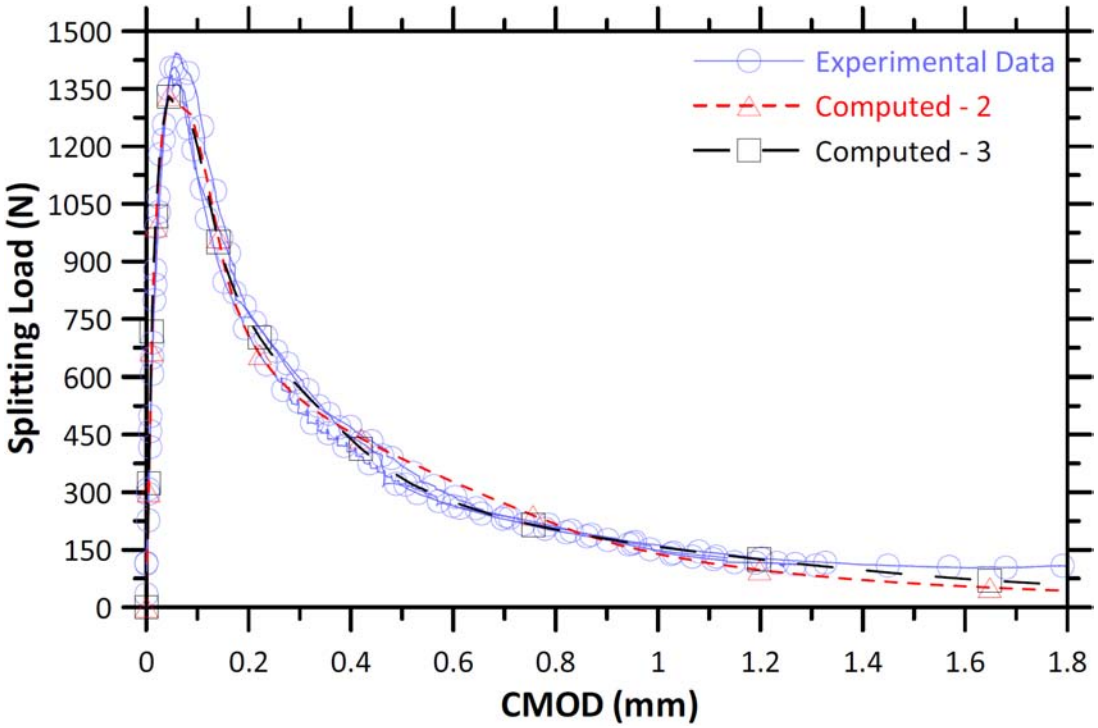

(a)

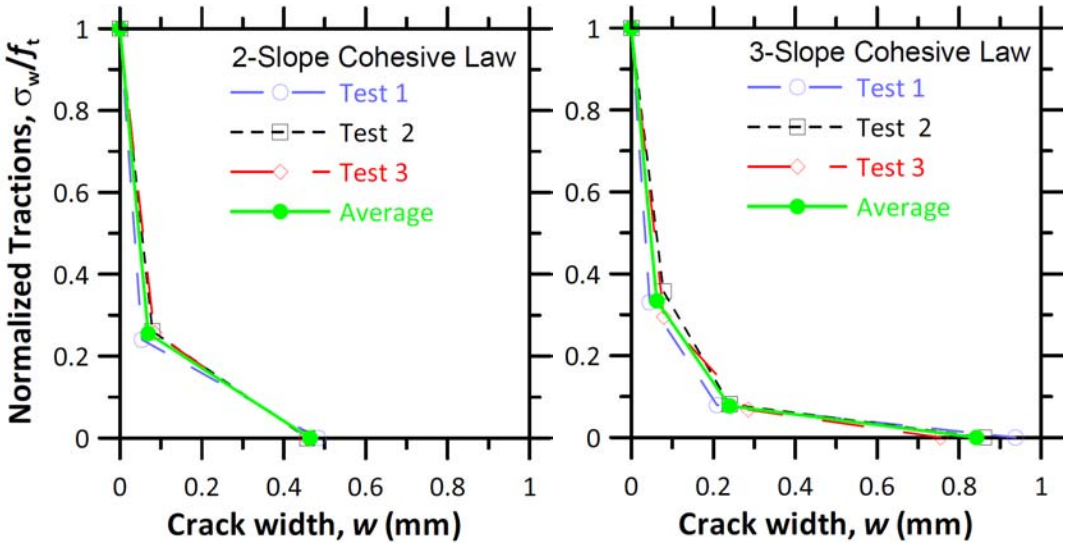

(b) (c)

Figure 2.19 *(a) Experimental and computed splitting load versus CMOD for Mixture 2, (b) 2–slope cohesive laws for individual tests and the averaged response, and (c) 3–slope cohesive laws for individual tests and the averaged response.*

2.3.2 Visual observations of cracking behavior

As discussed above (Section 2.2.4, Table 2.2), several plane and thin sections were prepared to assess the cracking behavior of the WST specimens. Images of and results from these sections are presented in the following sections.

Plane sections

Figures 2.20-2.23 show the cracked WST specimen after the first impregnation procedure, which fills only the coalesced crack extending from the notch. Figure 2.20, showing the peak load sample from Mixture 1, indicates cracking occurred under peak load to a small depth within the specimen. The average coalesced crack length (i.e. crack length measured after first impregnation) for each impregnated WST specimen was measured as described in Figure 2.14. The resulting crack length measurements are shown in Table 2.7. The length of the coalesced crack is measured as the depth from the bottom of the notch. It can be seen that an increase in CMOD causes the crack to propagate deeper into the WST specimen.

Table 2.7 *Location of coalesced crack tip with respect to notch bottom, results of first impregnation.*

Mixture I.D.	**1**			**2**		
Load level / Crack width	**Crack length (mm)**					
	Avg.	Min.	Max.	Avg.	Min.	Max.
Peak Load	-6.1	-3.2	-8.89	-	-	-
0.15 mm CMOD	-23.0	-20.9	-25.3	-	-	-
0.20 mm CMOD	-25.0	-21.1	-31.2	-39.8	-37.3	-41.5

The influence of aggregates on the coalesced crack path is apparent in Figures 2.20-2.23. In some cases (Figures 2.21(a), 2.22(d), and 2.23) the coalesced crack extends nearly vertically from the notch tip; however, in other cases (Figures 2.21(b)-(d) and 2.22(a)-(c)) the crack path is more tortuous due to aggregate blocking. The cracks typically propagated around, rather than through, aggregates, which can be expect with the relatively high w/c used.

Figures 2.20-2.23 also indicate the coalesced crack path varies in shape and length through the thickness of the specimens. For example, in Figure 2.21(c) the coalesced crack extended -31.2 mm from the notch bottom with an arcing path, while the crack in Figure 2.21(d) extended -21.1 mm from the notch bottom in a relatively straight path.

Figure 2.24 compares images after the first (a) and second (b) impregnations of the peak load, Mixture 1 specimen. The same specimen is shown in the two images; however, the surfaces differ slightly as in Figure 2.24(b) the surface was ground down approximately 3 mm to remove excess epoxy which penetrated into the cement paste, particularly at the paste-aggregate interface. The depth of the impregnated cracks in Figure 2.24 increased from (a) 5.8 mm to (b) 11.6 mm due to impregnation of cracks isolated from the coalesced

crack. Results from thin sections, presented in the following, also indicate isolated cracks formed ahead of the coalesced crack.

Another observation made from the impregnated plane sections is shown in Figure 2.25. The image is zoomed into the corner of the recess cast into the WST specimens. For all impregnated specimen, cracks were found to extend from these corners. An important assumption of the inverse analysis of the CHM is that the bulk specimen is uncracked (see Figure 2.9). The clip gage used to measure CMOD is placed in the cast in recess, above the corners where cracking occurred. Therefore, clip gage measurements include deformations from the corner cracks in the WST specimen and results from inverse analysis may be effected. The impact of the additional deformations measured on the cohesive law resulting from inverse analysis is shown in Figure 2.29 and discussed further below.
One possible solution to the avoid measuring the deformations induced by the corner cracks is to measure crack opening from the bottom of the notch. This was facilitated through the use of photogrammetry equipment and results are presented in Section 2.3.2.

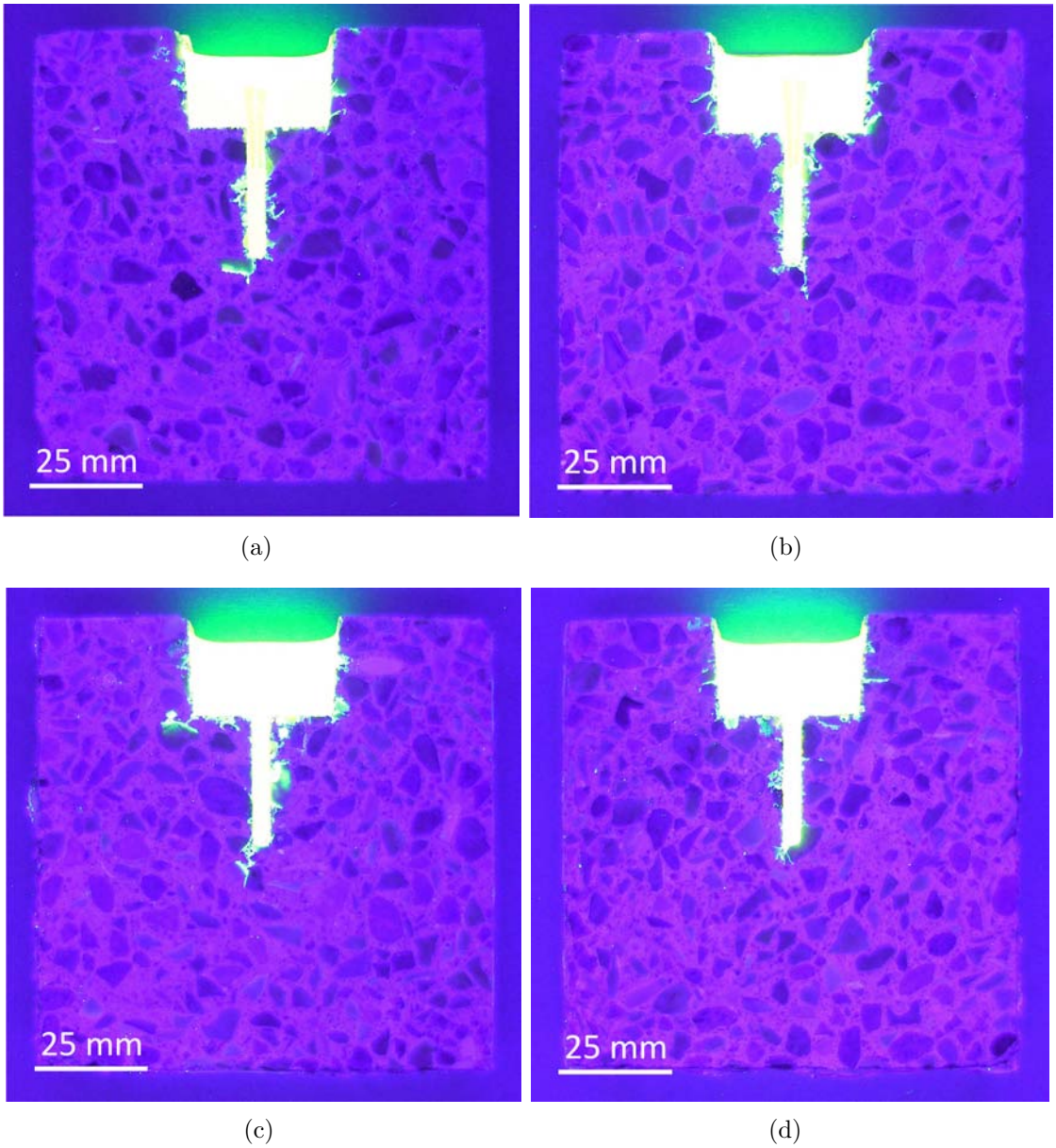

(a) (b)

(c) (d)

Figure 2.20 *Crack images from Mixture 1, peak load specimen after first impregnation. (Author's photos, taken at Pelcon Materials & Testing ApS)*

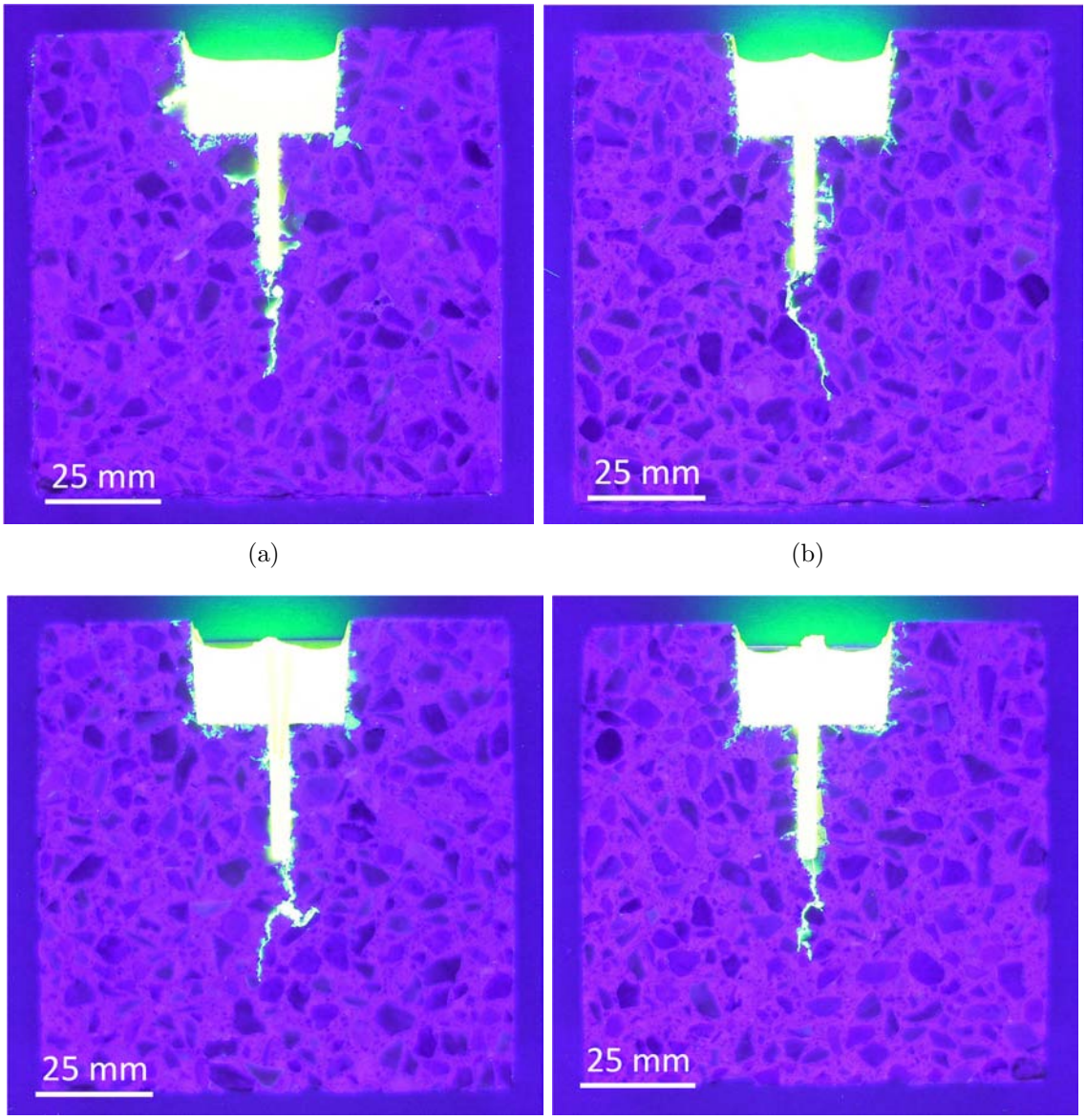

(a) (b)

(c) (d)

Figure 2.21 *Crack images from Mixture 1, 0.15 mm CMOD specimen after first impregnation. (Author's photos, taken at Pelcon Materials & Testing ApS)*

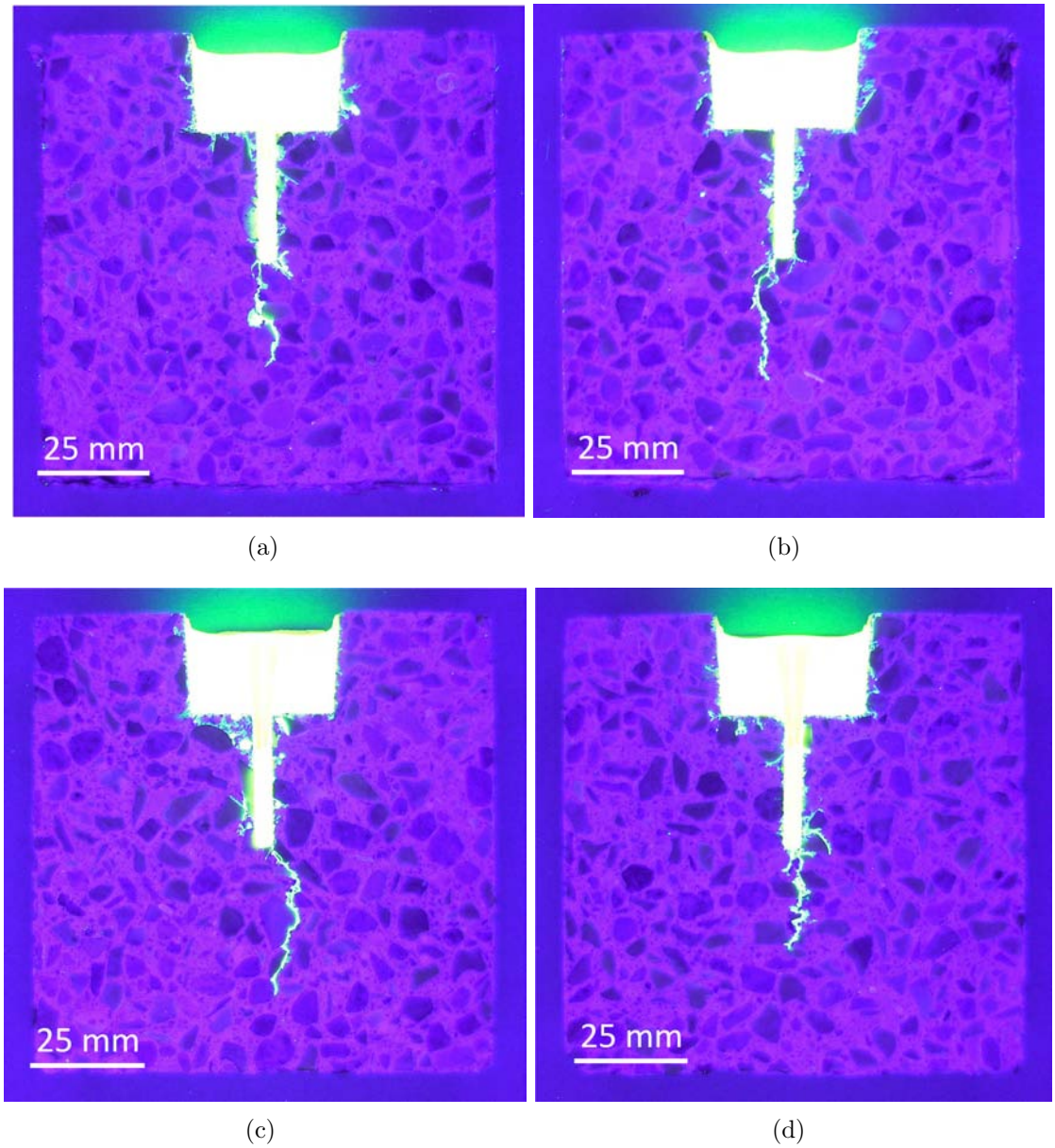

(a) (b)

(c) (d)

Figure 2.22 *Crack images from Mixture 1, 0.20 mm CMOD specimen after first impregnation. (Author's photos, taken at Pelcon Materials & Testing ApS)*

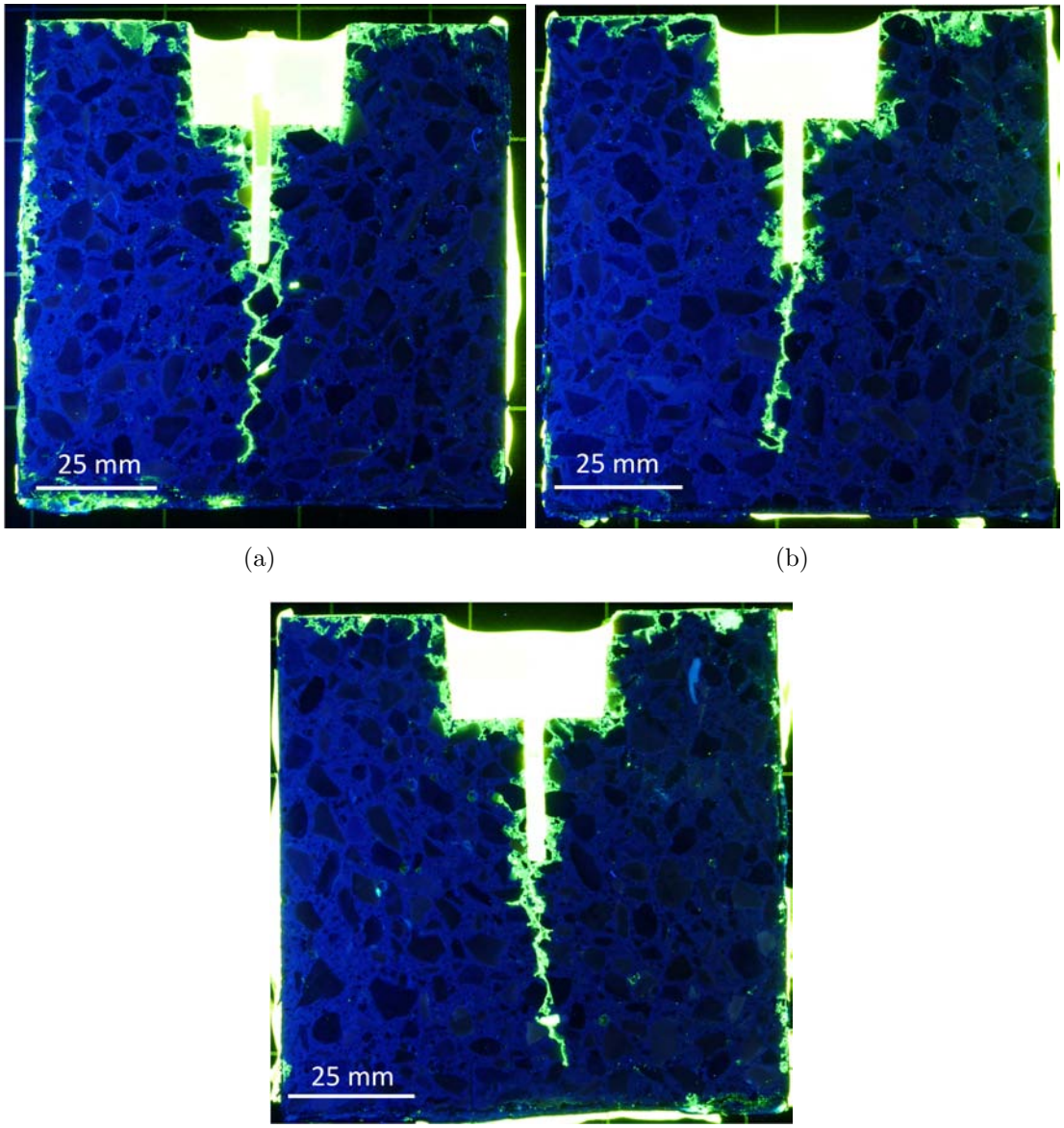

(a) (b)

(c)

Figure 2.23 *Crack images from Mixture 2, 0.20 mm CMOD specimen after first impregnation. (Author's photos)*

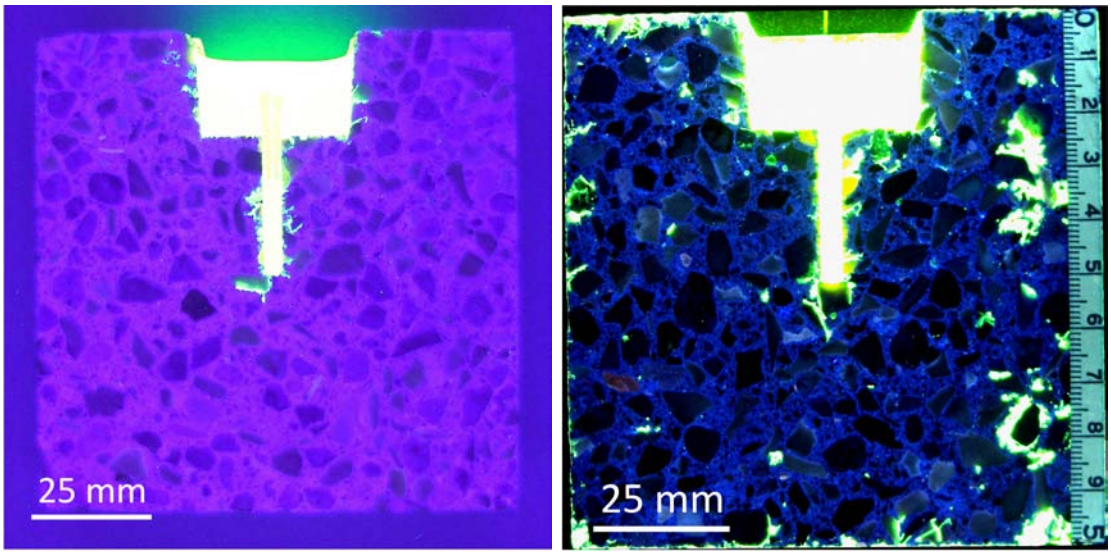

(a) (b)

Figure 2.24 *Mixture 1 - peak load specimen crack images under UV-light (a) after first impregnation and (b) a second impregnation to show isolated cracks. (Author's photos)*

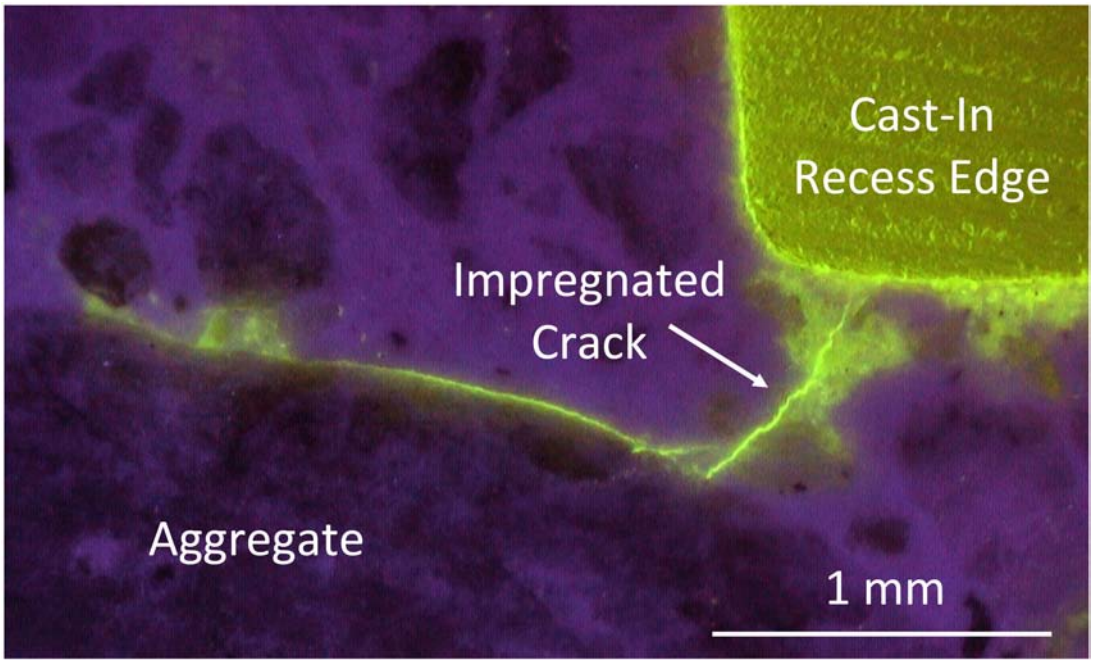

(a)

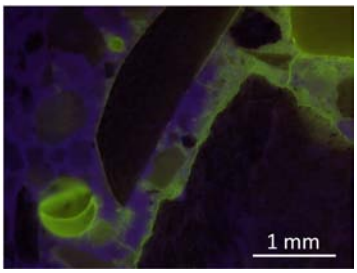

(b)

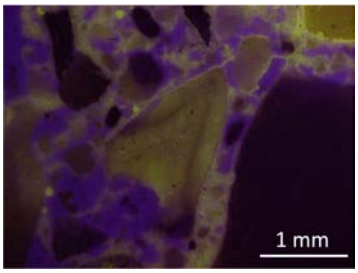

(c)

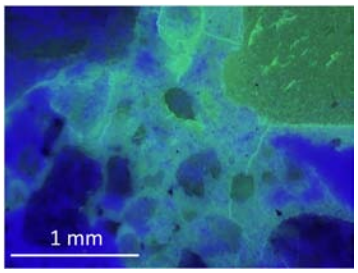

(d)

Figure 2.25 *Cracking from the corner of the WST cast in recess from Mixture 1 (a) peak load, (b) 0.15 mm CMOD, (c) 0.20 mm CMOD, and Mixture 2 (d) 0.20 mm CMOD. (Author's photos)*

Thin sections

Further details of the cracking behavior emerge from analysis of thin sections. Figures 2.26 and 2.27 show images taken under either UV-light (stereomicroscope images) or using proper filters (polarizing microscope) to highlight the impregnated cracks. Both figures show that epoxy was impregnated in the cement paste itself, as most clearly illustrated in Figure 2.27(b). The impregnation of the cement paste is likely due to the high w/c and curing temperature creating a relatively porous microstructure. Unfortunately, this makes identifying cracks in the cement paste more difficult. Figure 2.26(b), which shows cracks impregnated in an aggregate and in the cement paste, indicates a more dense cement microstructure may have lead to easier identification of cracks in thin sections. Regardless, many important observations are still possible.

Figure 2.26(a) and (c) show that a single crack may branch into multiple cracks. These multiple crack are narrower than a singe crack would be, and as discussed in Chapter 3, this may have further implications on transport of moisture and other substances into and out of the concrete. Figure 2.27(b) shows that crack branching also occurs on a smaller scale, and that these branches may reconnect to form a single crack again. By scanning down the figure, it is possible to see the two cracks originating at the top of the image reconnect near the middle of the image, only to branch and reconnect again at the bottom of the image. Again, as discussed in greater detail in Chapter 3, this tortuous path influence transport behavior.

Figure 2.27(c) shows the end of the crack tip of the 0.20 mm CMOD WST specimen. The crack appears to end and then restart in an isolated region. The isolated region of epoxy is thought to be caused by microcracks, which are not yet connected to the coalesced crack. Another explanation is that the cracks are connected, but at a different plane (as described using the plane section, cracks length varied throughout the specimens' thickness).

Figure 2.28 takes a closer look at a crack in the 0.20 mm CMOD, Mixture 1 WST specimen. The location of the images is indicated in Figure 2.27(b). The images have been rotated 90° counterclockwise from the orientation in Figure 2.27(b). Figure 2.28(a), taken under filtered light, clearly identifies the crack; however, other details are more apparent under natural light. Such details shown in Figure 2.28(b) include hydrated cement paste [A], aggregates [B], and apparent formation of ettringite crystals [D]. The ettringite crystals likely formed during the 24 hours the WST specimen was exposed to water. The image under natural light also shows the fractured surface of the cement paste is relatively rough compared to the surface of the sea-gravel.

Photogrammetry measurements

Using photogrammetry the crack opening displacement (COD) can be measured using virtual clip gages at nearly any point on the WST specimen (see Paper II for additional details on results of photogrammetry equipment). In this case, the COD at the tip of the notch (or crack edge) was measured and inverse analysis was completed as described in

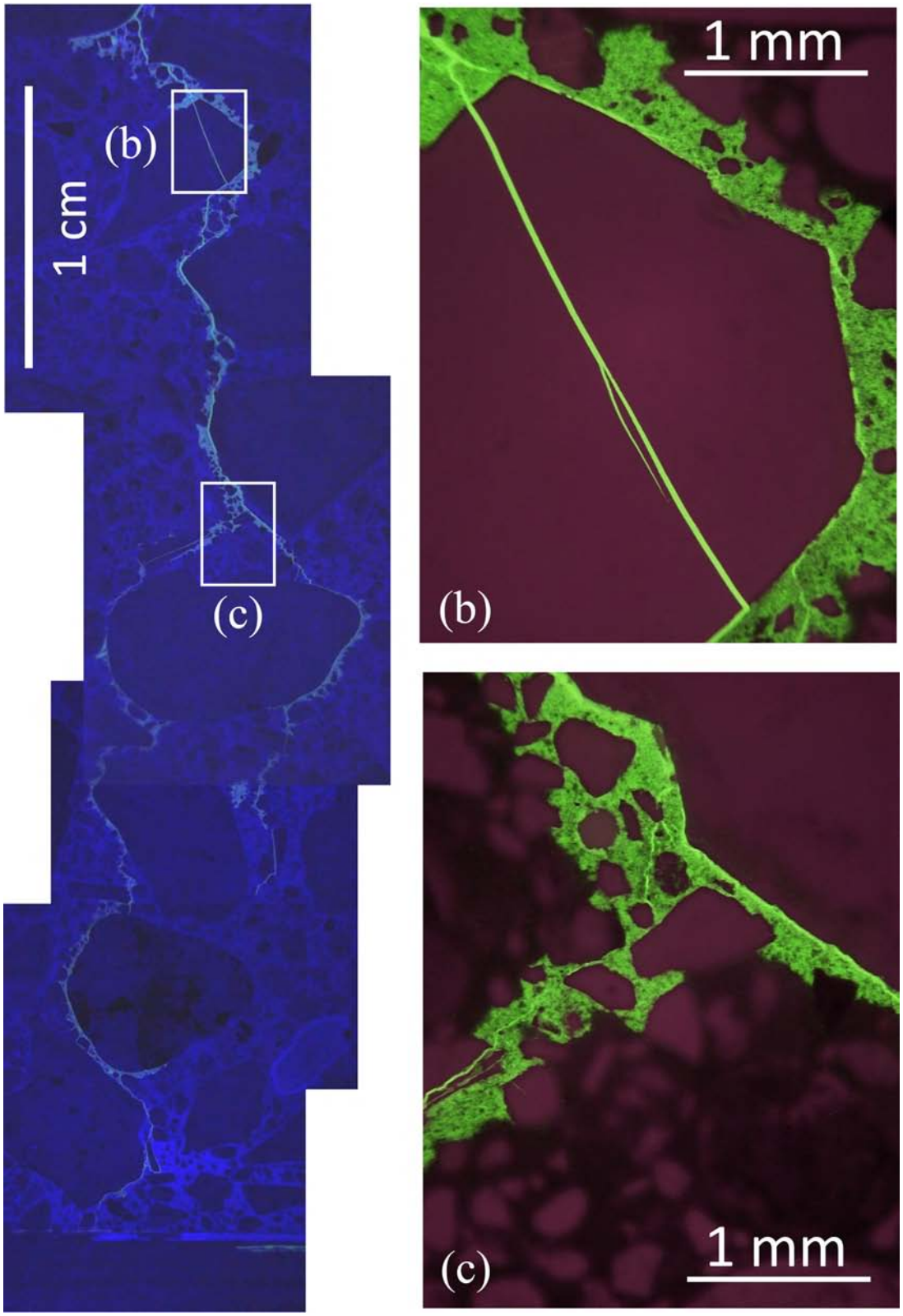

Figure 2.26 *Images of the 0.15 mm CMOD - Mixture 1 thin section (a) using a stereo microscope under low magnification to show entire crack path and (b),(c) using polarizing microscope under high magnification to show detailed cracking behavior. (Author's photos)*

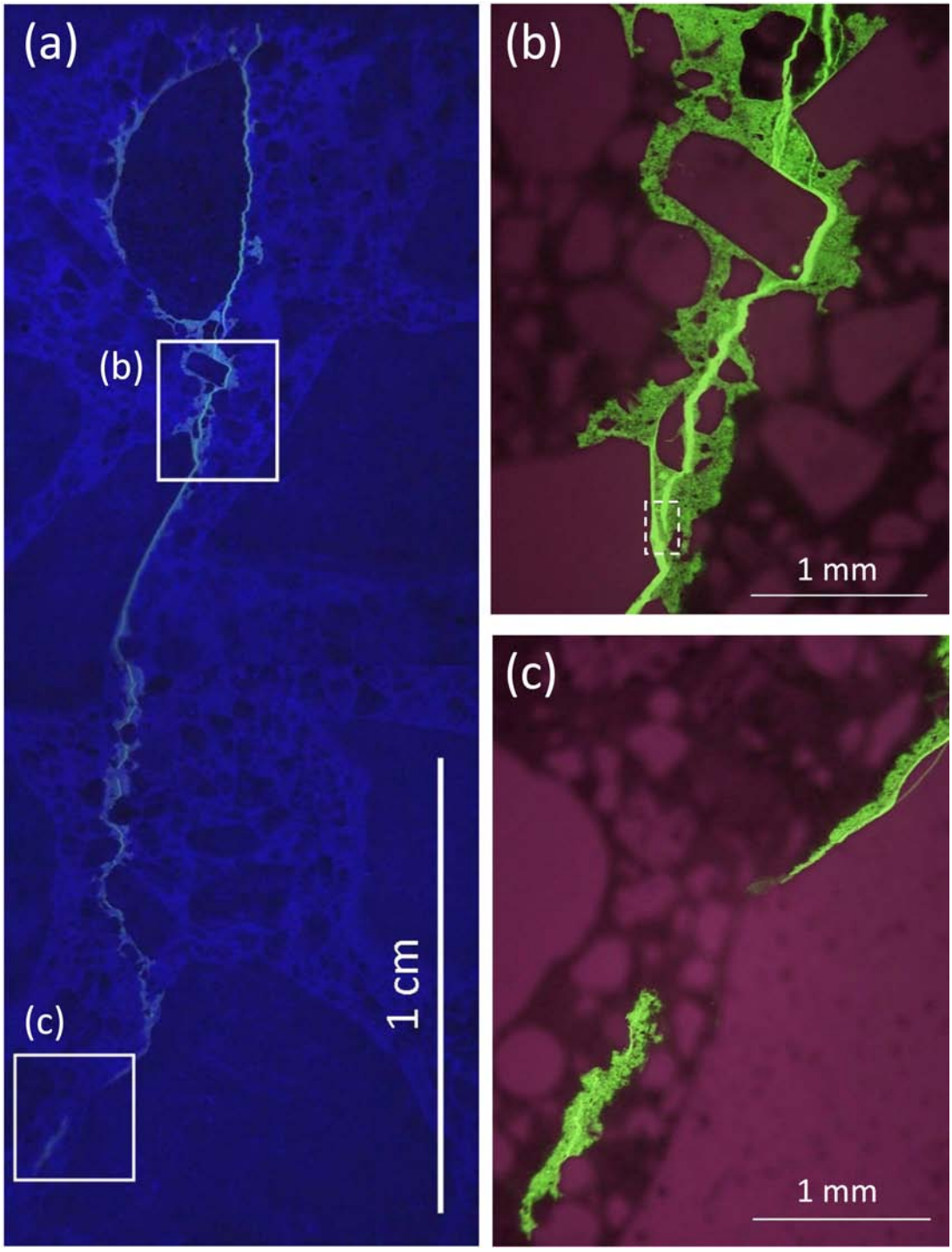

Figure 2.27 *Images of the 0.20 mm CMOD - Mixture 1 thin section (a) using a stereo microscope under low magnification to show entire crack path and (b),(c) using polarizing microscope under high magnification to show detailed cracking behavior. The box with a white broken line in (b) indicates the location of images in Figure 2.28. (Author's photos)*

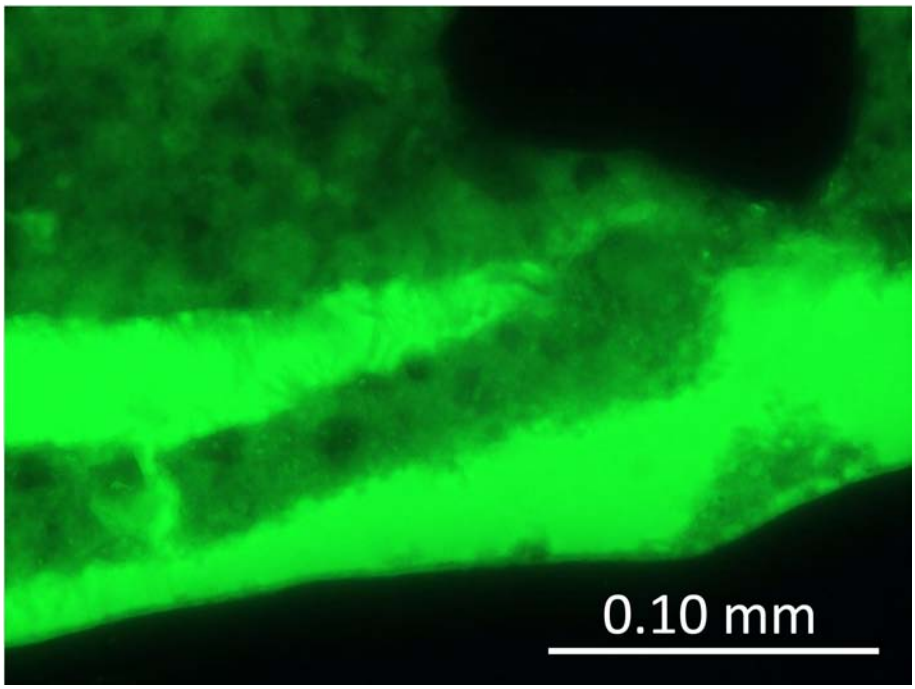

(a)

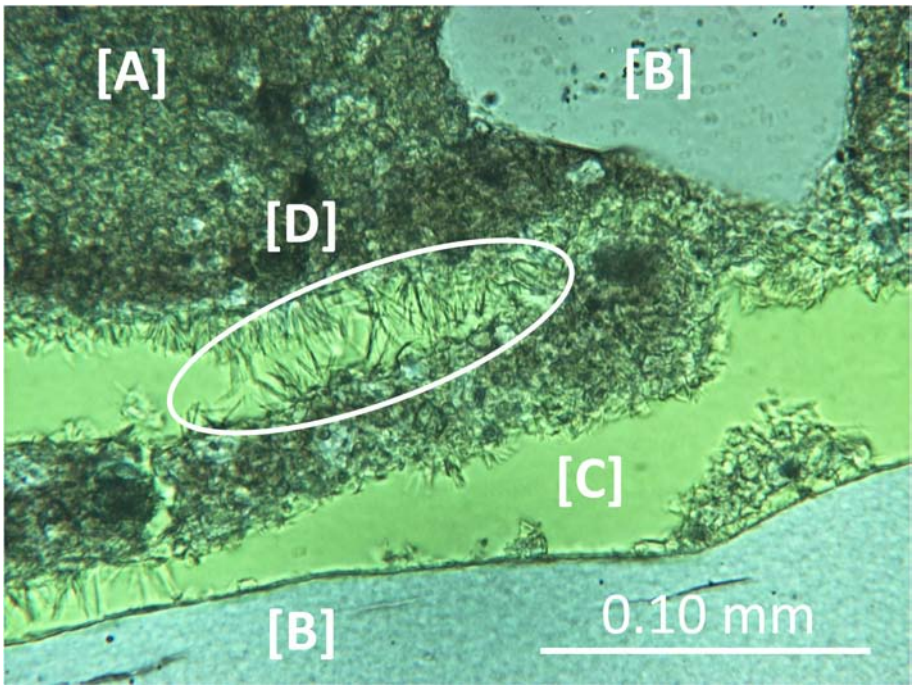

(b)

Figure 2.28 *Thin section images from the 0.20 mm CMOD Mixture 1 specimen under (a) filtered light to highlight the crack and (b) natural light showing [A] hydrated cement paste, [B] aggregate, [C] impregnated crack, and [D] ettringite crystals on the fracture surface. (Author's photos)*

Table 2.8 *Comparison of 3–slope cohesive law terms determined from photogrammetry and clip gage data.*

Property	**Mixture 1**		**Mixture 2**	
	Photogrammetry	Clip Gage	Photogrammetry	Clip Gage
a_1	17.313	19.302	8.921	11.56
a_2	7.877	6.405	1.446	1.087
b_2	0.833	0.697	0.487	0.355
a_3	0.334	0.290	0.171	0.132
b_3	0.173	0.127	0.149	0.098

Section 2.2.3.

Figure 2.29(a) shows the splitting load versus the COD measured by the clip gage at the crack mouth and at the crack edge through photogrammetry from a Mixture 2 (SFRC) WST specimen. Naturally, the COD at the crack edge is less than at the crack mouth due to reduced elastic deformation and lack of geometric amplification of the COD (δ_g, Equation 2.21). Additionally and importantly, the cracks extending from the cast in recess corners are not measured through photogrammetry. Figure 2.29(a) also shows the inverse analysis of the CHM (using 3–slope cohesive laws) provide accurate fits to the experimental load versus COD responses measured by both the clip gage and photogrammetry. As previously documented in [*Skoček and Stang*, 2009], the photogrammetry equipment is unable to measure elastic deformation of concrete due to resolution limitations, leading to unreasonably high elastic modulus estimates by the inverse analysis. Therefore, only the cohesive laws are compared from the clip-gage and photogrammetric analyses (Figures 2.29(b) and (c) for Mixture 1 (concrete) and 2 (SFRC), respectively). In both cases, critical crack width and normalized traction slightly increased using photogrammetry measurements. Critical crack width, w_c increased by up to 18%, while fracture energy, G_F increased by up to 10%.

Photogrammetry measurements ensure the measured deformation is from a single crack within the cracked hinge region (Figure 2.9(a)) and likely better represent the material's fracture behavior. Table 2.8 shows the cohesive law terms (i.e., a_i and b_i) for both Mixtures 1 and 2 determined using photogrammetry and clip gage data. It should be noted that these values are from a single test and are not averaged as was data presented in Tables 2.6.

2.3.3 Comparison of crack profiles from CHM and visual observations

Figure 2.30 shows the estimated and measured crack profiles from several cracked Mixture 1 WST specimens. Estimate crack profiles were determined using the CHM (Equation 2.7) using the average 3–slope cohesive law shown in Figure 2.18(c). Crack profiles were measured using plane impregnated (second impregnation) specimens as described in Figure 2.14. In addition, the coalesced crack depth is indicated for each cracked specimen along the estimated profiles.

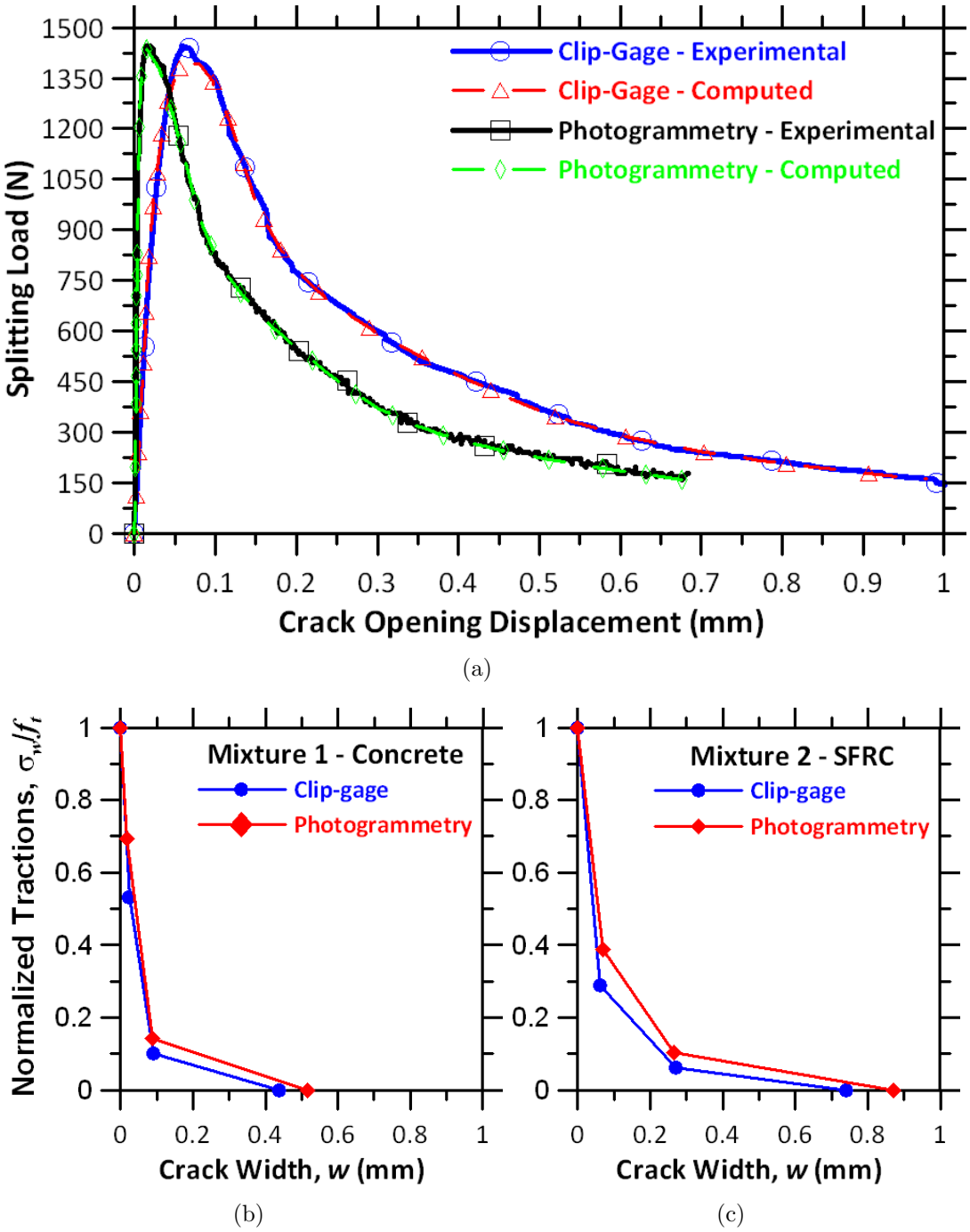

Figure 2.29 *Comparison of (a) experimental and computed (3–slope cohesive law) load-CMOD behavior measured by clip-gage and photogrammetry for Mixture 2. 3–Slope cohesive laws from inverse analysis of clip gage and photogrammetry for (b) Mixture 1 and (c) Mixture 2.*

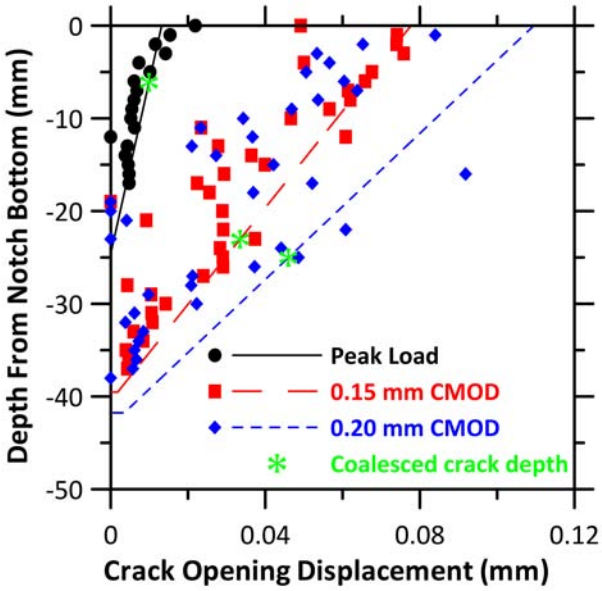

Figure 2.30 *Crack profiles for WST specimens loaded to peak load, 0.15 mm and 0.20 mm CMOD determined from CHM (plotted as lines) and from plane impregnated specimens (second impregnation, plotted as symbols). The stars indicate the depth of the coalesced crack (first impregnation).*

The CHM estimated crack profiles show V-shaped cracking occurs in the WST specimens, with crack width and depth increasing with increased CMOD. While the estimated profiles result in accurate fitting of experimental data (as shown in Figure 2.16 above), they do not provide insight on crack features such as tortuosity, branching, coalesced cracks versus isolated cracks, microcracking, etc.

Comparison of the coalesced crack length to the CHM estimated crack profiles; however, suggests that only a portion of the estimated crack profile is a coalesced crack. As seen in Figure 2.30, a significant length of the estimate crack profile was not comprised of a coalesced crack. Interestingly, the length of the estimated crack profile which resulted in crack coalescence was relatively consistent for Mixture 1 WST specimens. Estimated crack lengths varying from 16.5 mm to 18.5 mm resulted in the formation of a coalesced crack. The figure also shows crack opening displacement does not control crack coalescence. Based on these results, it may be possible to easily estimate the depth of the coalesced crack using the CHM.

As shown in Figure 2.30 crack profiles, measured after the second impregnation step, also show a V-shape trend in the crack shape. Peak load results most closely resemble the CHM estimated profiles, with variations from estimated profiles likely caused by inherent variability of concrete cracking and fracture properties. The portion of the crack beyond the depth of the coalesced crack consisted of disconnected cracks, and at some depths no cracking was observed. For example, the crack profile measured at peak load shows a crack width of 0 mm at a depth of approximately -12 mm. As discussed in detail in

Chapter 3, the depth of the coalesced crack seems to have a major influence on ingress behavior.

2.3.4 Effect of plastic shims on crack width recovery

As described in Section 2.2.2 above, specimens were cracked to CMOD's of 0.10 mm, 0.15 mm, 0.20 mm and 0.40 mm and held open using hard plastic shims (for moisture ingress measurements described in Chapter 3). This section discusses the effectiveness of the plastic shims at maintaining the crack width upon unloading the specimens.

Two WST specimens of Mixture 2 (SFRC) were loaded to 0.20 mm CMOD. One WST specimen had two plastic shims placed into opposite sides of the notch prior to unloading, while the other specimen was simply unloaded. SFRC specimens were used as the steel fibers promote additional crack width recovery, and therefore this is the worst case for assessing the functionality of the plastic shims. COD's were measured using both the clip gage and photogrammetry as shown in Figure 2.31. Figure 2.31(a) nearly half the CMOD (measured by the clip gage) is recovered if a shim is not used (0.20 mm CMOD reduced to 0.105 mm). Even using the plastic shims CMOD recovery occurs (Figure 2.31(b)), but to a lesser extent (0.20 mm CMOD reduced to 0.168 mm). However, CMOD recovery also occurs due to elastic unloading of the bulk (uncracked) specimen and recovery of other cracks (e.g., cracks extending from corner of recess). Therefore, photogrammetry measurements taken from the specimens' surface, which directly measure the crack width more reliably assesses the effectiveness of the shims.

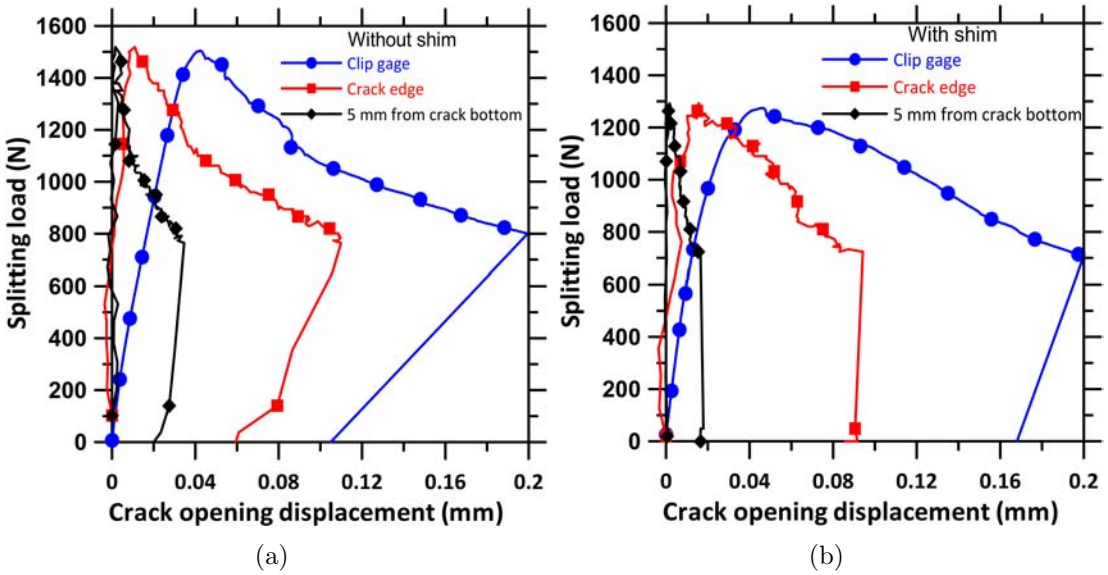

(a) (b)

Figure 2.31 *Splitting load versus COD measured using clip gage at the crack mouth and photogrammetry at the crack edge (bottom of notch) and 5 mm from bottom of crack from Mixture 2 WST specimens loaded to 0.20 mm CMOD and then unloaded (a) without and (b) with plastic shims inserted.*

COD measured by photogrammetry at the crack edge (bottom of notch) and 5 mm from the bottom of the crack, also shown in Figure 2.31, indicate the plastic shims effectively lessen crack width recovery. In Figure 2.31(a) the crack width at the crack edge reduced by 46% (from 0.110 mm to 0.060 mm) and by 42% (from 0.035 mm to 0.020 mm) near the crack bottom upon unloading. The plastic shims minimized crack width recovery, as shown in Figure 2.31(b). The crack width at the crack edge reduced by only 9% (from 0.095 mm to 0.085 mm) upon unloading, with shims in place. Near the bottom of the crack, the crack width reduced by 19 % (from 0.020 mm to 0.015 mm). Crack width values from photogrammetry have been rounded to the nearest 0.005 mm due to resolution of the measurement technique (see Paper II for more details on the resolution of the system).

2.4 Summary and conclusions

This chapter provides an introduction to fracture mechanics and its applicability to describe fracture in concrete and other cementitious materials. Test and analysis methods were presented for determining fracture parameters, and the results of experimental investigations using the wedge split test specimen to determine fracture parameters and cracking behavior were discussed. The following conclusions have been drawn from this portion of the work:

- Fracture parameters were estimated through inverse analysis of the cracked hinge model on experimental data collected using a clip gage and photogrammetry. Epoxy impregnated specimens indicated, however, that cracking occurred in all WST specimen at the corners of the recess. This cracking violates an assumption of the cracked hinge model. Therefore photogrammetry, which provides a local measurement of the crack opening, appears to be a better measurement tool for use when estimating cohesive laws.

- 3–slope cohesive laws were determined to be the optimal number of degrees of freedom for both accurate fitting of experimental data and acceptable computation times for the concrete and steel fiber reinforced concrete mixtures used here. Further increases in the number of degrees of freedom only provided minor improvements in fitting of experimental data and caused several issues, including non-unique inverse analysis solutions, convergence not being reached, and extensive increase in computation time. Fewer degrees of freedom (i.e., 2–slope cohesive law) provided a less refined fit of the experimental data, however results were presented as some modeling software is only capable of implementing 2–slope cohesive laws.

- Analysis of plane and thin sections indicated a complex cracking behavior for the WST specimens, including crack branching, formation of apparently isolated cracks and microcracks, and a rough cement paste fracture surface. Ettringite crystals were observed in all thin sections, likely caused by the 24 hours exposure to liquid water during moisture ingress testing described in the following chapter.

- Comparison of measured and estimated crack profiles indicate that for Mixture 1, a crack coalesces after approximately 16.5 to 18.5 mm of crack length as estimated

by the cracked hinge model. The cracked hinge model cannot provide detailed descriptions of crack morphology; however, the length of the non-coalesced portion of a crack may be relatively constant for a given mixture design. Therefore, the coalesced crack length may be estimated by the crack hinge model.

- Photogrammetry results indicated plastic shims effectively reduced crack width recovery when cracked WST specimens were unloaded. A WST specimen unloaded without shims placed in the notch recovered 46% of the crack opening displacement, while the hard plastic shims reduced recovery to 9%.

Chapter 3

Impact of cracks on transport of moisture and chloride ions

3.1 Introduction

This chapter presents an investigation on the impact of cracking on movement of various aggressive substances in concrete. Section 3.1 of this chapter provides a review of fundamental transport mechanisms in porous materials and various complications for estimating transport in cementitious materials. Transport mechanisms, which control ingress of moisture and/or ions in porous materials, are presented in Section 3.1.1. As the focus of this Ph.D. project is on the ingress of substances leading to corrosion of steel reinforcement embedded in concrete, attention is focused on ingress of moisture and chloride ions and various factors effecting ingress in concrete. Section 3.1.2 specifically discusses previous observations on the impact cracking has on transport mechanisms in concrete and other cementitious materials. Short descriptions of experimental methods previously used to monitor transport in cracked concrete are included. Section 3.2 describes the experimental techniques used here. Results and discussion of results are presented in Section 3.3. Conclusions of these investigations are presented in Section 3.4.

3.1.1 Transport mechanisms

The transport of gases and liquids through concrete and other cementitious materials takes place by various mechanisms depending on initial moisture conditions and the environmental exposure. The Nernst-Planck equation (Equation 3.1) describes the flow of ions through a porous material [*Nilsson et al.*, 1996; *Marchand*, 2001]:

$$F_i = -D_i \frac{\partial c_i}{\partial x} + \frac{z_i F}{RT} D_i c_i \frac{\partial E}{\partial x} + c_i F_e \tag{3.1}$$

where F_i is the total flow of ion, i. The first term accounts for diffusion, therefore D_i is the diffusion coefficient of ion i, c_i is the concentration of ion i, and x is the depth. The second term is the pure electrical migration caused by an electrical potential gradient $\frac{\partial E}{\partial x}$, where z_i is the electrical charge, F is Faraday's constant, R is the gas constant, and T is the temperature. The third term, F_e accounts for convection of ions through the flow of a solution. The effect of chloride binding, discussed below, is not considered by the

Nernst-Planck equation.

Transport may occur through a single or any combination of controlling mechanisms, depending on the conditions of the porous material and the exposure environment. The following sections provide additional details on individual transport mechanisms and explanations of which mechanism(s) controls based on initial conditions.

Diffusion

Diffusion of chloride ions in concrete is controlled by Fick's second law of diffusion, which describes non-steady state diffusion (or time-dependency of concentration) of a single diffusion ion (i.e., no interaction with other ions) as shown in Equation 3.2 [*Fick*, 1855]:

$$\frac{\partial c_i}{\partial t} = D\frac{\partial^2 c_i}{\partial x^2} \tag{3.2}$$

where, c_i is the concentration of the diffusing ion, t is time, D is the diffusion coefficient, and x is the depth. Typically, the complimentary error function (or Crank's) solution is applied to cementitious materials (e.g., [*Crank*, 1986; *Nilsson et al.*, 1996; *Neithalath et al.*, 2005; *Poulsen and Mejlbro*, 2006]), as presented in Equation 3.3

$$c_i(x,t) = c_{i,0}\left[1 - erf\left(\frac{x}{2\sqrt{Dt}}\right)\right] \tag{3.3}$$

where, $c_i(x,t)$ is the concentration of a substance as a function of depth, x and time, t, $c_{i,0}$ is the surface concentration, and the error function, erf is:

$$erf(z) = \frac{2}{\sqrt{\pi}}\int_0^z \exp(-u^2)du \tag{3.4}$$

Diffusion in concrete and cementitious materials is further complicated as the diffusion coefficient, D has been shown to vary with maturity age (or degree of hydration), w/c, temperature, degree of saturation (or relative humidity), concentration of chloride ions and associated cation, depth within the concrete, chloride binding, and the use of mineral and/or chemical admixtures. Detailed descriptions of these effects and models for calculated the diffusion coefficient considering the various factors are provided in the literature (see e.g., [*Saetta et al.*, 1993; *Sandberg*, 1995; *Nilsson et al.*, 1996; *Nielsen and Geiker*, 2003; *Poulsen and Mejlbro*, 2006; *fib Bulletin 34*, 2006; *Life-365 Consortium II*, 2010]); however several are described in the following which are considered central to this work.

The amount of moisture in the concrete pore structure has a major impact on diffusion coefficient [*Saetta et al.*, 1993; *Nielsen and Geiker*, 2003], which is of particular importance in this work as the specimens used were conditioned to 50% RH prior to exposure to chloride containing water. In [*Saetta et al.*, 1993] the diffusion coefficient was simply related to changes in relative humidity inside the concrete; with a critical relative humidity value of 75% causing a rapid drop in diffusivity. *Nielsen and Geiker* [2003] suggested the impact of degree of saturation may be estimated from the amount of water filled capillary pores, determined by simple volume calculations of the total amount of capillary pores (based on Power's model [*Powers and Brownyard*, 1947]), and sorption isotherms.

Binding of chloride ions

Chloride ions can be bound chemically and physically in concrete. Binding provides a 'chloride sink' that delays the ingress of chloride ions. Chemically, chlorides bind with cement to form Friedel's salt ($3CaO{\cdot}Al_2O_3 \cdot CaCl_2 \cdot 10H_2O$) [*Midgley and Illston*, 1984; *Nilsson et al.*, 1996; *Birnin-Yauri and Glasser*, 1998; *Xi and Bazant*, 1999]. Physical binding is generally thought to take place at the pore walls [*Nilsson et al.*, 1996; *Xi and Bazant*, 1999]. Bound chlorides may be partly liberated if the free chloride concentration reduces [*Luping and Nilsson*, 1993]. Therefore, the 'chloride sink' provided by binding may shift to a source of chloride ions. Binding may delay reinforcement depassivation as only free (unbound) chloride ions are available to interact with steel reinforcement. Still, the risk of reinforcement corrosion remains as binding is nearly completely reversible if pore solution pH drops below approximately 11 [*Tuutti*, 1982a; *Glass et al.*, 2000; *Glass and Buenfeld*, 2000; *Reddy et al.*, 2002].

Capillary suction

Capillary suction or wicking occurs in dried or partly dried porous materials. Capillary suction occurs due to pore pressure, P pulling water (and ions contained in the water) into the porous material as described by the Young-Laplace equation for an idealized (round) pore:

$$P = -\frac{2\gamma \cos\theta}{r} \tag{3.5}$$

where γ is liquid-vapor surface tension of fluid, θ is the contact angle between the liquid and solid phases, and r is the pore radius. Using the Young-Laplace equation, the pressure resulting from the collapse (i.e., drying) of water in a pore is calculated. Vapor pressure, $\ln(\frac{p}{p_0})$ is related to pore size using the Kelvin equation (Equation 3.6)

$$\ln\left(\frac{p}{p_0}\right) = -\frac{2\gamma V_m}{rRT} \tag{3.6}$$

where V_m is the molar volume, R is the gas constant, and T is temperature. Equation 3.6 describes the emptying (e.g., drying, evaporation, etc.) and filling of capillary pores (e.g., wetting, wicking, etc.) as a function of changing vapor pressure. Typically, when dealing with cementitious materials the vapor of interest is water vapor. According to Equation 3.5 pores with larger radius require less pressure to cause collapse of the water meniscus (i.e., drying). Therefore, during drying of a porous material with a distribution of pore sizes, large pores lose their moisture initially, followed by smaller pores. The opposite occurs during wetting, where smaller pores fill initially, followed by larger pores. Equation 3.7 is generally used to predict capillary suction (for one-dimensional ingress)

$$W/A = S\sqrt{t} \tag{3.7}$$

where, W is the volume of water absorbed, A is the exposed surface area, and S is the sorptivity (mm^2/s).

Capillary suction has been shown to relate to initial moisture content according to Equation 3.8. Equation 3.8, initially proposed to describe the influence initial moisture content had on capillary suction in soils [*Philip*, 1957] was found to be applicable to brick [*Hall et al.*, 1983] and later cementitious materials within a limited range of RH [*Hall*, 1989; *Geiker and Laugesen*, 2001].

$$S_i = S_0 \cdot (1 - \alpha\theta_i)^{0.5} \tag{3.8}$$

where, S_i is sorptivity at a given uniform moisture content, θ_i, S_0 is sorptivity of a dry sample, and a is 1.08 for cementitious materials.

Chloride ion transport through capillary suction Ions may be transported with water moving due to capillary suction. According to [*Nilsson et al.*, 1996], the amount of chlorides, Q_{Cl} (kg/m^3) pulled into concrete through capillary suction of chloride solutions is expressed as:

$$Q_{Cl}(t) = \frac{c}{\rho_w} \cdot S\sqrt{t} \tag{3.9}$$

where t is the duration of capillary suction (seconds), c is the salt concentration (kg/m^3),and ρ_w is density of water.

Dissolved chloride ions have been shown experimentally to rapidly ingress due to capillary suction; however, chloride binding still slows the ingress of chlorides compared to water ingress [*Volkwein*, 1993; *Akita and Fujiwara*, 1995]. Additionally, contamination of water with chloride ions (and the associated cation) have been shown to influence the solution surface tension, viscosity, and ingress behavior in accordance with Equation 3.10 [*Kelham*, 1988; *Weiss*, 1999]:

$$x(t) = \sqrt{\frac{4k\gamma\cos(\theta)t}{\phi\mu r}} \tag{3.10}$$

where, $x(t)$ is the penetration depth (m) at time t (sec), k is the intrinsic permeability (m^2), ϕ is the material porosity, μ is the viscosity of the fluid ($kg/(m \cdot s)$). Previous research, investigating the influence of shrinkage-reducing admixtures, has indicated absorption rate is proportional to the square root of the ratio of surface tension and viscosity of the fluid ($\sqrt{\gamma/\mu}$) [*Bentz*, 2006; *Pour-Ghaz et al.*, 2009, a; *Sant et al.*, 2010].

Further research in [*Spragg et al.*, submitted] indicates increasing concentrations of ions from salts (NaCl, $CaCl_2$, and $MgCl_2$) cause increased surface tension and viscosity (compared to deionized water), leading to reduced absorption of the solutions into concrete. The $\sqrt{\gamma/\mu}$-absorption proportionality holds for salt solutions; therefore, increased salt concentrations affects (i.e., slows) absorption of the solution into concrete.

Permeation

Permeation, or the flow of a liquid or gas through a porous material via a pressure gradient, is described (for laminar flow) using Darcy's law (Equation 3.9), which was discovered by

Henry Darcy [*Darcy*, 1856].

$$\frac{\partial q}{\partial t}\frac{1}{A} = k_p \frac{\partial h}{\partial x} \tag{3.11}$$

where, $\frac{\partial q}{\partial t}$ is the flow rate per unit area, A; k_p is the permeability coefficient, and ∂h is the pressure difference across the specimen thickness, x. Resistance to permeation (permeability coefficient) is affect by viscosity of the permeating material, tortuosity, and connectedness of pore network [*Nilsson*, 2002].

Chloride ions, which appear to have little effect on permeation [*Buenfeld et al.*, 1995; *Nilsson et al.*, 1996], can also ingress with water through permeation; however, the effects of binding and RH previously described still apply.

3.1.2 Review of literature on ingress in cracked concrete

The following sections present a review of previous efforts to characterize the influence of cracking on the various transport mechanisms described above.

Diffusion

The diffusion of chloride ions in saturated, cracked concrete has been investigated in [*Rodriguez and Hooton*, 2003; *De Schutter*, 1999], with diffusion of carbon dioxide also considered in the latter reference. In [*Rodriguez and Hooton*, 2003], cylindrical concrete specimens were completely split using either splitting tensile loading or by cutting (i.e., fractured and smooth surfaces were investigated) and the cracks were set to widths between 0.08 to 0.68 mm using shims between the split surfaces. The resulting cracks were therefore parallel and extended through the entire cross section of the specimen. In [*De Schutter*, 1999], cracks were simulated by casting inserts with varying widths and depths into mortar specimens. This method causes a higher paste content at the crack surface and an idealized crack geometry, which does not accurately portray an actual crack based on the descriptions of cracks in Chapter 2. The crack walls were parallel and did not extend through the entire specimen depth.

In both cases, diffusion of chloride ions increased at the location of the crack into the depth of the specimen. In [*Rodriguez and Hooton*, 2003], the fractured (and smooth) surfaces behaved as a free surface for diffusion (i.e., similar chloride ingress and diffusion coefficients from top surface and fracture surface) for all crack widths investigated. The minimum crack width used in these tests was 80 microns.

In [*De Schutter*, 1999], a crack influence factor, λ_{Cl} was introduced to estimate an average effect of crack width and depth on diffusion. Equation 3.12 describe the influence of cracks on chloride diffusion:

$$D_{Ca,Cl}(w,d) = \lambda_{Ca,Cl}(w,d) \cdot D_{Cl,Ca}(w=0,d=0) \tag{3.12}$$

where $D_{Ca,Cl}(w,d)$ is the crack width- and depth-dependent chloride ion or carbonation diffusion coefficient, $D_{Ca,Cl}(w=0,d=0)$ is the chloride ion or carbonation diffusion

coefficient of uncracked material, and λ_{Cl} and λ_{Ca} is given by Equations 3.13 and 3.14, respectively.

$$\lambda_{Cl} = exp\left[0.2541\left(\frac{d}{d_0}\right)^{0.5202}\left(\frac{w}{w_0}\right)^{0.2652}\right] \tag{3.13}$$

where, d_0 and w_0 are 1 mm. Similarly, a crack influence factor for carbonation, λ_{Ca} was determined in [*De Schutter*, 1999] as shown in Equation 3.14:

$$\lambda_{Ca} = exp\left[0.3173\left(\frac{d}{d_0}\right)^{0.3270}\left(\frac{w}{w_0}\right)^{0.6803}\right] \tag{3.14}$$

Equations 3.13 and 3.14 indicate that increasing crack width and/or depth causes increased average rate of diffusion of chloride ions and carbonation. The crack influence factor, λ is more significant for chloride ion ingress compared to carbonation. While the trends found in [*De Schutter*, 1999] are reasonable and the expressions are potentially important factors which could be implemented in service life prediction models, several issues should be noted. In addition to the fact that cracks were introduced by inserts as described above, the equations were derived from a limited range of crack widths (0.20, 0.30, and 0.50 mm wide inserts) and depths (5 and 10 mm long inserts).

In both cases, the induced cracks were somewhat idealized compared to the type of cracking described in Chapter 2; where cracks are described to consist of regions of coalesced and isolated cracks. Additionally, V-shaped or flexural cracks are not considered. Based on [*Rodriguez and Hooton*, 2003], coalesced crack with width at least greater than 80 microns have a free surface behavior; however, isolated cracks seen in V-shaped cracking have a much less significant effect on diffusion [*Nilsson et al.*, 1996].

Capillary suction

Both discrete (single) and distributed cracking influence the capillary suction of cementitious and other porous materials [*Van Geet*, 2001; *Roels et al.*, 2003; *Weiss et al.*, 2004; *Yang*, 2004; *Roels and Carmeliet*, 2006; *Pour-Ghaz et al.*, 2009; *Pease et al.*, 2009].

In [*Yang*, 2004], distributed cracks induced by freeze-thaw cycling caused increased initial and total sorptivity of the concrete. Comparisons of sorptivity and cracking behaviors in that study concluded that isolated cracks caused slight increases in the total sorptivity (due to increased voids in the concrete); however, the initial sorptivity was only significantly effected after significant freeze-thaw degradation caused a connected crack network.

Studies of discrete cracks indicate that cracks allow for a rapid (nearly instantaneous) ingress of water or solutions into the depth of the porous material [*Roels et al.*, 2003; *Roels and Carmeliet*, 2006; *Weiss et al.*, 2004; *Pour-Ghaz et al.*, 2009]. Detailed comparison of the cracking and water uptake behavior in concrete indicated the time-dependent saturation perimeter is related to the geometry of the coalesced crack [*Weiss et al.*, 2004].

As measurement of water uptake is a central focus of the work presented in this chapter, the application of several tomography measurement techniques is describe in below.

Tomography measurement techniques Several tomography techniques have been previously used to monitor water ingress in cracked and uncracked porous building materials such as γ-ray attenuation [*Nielsen*, 1972; *Kumaran and Bomberg*, 1985], NMR/MRI [*Gummerson et al.*, 1979; *Chen et al.*, 2003; *Mastikhin et al.*, 2002], and positron emission tomography (PET) [*Hoff et al.*, 1996]. Typically, these techniques measure moisture content at discrete points in a sample, requiring many measurements to provide a clear picture of the moisture distribution in the specimen. Additionally, for the PET scan a tracer radioisotope must be dissolved in the water to track movements; however, this tracer may bond with pore walls and not move with the moisture front [*Hoff et al.*, 1996]. A comparison of these different imaging techniques in [*Roels et al.*, 2004] indicated strong agreement except for γ-ray attenuation. This was attributed to the rapid ingress rate of the material used for comparison (calcium silicate); other work has shown better results for material with less rapid ingress. A further technique, thermal neutron tomography, is highly effective due to water's high thermal neutron attenuation coefficient (due to high hydrogen content of water) [*Masschaele et al.*, 2004]; however, few facilities are available for such testing.

Permeation

Cracking has a major impact on permeation and watertightness of concrete, and a significant amount of work has investigated the effect of cracking and self-healing on concrete permeability [*Saito and Ishimori*, 1995; *Greiner and Ramm*, 1995; *Wang et al.*, 1997; *Edvardsen*, 1999; *Aldea et al.*, 1999; *Ramm and Biscoping*, 1998; *Aldea et al.*, 2000]. Minutes crack widths (approximately 50 microns) result in increases in permeability coefficient, k_p (Equation 3.11) by over an order of magnitude [*Wang et al.*, 1997].

Models to estimate flow of liquids through parallel concrete cracks have been developed in [*Edvardsen*, 1999; *Aldea et al.*, 2000]. Both modeling approaches use Poiseuille's law, which describes liquid flow through a parallel, smooth crack (Equation 3.15).

$$q_0 = \frac{\Delta p \cdot b \cdot w^3}{12 \cdot \eta \cdot d} \tag{3.15}$$

Here, q_0 (m^3/s) is the initial flow rate in a smooth, parallel wall crack, Δp is the water pressure difference between the flow inlet and outlet, b is the crack length, w is the crack width, η is the solution's absolute viscosity, and d is the length of the flow path. As concrete fracture surfaces are typically not smooth, a 'roughness' factor, ξ must be included as shown in Equation 3.16:

$$q_r = \xi \cdot \frac{\Delta p \cdot b \cdot w^3}{12 \cdot \eta \cdot d} \tag{3.16}$$

Variation in the roughness factor, ξ range from 0.0045 and 0.53 in the literature [*Breysse and Gérard*, 1997; *Edvardsen*, 1999; *Aldea et al.*, 2000].

Self-healing (or autogenous healing) of cracks has been shown to drastically reduce permeation with time for both static and dynamic cracks [*Edvardsen*, 1999; *Ramm and Biscoping*, 1998]. The initial crack width was found to be the most important factor in the rate and degree of self-healing; therefore, the following simplified expression was proposed in [*Edvardsen*, 1999] to estimate the time dependent flow rate, $q(t)$:

$$\frac{q(t)}{q_0} = 65 \cdot w_m^{-1.05} t^{(-1.3+4w_m)} - 10^5 \cdot w_m^{5.8} \tag{3.17}$$

where, w_m is the mean surface crack width and t is the water exposure time.

In [*Aldea et al.*, 2000], the influence of crack geometry (parallel cracks versus V-shaped cracks) was investigated. Results concluded that parallel cracks caused greater increases in permeability coefficient, which was attributed to differences in crack geometry. This hypothesis is reasonable when comparing to results from other transport mechanisms, which indicate that isolated crack associated with V-shaped cracks have reduced effect on ingress parameters.

3.2 Experimental procedures

The following sections describe the experimental investigations completed as part of this study using the WST to study the effect cracking has on the ingress behavior of moisture and chloride ions. Moisture ingress was monitored through x-ray attenuation measurements, an increasingly common technique (see e.g., *Bentz et al.* [2001]; *Hu and Stroeven* [2003]; *Lura et al.* [2004]; *Roels and Carmeliet* [2006]; *Pour-Ghaz et al.* [2009]), as described in Section 3.2.2. Chloride ingress was detected by colorimetric testing using silver nitrate as described in Section 3.2.3.

3.2.1 Materials and specimen preparation

As described in Section 2.2.1, WST specimens were cast using Mixtures 1 (Table 2.1). The specimens were cured, cut, and conditioned to 50% ±3 % RH prior to application of load to induce cracking. Weight of several samples was monitored during conditioning and ingress testing did not proceed until weight change was at a minimum (± 0.02% weight change). Conditioning took place over a period of no less than one year.

Moisture ingress testing was completed for Mixtures 1 under varying load (unloaded and peak load) and cracking (0.10 mm, 0.15 mm, 0.20 mm, and 0.40 mm CMOD) conditions. Chloride ingress testing, which used a destructive procedure, was completed for Mixtures 1 with a CMOD of 0.20 mm. The peak load was the average peak load from tests discussed in Chapter 2. Loading and cracking of the WST specimens was completed following the procedures described in Section 2.2.2.
Once the target CMOD was reached for the cracked specimens, loading was paused and hard plastic shims were inserted into the notch to minimize crack recovery (Section 2.3.4). Immediately after removing specimens from the loading machine, aluminium foil tape

(a) (b)

Figure 3.1 *GNI X-ray attenuation systems at (a) the Technical University of Denmark and (b) Purdue University. (Author's photos)*

(2.5" Nashua 324A cold weather foil tape) was used to seal the sides and bottom of the specimen. It was found that placing individual strips of the 62.5 mm (2.5 inch) aluminum tape vertically (i.e., parallel to the crack in the WST specimen) provided the best sealing and minimized leakage. Individual strips of tape were overlapped by a minimum of 10 mm. As can be seen in Figure 3.2(a) only the top surface was left unsealed to allow for ponding with water or chloride solution. The partially sealed cracked specimens were stored in sealed plastic bags in a 50% ±3% relative humidity and 20°C ±2°C chamber until ingress testing. The specimens were placed in sealed plastic bags and ingress testing was completed within one month to minimize carbonation of the cracked surface.

3.2.2 X-ray attenuation measurement technique

Two GNI x-ray facilities were used during this research. One located at the Purdue University Charles Pankow Concrete Materials Laboratory (Purdue facility) [*GNI*, 2006] and one located at the Technical University of Denmark (DTU facility) [*GNI*, 2008]. Figure 3.1 shows both systems, which consist of an x-ray source, a scintillation counter (x-ray camera), and a programmable three-axis motion frame for moving the source and camera located in a shielded environmentally controlled chamber. As shown in Figure 3.2(a), specimens are located between the x-ray source and camera. The x-rays produced by the source interact with the specimen prior to reaching the x-ray camera. As the x-rays impact the specimen some are absorbed or deflected while others pass through unabated. As described below, the amount of x-rays passing through the specimen is effected by, among others, changes in moisture content. The following paragraphs describe the x-ray measurement technique in greater detail, including detailed descriptions of the scintillator, the underlying theory of the technique, and the measurement procedure.

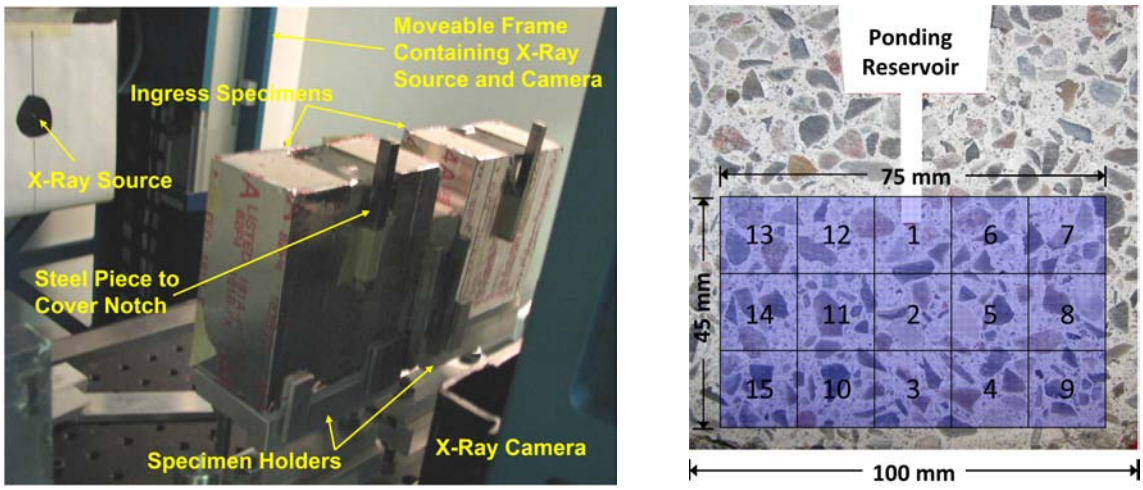

(a) (b)

Figure 3.2 *(a) The x-ray system setup includes a moveable frame, x-ray source and camera, and specimen holders and (b) the location of x-ray images taken on the WST specimens. (Author's photos)*

Scintillation counters

Scintillator are a group of materials which scintillate, or luminesces, when excited by ionized radiation (x-rays here). When coupled with a photomultiplier, that luminescence can be recorded and analyzed. Here, a 25 mm x 25 mm thallium doped sodium iodide (NaI(Tl)) crystal scintillator was coupled to a 252x256 pixel photomultiplier in an 'x-ray camera.' The photomultiplier records the number and location of scintillation events detected by each pixel during a preset period of time. This time period is called the integration time, and is akin to shutter speed in visible light cameras. The number of scintillations during the integration time is known as intensity, which has a unit of counts, or hits. Figure 3.3 shows grayscale images from the x-ray camera from both mixtures. The fibers in Mixture 2 are clearly visible in Figure 3.3(b) due to the increased attenuation coefficient of steel, as discussed below.

An important distinctions between the x-ray cameras used here and other scintillation counters, called x-ray detectors, commonly used should be noted. X-ray detectors measure x-rays at a single point (or small area) in a specimen over a period of time [*Bentz et al.*, 2001; *Hu and Stroeven*, 2003; *Lura et al.*, 2004; *Weiss et al.*, 2004]. Spatial data is therefore provided by repeating measurements at many locations, moving the x-ray source and detector relative to the specimen between measurements. For example, in [*Weiss et al.*, 2004] an x-ray detector was used to observe water ingress in WST specimen over an area similar to the size shown in Figure 3.2(b). A total of 91 measurements were taken for one observation using a 13 x 7 grid. Here, by using an x-ray camera a total of 15 measurements (Figure 3.2(b)) result in a total of 695506 points being monitored (1057x658 grid). In contrast, the x-ray camera used here only detects the intensity (i.e., counts), but not the energy of the individual counts. Most x-ray detectors are equipped with photomultipliers that not only detect scintillation events, but also analyze the brightness of these events.

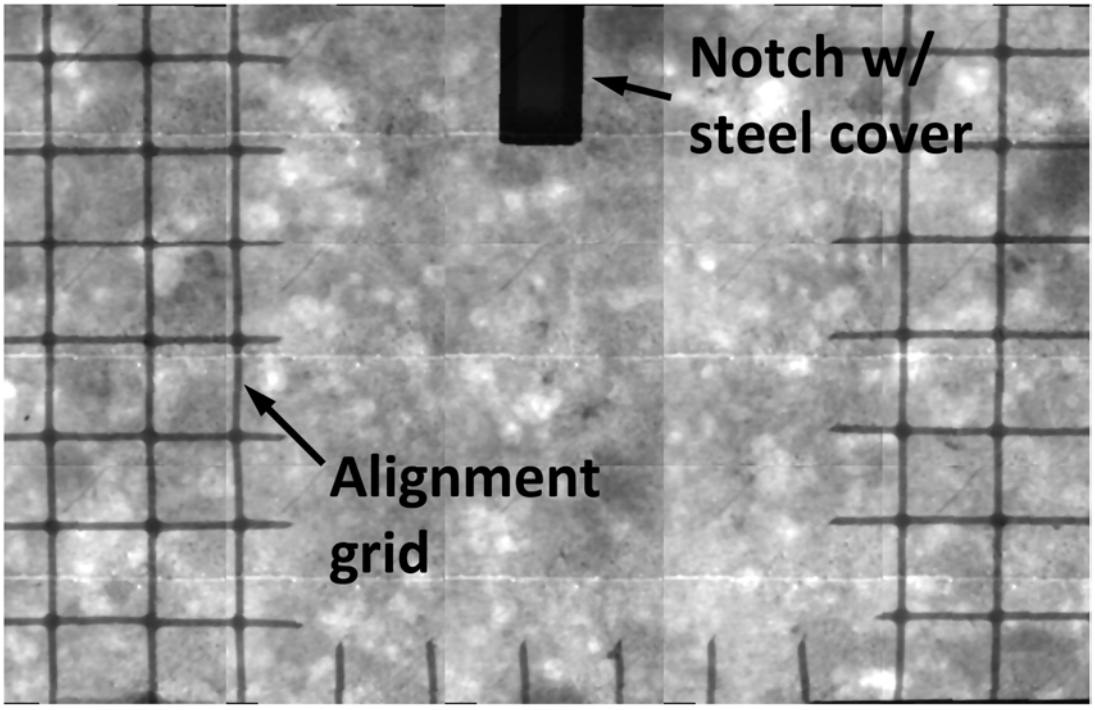

(a)

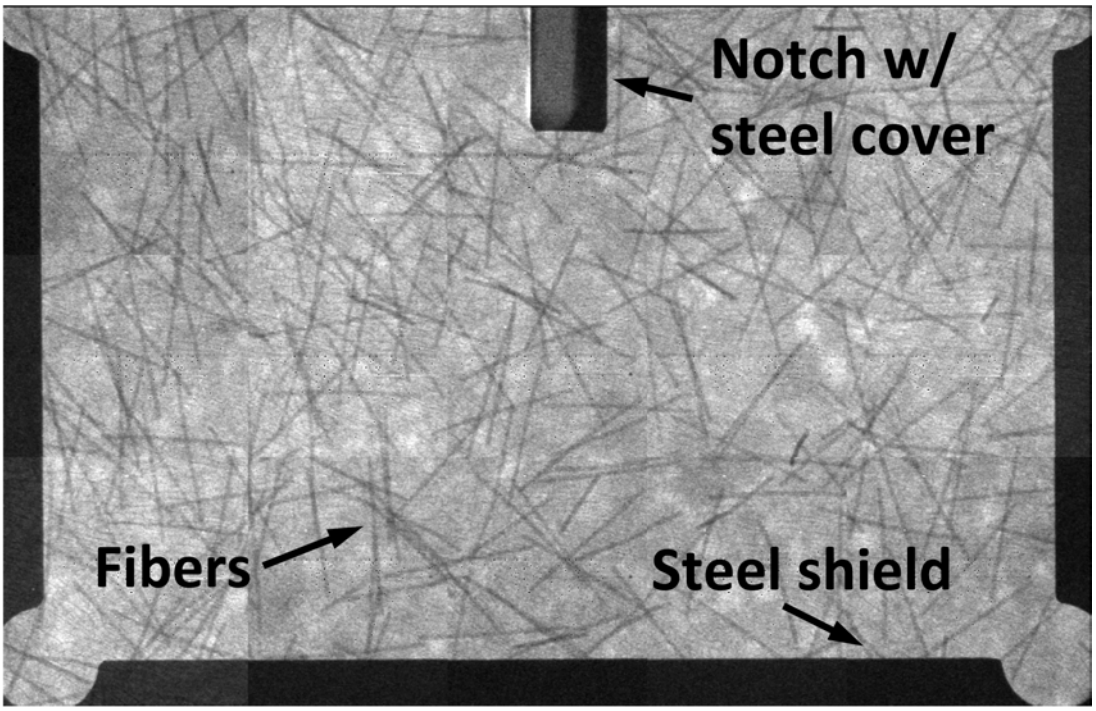

(b)

Figure 3.3 *Sample x-ray images compiled from 15 individual measurements for (a) Mixture 1 and (b) Mixture 2. The alignment grid in (a) was used to assure compiled images aligned properly.*

Brightness is related to the energy of the x-ray exciting the scintillator, which has been used in the past to characterize the x-ray spectra [*Weiss et al.*, 2004]. However, as describe in the following section, intensity variations alone can be used to detect moisture content changes in porous materials.

Theoretical background

Figure 3.4(a) shows the fundamental layout of the x-ray attenuation measurements. The x-ray source produces an x-ray beam with a given incident intensity, I_0, which passes through a test specimen with thickness, t. As the x-ray beam passes through the specimen a portion of the incident intensity, I_0 is attenuated (i.e., absorbed and scattered) and the transmitted intensity, I is recorded by an x-ray camera. The attenuation behavior is described for a homogeneous x-ray beam (x-rays of single energy level) by the Beer-Lambert law (Equation 3.18) [*Knoll*, 1989; *Hansen et al.*, 1999]:

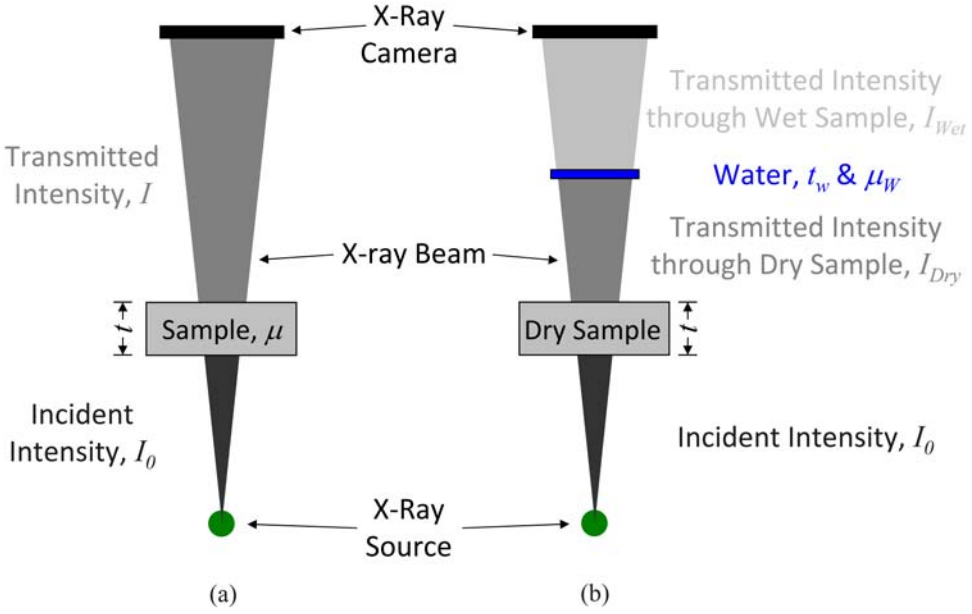

Figure 3.4 *Fundamental explanation of use of x-ray attenuation measurements. (a) Schematic description of Beer-Lambert law (Equation 3.18). (b) Effect of moisture movements on x-ray attenuation measurements as described by a composite of a dry specimen and an thickness of water representing moisture in the specimen.*

$$I = I_0 exp(-\mu t) \tag{3.18}$$

where, μ is the linear attenuation coefficient. The linear attenuation coefficient, μ is a material property shown to relate to a material's density, ρ and effective atomic number, Z_{eff} $\left(Z_{eff} = \sqrt[3.8]{\sum f_i Z_i^{3.8}}\right)$ and the x-ray source voltage, E (keV) as described in Equation 3.19 (for x-ray energies below 200 keV) [*Van Geet*, 2001; *Dyson*, 1973; *Curry et al.*, 1990].

$$\mu = \rho\left(a + b\frac{Z_{eff}^{3.8}}{E^{3.2}}\right) \tag{3.19}$$

where a and b are coefficients describing Compton scatter and photoelectric absorption, respectively [*Van Geet et al.*, 2001]. Based on Equations 3.18 and 3.19, it can be seen that changes in density, μ and/or effective atomic number, Z_{eff} in a porous material (due to changes in moisture content) will be marked by a change in the transmitted intensity, I. Furthermore, according to Equation 3.19 the incident x-ray energy reduces the linear attenuation coefficient, μ for a substance (discussed further in Section 3.3.1).

Figure 3.4(b) illustrates the effect moisture ingress has on the x-ray attenuation behavior by simplifying the process as a composite system consisting of a dry sample in series with liquid water with thickness, t_w. Previous works have shown Equation 3.20 can be used to describe the x-ray attenuation response of the series composite systems illustrated in Figure 3.4(b), and furthermore that this composite system can be used to describe moisture ingress in porous materials [*Hansen et al.*, 1999; *Roels and Carmeliet*, 2006; *Baker et al.*, 2007]. Equations 3.20 and 3.21 describe the attenuation of x-ray by the composite. The transmitted intensity through the dry specimen, I_{dry}, is calculated according to Equation 3.20 (analogously to Equation 3.18). The addition of water, with thickness t_w and linear attenuation coefficient μ_w, to the composite system simulates moisture ingress. The transmitted intensity through the wet specimen, I_{wet} is further reduced by the presence of water according to Equation 3.21.

$$I_{dry} = I_0 \cdot exp(-\mu t) \tag{3.20}$$

$$I_{wet} = I_{dry} \cdot exp(-\mu_w t_w) = I_0 \cdot exp(-\mu t - \mu_w t_w) \tag{3.21}$$

The series composite system describes moisture ingress by increasing the water thickness, t_w, while drying corresponds to a reduction in water thickness. The change in moisture content during exposure to water can be directly measured through x-ray attenuation measurements by comparing I_{dry} and I_{wet} [*Hansen et al.*, 1999; *Roels and Carmeliet*, 2006], as shown in the following.

Change in moisture content of a specimen, Δw (kg/m^3) is calculated as change in water volume within the specimen volume or, assuming a constant cross-section, a change in water thickness within the specimen thickness according to Equation 3.22:

$$\Delta w = \frac{\rho_w \Delta V_w}{V} = \frac{\rho_w \Delta t_w}{t} \tag{3.22}$$

where, ρ_w is the density of water (1 g/cm^3), ΔV_w is the change in water volume within the specimen's volume, V; and Δt_w is the change in water thickness within the specimen's thickness, t.Equation 3.21 can be therefore be rewritten as:

$$I_{wet} = I_{dry} \cdot exp\left(-\frac{\mu_w \Delta w t}{\rho_w}\right) \tag{3.23}$$

and solving for change in water content, Δw:

$$\Delta w = -\frac{\rho_w}{\mu_w t} ln\left(\frac{I_{wet}}{I_{dry}}\right) \tag{3.24}$$

The intensity I_{dry} is a measure of a specimens initial moisture condition, while I_{wet} is measured at various times after exposure to water. Equation 3.24 in this form describes a wetting experiment (i.e., specimen was initial dry and then exposed to water); however, by inverting the I_{wet}/I_{dry} ratio to I_{dry}/I_{wet} a drying experiment would be described.

Measurement procedure

Using the GNI X-ray systems two series of test were completed: 1) optimization of x-ray measurement settings 2) moisture ingress testing in cracked WST specimens.

Series 1 - Optimization of x-ray measurement setting Series 1 measurements were completed to assess how various factors are influenced by the x-ray settings, including the amount and variation of transmitted intensity and the linear attenuation coefficients of concrete. The settings considered in the optimization were the x-ray source voltage and current and integration time.

To assess the effect changing x-ray settings have on the amount and variation of transmitted intensity, I through a 50 mm thick concrete specimen, images were repeatedly captured using varying x-ray energy settings. The energy levels used included voltages of 40, 50, 60, 70, and 75 keV, all at a current of 100 μA. A total of 28 images were captured using an integration time of 5 seconds for each image. The average and standard deviation of the transmitted intensity detected by each pixel in the images were computed for all images take at each energy setting. The coefficient of variation, c_v was calculated by Equation 3.25:

$$c_v = \sum_{i=1}^{N} \frac{\sigma_i}{\mu_i} \Big/ N \times 100\% \tag{3.25}$$

where, σ_i is the standard deviation in transmitted intensity, μ_i is the average transmitted intensity and N is total duration of the measurements (seconds).

The linear attenuation coefficient of the concrete, μ was determined by measuring the transmitted intensity, I using a Mixture 1 cylinder cut into various thicknesses (0 (air), 4.4, 6.1, 11.9, 14.4, 16.6, 20.1, 31.6, 42.0, and 50.5 mm). Measurements were taken using various energy settings, including all combinations of 30, 40, 50, 60, and 70 keV and 20, 30, 40, 50, 60, 70 μA. Higher energy settings were not used due to potential damage to the x-ray camera associated with the 0 mm (air) measurements. The initial intensity, I_0 was assumed to be the transmitted intensity through air and the linear attenuation coefficient was determined using Equation 3.18.

The linear attenuation coefficient of water was determined using wedge-shaped and parallel-walled plastic containers with known dimensions placed in front of a 50 mm thick WST specimen. Transmitted intensity, I was measured from the from the empty and filled containers and the linear attenuation coefficient was determined using Equation 3.23.

Series 2 - Moisture ingress measurements As the size of the x-ray camera is smaller than the WST specimens, x- and y-axis movements were programmed into the motion frame to record images from the area shown in Figure 3.2(b). Images were recorded using 15 mm movements, both vertically and horizontally, in the order shown. At each measurement location the x-ray camera recorded the intensity for a total of 50 seconds. After each measurement, the dark current (image recorded by x-ray camera while x-ray source is switched off) was recorded. The dark current was removed from each imaged, and the resulting images were cropped, de-speckled, averaged, tiled, shifted, and analyzed using a batch code written in ImageJ [*ImageJ*, 2008; ImageJ Tiler, 2008; *Couch and Weiss*, 2009]. Figure 3.3 shows the results of the ImageJ procedure. Figure 3.3(a) shows that the individual images, which comprise the compiled image, are properly aligned an positioned. A steel shield, used to outline the specimens and to protect the x-ray camera, can be seen in Figure 3.3(b). Additional details on the basic use of the x-ray systems and image processing with ImageJ is available in Appendix D. For all measurements taken at the DTU facilities, the x-ray tube was allowed to warm-up for 200 seconds and stabilize for 600 seconds to minimize variations in incident intensity, I_0 based on an initial investigation of the equipment described in [*Scheffler et al.*, 2010]. Measurements taken at the Purdue University facilities utilized the automatic settings of system to control the warm-up and stabilization times. All measurements for Mixture 1 WST specimens were taken using the Purdue facility, while Mixture 2 WST specimens were measured at the DTU facility.

Three reference measurements were initially taken on the conditioned (50% ±3 % RH) specimens to determine I_{dry}. The three dry measurements were averaged. After the reference measurements were taken the specimens were ponded with tap water. Additional x-ray measurements were taken immediately after the introduction of water (i.e., 1 minute) as well as at varying times after exposure to water. These measurements were I_{wet} in Equation 3.24. The change in the moisture content was then calculated according to Equation 3.24 using ImageJ. An empirical water ingress ratio (ABS ratio) was computed using the x-ray images according to Equation 3.26:

$$ABS = \frac{(I_{x,y})_{dry} - (I_{x,y})_{wet,i}}{(I_{x,y})_{dry} - (I_{x,y})_{wet,n}} \cdot 100\% \tag{3.26}$$

where ABS is the empirical water ingress ratio, $(I_{x,y})_{dry}$ and $(I_{x,y})_{wet,i}$ are the transmitted intensity recorded by each pixel in the dry specimen and wet specimen image taken at each measurement time, i and $(I_{x,y})_{wet,n}$ is the wet image recorded after 6 hours. After 6 hours of ponding, the initial moisture front had passed through the measurement area. While the entire pore structure is likely not saturated after 6 hours, little change in x-ray attenuation was seen after this time. The normalization to 6 hour measurements accounts

for differences in intensity that occur due to variations in paste content in the concrete [*Weiss et al.*, 2004].

3.2.3 Chloride ingress testing

Due to the destructive nature of the silver nitrate ($AgNO_3$) colorimetric testing procedure, only two loading conditions were used including unloaded and ≈0.20 mm CMOD for Mixtures 1 and 2. Conditioned specimens were ponded using a 10% chloride solution for 1, 3, 6, 9, 12, and 24 hours. After ponding, the specimens were emptied and a 12 mm slice was removed using a concrete water saw. The surface of the larger piece was dried by passing the breeze from a fan above the surface until all excess water was evaporated (approximately 20 minutes). The top 2 mm of the surface was then removed by grinding. After grinding, a 0.10 N $AgNO_3$ solution was applied to the surface 3 to 4 times with a spray bottle. Images were captured using a digital camera and thresholds were applied to create binary images to distinguish the chloride contaminated regions. Image analysis software was used to extract the needed data.

3.3 Results and discussion

3.3.1 Series 1 - Optimization of x-ray measurement settings

Figures 3.5 illustrate the effect of changing x-ray voltage and current on the incident and transmitted intensity, I_0 and I, respectively. The incident intensity, I_0 is assumed to be the transmitted intensity through a 0 mm thick specimen (i.e., air). Figure 3.5(a) shows increasing x-ray source current caused a linear increase in transmitted intensity. Linear fitting of the data resulted in a worst-case coefficient of determination (R^2) value of 0.992. The figure also indicates specimen thickness affects the transmitted intensity in agreement with Equation 3.18. The affect of specimen thickness is discussed further in this section. Figure 3.5(b) shows increasing x-ray source voltage caused an exponential increase in transmitted intensity. Exponential fitting of the data resulted in a worst-case coefficient of determination (R^2) value of 0.901.

Table 3.1 shows the affect x-ray source voltage has on the average transmitted intensity and the coefficient of variation, c_v (Equation 3.25) measured using a 50 mm thick Mixture 1 specimen and a 30 second integration time. The average transmitted intensity is normalized to the specimen thickness. The average transmitted intensity increased rapidly when increasing voltage above 70 keV, similar to the trend in Figure 3.5(b). Increases in the transmitted intensity are accompanied by decreases in the coefficient of variation. Figure 3.6 shows the impact of integration time on c_v with an x-ray source voltage and current of 75 keV and 100 μA, respectively. Initially, increasing the integration time drastically reduces c_v; however, the benefits of increased integration time are less significant after approximately 40 seconds. An integration time of 60 seconds was used based on Figure 3.6, as it was found reliable without drastically increasing the total measurement time. Limiting the variation of the measurements is vital to Series 2 testing. If variation is too high the affect of the moisture ingress may be within the variation of measurements; therefore, proper x-ray source and integration time settings are needed to accurately as-

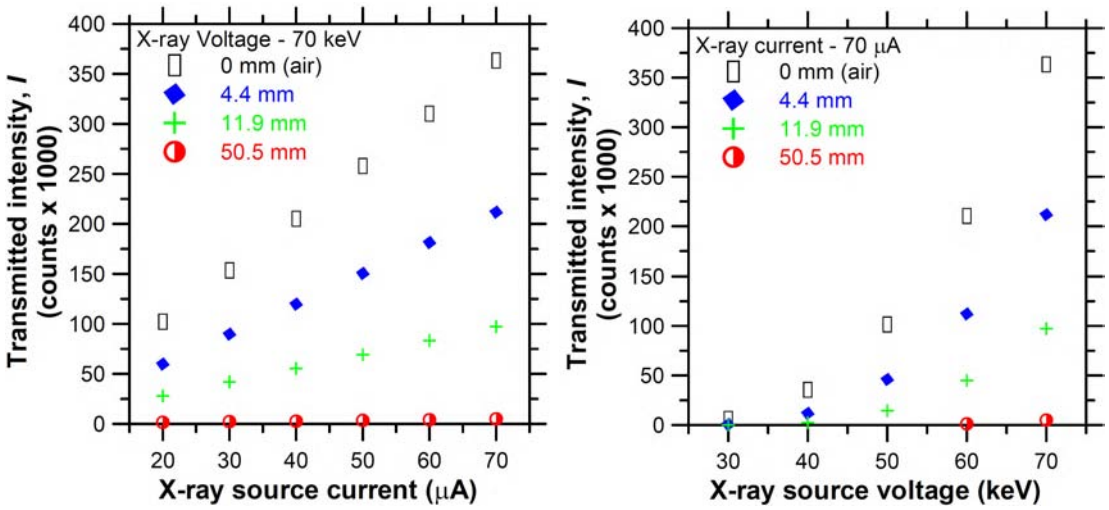

(a) (b)

Figure 3.5 *Influence of x-ray source (a) current and (b) voltage on the transmitted intensity through Mixture 1 specimens of varying thicknesses.*

sess moisture ingress.

Table 3.1 *The influence of x-ray source voltage on the average intensity per mm of specimen thickness per second of integration time and the coefficient of variation, using a 30 second integration time.*

Voltage (keV)	**Current (μA)**	**Average intensity (counts/mm/sec)**	c_v %
50	100	0.60	4.09
60	100	1.35	0.98
70	100	5.41	0.70
75	100	25.80	0.45

Figure 3.7 is a graphical determination of the linear attenuation coefficient of Mixture 1 concrete using Equation 3.18. The value of $-ln(I/I_0)$ is plotted on the vertical axis, while specimen thickness is plotted on the horizontal. The linear attenuation coefficient, μ is assumed to be the slope from the origin to the first measured point (4.4 mm thick specimen), and the resulting slope is included in the figure. The measured data points in the figure rapidly drop below the linear attenuation coefficient slope due to beam hardening, as described in the following paragraph. Error bars in the figure indicate variations in the measurements provided by the different current settings used (20, 30, 40, 50, 60, 70 μA). Error bars for the 50 keV measurements are black and increase rapidly with increased specimen thickness (50 keV and 20 μA resulted in complete attenuation). Error bars for the 70 keV measurements are white and fit within the symbols indicating the average values, indicating minimal variability. The linear attenuation coefficient, μ reduced with an increased x-ray source voltage, which is in agreement with Equation 3.19.

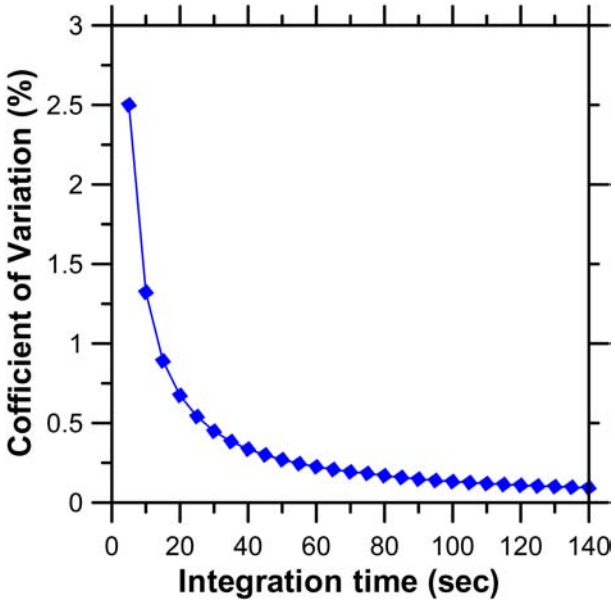

Figure 3.6 *Influence of integration time on coefficient of variation, c_v using an x-ray source voltage and current of 75 keV and 100 μA.*

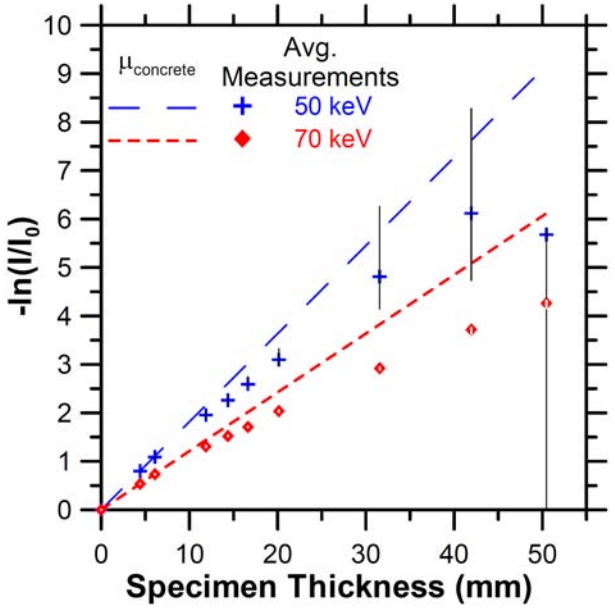

Figure 3.7 *Determination of linear attenuation coefficient for concrete using Equation 3.18. Symbols indicate measured data, broken lines are the linear attenuation coefficient as determined by extending the slope from the 4.4 mm specimen measurement, vertical lines are error bars.*

The linear attenuation coefficient, μ in the Beer-Lambert law (Equation 3.18) describes the attenuation of x-rays from a homogeneous x-ray source. However, the x-ray sources

used here produced heterogeneous x-ray beams across a spectrum of energies [*Weiss et al.*, 2004; *Sant and Weiss*, 2009]. According to [*Brooks and Chiro*, 1976], all substances are more effective at attenuating low energy x-rays compared to higher energies. Therefore, "a heterogeneous beam traversing an [x-ray] absorbing medium become proportionally richer in high-energy photons, and hence more penetrating, or 'harder'." Thus, the term beam hardening is used to describe this phenomenon. Figure 3.7 clearly shows the distortion caused by beam hardening. According to the linear attenuation coefficient, μ at 75 keV, the value of $-ln(I/I_0)$ should be 6.12 at a thickness of 50.5 mm; however, the average measured value was found to be 4.26, a 32% reduction. Similar distortions in the linear attenuation coefficient of brick have been seen previously [*Roels and Carmeliet*, 2006]. The use of prefilters, to filter out low energy x-rays, has been used in the past [*Brooks and Chiro*, 1976]; however, further investigations are needed to determine suitable prefilters for this application. Due to the distortion caused by beam hardening and variations in paste content (discussed previously), all results from Series 2 testing were calculated using Equation 3.26.

Figure 3.8 further illustrates the influence of x-ray source voltage settings on linear attenuation coefficients, μ. This figure was developed based on a procedure in [*Hubbell and Seltzer*, 2004; *Sant and Weiss*, 2009] to calculate μ for the major constituents of cement paste (H_2O, CaO, SiO_2, and air) and steel (Fe) as a function of incident x-ray energy. The linear attenuation coefficient for complex compounds is calculated using the mass attenuation coefficients of the constituent elements, $(\mu/\rho)_i$ (available in *Hubbell and Seltzer* [2004]) as shown in Equation 3.27:

$$\left(\mu/\rho\right)_{comp} = \sum_i w_i(\mu/\rho)_i \tag{3.27}$$

where $(\mu/\rho)_{comp}$ is the compound's mass attenuation coefficient and w_i is the weight fraction of the i^{th} atomic constituent. The compound's linear attenuation coefficient (μ_{comp}) is the expressed as:

$$\mu_{comp} = (\mu/\rho)_{comp} \cdot \rho_{comp} \tag{3.28}$$

where ρ_{comp} is the compound's density. Figure 3.8[A]; showing μ_{comp} for Fe, H_2O, CaO, SiO_2, and air; indicates the linear attenuation coefficient, μ for all materials decreases by at least four orders of magnitude as the x-ray source voltage increases. This indicates that as x-ray source voltage increases the materials are increasingly less effective at attenuating x-ray. Figure 3.8[B] shows the model fit from Equation 3.19 for the various materials, except air. The figure shows that Fe is the most effective constituent material at attenuating x-rays (Figure 3.3(b) also clearly indicates the steel fibers and shield are more effective at attenuating x-rays). After Fe, CaO, SiO_2, H_2O, and air have decreasing linear attenuation coefficients. Equation 3.19 describes the relatively low density (1 g/cm^3) and effective atomic number (7.544) of water equates to a smaller attenuation coefficient which is more sensitive to increased incident x-ray energy than the solid phases. Values for Z_{eff} are provided, along with values for coefficients a and b in Table 3.2 for all compounds. Measured linear attenuation coefficients of Mixture 1 concrete are shown in Figure 3.8

indicated by the [C]. Based on Figure 3.8 the lowest feasible x-ray source voltage setting should be used for measurements of moisture movement in order to maximize water's effect on x-rays.

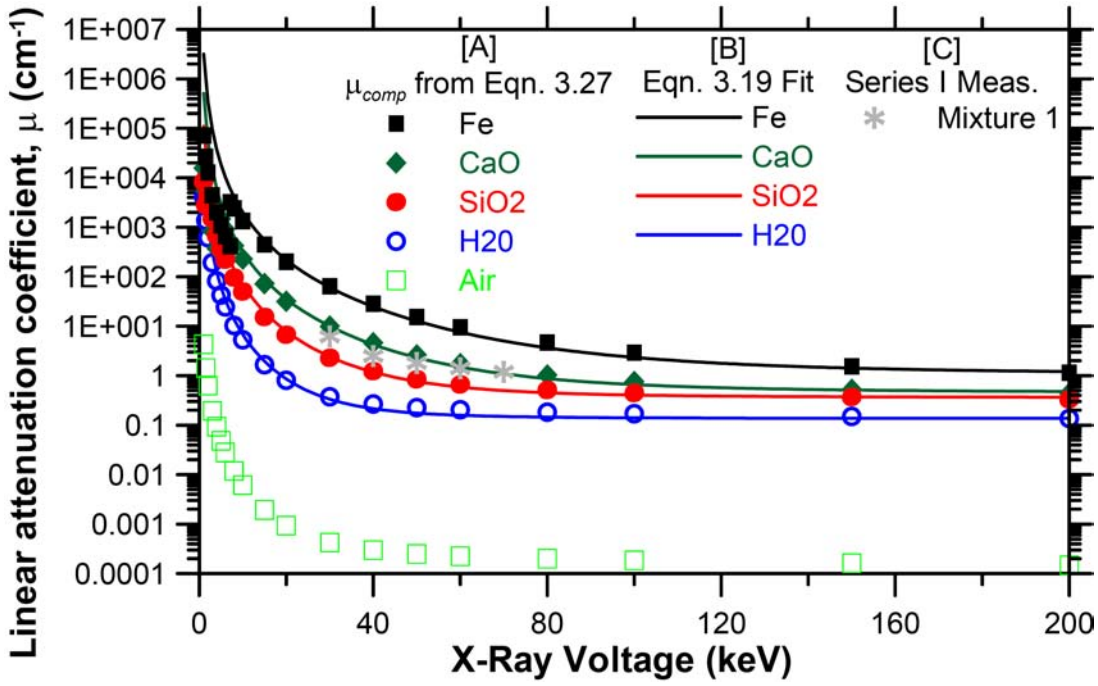

Figure 3.8 *The linear attenuation coefficient as a function of incident x-ray voltage from [A] μ_{comp} determination in Equation 3.28, [B] model fit from Equation 3.19 and [C] Series 1 measurements of the linear attenuation coefficient for Mixture 1 concrete specimens.*

Table 3.2 *Values of Z_{eff}, ρ, a, and b for each compound.*

Compound	Z_{eff}	ρ (g/cm^3)	a	b
Fe	26	7.87	0.137	1.7
CaO	18.364	3.35		2.4
SiO_2	11.847	2.65		3.5
H_2O	7.544	1		4.9

Based on these Series 1 measurements x-ray voltage and current settings were 75 keV and 100 μA for Series 2 measurements. These values were found to both reliably track the moisture ingress and provide reasonable measurement times for Series 2 measurements.

3.3.2 Series 2 - Moisture ingress measurements

Figure 3.9 show typical results of computed images of the *ABS* ratio from x-ray measurements. The notch (indicated by the blue box in the figure) and the cast in recess

were filled with water during moisture ingress measurements. Dark regions in the images indicate areas where the concrete remains dry, while light regions indicate the addition of moisture. The images indicate that water penetrated deeper into the 0.40 mm CMOD WST specimen (Figure 3.9(b)). Grayscales were exported from the calculated images ABS ration to produce contour plots shown in Figures 3.10-3.20 below.

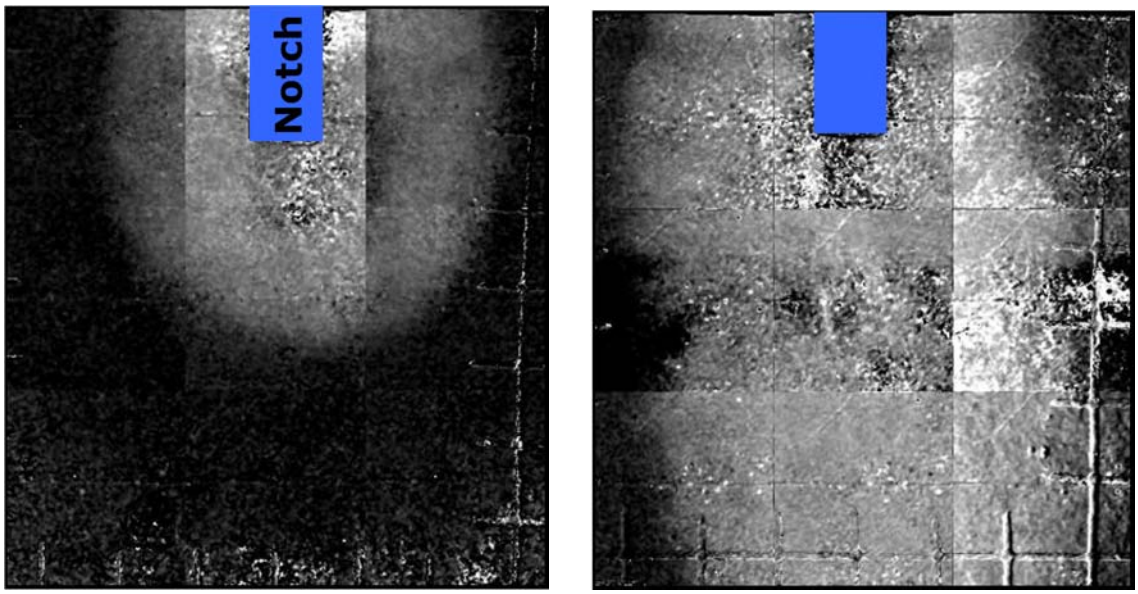

(a) (b)

Figure 3.9 *Calculated images of ABS ratio (Equation 3.26) from (a) 0.15 mm and (b) 0.40 mm CMOD Mixture 1 WST specimen after 40 minutes exposure.*

Figures 3.10-3.20 show contour plots of the ABS ratio after varying exposure times for Mixture 1 specimens at varying load levels or CMOD's. The black rectangle indicates the location of the notch. In all cases, moisture ingress increased with time. The figures also indicate water traveled rapidly through cracks resulting in an accelerated ingress behavior into the depth of the cracked WST specimens. The times of measurement indicated in the figures captions are the time when x-ray measurements were started after exposure to water. So, 1 hour indicates the x-ray measurement process was commenced one hour after water was exposed to the specimen. Measurements taken at less than 5 minutes from exposure to water seem to show an influence of the measurement time period (see e.g., Figure 3.19(a) - the odd ingress shape may have been affected by the time between measurements at individual locations). However at later times, changes in the moisture content occur at a slower rate, and the time period of the measurement process has a less significant effect.

Figures 3.10 and 3.11 show the moisture ingress in an unloaded Mixture 1 WST specimen after 40 minutes, 1 hour, 2 hours and 18 minutes, 3 hours and 4 hours. For x-ray measurements taken at early exposure times ($<$ 3 hours), the outermost regions of the specimens were not expected to change. Therefore, the two outer columns of measurements shown

in Figure 3.3(b) (location numbers 7-9 and 13-15) were not recorded during these times. Skipping these locations reduced the measurement time to approximately 18 minutes.

Figures 3.12(a), 3.15(a), 3.17(a), 3.19(a) show the moisture ingress after less than 5 minutes of exposure to water in WST specimens at peak load, 0.15 mm, 0.20 mm, and 0.40 mm CMOD. The figures show that as crack width (and length) increases, water penetrates more rapidly into the specimen. In the case of the 0.40 mm CMOD specimen, water penetrated the entire depth of the measurement area within approximately 1 minute.

Using the 75% ABS ratio contour lines from the x-ray measurements taken 1 hour after water exposure, the lateral ingress was determined at varying depths in the specimens (Y-position) as shown in Figure 3.21. The ABS ratio contour lines in the previous figures were exported to AutoCAD and the total lateral ingress was measured at various depths (0.50 mm vertical steps used starting from 5 mm above notch). The lateral ingress was averaged at each depth and the results are shown as ingress profiles in Figure 3.21. The 0.40 mm CMOD specimen was not included as rapid moisture ingress occurred in the vertical direction beyond the measurement area. The average lateral ingress from 0 to +5 mm (highlighted region) indicates the ingress behavior from the sides of the notch.

The notch in the WST specimens may be considered a free surface for water ingress. Similar average lateral ingress distances were observed in the cracked specimens above and below the notch bottom to a given depth (Figure 3.21). This indicates a free surface condition for moisture ingress may exist below the notch bottom in the cracked WST specimens, possibly in the form of a coalesced crack. This is discussed further in Section 3.3.3.

As described in Chapter 2 (Figures 2.20-2.23), the crack path varies across the thickness of the various cracked WST specimens due to the influence of aggregates. Variations in the crack path likely impact the ingress of water as the water appeared to initially, rapidly fill the cracks (based on Figures 3.12,3.15,3.17,3.19(a)) and lateral ingress proceeds from the surfaces of the crack. In contrast, the path of the notch, which was cut into each WST specimen, does not vary through the specimen thickness. The x-ray attenuation measurements provide an averaged measure of moisture ingress through the 50 mm thick WST specimens. As shown in the figures below, a similar lateral ingress is seen above and below the notch. Therefore, the results indicate the 50 mm specimen thickness used seems to adequately average any local variations in the lateral ingress caused by the fluctuating crack path.

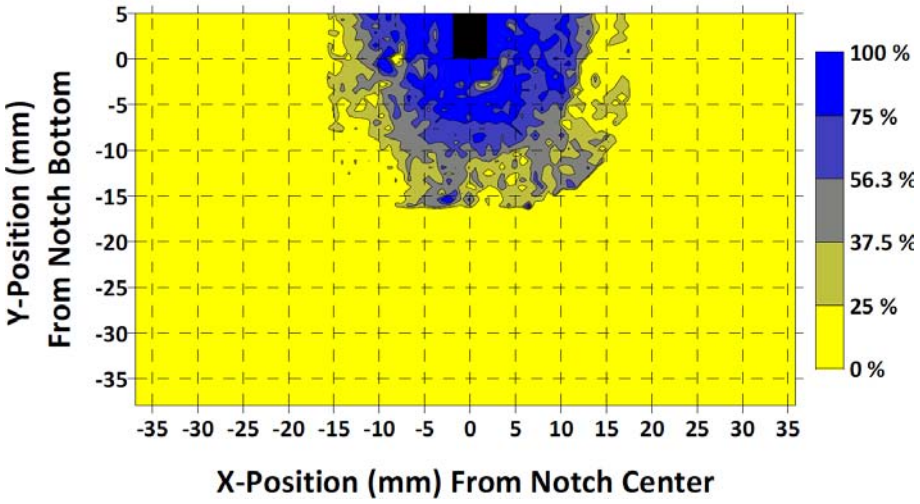

(a)

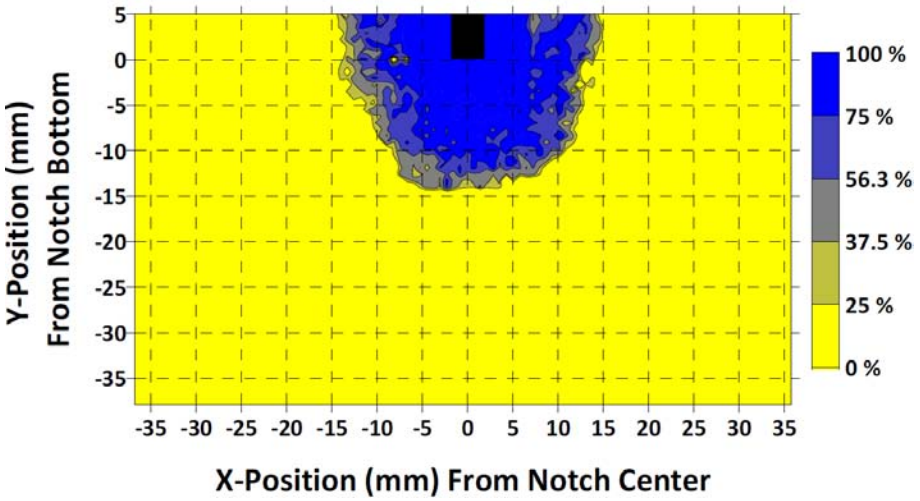

(b)

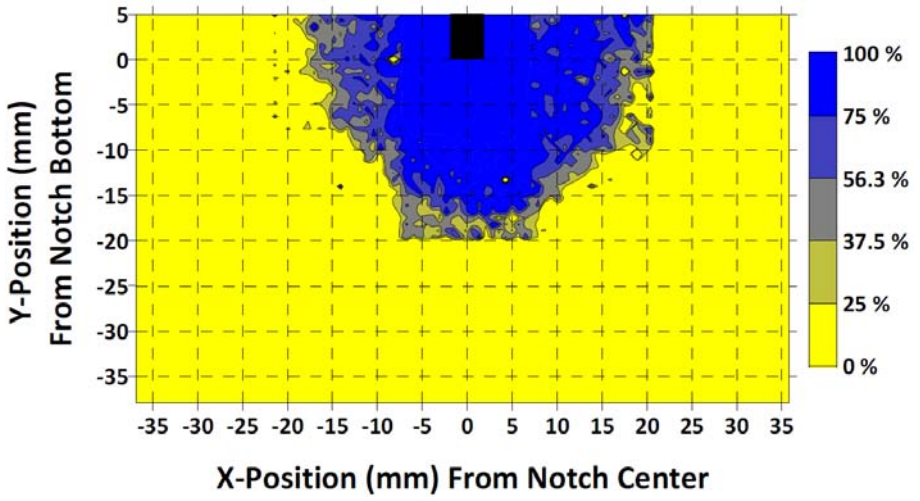

(c)

Figure 3.10 *ABS ratio for Mixture 1 unloaded WST after (a) 40 minutes, (b) 1 hour, and (c) 2 hours 18 minutes.*

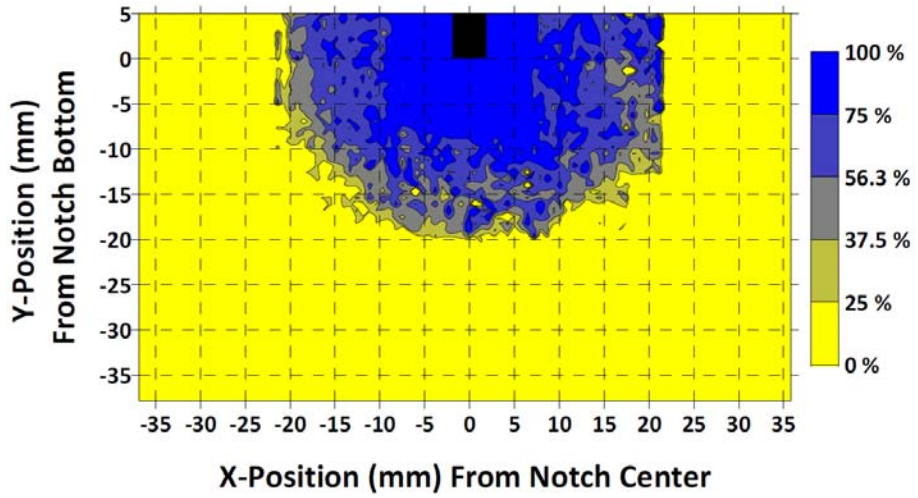

(a)

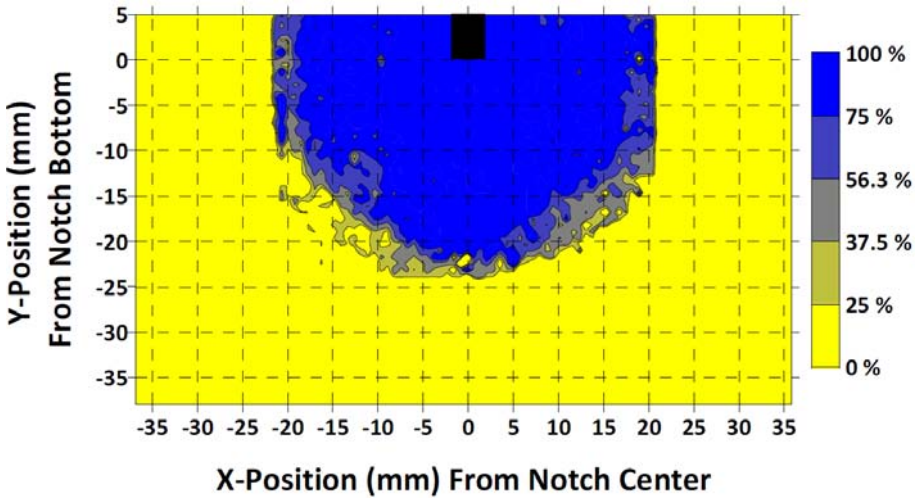

(b)

Figure 3.11 *ABS ratio for Mixture 1 unloaded WST after (a) 3 hours and (b) 4 hours.*

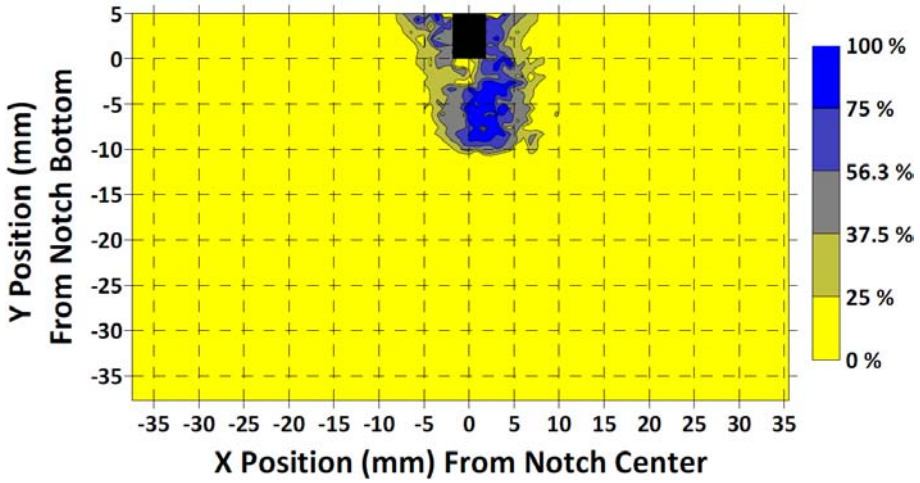

(a)

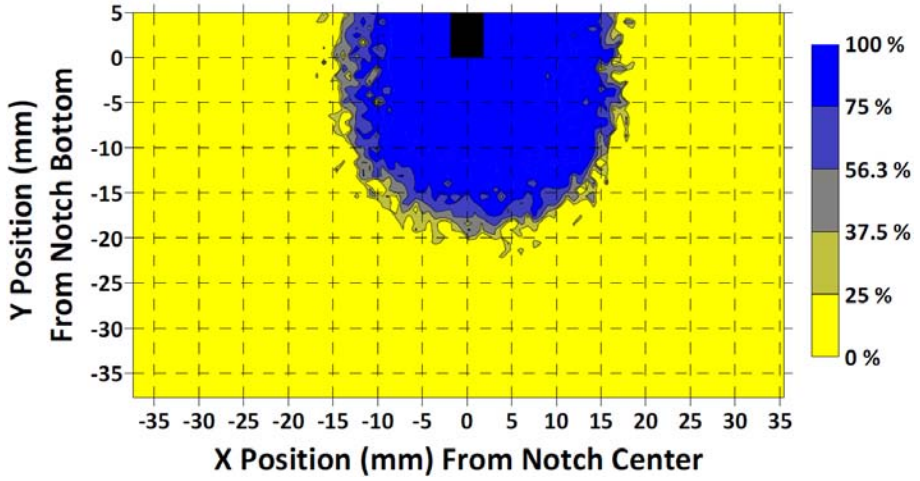

(b)

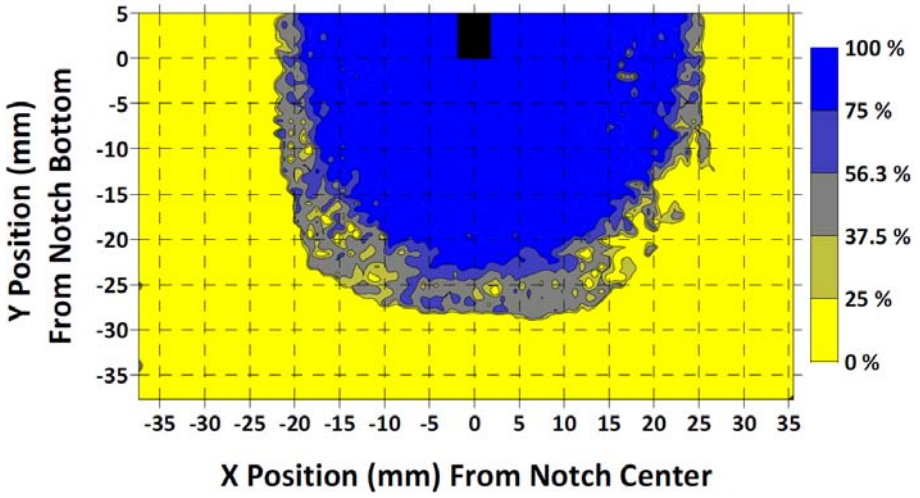

(c)

Figure 3.12 *ABS ratio for Mixture 1 WST at peak load after (a) approximately 3 minute, (b) 1 hour, and (c) 2 hours.*

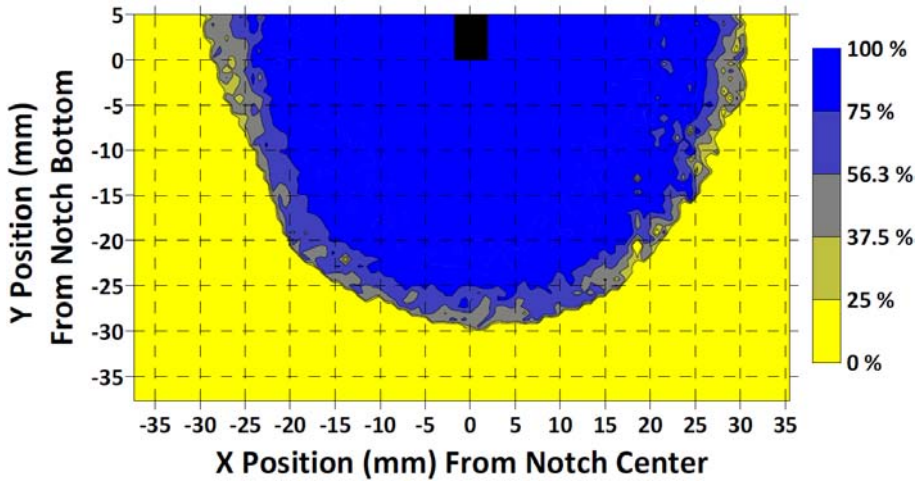

(a)

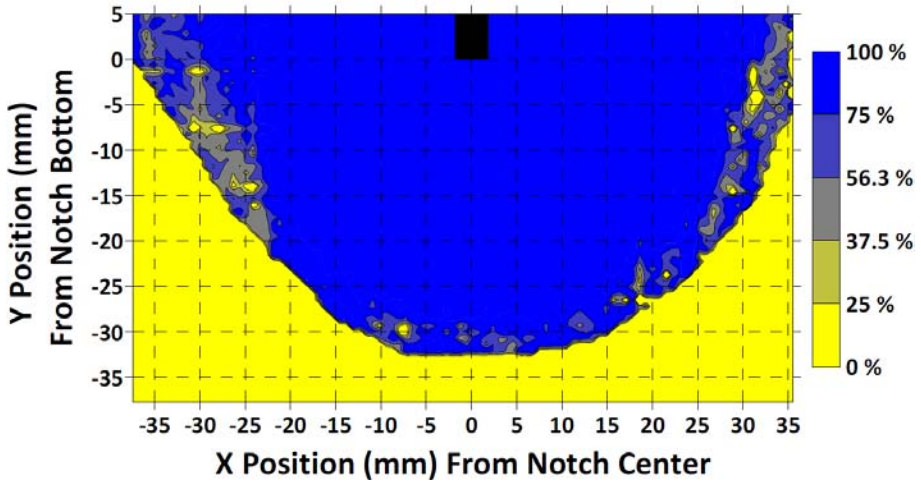

(b)

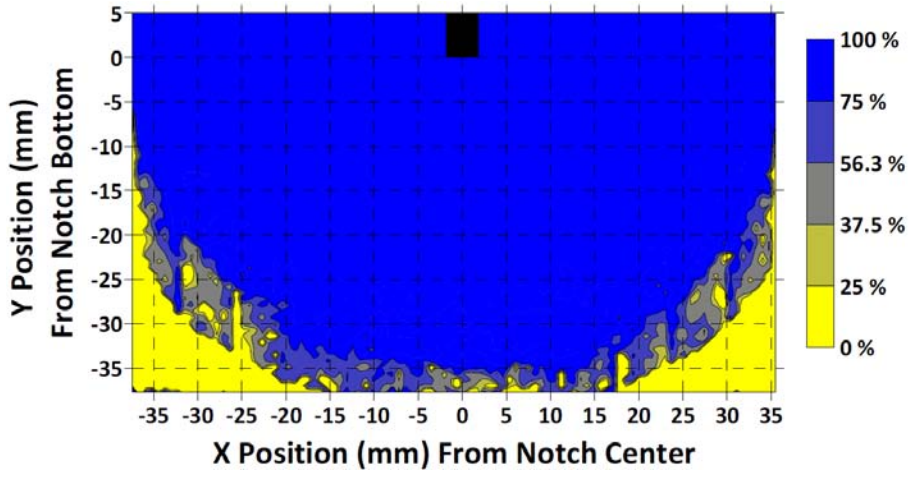

(c)

Figure 3.13 *ABS ratio for Mixture 1 WST at peak load after (a) 3 hours, (b) 4 hours, and (c) 6 hours.*

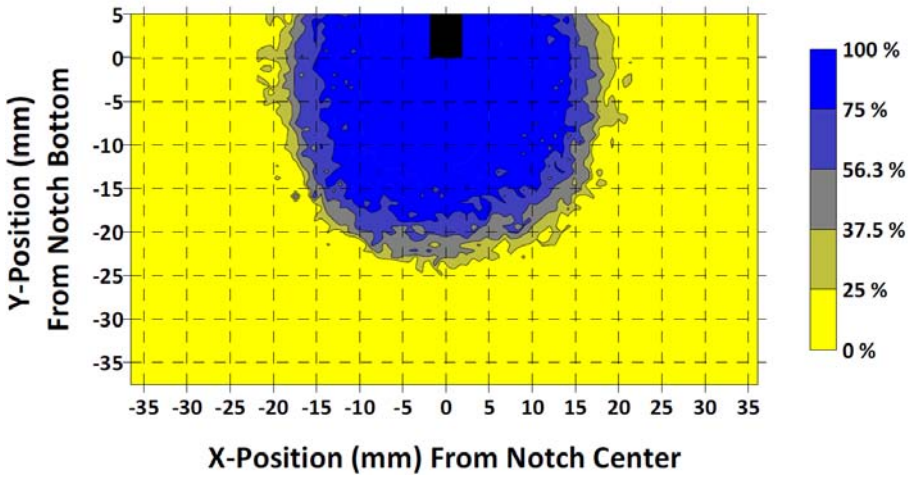

Figure 3.14 *ABS ratio for Mixture 1 WST at 0.10 mm CMOD after 1 hour.*

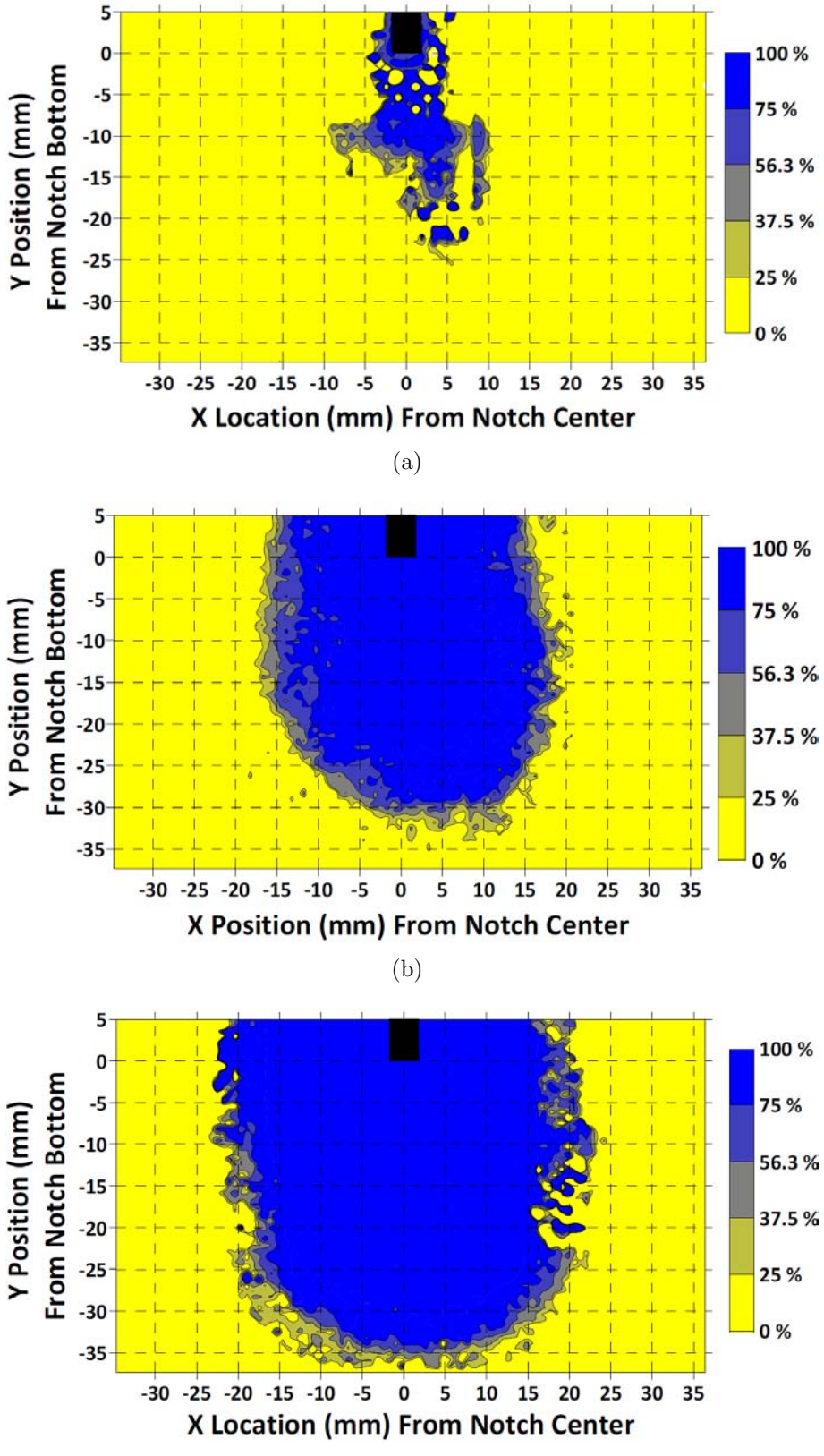

Figure 3.15 *ABS ratio for Mixture 1 WST at 0.15 mm CMOD after (a) approximately 3 minute, (b) 1 hour, and (c) 2 hours.*

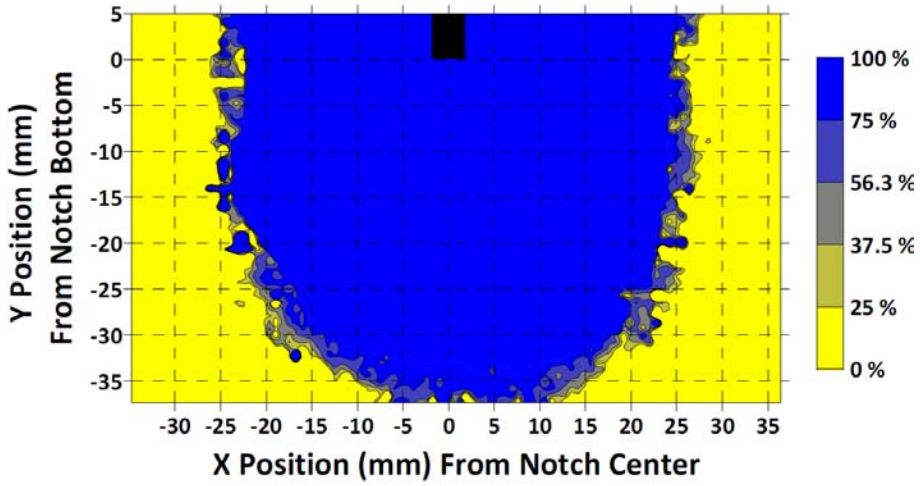

(a)

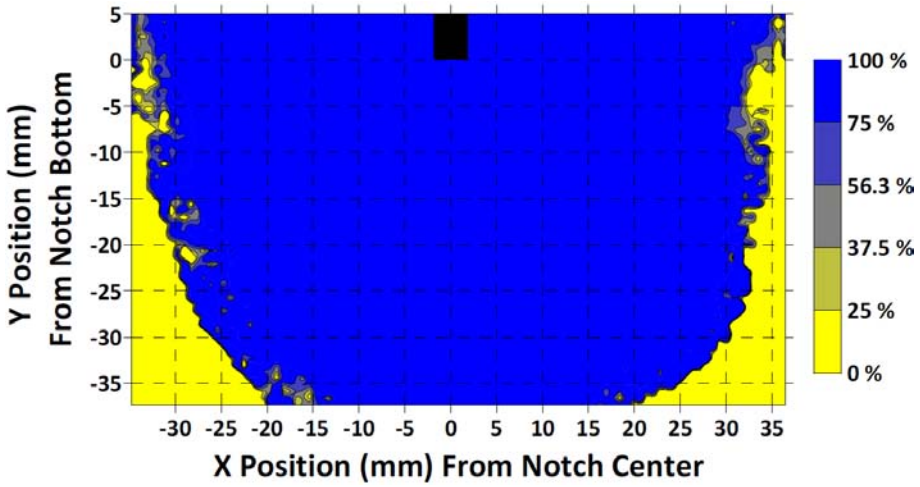

(b)

Figure 3.16 *ABS ratio for Mixture 1 WST at 0.15 mm CMOD after (a) 3 hours and (b) 4 hours and 50 minutes.*

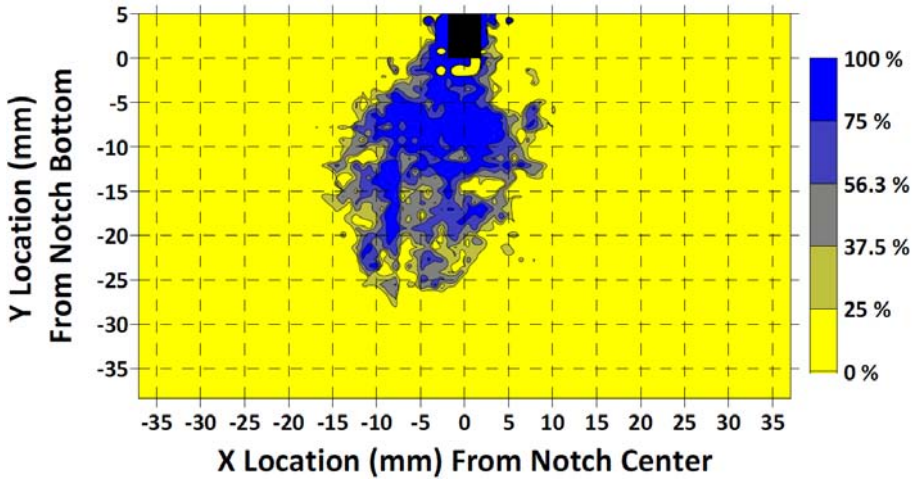

(a)

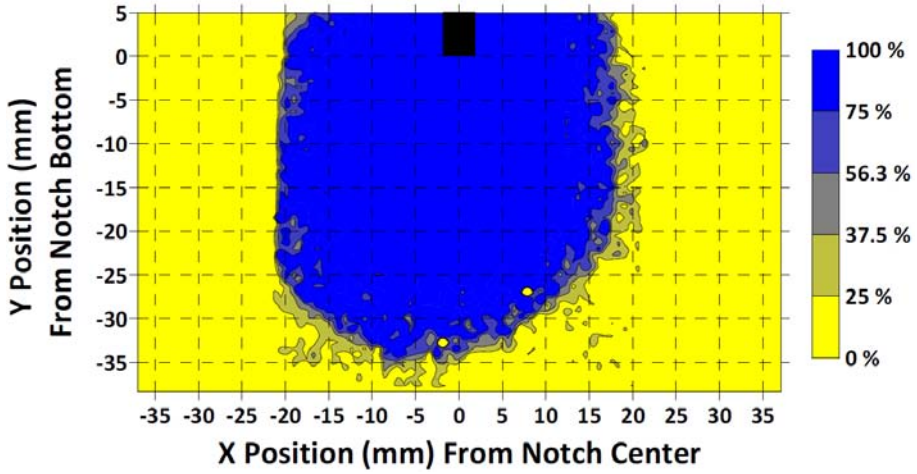

(b)

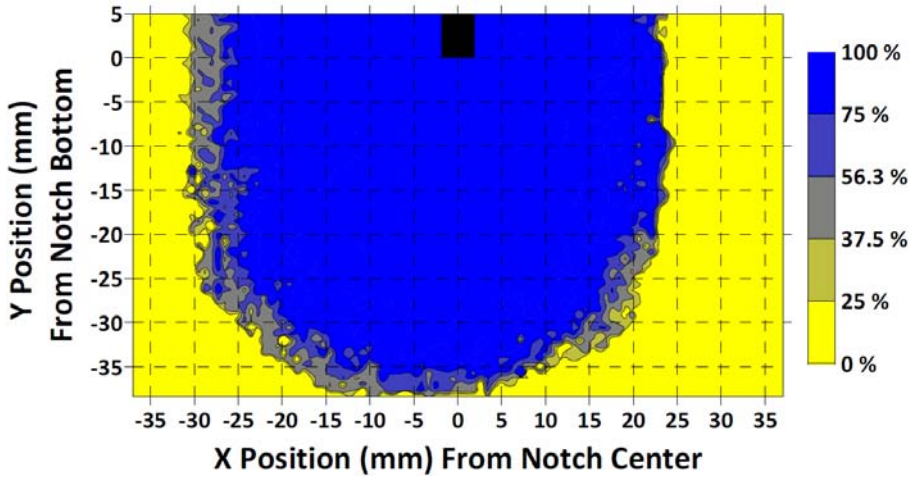

(c)

Figure 3.17 *ABS ratio for Mixture 1 WST at 0.20 mm CMOD after (a) approximately 3 minute, (b) 1 hour, and (c) 2 hours.*

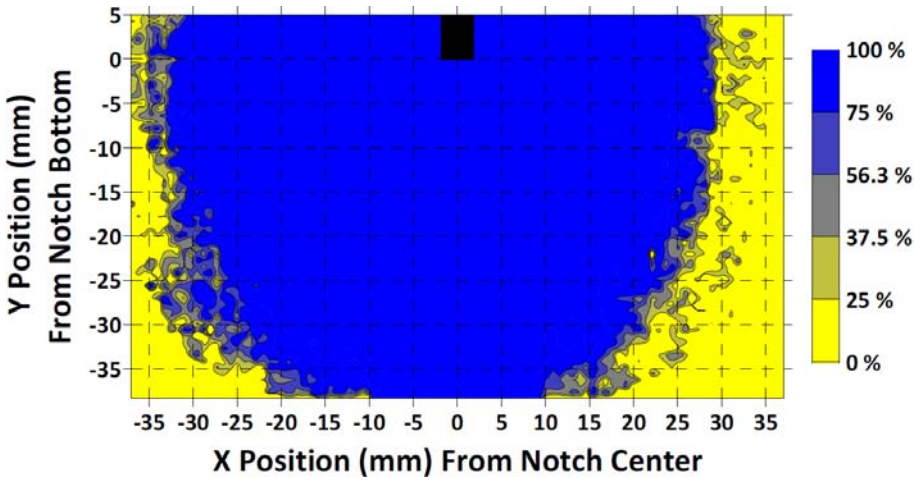

(a)

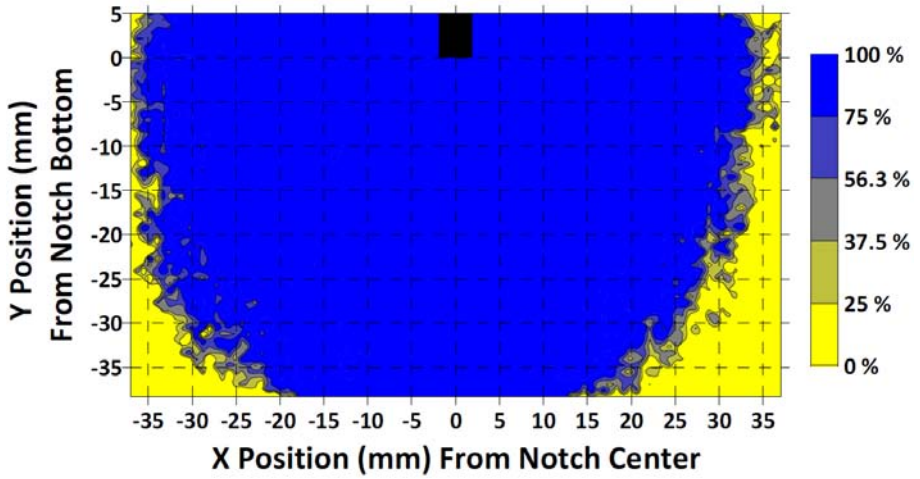

(b)

Figure 3.18 *ABS ratio for Mixture 1 WST at 0.20 mm CMOD after (a) 3 hours and (b) 4 hours 7 minutes.*

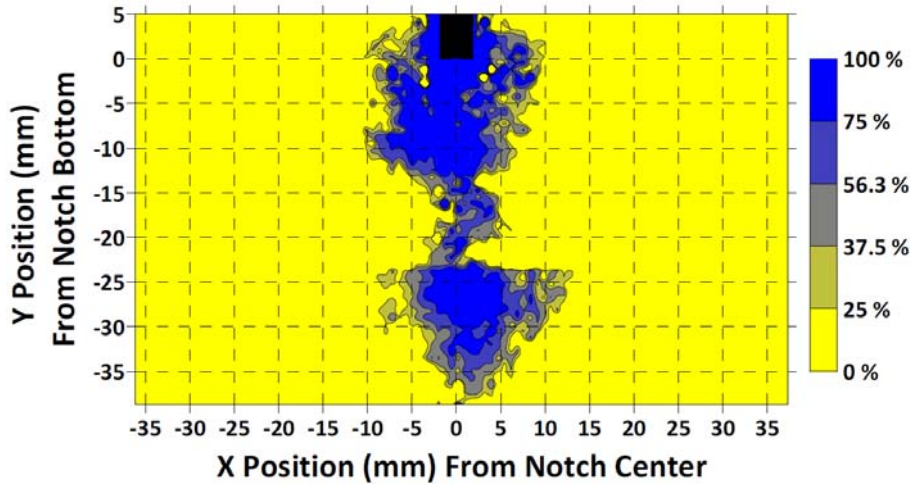

(a)

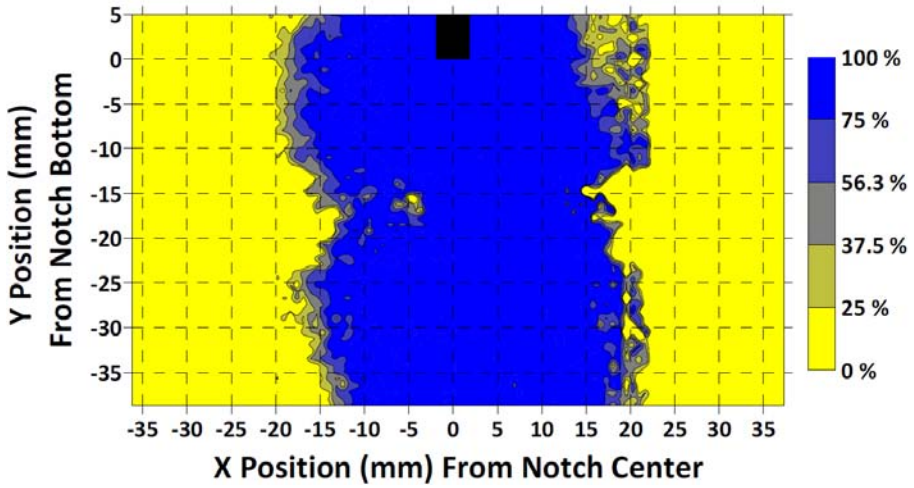

(b)

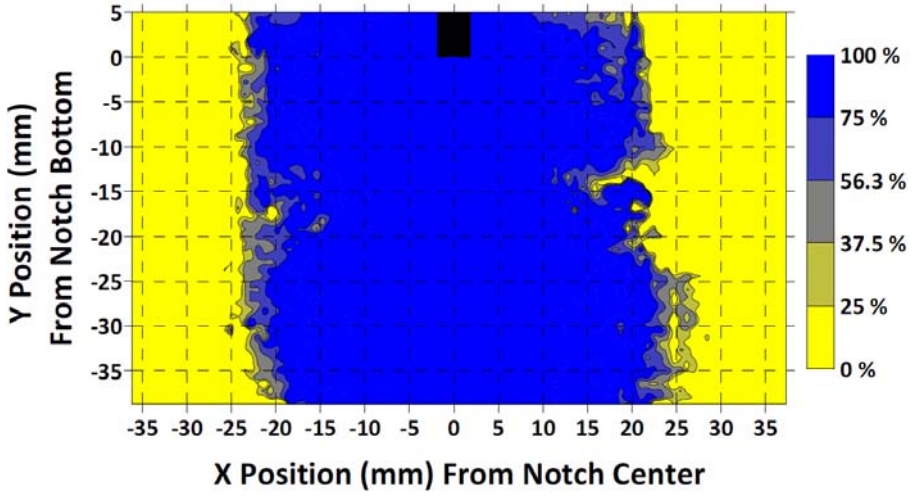

(c)

Figure 3.19 *ABS ratio for Mixture 1 WST at 0.40 mm CMOD after (a) approximately 1 minute, (b) 1 hour, and (c) 2 hours.*

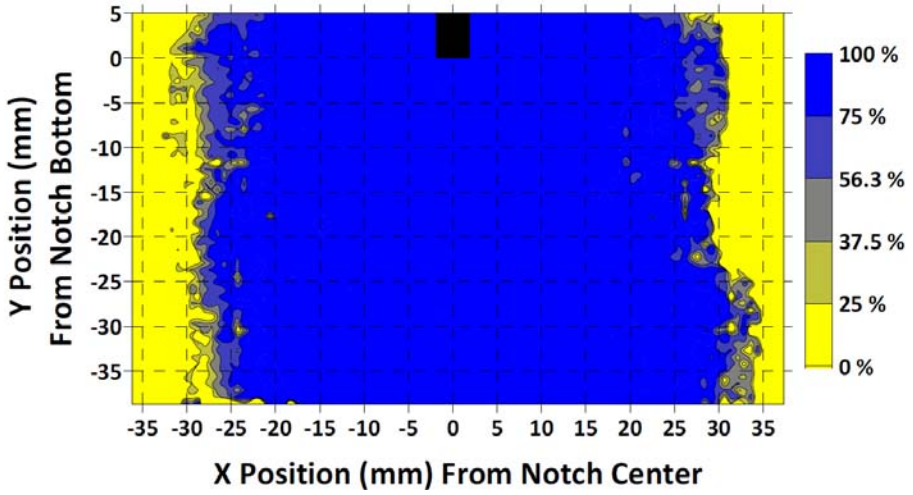

(a)

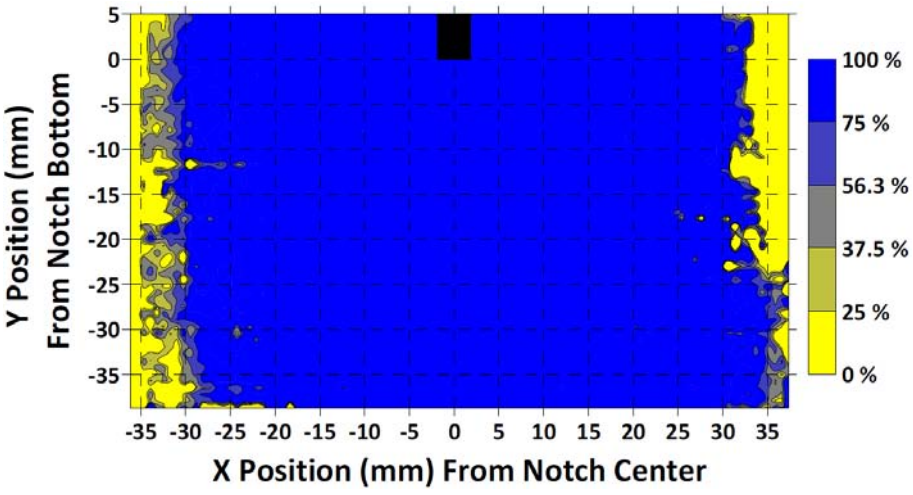

(b)

Figure 3.20 *ABS ratio for Mixture 1 WST at 0.40 mm CMOD after (a) 4 hours and (b) 6 hours.*

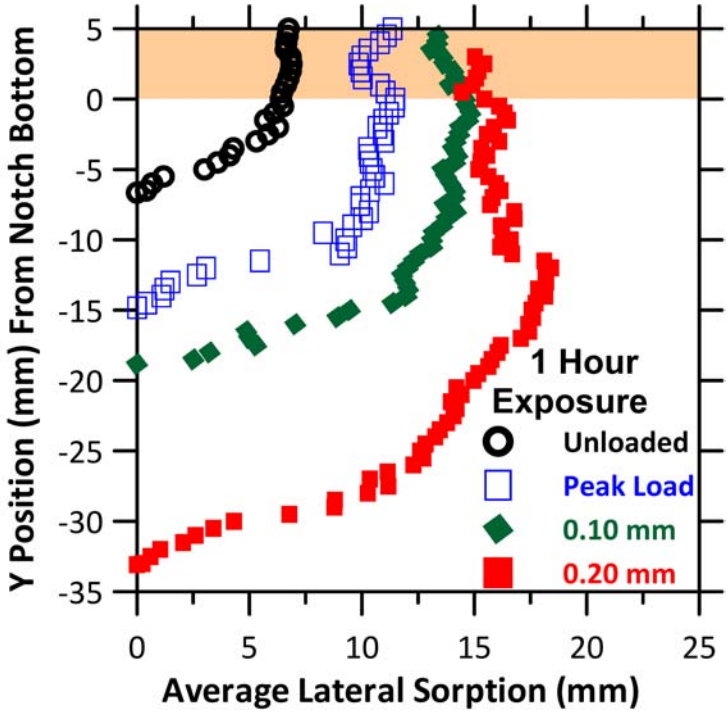

Figure 3.21 *75% ABS profiles for WST specimens after 1 hour of ponding under varying crack conditions.*

3.3.3 Comparison of crack length & x-ray attenuation measurements

The maximum moisture ingress depth into the cracked WST specimens after 1 hour of water exposure (from Figure 3.21) and the depth of the coalesced crack (from Table 2.7) are plotted over the corresponding crack profile in Figure 3.22(a) as blue circles and green squares, respectively. Figure 3.22(a) indicates that portions of the cracks are not coalesced and the flow of epoxy and water are partly restricted. Figure 3.21 indicated that although water traveled rapidly through cracks and free surface ingress behavior was observed below the notch bottom in cracked specimens, only a portion of the total crack length contributes as a free surface to water ingress while the remaining portion of the crack length inhibits ingress. Figure 3.22(a) shows that after 1 hour of exposure water has yet to reach the full extent of the estimated crack length.

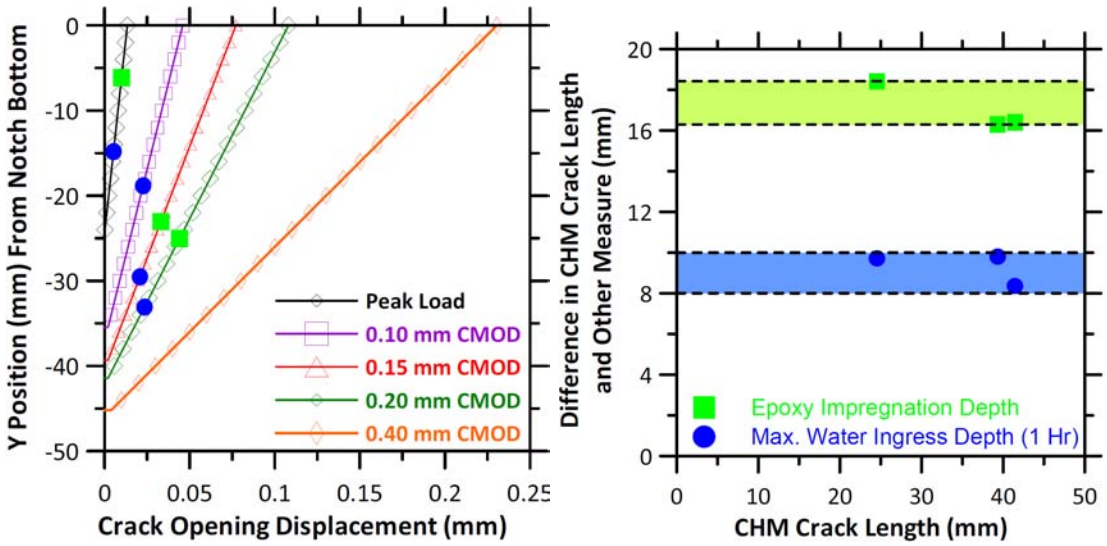

(a) (b)

Figure 3.22 *(a) Crack profiles from the CHM with green squares indicating the depth of epoxy impregnation and blue circles indicating maximum ingress depth after 1 hour of ponding. (b) The difference in crack depth and maximum ingress depths (of epoxy and water ingress after 1 hour) for specimens with varying crack lengths.*

Figure 3.22(b) shows the difference between the CHM crack length and the maximum ingress depth for the specimens with varying crack lengths as well as the length of the impregnated crack. For three of the cracked specimens tested (peak load, 0.15 mm CMOD, and 0.20 mm CMOD) the difference between the maximum water ingress depth and the CHM crack length had a consistent range of 8 mm to 10 mm. Assuming the maximum ingress depth after 1 hour of exposure relates to the location of free surface behavior through the controlling ingress mechanisms, Figure 3.22(b) may indicate that a consistent length of the crack inhibits ingress. In other words, the results indicate the crack length consists of two portions, an apparent crack and an inhibiting crack. The apparent crack behaves approximately as a free surface in terms of ingress, while the inhibiting crack

may have a consistent length and impedes moisture ingress. The results of the epoxy impregnation also shows a consistent length of non-coalesced cracks between 16.5 and 18.5 mm, further indicating the inhibiting crack has a consist length.

3.3.4 Chloride ion ingress

Figure 3.23 shows typical result of silver nitrate spraying on the cut and ground surface of the WST specimens. The whitish/purple precipitate on the surface of the concrete indicates the presence of chloride ions. Using the image analysis procedure described previously in Figure 2.14 (Section 2.2.4), the average lateral ingress of chloride ions were measured. Figure 3.24(a) and 3.24(b) show the chloride ingress behavior for Mixture 1 specimens which were unloaded and cracked to a 0.20 mm CMOD, respectively. Figure 3.24(c) and 3.24(d) show results from Mixture 2, unloaded and at 0.20 mm CMOD, respectively. Similarly to the moisture ingress behavior, the presence of the crack allowed for an accelerated ingress behavior. Ingress increased both into the depth of the specimen and laterally into the cracked WST specimens.

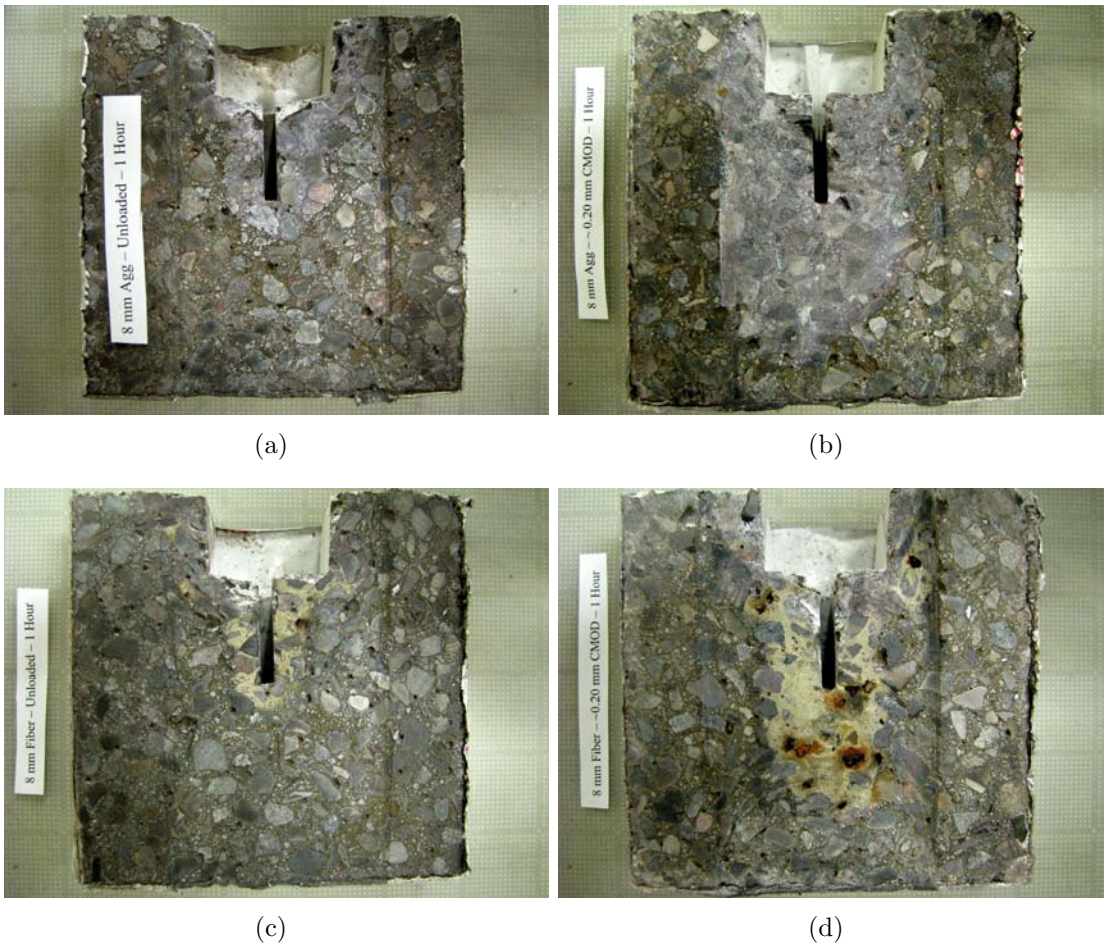

(a) (b)

(c) (d)

Figure 3.23 *$AgNO_3$ spraying on the surface of WST specimens exposed to 10% chloride solution for 1 hour for Mixture 1 (a) unloaded and (b) 0.20 mm CMOD specimens, and Mixture 2 (c) unloaded and (d) 0.20 mm CMOD specimens. (Author's photos)*

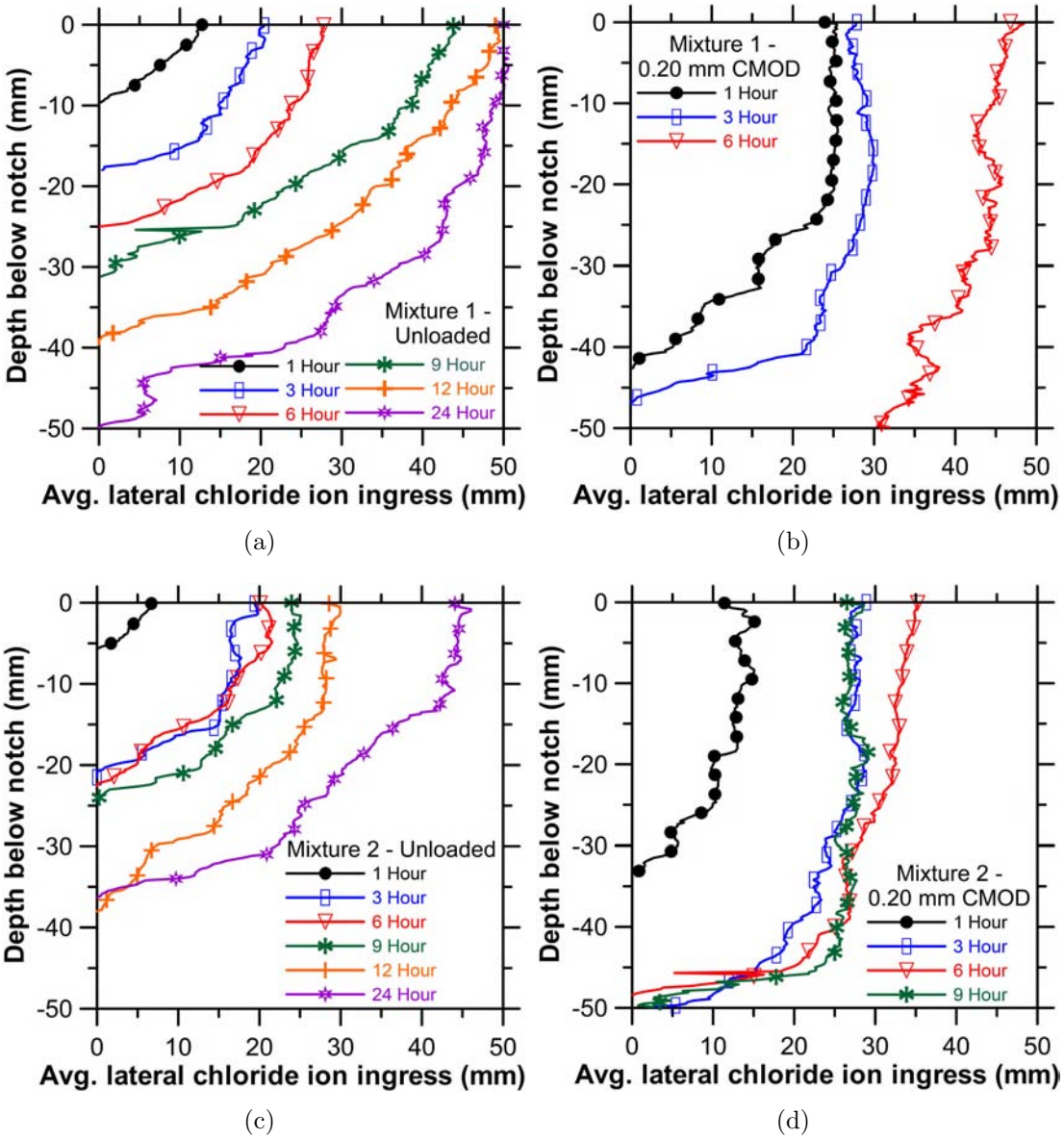

Figure 3.24 *Chloride ion ingress testing results at varying exposure times for Mixture 1 (a) unloaded and (b) at 0.20 mm CMOD and for Mixture 2 (c) unloaded and (d) at 0.20 mm CMOD.*

3.3.5 Comparison of moisture and chloride ion ingress

Figure 3.25 compares moisture and chloride ion ingress measurements from Mixture 1 after 1 hour of exposure. The specimens used for comparison were unloaded and with a CMOD of 0.20 mm; however, it should be noted that the two measurements were taken from different specimens. The ingress of chloride ions was restricted compared to water ingress, particularly for the 0.20 mm CMOD specimen. As described in Section 3.1.1, chloride binding and the $\sqrt{\gamma/\mu}$-absorption proportionality are know to restrict chloride ion ingress.

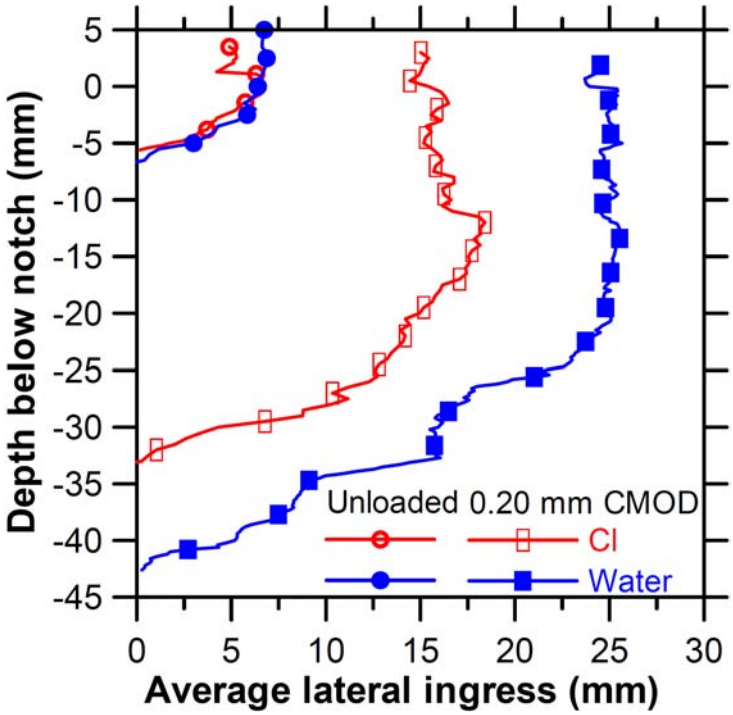

Figure 3.25 *Comparison of chloride ions (red symbols) and water (blue symbols) ingress into Mixture 1 unloaded and 0.20 mm CMOD WST specimens after 1 hour of exposure.*

3.4 Summary and conclusions

This chapter provides an introduction to transport mechanisms in concrete and other cementitious materials, a literature review on the effect cracking has on ingress behavior, and descriptions of experimental works completed on cracked wedge splitting tensile specimens. X-ray attenuation measurements were used to track moisture movements while silver nitrate spraying was used to track chloride ion ingress in crack concrete specimens. The following conclusions have been drawn from this portion of the work:

- X-ray attenuation measurements track moisture movements in concrete due to changes in specimen density and the linear attenuation coefficient of the composite material caused by the addition of water. The use of an x-ray camera provides

higher spatial resolution imagery of moisture ingress in concrete specimens. Previous measurements taken with x-ray detectors required many more measurement location to assess moisture profiles. Additionally, despite the inability of the camera to measure x-ray energy levels, the moisture profile can be accurately monitored by the transmitted intensity.

- Moisture ingress proceeded more rapidly with increased load level and crack mouth opening displacement of the wedge splitting test specimens. As the crack mouth opening displacement increased, moisture reached greater depths immediately after exposure. Lateral ingress of moisture was similar to free surface (notch) ingress through a portion of the depth of cracked wedge splitting test specimens. It was hypothesized that a coalesced crack formed in the crack wedge splitting test specimens. The coalesced cracks appeared to rapidly fill with water after exposure, and the coalesced crack surface appeared to behave as a free surface for water ingress. Non-coalesced cracks, which form ahead of the coalesced crack (see Chapter 2) delay moisture ingress. The complex fracture and ingress behaviors are likely not replicated by using inserts to cast in 'cracks' in fresh concrete.
- Ingress of chloride ions was delayed compared to the moisture ingress behavior. This is likely caused by binding of chloride ions and the effect influence of NaCl on surface tension and viscosity of the ponding solution.

Chapter 4

Impact of cracks on reinforcement corrosion

4.1 Introduction

This chapter presents an investigation of reinforcement corrosion and includes the development of a new instrumented rebar designed to provide location-dependent potential measurements while still inducing realistic cracks and behaving mechanically similarly to standard rebar. The chapter is comprised of four main sections. Section 4.1 provides a focused review of the fundamentals of reinforcement corrosion, the impact cracks have on corrosion, and an assessment of previously used techniques to assess the impact of cracks on corrosion. In Section 4.2 details of the experimental investigation completed as part of this project are presented. Results are presented and discussed in Section 4.3 while conclusions are presented in Section 4.4.

4.1.1 Fundamentals of corrosion

Corrosion occurs as two half-cell reactions, an anodic (oxidation) and a cathodic (reduction) reaction. Both the anodic and cathodic reactions are necessary and ceasing one leads to the termination of corrosion. A typical fundamental corrosion process is illustrated in Figure 4.1, where a divalent metal, M (such as iron in the Fe^2+ state) is in contact with an electrolytic solution. The anodic half-cell consists of the divalent metal dissolving in the electrolytic solution to its ionic form, M^{2+}. Electrons liberated by the anodic half-cell are conducted through the metal and are consumed by a cathodic half-cell. The reduction of oxygen has been shown in the illustration; however, reduction of hydrogen ($2H^+ + 2e^- \rightarrow H_2$) or other oxidized species may also occur. In this example metal hydroxides form in the electrolytic solution and deposit on the surface of the metal.

To fully assess corrosion reactions two distinct areas must be considered, namely thermodynamics and kinetics of corrosion. Thermodynamics controls which, and under what conditions, corrosion reactions may take place. Kinetics describes the rate at which corrosion progresses.

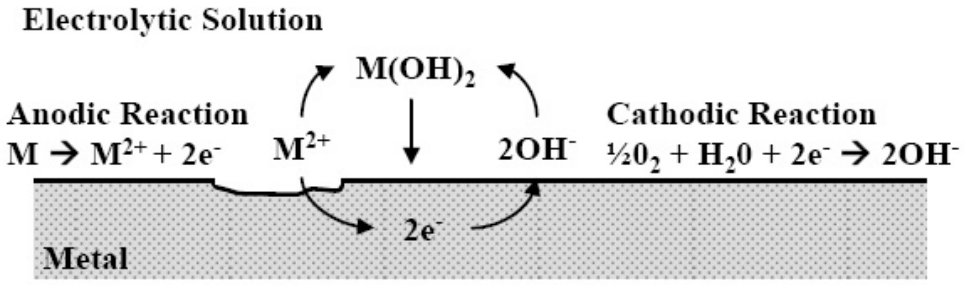

Figure 4.1 *Schematic example of a wet corrosion process involving a divalent metal in an electrolytic solution containing oxygen, after [Bardal, 2004].*

Thermodynamics of the corrosion process

Corrosion reactions are controlled by Equation 4.1, which relates the change in Gibbs free energy, ΔG (J) caused by the reaction to the equilibrium potential, E_0 (mV) [*Bardal*, 2004]:

$$\Delta G = -zFE_0 \tag{4.1}$$

where z is the valence and F is Faraday's constant (96,485 C/mol e^-). A negative value of Gibbs free energy indicates the reaction is thermodynamically feasible and would proceed spontaneously and irreversibly. Positive values indicate that additional energy must be supplied for the reaction to occur. A value of zero indicates equilibrium, meaning the reaction is thermodynamically not favored to proceed in either direction.

Equilibrium potential, E_0 from Equation 4.1 can be determined theoretically using Nernst's equation (Equation 4.2), in its general form [*Bardal*, 2004]:

$$E_0 = E_0^0 - \frac{RT}{zF} ln\left(\frac{a_L^l a_M^m \dots}{a_B^b a_C^c \dots}\right) \tag{4.2}$$

for the reaction

$$bB + cC + ... + ze^- \rightarrow lL + mM + ... \tag{4.3}$$

where E_0^0 is the standard equilibrium potential (i.e., standard conditions), a_L^l is the activity of substance L raised to the stoichiometric coefficient, l, etc.

As Pourbaix first discovered, by using the Nernst equation and considering selected theoretically feasible reactions (i.e., reactions with negative Gibbs free energy) an illustration of potential corrosion reaction products can be determined over a range of pH values [*Pourbaix*, 1974]. A Pourbaix diagram, as shown in Figure 4.2, is a graphical representation of Nernst's equation and a useful tool for assessing possible corrosion issues of metals exposed to solutions.

Figure 4.2, from [*Küter*, 2009], shows the Pourbaix diagrams for iron, Fe (which is commonly used to describe the corrosion behavior of carbon steel) exposed to water. Three

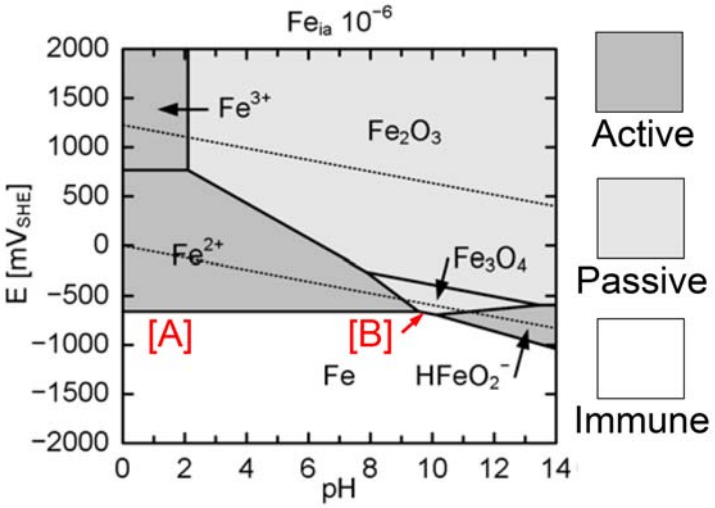

Figure 4.2 *Pourbaix diagram for Fe-H_2O system at 25 °C and an Fe ion activity of 10^{-6} mol/L from [Küter, 2009] indicating regions of immunity, passivity and active corrosion. Lines [A] and [B] indicate boundaries of the Pourbaix diagram calculated in the text.*

distinct and important thermodynamic corrosion states are highlighted in the Pourbaix diagram including the immune state as well as the passive and active corrosion states. In the immune state Fe is thermodynamically stable and corrosion cannot take place. The boundary line [A] of the immunity region corresponds to the computation for E_0 for the reaction:

$$Fe^{2+} + 2e^- \rightarrow Fe \tag{4.4}$$

The corresponding Nernst's equation states:

$$E_0 = -0.44 + 0.0295 \cdot log(a_{Fe^{2+}}) \tag{4.5}$$

Using the standard activity for Fe^{2+} ($a_{Fe^{2+}} = 10^{-6} mol/L$) the equilibrium potential at 25°C is found to be -0.617 V.

The passivity region indicates that oxidation of Fe^{2+} ions and the formation of a solid passivating film of Fe_2O_3 or Fe_3O_4 over the Fe substrate is thermodynamically favored. Passivating films, which are electrochemically stable compounds with low porosity, ionic conductivity, and adhere well to the substrate, greatly reduce ion transport and therefore the corrosion rate. Boundary line [B] between the Fe_3O_4 passive corrosion region and the immune state region corresponds to E_0 for the reaction:

$$Fe_3O_4 + 8H^+ + 8e^- \rightarrow 3Fe + 4H_20 \tag{4.6}$$

As pH reflects hydrogen ion activity (i.e., $pH = -log(a_{H^+})$), this electrode reaction bears a pH dependency. Nernst's equation for the anodic reaction is expressed as:

$$E_0 = 0.085 - 0.059 \cdot pH \tag{4.7}$$

assuming $a_{Fe} \approx a_{Fe_3O_4} \approx a_{H_2O} = 1$ and $T = 25°C$.

Regions of active corrosion correspond to areas where the thermodynamically possible corrosion products are soluble ions (Fe^{2+} or Fe^{3+}) or compounds (e.g., $HFeO_2^-$, $FeCl^+$), which do not provide a barrier against continued corrosion.

Open circuit corrosion potential (OCP, or half-cell potential) is a measure of the thermodynamic state of a metallic surface. OCP is measured as a potential difference (voltage) between the surface of a metal and a reference electrode. Reference electrodes commonly used in practice for RC are shown in Table 4.1. Using a Pourbaix diagram as shown in Figure 4.2, the thermodynamic state (i.e., immune, passive corrosion, or active corrosion), and possible corrosion product can be assessed from OCP measurements. For example, based on Figure 4.2 an OCP of 0 mV_{SHE} in concrete (i.e., pH $\sim$ 11-14) the formation of a passive corrosion product, Fe_20_3 is thermodynamically favored; while with an OCP of -750 mV_{SHE} an active corrosion product, $HFeO_2^-$ is thermodynamically favored. Reference electrodes may be embedded in the concrete, placed temporarily on the concrete surface, or placed into an electrolytic ponding solution (more common for laboratory assessments).

Table 4.1 *Potential versus standard hydrogen electrode (SHE) at 25° C and temperature dependency for selected reference electrodes commonly used in practice [Myrdal, 2007].*

Reference electrode	Potential [mV versus SHE]	Temperature dependency [mV/° C]
Copper/copper sulfate sat. (CSE)	+318	+0.90
Standard calomel electrode (SCE)	+240-245	+0.22
Silver/silver chloride sat. (SSCE)	+199	+0.09

While OCP measurements, Nernst's equation, and the Pourbaix diagram describe the thermodynamic state of a metal, to provide a complete description of corrosion the reaction kinetics (i.e., rate) must also be considered. In some cases, the reaction rate may be insignificant compared to the service life of a RC structure.

Kinetics of corrosion process

Kinetics (rate) of electrochemical reactions (corrosion), defined as the amount of metal ions removed from a metal per unit area and unit time, can be expressed as an electric current density. The corrosion current density, i_{corr} (A/cm^2) is related to a cross-sectional (thickness) reduction per unit time, $\frac{ds}{dt}$ (cm/s) using Faraday's equation (Equation 4.8) [*Bardal*, 2004]:

$$\frac{ds}{dt} = \frac{i_{corr} M}{zF\rho} \tag{4.8}$$

where M is the molecular weight (55.845 g/mol for Fe), and ρ_{Fe} is the material density (7.87 g/cm^3), z is the valence (2 for Fe $\rightarrow$ Fe^{2+}).

As discussed below the corrosion current, I_{corr} (A) is measured by electrochemical techniques and the corrosion current density, i_{corr} (A/cm^2) is calculated as shown in Equation 4.9

$$i_{corr} = \frac{I_{corr}}{A_a} \tag{4.9}$$

where, A_a (cm^2) is the anodic area. While this is an exceedingly simple concept, measurement of the anodic area is complicated, particularly in RC where the anode is not visible. The cathode used for measurement of I_{corr} is typically a more noble metal, such as stainless steel [*Gautefall and Vennesland*, 1983], copper [*Wang et al.*, 2000; *Yoon et al.*, 2000b], or ruthenium-iridium mixed metal oxide activated titanium [*Küter*, 2009; *Nygaard*, 2008], etc. Corrosion current has also been measured between different layers of reinforcing steel [*ASTM G 102*, 1999; *Berke et al.*, 1993; *Lorentz and French*, 1995], where the steel cast deeper in the specimen is assumed to be more noble. Problems with this may exist if corrosion of the deeper reinforcement occurs [*Berke et al.*, 1993].

Corrosion current, I_{corr} may be measured using a zero-resistance (or zero-impedance) ammeter. The corrosion current density, i_{corr} is related to the inflow and outflow currents, I_o and I_i respectively, as shown in Equation 4.10 [*Nagataki et al.*, 1996].

$$i_{corr} = \frac{I_o - I_i}{A_a} \tag{4.10}$$

Here, if the value of i_{corr} is positive, the corrosion current is anodic while negative values indicate the corrosion current is cathodic [*Nagataki et al.*, 1996; *Mohammed et al.*, 2001].

Corrosion current density, i_{corr} can also be measured using linear polarization resistance (LPR) measurements which use a three electrode arrangement including the embedded steel (working electrode), a reference electrode, and a counter electrode. i_{corr} is determined using the Stern-Geary equation (Equation 4.11). A potential (voltage), ΔE_p (mV) is applied to the embedded steel and the resulting current density change, Δi_p (A) is measured. The polarization resistance of the corroding electrode, R_p (Ω) is then calculated as:

$$R_p = \frac{\Delta E_p}{\Delta i_p} \tag{4.11}$$

Corrosion current density, i_{corr} is calculated from the polarization resistance, R_p as shown in Equation 4.12

$$i_{corr} = \frac{B}{R_p \times A_p} \tag{4.12}$$

where B is a proportionality factor related to the anodic and cathodic Tafel constants, b_a and b_c (mV/A) as shown in Equation 4.13, and A_p (cm^2) is the polarized surface area of the reinforcement. Controlling and knowing the polarized surface area, A_p is vital to the LPR measurement process [*Nygaard*, 2008].

$$B = \frac{b_a \cdot b_c}{2.303 \cdot (b_a + b_c)} \tag{4.13}$$

Standard methods for estimating Tafel slopes and performing LPR can be determined through standardized methods [*ASTM G 102*, 1999] and [*ASTM G 59*, 2009], respectively.

Corrosion rate is largely influenced by the electrode and electrolyte materials, and to a lesser degree by temperature, pressure and solution concentrations [*Bardal*, 2004]. Additionally, the rate of electrochemical reaction is limited by three polarization factors, which may act individually or in combination. Activation polarization is the resistance to electrochemical reaction at the metal-electrolyte interface caused by an energy barrier, which must be overcome to convert species involved in the corrosion reaction. Concentration polarization occurs as a results of a deficiency of necessary reactant (e.g., oxygen) at the metal surface. Resistance or Ohmic polarization results from electrolytic solutions, passive layers, or other covering materials (dry concrete, paint, etc.) providing a significant ohmic resistance.

As shown in Figure 4.3 from *Bardal* [2004], the ratio of cathode-to-anode size may have major implications on corrosion kinetics. The figure illustrates the effect of varying cathode-to-anode ratio on galvanic corrosion between stainless and carbon steel in aerated water with a pH of 6.0. The anode (carbon steel) size is constant at 1 cm^2, while the cathode (stainless steel) size is varied from 1, 10, and 100 cm^2. The corrosion current density (intersection point between cathodic and anodic curves) increases from approximately 30 $\mu A/cm^2$ to 3000 $\mu A/cm^2$ with increasing cathode-to-anode ratio. While this example describes two dissimilar metals, similar effects are seen if one metal is exposed to varying environments. For instance, steel coatings (e.g., paint or concrete) with small defects can create a vary large cathode-to-anode ratio and rapid corrosion of the steel at the location of the defect.

Further details on influencing factors of reaction kinetics can be found in the literature, see e.g., [*Ahmad*, 2003; *Bardal*, 2004; *Perez*, 2004; *Küter*, 2009].

Both the presented electrochemical measurements, LPR and zero-resistance ammeters, can be used to determine the time of corrosion initiation. However, to accurately assess corrosion rate, the size of the corroding area must be measured through inspections. As discussed further in Section 4.1.5 the application of electrochemical measurement techniques to steel reinforcement embedded in concrete can be difficult due to the need for inspection of the reinforcement. To avoid the necessary inspection and to allow for location dependent measurements several specialized rebar configurations were developed as discussed in Section 4.1.5.

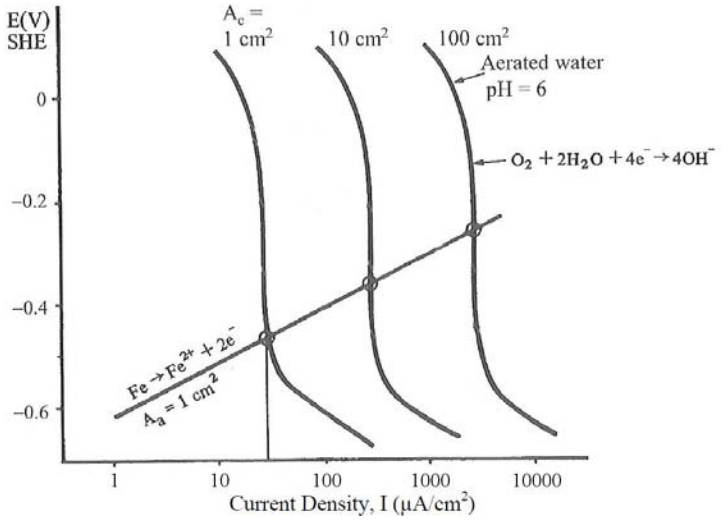

Figure 4.3 *Effect of cathode-to-anode ratio on corrosion rate, where the cathode material was stainless steel and the anode material is carbon steel, from [Bardal, 2004].*

4.1.2 Corrosion processes in reinforced concrete

An overview of the electrochemical and physical processes taking place during corrosion of steel reinforcement is shown in Figure 4.4, as proposed in [*Küter*, 2009]. The covering concrete containing an alkaline pore solution (pH ≈ 11-14), analogous to the electrolytic solution in the wet corrosion process (Figure 4.1), allows for ionic current exchange. Resistance to ionic current exchange (resistance polarization) increases with a decreasing concrete moisture content, caused by hydration and/or drying. The figure illustrates that concrete provides a diffusion barrier to oxygen, chloride ions, and carbon dioxide. Restriction of oxygen - oxygen which is required in the cathodic processes described in the figure - may lead to a concentration polarization. Chloride ions and/or carbon dioxide in concrete leads to the eventual breakdown of the passive layer, in addition to affecting the feasible anodic reaction products. Based upon Figure 4.4 and a multitude of experimental results (see e.g., [*Tremper*, 1947; *Rehm and Moll*, 1964; *Kamiyama*, 1972; *Schiessl*, 1976; *Makita et al.*, 1980; *O'Neil*, 1980; *Francois and Arliguie*, 1998; *Francois et al.*, 2006; *Gautefall and Vennesland*, 1983; *Schiessl and Raupach*, 1997; *Ahmad*, 2003]), it has been concluded that concrete cover thickness and quality (i.e., water-to-cement ratio) are the most significant factors influencing the initiation and propagation of reinforcement corrosion in an aggressive environment. As discussed further in Section 4.1.3 cracking and other defects also have a major influence, particularly regarding corrosion initiation.

Reinforcement corrosion can be described using a two phased time-related deterioration model including initiation and propagation phases as illustrated by the model shown in Figure 1.3. The figure illustrates the service life of a concrete structure as an increased deterioration with time. Deterioration is measured from a chosen durability criteria such as cross-section reduction of reinforcement, degradation of cover concrete, etc. During the initiation phase of the model substances such as carbon dioxide and chloride ions penetrate the concrete cover, eventually leading to a situation wherein corrosion initiation is

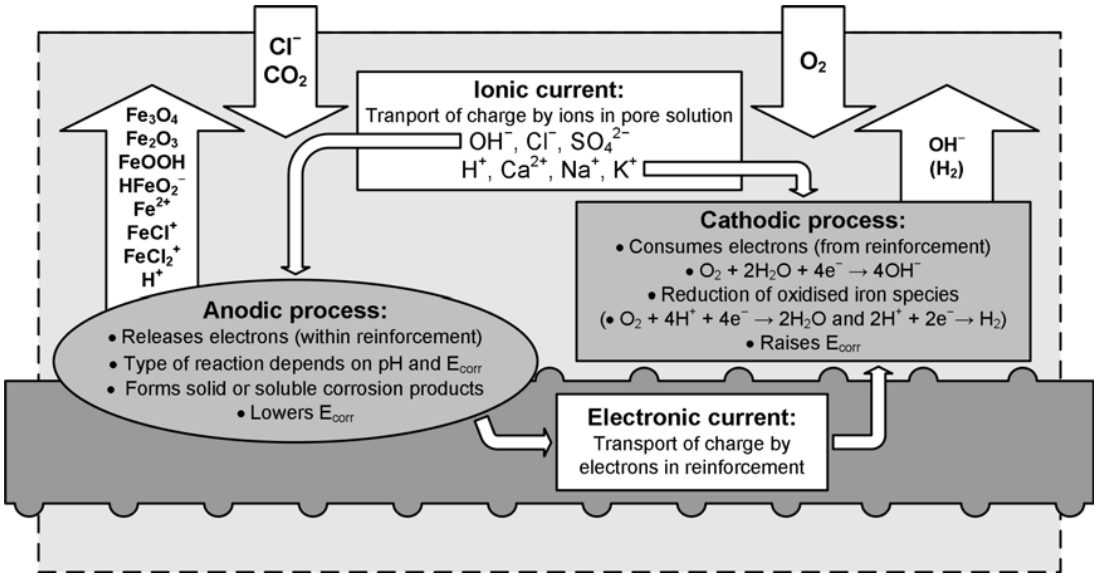

Figure 4.4 *Comprehensive schematic of passive and active reinforcement corrosion, developed in [Küter, 2009].*

thermodynamically favored.

Once corrosion initiates the propagation phase begins, marked by an acceleration in deterioration. The propagation phase is controlled by kinetics as the corrosion rate effects the rate of deterioration. The temperature and access to moisture and oxygen partially control the propagation rate. Once the acceptance criteria is reached, remediation efforts are required.

Carbonation-induced corrosion

The Pourbaix diagram in Figure 4.2 shows Fe exposed to concrete pore solution is likely in a passive corrosion region due to the high pH ($\geq$ 11). As shown in Figure 4.2 reducing pH leads to the theoretical feasibility of corrosion initiation.

Carbonation of pore solution results in potentially detrimental pH reductions approaching neutrality [*Tuutti*, 1982a]. Leaching, which occurs due to repetitive exposure to external water sources, also results in a pH reduction [*Hasegawa et al.*, 2006]. Experimental observations in a synthetic pore solution indicate instability of the passive layer may begin to occure at pH values between 11.3-11.5 [*Xu et al.*, 2009]. Corrosion in concrete with low pH is typically a more general corrosion, as shown in Figure 4.5. The image shows corrosion attack covering the entire steel surface after anodic polarization in a synthetic, carbonated pore solution with pH 9.0.

Carbonation decreases chloride ion binding capacity, potentially freeing bound chloride ions to interact with reinforcing steel [*Tuutti*, 1982a; *Kayyali and Haque*, 1988; *Glass et al.*, 2000; *Glass and Buenfeld*, 2000; *Reddy et al.*, 2002; *Meijers et al.*, 2005]. Experimental

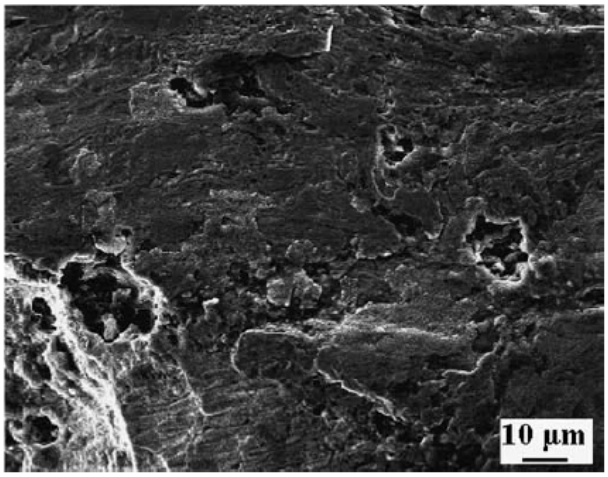

Figure 4.5 *General corrosion attack observed on steel surface after anodic polarization in 0.015 M $NaHCO_3$ + 0.005 M Na_2CO_3 + 0.01% chloride ion solution with pH = 9.0 [Moreno et al., 2004].*

results indicate the occurrence of corrosion increases when RC is both carbonated and exposed to chloride ions compared to RC which is simply carbonated [*Rehm and Moll*, 1964; *Schiessl*, 1976].

Chloride-induced corrosion

The Pourbaix diagram in Figure 4.2 shows Fe exposed to an alkaline pore solution (pH $\approx$ 11-14) is inherently in a thermodynamically passivity region. However, the presence of chloride ions can breakdown steel passivity. Concrete provides protection against steel reinforcement corrosion by providing a diffusive barrier for aggressive substances and by binding chlorides (Section 3.1.1). However, in time a critical amount of chloride ions may reach the level of the reinforcement, initiating corrosion. Experimental [*Tuutti*, 1977; *Moreno et al.*, 2004; *Vidal et al.*, 2007] and in-situ [*Schiessl*, 1976; *Mangat and Molloy*, 1992; *Mouri and Miyazato*, 2005] observations have verified the breakdown of passivity of reinforcement steel occurs in uncracked concrete exposed to chloride ions.

Figure 4.6(a) from *Moreno et al.* [2004] shows an SEM image of the corrosion attack on steel exposed to chloride contaminated solutions after anodic polarization. The steel was submerged in solution with a pH of 13.9 and 3% chloride. The image indicates chloride ions may induce reinforcement corrosion in the form of pitting.

Figure 4.6(b) shows a deep corrosion pit in a steel bar embedded in concrete exposed to a marine environment for 15 years [*Mohammed et al.*, 2002]. The deep corrosion pit was found to be located at a defect (air void) in the steel-concrete interface. Other investigations have also reported reinforcement corrosion tends to initiate at defects in the interface, such as cold joints [*Yano et al.*, 2002], air voids [*Mohammed et al.*, 2002], bleed channels [*Castel et al.*, 2003; *Vidal et al.*, 2007], and cracks (see Table 4.4 for references).

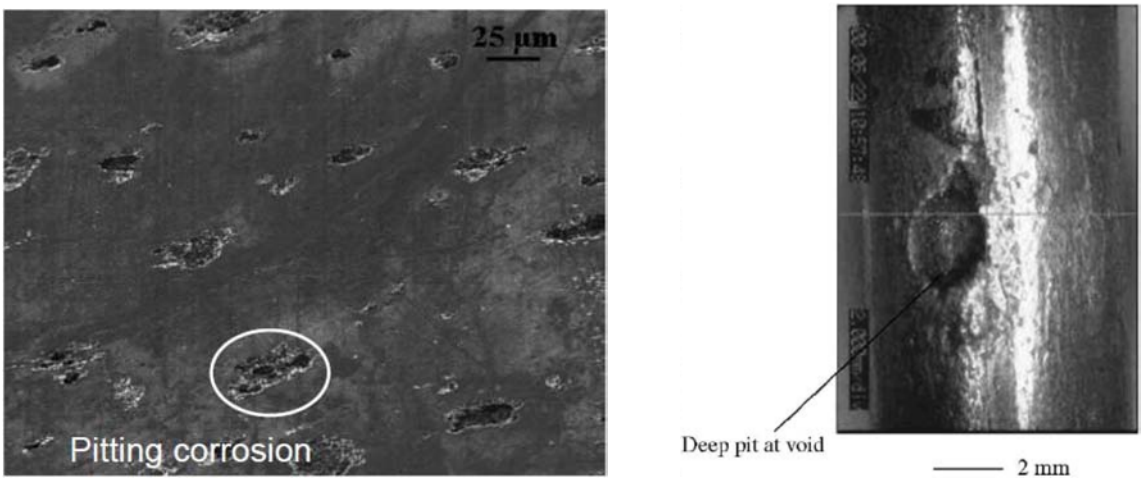

(a) (b)

Figure 4.6 *Pitting corrosion attack observed on steel surface after (a) anodic polarization in 0.90 M NaOH + 3% chloride solution with pH = 13.9 [Moreno et al., 2004], and (b) 15 years embedded in concrete exposed to marine environment (corrosion pit was located adjacent to a defect in the steel-concrete interface) [Mohammed et al., 2002].*

Analysis of thermodynamically possible corrosion products indicate this rapid reduction may be caused by formation of soluble Fe-Cl complexes ($FeCl_2^+$ and $FeCl^+$ at higher chloride concentrations) [*Küter*, 2009]. In an anaerobic chloride-containing environment, an additional possible hazard is the formation of so-called green rust; named after its green-colored aqueous corrosion product [*Sagoe-Crentsil and Glasser*, 1993].

4.1.3 Theoretical implications of concrete cover cracking on reinforcement corrosion

As discussed in Chapter 3, cracking of concrete allows for a more rapid ingress of chloride ions and other aggressive substances which may lead to reinforcement corrosion. Localized corrosion may initiate in one of two possible processes when a crack intersects reinforcing steel. Figure 4.7 from [*Schiessl and Raupach*, 1997] illustrates possible corrosion processes in the cracked area. In Figure 4.7(a) a corrosion microcell forms in which anodic and cathodic reactions both take place within the crack and carbonated concrete. This type of corrosion consists of small, neighboring cathodic and anodic areas and O_2 required for the cathodic reaction is provided readily through the crack. In Figure 4.7(b) a corrosion macrocell forms in which the anodic processes take place at the steel intersecting the crack zone and carbonated concrete, while the steel contained in the undamaged concrete is cathodic. In this case, the cathode may be much larger than the anode, yielding a rapid local corrosion rate at the crack. This theoretical condition, with an anodic cracked region and cathodic region in the uncracked concrete, has been experimentally verified in [*Schiessl and Raupach*, 1997; *Mohammed et al.*, 2001; *Miyazato et al.*, 2001], as discussed further below.

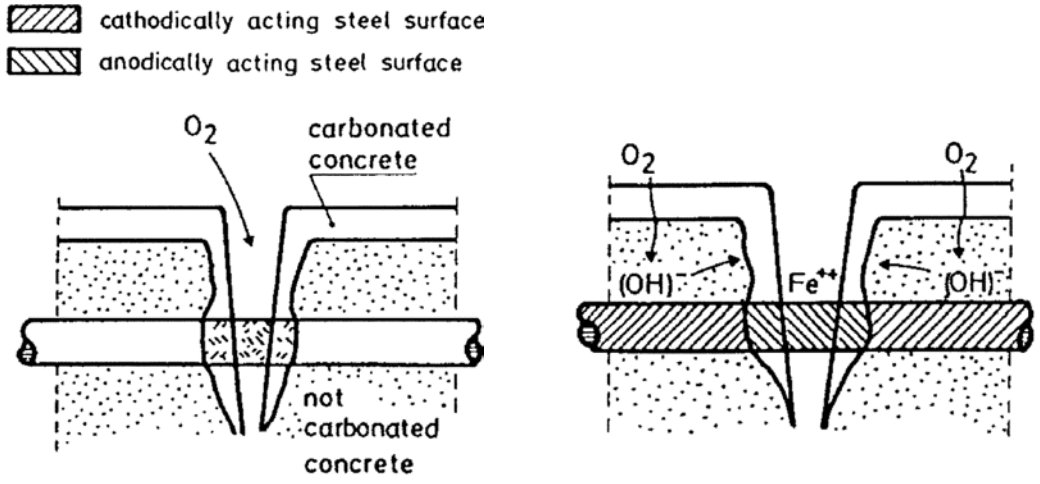

Figure 4.7 *Illustration of (a) microcell and (b) macrocell corrosion processes in cracked RC, from [Schiessl and Raupach, 1997].*

As discussed further in Section 4.1.6 experimental results have indicated corrosion propagation is not related to the width of intersecting cracks (see e.g., [*Schiessl*, 1976; *Yachida*, 1987; *Schiessl and Raupach*, 1997; *Tottori et al.*, 1999; *Mohammed et al.*, 2001]).

The cracks in Figure 4.7 likely illustrate plastic shrinkage cracks, as damage along the concrete-steel interface is not included. Mechanical load-induced cracks create damage, including slip and separation, between the concrete and the steel (See Paper II). The impact of this damage is a central focus of the experimental results described later in this chapter.

Influence of crack spacing

Macrocell reinforcement corrosion in cracked concrete (Figure 4.7(b)) may also be influenced by crack spacing, or frequency. As shown in Figure 4.3 an increase in cathode-to-anode ratio results in increased corrosion rate. Multiple cracks located within a close proximity may alter the size of the cathodic region in the undamaged concrete, changing the corrosion rate of the macrocell. Model and experimental results are presented on the influence of crack spacing in Section 4.1.6 below.

Influence of crack orientation

Typically cracks are classified with respect to the main reinforcement into one of two categories - transverse or longitudinal. While the scope of this project only includes transverse cracking, previous result indicated crack orientation is another important parameter. Longitudinal cracking can result in two situations, shown in Figure 4.8(a) and (b). Longitudinal crack are typically induced by plastic shrinkage/settlement; therefore, plastic cracks (i.e., no damage of concrete along interface of transverse rebar) are indicated in the figures. In Figure 4.8(a) the longitudinal crack leads to the formation of

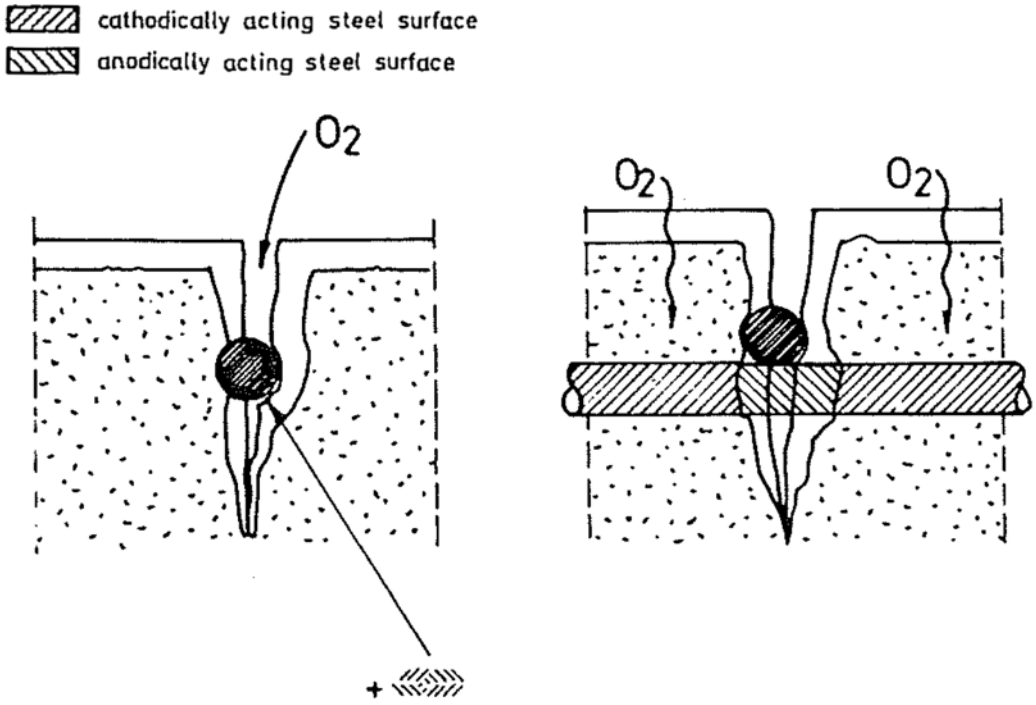

(a) (b)

Figure 4.8 *The effect of longitudinal (plastic) cracking on the corrosion process, from [Schiessl, 1986]. In (a) a corrosion microcell process takes place in the cracked region and carbonated concrete and in (b) a corrosion macrocell process takes place with the anodic regions in the cracked and carbonated concrete and cathodic regions in the undamaged concrete.*

a corrosion microcell, where the anodic and cathodic reactions take place in close proximity on the steel surface within the cracked area and carbonated concrete. In Figure 4.8(b) the crack has a longitudinal orientation to one reinforcing bar and a transverse orientation to another, and the two reinforcing bars are electronically connected. Here, a corrosion macrocell forms in which the anodic processes take place at the steel in the cracked area and carbonated concrete, while the steel contained in the undamaged concrete is cathodic. Longitudinal cracks do not confine sites of possible corrosion initiation as intersecting cracks do and therefore may result in the loss of passivity in multiple locations along the reinforcement.

4.1.4 Cracking in reinforced concrete

Tensile load applied to reinforcing steel (either through direct tensile or flexural loading) causes complex cracking and deformation behaviors as idealistically illustrated in Figure 4.9. The tensile load creates a primary crack in the concrete, which is wider at the concrete surface than at the rebar, followed by secondary crack upon additional loading [*Goto*, 1971; *ACI Committee 224*, 1992]. Secondary cracks (labeled internal crack in Figure 4.9), which form due to the transfer of tensile load through the rebar ribs into the concrete, cause additional damage at the concrete/reinforcement interface, but do not reach the outer surface of the concrete. Multiple primary cracks may occur, depending on the load level, cover thickness, and material properties [*ACI Committee 224*, 1992].

Figure 4.10 shows results from Paper II on cracking of reinforced concrete, under flexural loading, as measured by photogrammetry. In Paper II the covering concrete was removed from one side of the beam specimens, exposing the concrete-reinforcement interface as pointed out in the figure. In Figure 4.10(a) the beam was loaded to the estimated cracking load, inducing a V-shaped crack. The crack width near the tensile surface was 0.033 mm, while only a minute crack width was visible near the level of the reinforcement. Secondary cracking is not seen under the low load level. However, as shown in Figure 4.10(b), with additional loading (35.0 kN) extensive secondary cracking is seen within the concrete. Furthermore, gaps (i.e., separation) and translation (i.e., slip) between the reinforcement and concrete occur. As discussed further in Paper II, cyclic loading appears to reduce crack tortuosity and increase connectivity of cracks, which would likely allow more rapid ingress of various aggressive substances based on results presented in Chapter 3. Existence and extent of secondary cracking (including slip and separation), as shown in Figures 4.9 and 4.10, is therefore dependent on load level. Previous work has also indicated concrete properties influence secondary cracking [*Win et al.*, 2004].

In order to induce secondary cracks (i.e., realistic cracking) in reinforced concrete under either tensile of flexural loading, the reinforcement must have an adequate length to develop and transfer tensile stresses into the concrete. As discussed in the following section, several studies utilized arrangements of short reinforcement segments to investigate the influence cracking has on reinforcement corrosion. Figures 4.9 and 4.10 indicate such arrangements may not induce realistic cracking of the concrete.

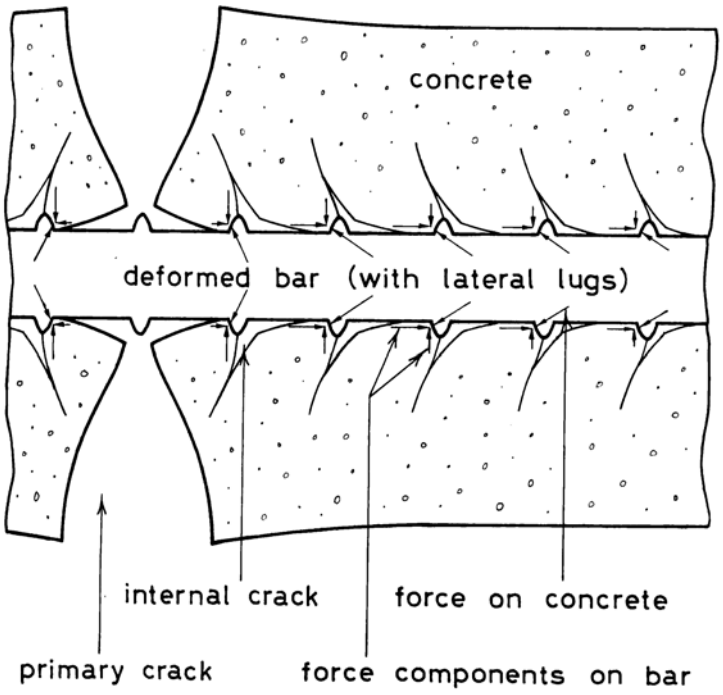

Figure 4.9 *Idealized schematics of concrete deformation around reinforcement under tensile loading from [Goto, 1971].*

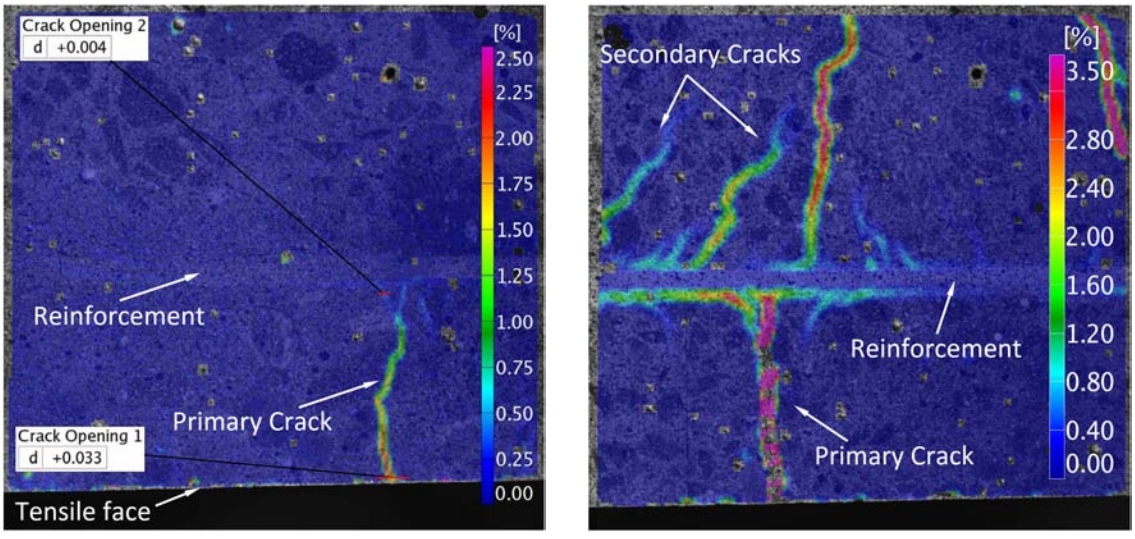

(a) (b)

Figure 4.10 *Photogrammetric assessment of cracking in reinforced concrete beams with covering concrete removed to expose concrete-reinforcement interface. Beam loaded to (a) the estimated cracking load (13.0 kN) and (b) 35.0 kN.*

4.1.5 Review of experimental methods for corrosion in cracked concrete

Tables 4.2 and 4.3 provide overviews of experimental techniques presented in the literature to assess the effect of cracking on initiation and propagation reinforcement corrosion, respectively. Attributes of each experimental technique are included in the tables. The basic electrochemical experimental techniques discussed below can be applied to various special rebar configurations described in Section 4.1.5 as well as standard rebar. Further details on the experimental techniques are presented in the following sections. in Tables 4.2 and 4.3. Details on the rebar configurations are provided in Section 4.1.5.

Table 4.2 *Attributes of various methods to assess corrosion initiation in cracked concrete.*

Experimental technique		NDT	Continuous	Location dependent information	Realistic cracking
Electrochemical techniques applied through:	Standard rebar	•†	•		•
	Standard rebar, partially coated	•†	•	•	
	Segmented rebar	•†	•	•	
	Rebar segments	•†	•	•	
Acoustic measurements*		•	•	•	•

* Limited background for interpretation
† Technique is an NDT, however destructive testing often used for verification

Table 4.3 *Attributes of various methods to assess corrosion propagation in cracked concrete.*

Experimental technique		NDT	Continuous	Location dependent information	Realistic cracking
Electrochemical techniques applied through:	Standard rebar	•†	•		•
	Standard rebar, partially coated	•†	•	•	
	Segmented rebar	•†	•	•	
	Rebar segments	•†	•	•	
Measurement on rebar:	Gravimetric (weight loss)			•	•
	Corroded area including microscopy			•	•
Acoustic measurements*		•	•	•	•
Ground penetrating radar		•		•	•
γ-ray imaging		•		•	•
Ultrasonic pulse analysis		•		•	•

* Limited background for interpretation
† Technique is an NDT, however destructive testing often used for verification

The presence of cracks has been shown to have less of an impact on corrosion propagation, as discussed further in Section 4.1.6. Several theoretical explanations for this have been

discussed in the literature. In [*Tuutti*, 1978] a situation is described where reinforcement corrosion initiated by carbonation of concrete nearby a crack produced a fine-pore corrosion product which helps to seal the crack. Alkaline pore solution may then diffuse through the corrosion products and, as previously shown in Figure 4.2, create a situation wherein the steel is thermodynamically passive. Longitudinal cracks are less likely to seal as the corrosion products are less confined, possibly allowing corrosion to continue unabated or to accelerate [*Arya and Wood*, 1995]. Concrete may also self-heal (autogenously heal) when exposed to water and either static or dynamic mechanical loads, leading to reduced flow rates of liquids [*Clear*, 1985; *Jacobsen et al.*, 1996; *Ramm and Biscoping*, 1998; *Edvardsen*, 1999] and corrosion rates [*Ramm and Biscoping*, 1998] over time.

Specialized rebar configurations for corrosion measurements

Electrochemical measurement techniques can be applied to standard rebar; however, location-dependent information on the corrosion behavior is not provided without destructive removal and inspection of the reinforcement. Therefore, various specialized rebar configurations were developed to assess the location dependencies of reinforcement corrosion in cracked concrete. Configurations include partially epoxy coated standard rebars [*Schiessl and Raupach*, 1994, 1997; *Ramm and Biscoping*, 1998] (Figure 4.11), 'rebar segments' consisting of mechanically and electrically discontinuous reinforcement sections attached to a black steel backbone [*Marcotte and Hansson*, 2003; *Poursaee and Hansson*, 2008] (Figure 4.12), and 'segmented rebar' consisting of reinforcement sections connected mechanically with epoxy [*Mohammed et al.*, 2001; *Miyazato et al.*, 2001] (Figure 4.13). The 'Specialized rebar configurations' columns in Table 4.4 provides an overview of previous studies investigating corrosion in cracked concrete using such arrangements. The author is unaware of a comparison between the cracking behavior of concrete surrounding these specialized rebar configurations and standard rebar. The following paragraph provides additional details and potential issues of these specialized rebar systems.

Figure 4.11 shows an arrangement where a standard rebar was partially coated in epoxy creating a 20 mm segment of uncoated steel at the location of a bending crack (anode segment). The six rebar sections in the uncracked portion of the concrete are anticipated to behave as cathodes in a corrosion macrocell. All the segments were connected through zero-resistance ammeters to assess the effect bending cracking had on corrosion initiation and propagation.

In the configuration in Figure 4.12 segments of steel are mounted, electronically isolated, to a standard black steel rebar which acts as a 'backbone' to carry load and induce cracking. A single stainless steel segment is used as a counter electrode for LPR measurements. Additionally, OCP measurements may be taken using a standard reference electrode.

In another commonly used arrangement in Figure 4.13 individual steel segments are joined with epoxy creating a 'segmented rebar'. As shown, epoxy establishes mechanical bond, while maintaining electrical isolation, between individual steel segments. The lead wires extending from each steel segment are connected using zero-resistance ammeters. Typi-

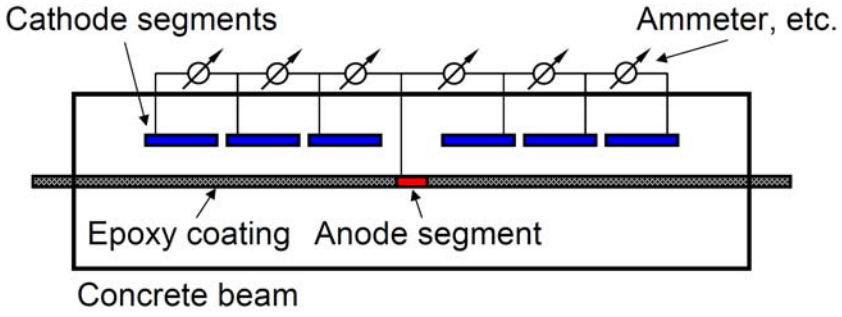

Figure 4.11 *Special rebar configuration consisting of a partially epoxy-coated standard rebar anode and disconnected steel segments acting as cathodes (after [Schiessl and Raupach, 1994, 1997; Ramm and Biscoping, 1998])*

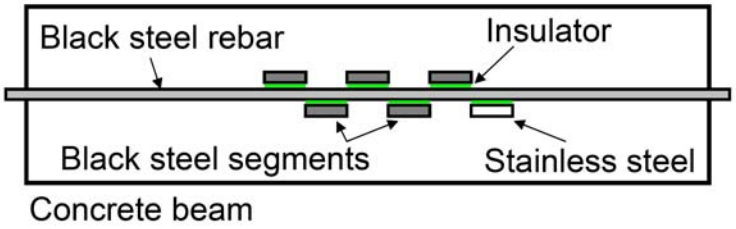

Figure 4.12 *Special rebar configuration consisting of steel segments fixed, isolated, on a black steel rebar (after [Marcotte and Hansson, 2003; Poursaee and Hansson, 2008]). In [Poursaee and Hansson, 2008] a single stainless steel segment was also fixed, isolated, on the black steel rebar as a counter electrode in LPR measurements.*

cally an epoxy coated dummy rebar is placed in close proximity to the 'segmented rebar' to avoid failure of the beam during cracking [*Mohammed et al.*, 2001; *Miyazato et al.*, 2001].

While each of these specialized rebar configurations provide location dependent information of reinforcement corrosion, several possible issues should be considered including consolidation of the fresh concrete, excessive voids at the concrete-reinforcement interface, and realistic cracking of the concrete.

In Figure 4.11 the maximum anode size is limited to 20 mm by partially coating the rebar with epoxy. Therefore, anodic reactions cannot occur beyond the preset 20 mm region even if a critical chloride content is reached at the concrete-steel interface. This limitation may lead to the possible underestimation of the effect the crack has on the anodic area. Crevice corrosion can also potentially occur at the ends of the epoxy coated region when using this arrangement, leading to an overestimation of the effect of the crack. In addition, observations indicate that even lengths of steel less than the 20 mm preset 'anode' size may not necessarily behave as a pure anode as corrosion microcells may form [*Nygaard*, 2003].

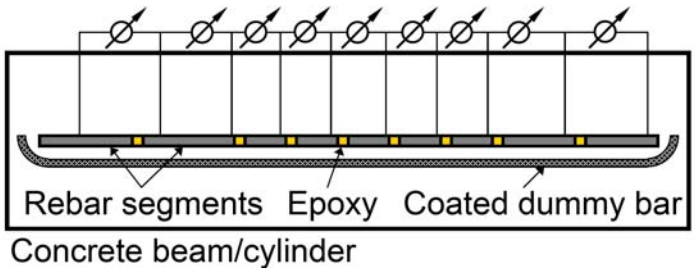

Figure 4.13 *Special rebar configuration consisting of steel segments connected (but electronically isolated) using epoxy and an epoxy-coated dummy bar (after [Mohammed et al., 2001; Miyazato et al., 2001]).*

Care should be taken to avoid entrapping air or casting in other defects in these specialized rebar configurations. Particularly in Figure 4.12, the interface of the steel 'backbone' and the isolated segments may be difficult to cast free of defects. Such defects have been shown to provide an ideal location for corrosion initiation [*Mohammed et al.*, 2002; *Yano et al.*, 2002; *Castel et al.*, 2003; *Vidal et al.*, 2007] due to the reduced chloride threshold required to induce corrosion [*Nygaard*, 2003].

Finally, as these special configurations are meant to determine the effect cracking has on reinforcement corrosion, it is vitally important that realistic cracks are induced. However, results of the cracking behavior of the concrete surrounding these specialized rebar configurations have not been reported in the literature. Variations in the cracking behavior are likely due to interfacial bond of epoxy coated rebar (Figure 4.11), the influence of the fixed 'rebar segments' (Figure 4.12), variations in stiffness of the steel and epoxy (Figure 4.13), and the close proximity of the 'dummy' rebar (Figure 4.13).

Destructive techniques

Common destructive methods used to assess the effect of concrete cover cracking on reinforcement corrosion include gravimetric and visual (including microscopy) analysis. For these methods, the reinforcement is excavated from the covering concrete for visual inspection and measurement of cross-section or weight reduction. Through microscopy of extracted steel samples information on the corrosion attack type can be assessed. Additionally, the corrosion products can be detected using SEM/EDS (e.g., [*Jaffer and Hansson*, 2009]); however, the possible oxidation of corrosion products during sample preparation and analysis should be considered.

Non-destructive techniques

Several non-destructive tests (NDT's) have also been used for inspection of concrete and reinforcement corrosion including ground penetrating radar (GPR) [*Hubbard et al.*, 2003], γ-ray imaging [*Mariscotti et al.*, 2009], acoustic emission [*Yoon et al.*, 2000a; *Ohtsu and Tomoda*, 2008] and ultrasonic pulse analysis [*Miller et al.*, 2009].

GPR measurements, which uses radar waves to provide profiles of RC, are affected by reinforcement when repeating measurements over time [*Hubbard et al.*, 2003]. While this NDT naturally provides location-dependant information, the method is currently unable to quantify the extent of corrosion and "further study is necessary to quantify how other parameters (such as concrete wetness, chlorides, and cracks) influence the geophysical signatures" [*Hubbard et al.*, 2003].

Figure 4.14 shows a γ-ray image taken from an in-situ RC column. The image shows areas of very severe corrosion. A technique is presented in [*Mariscotti et al.*, 2009] to estimate the diameter of the corroded bars. However, resolution of γ-ray images is limited, complicating accurate estimations and likely limiting the technique to only identifying areas of severe corrosion-induced cross-sectional reduction. Comparison of estimated diameter from γ-ray images and actual diameters were not presented in [*Mariscotti et al.*, 2009].

Active and passive acoustic measurement techniques have been utilized in corrosion investigations as presented in [*Miller et al.*, 2009] and [*Yoon et al.*, 2000a; *Ohtsu and Tomoda*, 2008], respectively. Results of active acoustic measurements indicated an increase in degree of corrosion reduced the amplitude of ultrasonic waves transmitted through the reinforcement, which may be possible to see through continued monitoring. The reduced amplitude was thought to be caused by scatter of the wave by the roughened, corroded reinforcement surface. However, as presented in [*Miller et al.*, 2009] other factors such as changing loading also effect the transmission of ultrasonic waves through reinforcement. Passive acoustic measurements detect tensile micro- and macro-cracking of the concrete induced by, among other factors, reinforcement corrosion. The location of damage can be

Figure 4.14 *γ-ray image with areas of severe corrosion indicated in red [Mariscotti et al., 2009].*

detected by using multiple passive sensors.

Tests for characterization of impact of corrosion

Crack mapping, completed at varying times after exposure to a corrosive environment, provides insight on the evolution of concrete damage due to corrosion. Additionally, in [*Wang et al.*, 2000; *Yoon et al.*, 2000b] mechanical testing was completed subsequent to an investigation of reinforcement corrosion in cracked concrete. Results indicated reinforcement corrosion caused a shift in the failure mode as well as a reduction in the overall load capacity.

4.1.6 Review of literature on corrosion in cracked concrete

The following sections provide an overview of previous research findings concerning the effect cracking has on reinforcement corrosion including the influence of crack width and spacing. Table 4.4 provides an overview of the literature on the effect of transverse cracks on reinforcement corrosion. The following information is included in the table for each reference, where available:

- Material used, including:
  - Water-to-cement ratio,
  - Type of material (i.e. mortar, concrete, etc.).
- Specimen details, including:
  - Clear cover depth,
  - Dimensions,
  - Details of reinforcement.
- Mechanical exposure, including:
  - Loading details (i.e. TPBT or four point bending),
  - State of crack (held open or closed) during environmental exposure,
  - Range of crack widths investigated,
  - Crack spacing.
- Environmental exposure, including:
  - Type of environment,
  - Duration.
- Test methods
- Main observations

It should be noted that in some cases [*Arya and Ofori-Darko*, 1996; *Ramm and Biscoping*, 1998] 'cracks' are introduced by placing plastic or metal inserts into the fresh cast concrete. As previously discussed (Chapter 3), this influences the ingress behavior and likely also influences the results of corrosion investigations. Results from these papers are included in the table for completeness, however results are likely effected by the method of crack introduction. Finally, the author's comments are provided for several references.

The overview of previous research in Table 4.4 is subdivided in this section to discuss results from concrete reinforced by standard rebars and the various specialized rebar configurations described in Section 4.1.5.

Crack width

Results from standard rebar References using standard rebars to assess the influence of crack width on corrosion included [*Tremper*, 1947; *Voelmy and Bernardi*, 1957; *Shalon and Raphael*, 1964; *Rehm and Moll*, 1964; *Schiessl*, 1976; *Halvorsen*, 1966; *Houston et al.*, 1972; *Makita et al.*, 1980; *O'Neil*, 1980; *Yachida*, 1987; *Berke et al.*, 1993; *Gautefall and Vennesland*, 1983; *Lorentz and French*, 1995; *Arya and Ofori-Darko*, 1996; *Francois and Arliguie*, 1998, 1999; *Vidal et al.*, 2007; *Tottori et al.*, 1999; *Wang et al.*, 2000; *Yoon et al.*, 2000b; *Hartl*; *Kashino*, 1984; *Fidjestol and Nilson*, 1980] and while details were not able to be found, it is likely that standard rebar was also used for [*Kamiyama*, 1972; *Seki*, 1973; *Nishiyama*, 1975; *Katawaki*, 1977; *Suzuki et al.*, 1989; *You and Ohno*, 2002].

The extent of reinforcement corrosion in cracked concrete is commonly compared to the crack width. For standard rebar, good correlations were reported for this relationship for single experimental results after relatively short ($\leq\sim$3 year) exposure to natural conditions [*Katawaki*, 1977; *Rehm and Moll*, 1964; *Makita et al.*, 1980]. However, with additional time the influence of concrete crack width diminishes and factors including concrete quality and cover thickness seem to dominate the extent of reinforcement corrosion in RC exposed to natural conditions [*Schiessl*, 1976; *Tottori et al.*, 1999]. Laboratory studies using standard rebar also indicate crack width and reinforcement corrosion are related [*Berke et al.*, 1993; *Francois and Arliguie*, 1999; *Gautefall and Vennesland*, 1983; *Houston et al.*, 1972; *Lorentz and French*, 1995; *Wang et al.*, 2000; *Yoon et al.*, 2000b], and that other factors seem to dominate corrosion propagation [*Schiessl and Raupach*, 1997; *Mohammed et al.*, 2002].

Results from specialized rebar configurations References using specialized rebar configurations to assess the influence of crack width on corrosion included [*Schiessl and Raupach*, 1997; *Ramm and Biscoping*, 1998; *Mohammed et al.*, 2001, 2002; *Marcotte and Hansson*, 2003; *Miyazato and Hiraishi*, 2005; *Hiraishi et al.*, 2003, 2006]. While each of these specialized rebar configurations have their own possible issues (see Section 4.1.5), common observations have been made. In all cases, reinforcement corrosion initiates rapidly in cracks greater than 0.10 mm. It has also been observed in all papers that the anodic regions of the steel are found near or at the location of the transverse crack. Results indicate the corrosion rate tends to be at their maximum relatively soon after exposure and tend to reduce with continued exposure [*Schiessl and Raupach*, 1997; *Mohammed et al.*, 2002]; however, this may be caused by assumptions concerning the anode size.

Table 4.4 *Overview of literature concerning reinforcement corrosion in concrete with transverse cracks. Numbered footnotes correspond to author's comments on selected works provided in Table 4.5.*

* Indicates reference was included in a previous review in [*Tuutti*, 1978]
† Indicates reference was included in a previous review in [*Imamoto et al.*, 2007]
‡ Indicates reference was included in a previous review in [*Schiessl*, 1986]

Reference(s)	Materials		Specimen			Mechanical Exposure (Cracking)				
						Loading Details				
	w/c or w/b	Notes	Cover depth (mm)	Specimen dimensions (cm^3)	Notes	3-Point bending	4-Point bending	Notes	Width Range (mm)	Spacing (mm)
[Tremper, 1947]	0.40, 0.58, 0.75	Concrete	31	6.3x20x20	Deformed and smooth steel	•		Crack held open	0.13 – 1.30	N/A
[Voelmy and Bernardi, 1957]*	Not available		20, 30	Not available		Not available				
[Shalon et al., 1964]†	Not available		Not available			Not available				
[Rehm and Moll, 1964; Schiessl, 1976] 1)	0.80	Concrete	0, 15, 23	15x25x195	Deformed and smooth steel 0 mm cover indicates bare steel		•	Cracks held open, 100 cm constant moment span	0 – 1.50	N/A
[Halvorsen, 1966]*	Not available	Mortar	~30	Not available		•		Crack held open	< 0.05 – 1.50	N/A
[Houston et al., 1972]*	0.54	Concrete	25, 50	Not available			•		~0.05 – 0.30	Average 96.8 and 203.2 mm spacing
[Kamiyama, 1972]†	Not available		25, 50, 75	Not available		Not available				

Environmental Exposure		Test Method										Main Observations	
				Solid Rebar			Segmented Rebar						
Environment	Duration (Years)	Inspection of concrete	Inspection of rebar	Corrosion Potential	Macrocell Current	LPR	Corrosion Potential	Macrocell Current	LPR	Microcell Current	Notes	Critical surface crack width (mm)	Other
Marine atmosphere, 1.28 m average annual rainfall	10	•	•								Exposed from 1936-46	< 0.13	Minor steel cross-sectional reductions, but steel depassivated
Industrial atmosphere	10		•									0.20	--
Desert, Extreme temperature and RH cycles, and coastal areas	Not available	Not available										0.15	Corrosion progresses with increasing surface crack width; RH has major influence
City (Munich), industrial (Ruhrgebeit), tidal (North Sea)	10		•								Observations after 1, 2, 4, 10 years	< 0.10	Results after 4 and 10 years indicated marginal relation between surface crack width and corrosion; Initially frequency, probability, and amount of corrosion increases with surface crack width; Corrosion at cracks was greater than corrosion of unprotected bars
Alternating 50% - 100% RH, CaCl admixed	3	•	•									0.10	Length of corrosion from crack increased with crack size; Carbonation at depth of steel for all surface crack widths
Daily 3% NaCl solution spray, extremely warm temperature	1		•									--	Cracking primarily effected corrosion initiation; shorter crack spacing led to general corrosion; larger spacing emphasized effect of cracks on corrosion
Tidal (Tokyo Bay)	8	Not available										<0.10 mm for 25 mm cover, no corrosion for 50, 75 mm cover	Corrosion depends on cover thickness

Reference(s)	Materials		Specimen			Mechanical Exposure (Cracking)				
						Loading Details				
	w/c or w/b	Notes	Cover depth (mm)	Specimen dimensions (cm^3)	Notes	3-Point bending	4-Point bending	Notes	Width Range (mm)	Spacing (mm)
[Seki, 1973]†	0.44 – 0.78	Concrete	15	15x30x180	13 mm dia. Round steel main rebar		•	Multiple cracks seen	0.02 – 0.90	
[Nishiyama, 1975]†	0.59		30, 60	15x21x200, 15x25x200, 20x40x250, 25x50x250, 38x55x310			•		0.1, 0.2, 0.3	N/A
[Katawaki, 1977]†	0.55	Concrete	70, 120	20x20x150, 30x30x150	Round steel bar	•		Crack held open	0.05 – 0.20	N/A
[Fidjestol and Nilson, 1980]‡	Not available					Not available				
[Makita et al., 1980] 2)	0.40, 0.55, 0.70	Concrete, Mixed with sea and tap water	20, 70, 120	20x20x75, 20x20x150, 30x30x150	Round steel bar	•		Crack held open	0.05 – 0.20	N/A
[O'Neil, 1980]	Not available	Concrete	19, 50	Not available		•		Varying stress levels	0 – 0.40	N/A
[Gautefall and Vennesland, 1983] 3)	0.37, 0.45, 0.53, 0.77, 1.00	Concrete, 0, 10% silica fume mixtures	95	10x10x60		•		Unloaded during exposure	0.10 – 1.40	N/A
[Kashino, 1984]‡	Not available					Not available				
[Yachida, 1987]†	Inspection of 75 real reinforced concrete bridges in Japan									

Environmental Exposure		Test Method										Main Observations	
				Solid Rebar			Segmented Rebar						
Environment	Duration (Years)	Inspection of concrete	Inspection of rebar	Corrosion Potential	Macrocell Current	LPR	Corrosion Potential	Macrocell Current	LPR	Microcell Current	Notes	Critical surface crack width (mm)	Other
Simulated tidal and submerged in seawater (Tidal cycle of once a day under open sky)	9	•	•									0.15 for tidal, 0.20 for submerged (Threshold – corrosion area of 50% of steel bar)	
Near Haneda highway (Japan)	12	•	•										For same surface crack width: less corrosion when the specimen has a relatively large cover thickness
Tidal (Tokyo Bay)	2.74	•	•	•	•							--	Corrosion progresses with increase in surface crack width. Corrosion rate was slight for a surface crack width < 0.10 mm.
Norway west coast, underwater	Not available			•	•							--	Anodic behavior in cracked area, cathodic between cracks; Corrosion stopped after 1 year due to lack of oxygen
Tidal (Tokyo Bay)	2.74	•	•	•	•							--	Corrosion progresses with increase in surface crack width. Corrosion rate was slight for a surface crack width < 0.10 mm. For tap water – greater surface crack width caused degree of corrosion. Using sea water for mixing caused significant corrosion. Higher corrosion current measured near cracks
Tidal (Cobscock Bay, Maine) + Natural freeze/thaw (Avg. 135 cycles pr. Yr.)	24.33	•	•								Tensile testing of corroded rebar	0.40	Ultimate load capacity maintained design levels; Steel heavily corroded at spalled areas with no corrosion under cover
Submerged in seawater; room temperature	0.72				•						Steel vs. stainless steel galvanic current	0.40	No distinct difference observed in silica fume mixtures
Exposure in chloride containing environment	2		•									0.10	Significant corrosion after 2 years for surface crack width greater than 0.10 mm
	10 to 60	•	•									Not available	Over 40 years: No relation exists between surface crack width and steel corrosion.

Reference(s)	Materials		Specimen			Mechanical Exposure (Cracking)				
						Loading Details				
	w/c or w/b	Notes	Cover depth (mm)	Specimen dimensions (cm^3)	Notes	3-Point bending	4-Point bending	Notes	Width Range (mm)	Spacing (mm)
[Suzuki et al., 1989][†]	0.45	Concrete	20	14x11x60	13 mm diameter deformed steel		•		0.06-0.18	
[Berke et al., 1993] [4)]	0.40, 0.50	Concrete	25, 38	15.2x15.2x76.2	Single 'anode' rebar at cover depth, two 'cathode' bars cast below	•		Crack held open by plastic shim	0.25 – 0.51	N/A
[Lorentz and French, 1995]	0.35	Concrete; 0, 7.5, 10% silica fume mixtures	25	18x30x120			•	Cracks held open; 230 mm constant moment span	0.25 – 0.60	N/A
[Arya and Ofori-Darko, 1996]	0.65	Concrete	42	10x13.5x136	2 black steel rebar cast with central stainless steel rebar			'Cracks' introduced by shims	0.12, 0.15, 0.20, 0.30, 0.60, 2.4	65, 80, 105, 151, 272
[Schiessl and Raupach, 1997]	0.5, 0.6	Concrete	15, 35	9.7x15x70	Rebar consists of individual segments	•		Cracks held open by constant load	0.10, 0.20, 0.30, 0.50	N/A
[Ramm and Biscoping, 1998]	0.55	Concrete	Not available	18x18x70	Rebar consists of individual segments			'Cracks' introduced by shims	0.10, 0.20, 0.30, 0.40	N/A

Environmental Exposure		Test Method										Main Observations	
				Solid Rebar			Segmented Rebar						
Environment	Duration (Years)	Inspection of concrete	Inspection of rebar	Corrosion Potential	Macrocell Current	LPR	Corrosion Potential	Macrocell Current	LPR	Microcell Current	Notes	Critical surface crack width (mm)	Other
Cyclic wetting (24 hours, 3.1% NaCl solution) and drying (24 hours) at 65°C	0.38	•	•	•		•						< 0.10	Corrosion begins at the largest crack in the specimen. Formation of a galvanic cell between primary and secondary cracks is an important corrosion mechanism.
3% NaCl solution, 14 days dry – 14 days ponded, 22°C	1.33		•	•	•						Current between upper and lower rebars; Potential vs. SCE	< 0.25	Reduction in w/c provided ~1 order of magnitude improvement in corrosion resistance; Addition of $Ca(NO_2)_2$ drastically reduced corrosion
Cyclic saltwater ponding – drying	0.67			•	•						Current between upper and lower rebars; Potential vs. Cu-$CuSO_4$ electrode	--	Cracks allowed much faster corrosion initiation; Corrosion current density increased by an order of magnitude due to cracking; Epoxy coating effectively protected reinforcement.
3% NaCl solution spray; First 7 months 3x weekly, next 5 months 3x monthly	1				•	•					Steel vs. stainless steel galvanic current; LPR used Ag-$AgNO_3$ electrode	< 0.12	Frequency of cracking is a more fundamental factor influencing corrosion
1% Cl^- solution ponding weekly for 24 hrs. for 12 weeks followed by weekly ponding with tap water for 24 hrs. for 2 weeks, stored at 80% RH for 1 year, repeated	2							•				0.20 for w/c 0.5 and 35 mm cover depth	Influence of surface crack width declines with increased time of exposure; Cover depth and concrete composition much greater influence
Varying pH = 7.0, 6.1, 5.2	2		•					•				0.20	Surface crack width of 0.10 did not cause corrosion; Insignificant cross-section reductions for all surface crack widths

Reference(s)	Materials		Specimen			Mechanical Exposure (Cracking)				
						Loading Details				
	w/c or w/b	Notes	Cover depth (mm)	Specimen dimensions (cm^3)	Notes	3-Point bending	4-Point bending	Notes	Width Range (mm)	Spacing (mm)
[Francois and Arliguie, 1998, 1999, Vidal et al., 2007] [5)]	0.50	Concrete	10, 40	15x28x300		•		Crack held open, 3 load levels used	0.05 – 0.50	N/A
[Tottori et al., 1999][†]	0.43, 0.45	Concrete	13, 20, 25	20x22x60	6 mm diameter rebar used for 13 and 20 mm cover, 13 mm mm diameter rebar used for 20 and 25 mm cover	•			0.10 – 0.40	
[Wang et al., 2000; Yoon et al., 2000]	0.50	Concrete	30	10x15x117			•	Cracks held open; 230 mm constant moment span	45, 60, 75% Ultimate load; Surface crack width not measured	Not considered in investigation
[Mohammed et al., 2001]	0.30, 0.50, 0.70	Concrete	25 (single crack specimen) 45 (multi-crack specimen)	10x10x40 (single crack specimen) 15x15x125 (multi-crack specimen)	Single crack specimen: Deformed and smooth steel rebar segments Multi-crack specimen: Deformed rebar	•	•	Single crack specimen: Cracks held by load, stainless steel plate inserted to keep constant surface crack width	0.1, 0.3, 0.7 (single crack) 0, 0.1, 0.3, 0.7 (Multicrack)	

Environmental Exposure		Test Method										Main Observations	
				Solid Rebar			Segmented Rebar						
Environment	Duration (Years)	Inspection of concrete	Inspection of rebar	Corrosion Potential	Macrocell Current	LPR	Corrosion Potential	Macrocell Current	LPR	Microcell Current	Notes	Critical surface crack width (mm)	Other
Alternating salt water fog – drying, 20°C	17	•	•								Observations after 0.25, 0.5, 1, 5, 6, 7, 11, 12, 17 years	--	Load level and cover thickness more significant than surface crack width; Chloride threshold at rebar depth needed, but insufficient as a single parameter in service life prediction; Interface debonding from bleeding important factor in corrosion propagation; Large variation in degree of corrosion seen highlights difficulty in modeling corrosion
Snowy area	40	•	•	•								Not available	Surface crack width affects corrosion initiation but not corrosion rate over extended amount of time
3% NaCl solution; 4 days wetting, 3 days drying; After 50 days – 27 volts applied	0.19			•	•						Beams failed after exposure; Potential vs. Cu-$CuSO_4$ electrode; Current between steel and copper plate	N/A	Time of corrosion initiation decreased with increasing load level; Sustained loading exhibited increased corrosion; Degree of reinforcement corrosion effected beam failure mechanism.
Single crack specimen: Wetting (3.5% saltwater spray for 24 hours at 60°C) and drying (60 hours at 80% RH, 60°C) Multi-crack specimen: Weekly 3.5% saltwater spray, outdoor exposure	0.25 (single crack specimen) 1.33 (multi-crack specimen)	•	•			•		•		•	Single crack specimen: Inspection of concrete/rebar, Macro/micro-cell current Multi-crack specimen: Inspection of concrete/rebar, LPR	< 0.10	Relation observed in very beginning between surface crack width and corrosion. Relationship between w/c and corrosion rate of steel bar in concrete is more significant than the relationship between surface crack width and corrosion rate. Deformed bar are more prone to corrosion than smooth bar in cracked concrete

Reference(s)	Materials		Specimen			Mechanical Exposure (Cracking)				
						Loading Details				
	w/c or w/b	Notes	Cover depth (mm)	Specimen dimensions (cm^3)	Notes	3-Point bending	4-Point bending	Notes	Width Range (mm)	Spacing (mm)
[You and Ohno, 2002][†]	0.30, 0.50, 0.70	Concrete	20, 40	93x121, 93x141		•			0, 0.10, 0.20	N/A
[Marcotte and Hansson, 2003]	0.25, 0.27	Concrete, 0, 10% silica fume mixtures	Not available	10x10x50	Rebar consists of individual segments cast immediately next to solid rebar	•		Cracks held open with stainless steel wedges	0.30	N/A
[Mohammed et al., 2002]	0.45	Concrete; Slag and fly ash mixtures	45.5	10x10x60		•			0.10 – 5.0	N/A
[Miyazato and Hiraishi et al., 2005, 2006] [6)]	0.30, 0.60	Concrete and Engineered cementitious composite	20	10x10x40	Rebar consisted of individual segments epoxied together	•		20 kN load applied resulting in surface crack widths shown	~0.30-0.40 for RC, single crack; ≤ 0.10 for ECC, multiple cracks	N/A
[Otieno et al., 2010]	0.40, 0.55	OPC Concrete and 50/50 GGCS/OPC	40	10x10x50	Stainless steel counter electrode plate cast 30 mm below rebar	•		Cracked using crack frame, cracks 'reopened' after 9-10 and 18-19 weeks exposure	0, Unloaded cracked sample, 0.40, 0.70	N/A
[Hartl][‡]	0.50, 0.70	Not available	35	Not available		•			0-0.40	N/A

Environmental Exposure		Test Method										Main Observations	
				Solid Rebar			Segmented Rebar						
Environment	Duration (Years)	Inspection of concrete	Inspection of rebar	Corrosion Potential	Macrocell Current	LPR	Corrosion Potential	Macrocell Current	LPR	Microcell Current	Notes	Critical surface crack width (mm)	Other
3.1% NaCl, cyclic wetting and drying	0.19	•	•		•							--	Surface crack width affects corrosion in uncarbonated specimens; Surface crack width does not affect the corrosion on fhe carbonated specimens (the existence or nonexistence of cracks affects the corrosion of the specimen)
ASTM D1141 Simulated seawater	4						•		•		Potential vs. SCE; LPR used stainless steel counter electrode	0.30	Special attention to cracking should be paid to silica fume mixtures
Tidal pool (7 h wetting, 5 h drying); no freezing	15	•	•									0.10	Narrower cracks healed (surface crack width < 0.50 mm); Crack healing reduced corrosion rate; Accumulation of chlorides in unhealed cracks leads to increased corrosion; Voids at interface resulted in deep corrosion pits
3.1% NaCl spray at 90% RH for 2 days followed by 60% RH for 5 days	Not specified							•				Not considered	Corrosion rate in ECC is lower than RC, Chloride and carbonation ingress reduced in ECC
Cyclic - 3 days ponding with 5% NaCl solution, 4 days air drying for 32 weeks	0.57			•		•					Corrosion potential measured using silver/silver chloride reference electrode (ASTM C 876-91)	Unloaded cracks for OPC concretes and 0.55 w/b GGCS/OPC concrete, <0.40 mm for 0.40 w/b GGCS/OPC concrete	'Reopening' of cracks increased corrosion rates, particularly if active corrosion was taking place prior to 'reopening'; Concrete quality may help to control corrosion in cracked (and uncracked) concrete
3% NaCl varying humidity	4		•								Chloride levels were measured at the crack surface	0.20-0.30	Corrosion initiated after 1-1.5 years for surface crack widths greater than ~0.20-0.30 mm; Pitting corrosion occurred for w/c = 0.70 in cracked region; w/c = 0.50 and 35 mm cover – no influence of surface crack width

Reference(s)	Materials		Specimen			Mechanical Exposure (Cracking)				
						Loading Details				
	w/c or w/b	Notes	Cover depth (mm)	Specimen dimensions (cm^3)	Notes	3-Point bending	4-Point bending	Notes	Width Range (mm)	Spacing (mm)
[Pease et al., 2010 (Paper IV)]	0.50	Concrete – 8 mm maximum aggregate size	40	10x10x60	Hollowed, instrumented rebar	•		Cracked using crack frames	0.3-1.2	N/A

Crack spacing

In [*Raupach*, 1992; *Schiessl and Raupach*, 1997] an analytical model system illustrates the effect of reducing crack spacing on corrosion current. The model systems consisted of a single steel reinforcing bar and covering concrete with resistivity of 100 Ω/cm and a varying spacing of cracks, including 10, 20, and 100 cm spacing. The cathode size was assumed to be the same as the crack spacing, while the anode is contained within the cracked region. In this case, the anode current ($I_{a,i}$) is approximately doubled by increasing the crack spacing from 10 to 20 cm, and further approximately doubled by increasing the crack spacing from 20 to 100 cm. While these results are specific to the given conditions, they indicate cathode size influences the corrosion rate in RC. Experimental measurements in [*Houston et al.*, 1972; *Arya and Ofori-Darko*, 1996; *Hiraishi et al.*, 2003; *Miyazato and Hiraishi*, 2005] also show an effect of crack spacing on corrosion rate.

Experimental investigation into the effect of crack spacing on reinforcement corrosion was presented in [*Arya and Ofori-Darko*, 1996]. Reinforced beams contained idealized cracks, which were cast into the cover concrete using plastic inserts. It should be noted that the use of inserts creates cracks with an idealized and unrealistic crack morphology, affecting ingress behavior. Samples contained 0, 1, 2, 4, 8, 12, 16, or 20 equally spaced idealized cracks over a distance of 1.36 m with a total crack width of 2.4 mm. Results of this study indicate that cumulative weight loss through corrosion (i.e. amount of corrosion) increases with increasing number of cracks (i.e., reduced crack spacing) from 0 to 16 cracks. However, when the number of cracks increases from 16 to 20 cracks (85 mm and 68 mm crack spacing, respectively) there was a rapid decrease in the amount of corrosion. Possible self-healing was cited as an explanation for this reduction in [*Arya and Ofori-Darko*, 1996]. However, the reduced corrosion rate may also be explained by the reduced size of the cathode with the smallest crack spacing as described in [*Schiessl and Raupach*, 1997].

Environmental Exposure		Test Method									Main Observations	
				Solid Rebar			Segmented Rebar					
Environment	Duration (Years)	Inspection of concrete	Inspection of rebar	Corrosion Potential	Macrocell Current	LPR	Corrosion Potential	Macrocell Current	LPR	Microcell Current	Notes	Critical surface crack width (mm)	Other
10% chloride (NaCl) solution ponded for up to 62 days	0.17	•	•				•				Instrumented rebar monitored local corrosion potentials	< 0.30	Steel-concrete interfacial damage is more important than surface crack width, Varying surface crack width results in different corrosion behaviors, Local environmental conditions favor larger areas of corrosion than actually seen due to protection provided by actively corroding regions

Engineered cement composites (ECC) which undergo multiple cracking with a controlled crack width [*Li*, 2003a] may similarly provide reduce corrosion rates. Investigations in [*Hiraishi et al.*, 2003] and [*Miyazato and Hiraishi*, 2005] have shown that the crack width control provided by ECC materials significantly reduces the (ingress rate of chloride ions and the subsequent) reinforcement corrosion rate.

4.2 Experimental procedures

As discussed in Section 4.1.5 several specialized rebar configurations have been developed to assess the influence of transverse cracking on reinforcement corrosion. However, potential issues exist with these setups, particularly a realistic cracking behavior of the concrete. Therefore, this section describes an instrumented rebar designed to provide location-dependent corrosion measurements. In addition, the instrumented rebar should be capable of carrying and transferring loads and inducing realistic cracks.

4.2.1 Instrumented rebar configuration

The instrumented rebar consists of four sections of standard 10 mm diameter deformed rebar cut to lengths shown in Figure 4.15. The central section of the rebar (i.e. the 340 mm instrumented part) was bored, providing a 4 mm diameter void along the center. Seventeen (17) 1.5 mm diameter holes were drilled through the outer surface into the inner void. The holes were spaced 11 mm apart and carefully located between reinforcement ribs. Sensors protruded 5 mm from the reinforcement at each hole. The sensors were constructed by soldering 1 mm diameter steel pins (∼10 mm in length) to individual lead wires. Glue-coated heat-shrink tube encased each steel pin to protect the soldered connection and electronically disconnect the steel pins from the reinforcement. The 5 mm length protruding from the reinforcement was not covered by the heat-shrink tube. All 17 lead wires were bundled and sealed with heat-shrink tube. The bundle was passed

Table 4.5 *Comments to works presented in Table 4.4.*

Comment number	Comment
1)	Very high w/c used.
2)	Description of experiments is insufficient to fully comprehend reported results.
3)	Specimens were unloaded during testing, likely allowing crack width recovery, which was not measured.
4)	Electrochemical results are suspect as the authors reported the 'cathode' rebar corroded in some specimens.
5)	Conclusion in papers that corrosion is "...not influenced by the widths of cracks or the existence of the crack itself" disagrees with the presented results.
6)	Information on exposure time is not provided in papers, making results unclear and conclusions vague.

through a hole in the 30 mm long hollowed section as shown in Figure 4.15. Epoxy was then injected into the hollowed section to protect the wires, electrical connections and sensors. To provide adequate length of the instrumented rebar, two end parts of solid rebar were attached using threaded connections. Teflon tape was used at all threaded connections of the instrumented rebar.

4.2.2 Materials and specimen preparation

Details on the materials used and mixture procedure are found in Section 2.2.1. Only Mixture I.D. 1, from Table 2.1, was used for corrosion testing.

The fresh concrete was placed and vibrated into 100x100x600 mm^3 molds and covered by plastic for 24 hours at ambient conditions (i.e., 18°C ±2°C). Upon demolding the specimens were sealed with multiple layers of plastic followed by aluminum foil and packaging tape and were stored at 20°C ±1°C until testing. As shown in Figure 4.16, the concrete beam specimens were cast with an instrumented rebar, a standard rebar, and a ruthenium/iridium mixed metal oxide activated titanium (MMO-Ti) mesh. The sensors in the instrumented rebar were cast to face the tension surface of the beam, while the MMO-Ti mesh was cast 10 mm ± 3 mm from the compression surface, opposite the instrumented rebar. Additional information on the use of MMO-Ti mesh as a counter electrode in concrete can be found in the literature [*Nygaard*, 2008; *Küter*, 2009].

4.2.3 Mechanical loading and environmental exposure

Steel cracking frames, shown in Figure 4.16 in gray, were used to load the beams to 2, 3, 4, and 5 mm mid-span deflection (MSD) to induce cracking (Table 4.6). Bolts were finger-tightened then the defined MSD was applied by turning the bolts a required number of revolutions, using a wrench.

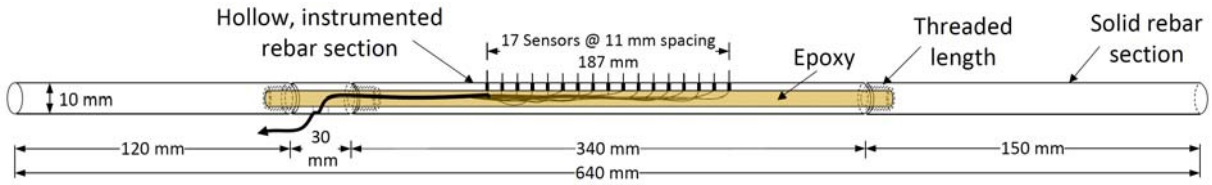

Figure 4.15 *Schematic of the instrumented reinforcement used for corrosion investigations (Note: Deformed reinforcement was used, ribs not shown in drawing).*

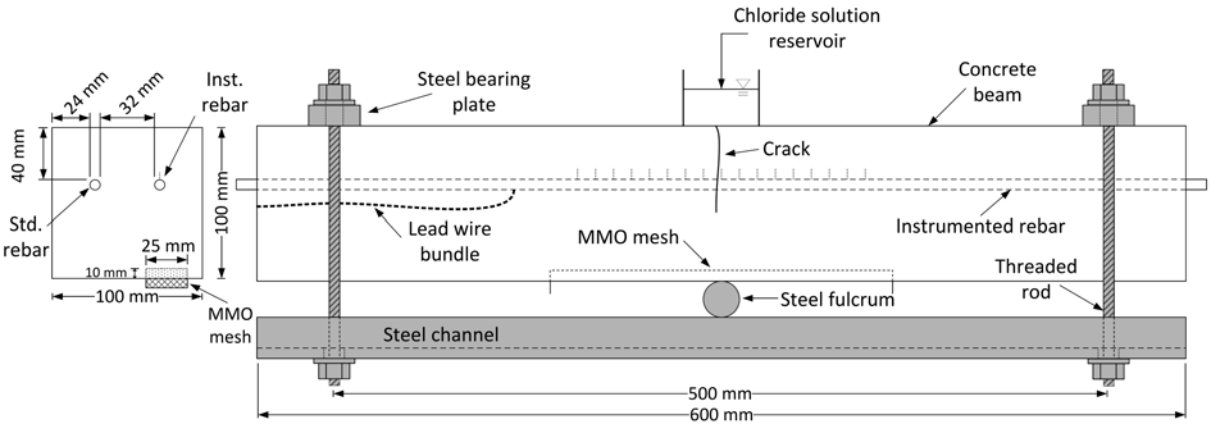

Figure 4.16 *Beam specimen design including instrumented rebar, MMO-Ti mesh, and reservoir for chloride solution. Cracking frame is shown in gray.*

Table 4.6 *Loading conditions, average crack width as measured from the tension surface of the concrete, and exposure durations for all beams.*

Beam I.D. —	Mid-Span Deflection mm	Avg. Crack Width mm	Exposure Duration days
0*	2	0.4	—
1	2	0.4	62
2	2	0.3	35
3	3	0.6	14
4	3	0.7	62
5	4	0.9	35
6	5	1.2	62

* Beam 0 used for fluorescent epoxy impregnation

Prior to application of mechanical load, the sides of the specimens (i.e., not the compression and tension surfaces) were sealed using silicon caulk. This was completed prior to loading as to not seal the induced crack(s). The hardened silicon did not rupture during loading of the beam specimens. After loading, a plastic ponding dike (40x80 mm^2) was placed over the crack and the tensile surface outside the ponding area was sealed with silicon caulk. In cases where multiple cracks occurred only the crack directly over the steel fulcrum (Figure 4.16) was ponded. The compression surface was left unsealed. The ponding dike was then filled with a 10% chloride solution by weight (using NaCl). The ponding dike was refilled as necessary during testing.

4.2.4 Assessment of cracking behavior

To compare the cracking behavior of the concrete surrounding the instrumented rebar, epoxy impregnated plane and serial sections were investigated using Beam 0, a 2 mm MSD beam. Beam 0 was used as part of an trial investigation presented in [*Hansen*, 2009]. The corrosion data from Beam 0 is not presented here due to an error, which was corrected through the trial investigation. The impregnated beam was kept loaded in a cracking frame during the impregnation process described below.

To impregnate the cracked beam the crack was rinsed with deionized water multiple times to minimize crystallization of NaCl, which may impede the flow of epoxy. The specimen was allowed to dry for 7 days at 20°C ±1°C and 50% ±2% relative humidity. The beam compression surface was coated using a thick layer (∼5 mm) of silicon to seal the specimen (needed to draw a vacuum). A 5 mm thick cylindrical acrylic vacuum chamber with an inner diameter of 85 mm was placed over the crack. Channel-shaped rubber gaskets coated with vacuum grease placed on each end of the acrylic chamber provided an adequate seal. The chamber was then evacuated to a pressure of 10 mBar and fluorescent epoxy was impregnated as described in accordance with the procedures in [*DSF 423.39*, 1998; *Laugesen*, 2005]. After 24 hours the epoxy hardened and the specimen was removed from the cracking frame and sectioned using a wet saw as shown in Figure 4.17. The transverse and parallel sections were used to compare the cracking behavior of the concrete immediately surrounding the instrumented and standard rebars. The location of transverse and parallel sections discussed in Section 4.3.1 are indicated in Figure 4.17. Additional details on the epoxy impregnation process can be found in Section 2.2.4 of this thesis and in [*Laugesen*, 2005].

4.2.5 Corrosion testing

The OCP of each sensor was measured versus a standard calomel electrode (SCE) placed in the pond and versus the embedded MMO-Ti mesh. OCP of the MMO-Ti mesh was also measured against the SCE. OCP measurements were adjusted to the standard hydrogen electron (SHE) using an offset of 244 mV (values range from 240 mV to 245 mV in the literature [*Elsener et al.*, 2003; *Bardal*, 2004; *Myrdal*, 2007; *Küter*, 2009]).

Potential measurements were recorded every 2 hours by a LabVIEW controlled corrosion measurement system which is described in [*Küter*, 2009; *Küter et al.*, 2010]. The system

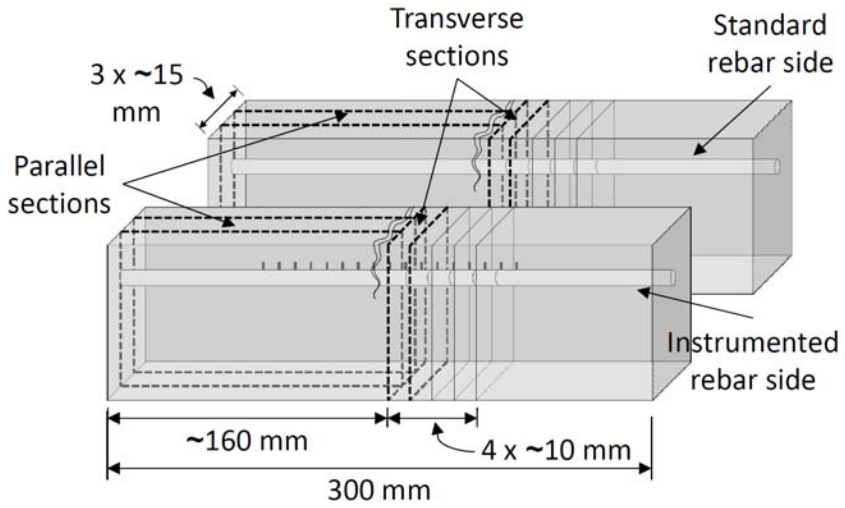

Figure 4.17 *Locations of the parallel and transverse epoxy impregnated sections. 150 mm was removed from each end of the beam prior to cutting sections.*

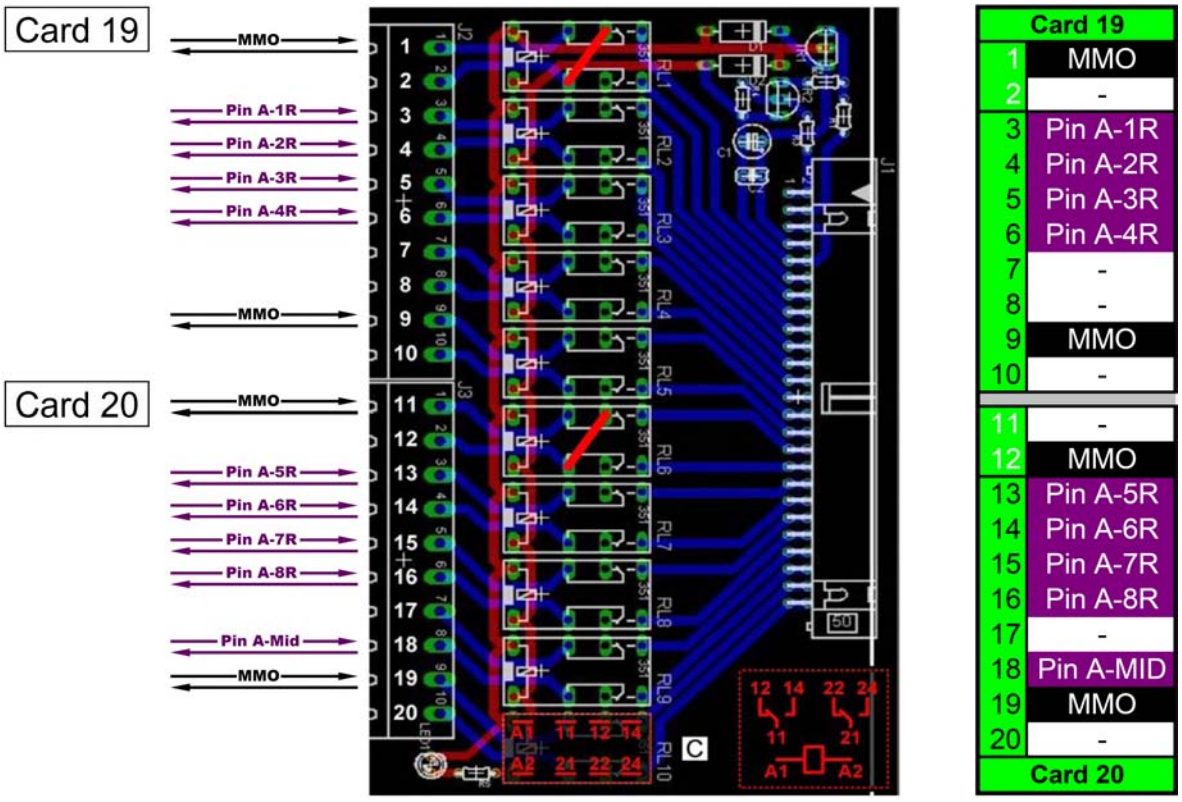

(a) (b)

Figure 4.18 *(a) Schematic of the printed circuit board which consists of two switch cards, Cards 19 and 20, with connections being made to the indicated electrodes. (b) The wiring diagram for Cards 19 and 20.*

utilizes specially designed printed circuit boards to cluster up to 8 electrodes and connect them to a to a reference electrode simultaneously. This minimizes the required number of data acquisition channels. Figure 4.18(a) illustrates the printed circuit board, which consisted of two 'switch cards.' Cards 19 and 20 are shown in the figure. Lead wires from the various electrodes (sensor pins in the instrumented rebar and MMO-Ti mesh) are connected to the switch card. It should be noted that connections 2 and 12 (Figure 4.18), used to measure corrosion current, were not used in this initial investigation. Figure 4.18(b) shows the corresponding wiring diagram for switch cards 19 and 20. Figure 4.19(a) shows wiring diagrams for all cards used for measurements and as seen a total of 6 cards were required to record data from three beams at the same time. Figure 4.19(b) identifies the location of each sensors in relation to the crack.

OCP measurements are conducted in sweeps wherein an electrical connection is initially established between a switch card and a reference electrode. After establishing the electrical connection a delay period is set in the program (2 minutes) at which time the corrosion potential of the sensors is measured and recorded. The program automatically switches to the next card, establishes an electrical connection between the card and the reference electrode material, measures and records the corrosion potential of the sensors. Additional information on the measurement system and modifications made to the system for this testing is available in [*Küter*, 2009; *Küter et al.*, 2010] and [*Hansen*, 2009], respectively.

At the conclusion of corrosion measurements the concrete covering the standard and instrumented rebar was removed from the side of the beam for inspection of the concrete and rebars. To facilitate this, 25 mm deep notches were cut above and below the rebars (standard and instrumented) and the concrete was removed by chisel and hammer. Silver nitrate, $AgNO_3$, and Rainbow Indicator were sprayed on opposite exposed surfaces to assess the ingress behavior of chloride ions and change in pH, respectively. Rainbow Indicator is an aqueous pH indicator that changes color based on the pH range of concrete pore solution [*Campbell et al.*, 1991; *Instruments*]. As shown in Figure 4.20 pH ranges include 5 to 7, 7 to 9, 9 to 11, and 11 to 13. Inspection of the rebars included removing the steel pins from selected sensors to assess the corrosion behavior and assessment of corrosion of the standard rebar.

4.3 Results and discussion

4.3.1 Performance of instrumented rebar

Three potential problems with the instrumented rebar were investigated: 1) change in mechanical behavior in the rebar due to the hollow sections and sensor pin holes, 2) the cracking behavior of the concrete immediately surrounding the instrumented rebar, and 3) the corrosion behavior of the sensors. Basic structural analysis on the impact of hollowing the instrumented rebar and microscopic observations concerning impact of stress concentrations caused by sensor pin holes in the instrumented rebar are discussed in Section 4.3.1. Fluorescent epoxy impregnated cracks in the concrete immediately surrounding

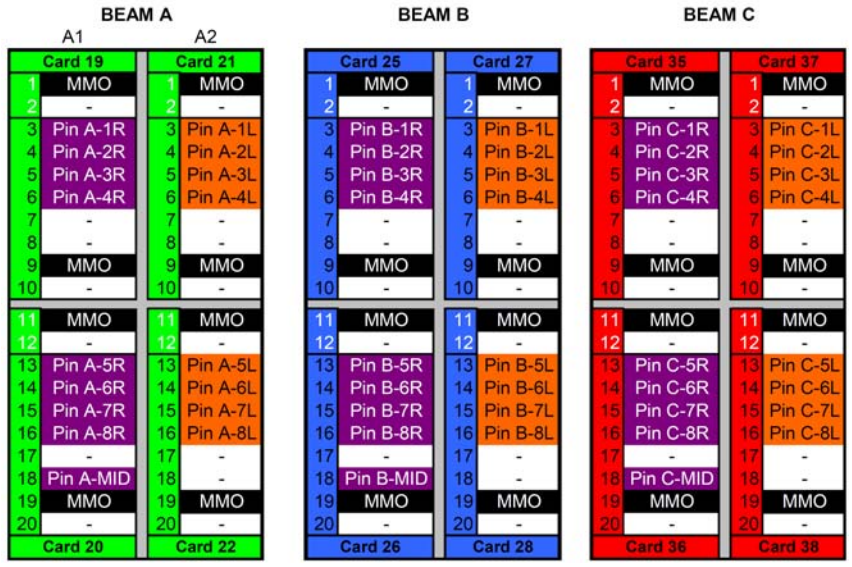

(a)

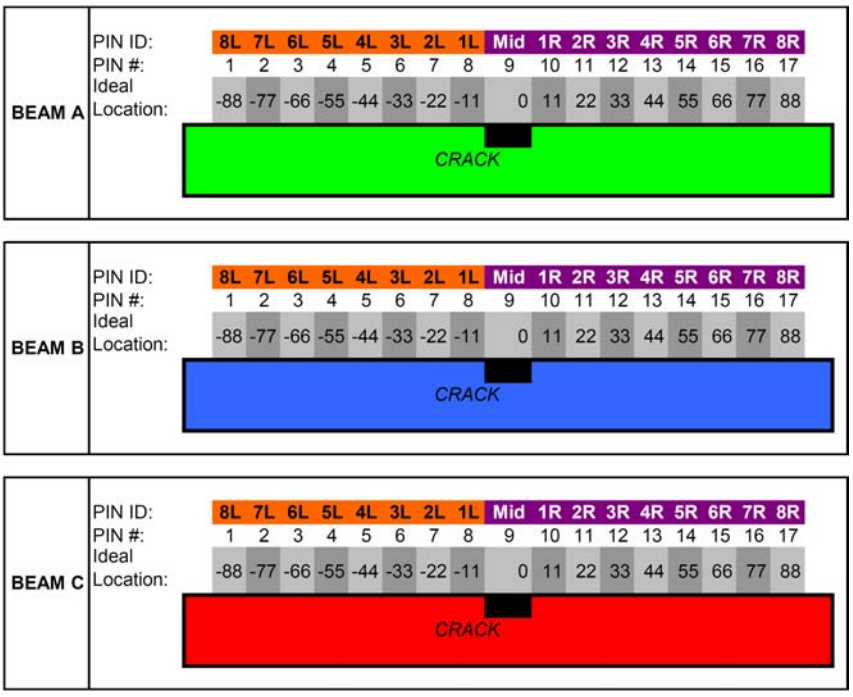

(b)

Figure 4.19 *(a) Wiring diagrams for all cards used for corrosion testing. (b) The location of sensors are indicated with the Pin ID corresponding to that shown in (a) for Beams A, B, and C.*

Figure 4.20 *Color variations indicated by Rainbow Indicator as a function of pH, from [Instruments].*

the instrumented and standard rebars are compared using the parallel and transverse sections in Section 4.3.1. The individual sensors consist of a steel pin sealed partly using glue-coated heat-shrink tube which creates a potential site of crevice corrosion. Upon completion of corrosion testing of each beam, randomly selected pins were removed to check for crevice corrosion as discussed in Section 4.3.1.

Mechanical behavior of hollow rebar with holes

Hollowing of the instrumented rebar results in a 2.56% reduction in bending stiffness (i.e., $E \cdot I$) and a 16% reduction in cross-sectional area of the rebar (using nominal diameter, 10 mm and considering the 4 mm diameter bore is centered). The axial stiffness (i.e., $E \cdot A$) of the instrumented rebar is equivalent to a standard rebar with a 9.17 mm nominal diameter.

Stresses are known to concentrate at holes in steel, which can modify deformation and failure. However, visual and microscopic inspections of all instrumented rebar and sensor holes indicated no excessive deformations or diameter reductions due to yielding or rupture of the steel occurred.

Comparison of cracking behavior

Parallel and transverse sections from the instrumented and standard rebar sides of the impregnated beam are shown in Figure 4.21 and 4.22, respectively. Images were taken under ultraviolet light, causing the fluorescent epoxy to glow. Similar primary cracks (indicated by [A] in Figure 4.21) were seen from both sides of the beam. Once the primary crack (i.e., crack perpendicular to rebar) intersects the rebars additional tensile stresses are developed in the steel, which induce slip and separation between the concrete-steel interface and subsequent cracking in the concrete [*Pease et al.*, 2006; *Spangenberg*, 2009]. This damage is particularly visible at the concrete-rebar interface above both the instrumented [B] and standard [C] rebars (i.e., tension surface of beam). Figure 4.22, discussed below, provides additional details on cracking in the concrete and slip and separation at the concrete-steel interface. The primary crack continued, beyond the rebar [D], deeper towards the compression side of the beam on the instrumented rebar side. This is possibly caused by the reduced cross-sectional area of steel in the instrumented rebar; however, intrinsic variations of the material may explain this behavior. For example, the crack length in impregnated WST specimens presented in Chapter 2 also varied through the specimen thickness. Direct comparison of cracking behaviors in Figure 4.21 is hindered as the standard rebar [C] was not sliced directly in the middle, however less damage appeared to occur in the concrete neighboring the instrumented rebar [B]. Transverse sections in Figure 4.22 provide additional comparison of the cracking behavior.

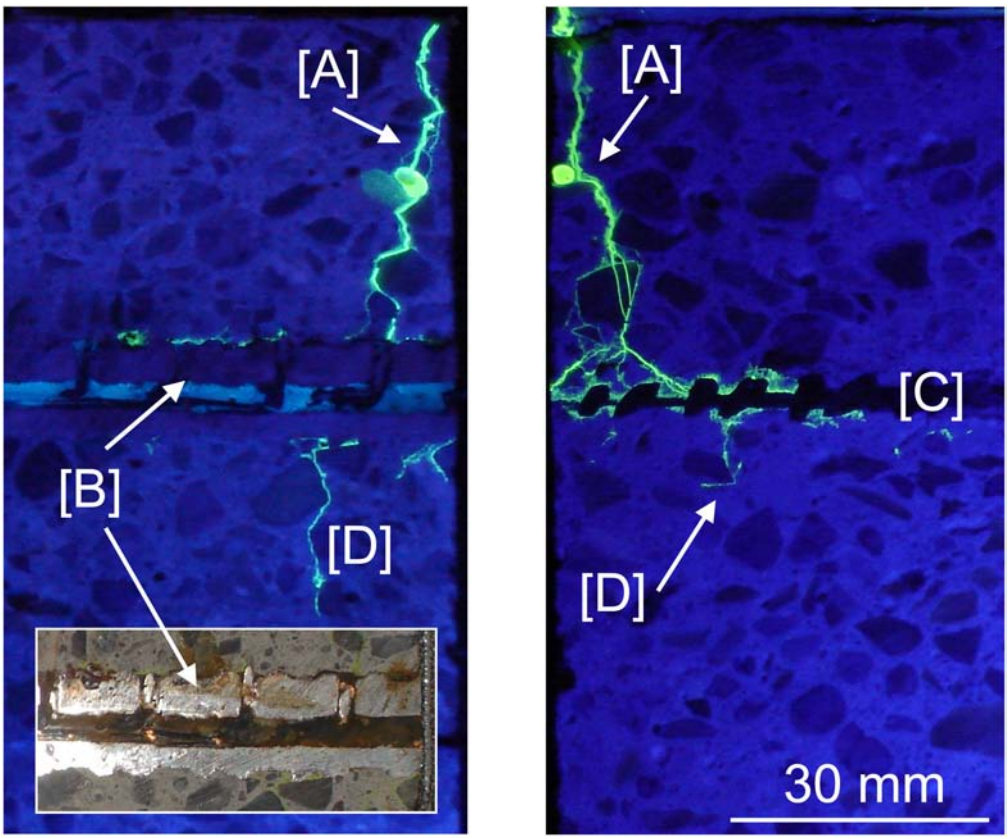

(a) (b)

Figure 4.21 *Parallel sections showing the (a) instrumented rebar and (b) standard rebar, with the following details indicated [A] - primary crack, [B] - instrumented rebar, [C] - standard rebar, and [D] - reflected cracking. The top of the image was the tension surface of the beam. (Author's photos)*

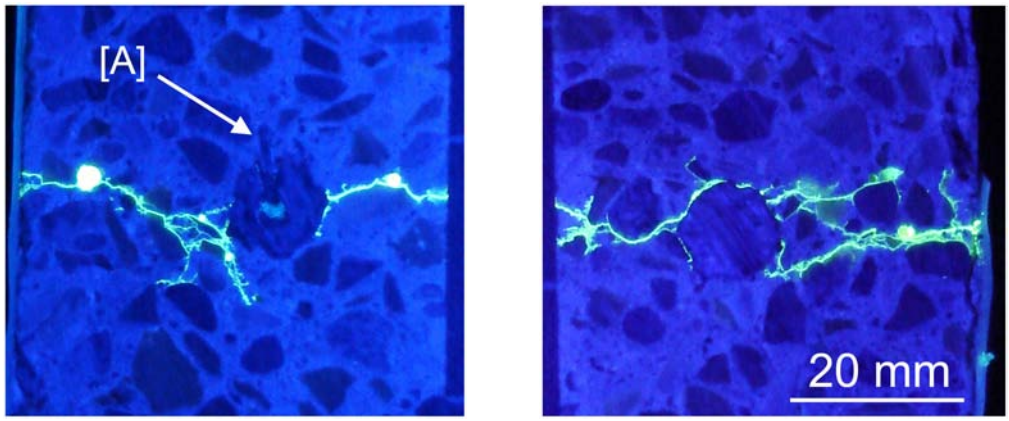

(a) (b)

Figure 4.22 *Transverse sections from the (a) instrumented rebar and (b) standard rebar. Sections were located ∼5 mm from primary crack. [A] indicates the location of a sensor. (Author's photos)*

Figure 4.22 show cracks extend radially from both rebars to the outer sides of the beams. The radial cracks separate the compressive and tension sides of the beam. Observation from additional transverse sections (see Figure 4.17) showed epoxy impregnation of radial cracks terminated between 36 and 44 mm from the primary crack along both rebars. On the standard rebar side (Figure 4.22(b)), separation at the concrete-steel interface is seen on the tension side. As indicated by [A] in Figure 4.22(a) the sensor extends from the instrumented rebar into the concrete, reducing interfacial separation. For future investigations, it is recommended to place the sensors flush with the reinforcement surface to eliminate this effect on interfacial separation.

It should be noted that in other investigations slip and separation between the reinforcement and concrete did not occur [*Win et al.*, 2004]; however, as discussed in Section 4.1.4 damage at the interface is dependant on load level, cover thickness, and material properties.

Corrosion of sensors

Figure 4.23(a) shows a typical sensor (from Beam 2) after corrosion testing, still inside the instrumented rebar. In Figure 4.23(b) the pin was partially removed to expose the portion of the pin which was inside the instrumented rebar. The broken line indicates a significant cross-sectional reduction in the portion of the sensor which was embedded in the concrete; however, cross-sectional reduction is not apparent from inside the glue-coated heat-shrink tube. Crevice corrosion was not observed on the sensors.

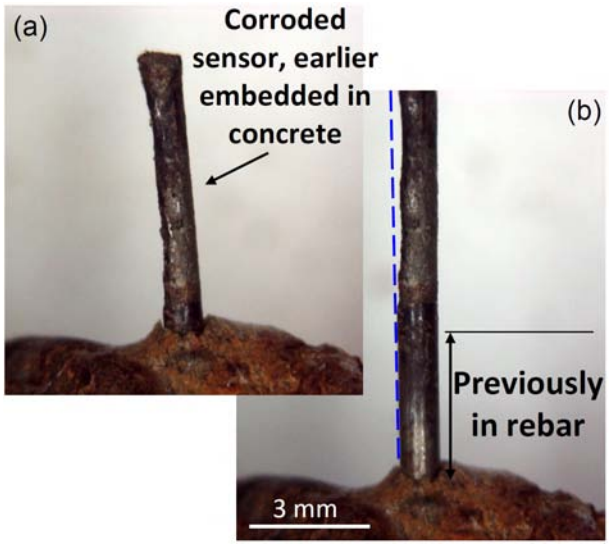

Figure 4.23 *(a) An individual sensor pin from Beam 1 after corrosion testing. (b) The sensor pin was partially removed to check for corrosion inside the instrumented rebar. (Author's photos)*

4.3.2 Influence of cracking on reinforcement corrosion

Ingress of chloride ions

Chloride ions ingress, as indicated by $AgNO_3$, occurred through the primary crack on the tension side of the beam. Chloride ions reached the level of the MMO-Ti mesh in all beams during corrosion testing, causing variable moisture and chloride conditions at the MMO-Ti mesh surface. After chloride ions penetrated through the primary crack the chloride ions penetrated along the reinforcement, likely due to the interfacial separation and radial cracking shown in Figures 4.21 and 4.22. Maximum lengths of lateral ingress for all beams are listed in Table 4.7.

Open circuit corrosion potential measurements

Figure 4.24 shows OCP's of the embedded MMO-Ti mesh during the exposure time of Beam 3. As shown in the figure, the OCP of MMO-Ti mesh embedded in concrete was stable under the varying chloride contents indicated in section 4.3.2. The average OCP of the MMO-Ti mesh embedded in all beams was 183 mV_{SHE} with maximum fluctuations of ± 22 mV_{SHE}. Based on these measurements, the MMO-Ti mesh is considered suitable for use as a second reference electrode. Similar OCP's were measured when using the SCE and MMO-Ti mesh as the reference electrode, as shown for the selected sensors in Figure 4.24. It should be noted that, while the MMO-Ti mesh potential remained stable and correlated well with previous measurements in cementitious materials (180 $mV_{SHE} \pm \sim 22$ mV_{SHE} in mortar [*Küter*, 2009]), a pH dependency has been observed [*Castro et al.*, 1996]. The pH of the concrete neighboring the reinforcement ranged between 11-13, as indicated by Rainbow Indicator [*Campbell et al.*, 1991; *Instruments*] (Figure 4.20), after testing as shown in Figure 4.25. The deformations from the reinforcement are clearly seen

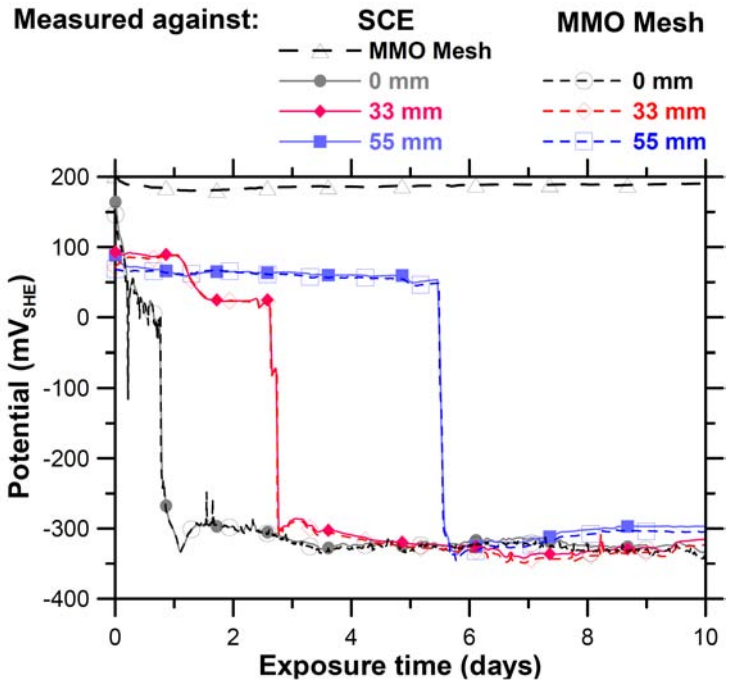

Figure 4.24 *OCP measurements of the MMO-Ti mesh and selected sensors in the instrumented rebar from Beam 3. OCP of the sensors were taken against both the SCE (solid lines) or MMO-Ti mesh (broken lines). Sensors are identified by their distance from the primary crack.*

in the concrete with purple and blue coloration. The red color, seen at the mid-span and the inset zoomed image, is corrosion product.

Figure 4.24 also shows typical OCP measurements of sensors in the instrumented rebars using both the SCE and MMO-Ti mesh as the reference electrodes. As can be seen, the OCP's all undergo a rapid drop, but at varying times. This rapid drop likely corresponds to a change in the thermodynamically favored corrosion state (i.e., passive to active) of the individual sensors. An OCP drop of -200 mV_{SHE} or larger typically indicates active corrosion [*Küter*, 2009]. While this value may be up to debate [*Elsener et al.*, 2003], corrosion was observed on 80% of sensors with a potential drop in excess of -200 mV_{SHE}. Gradual changes in OCP of sensors are likely due to variations in the concrete resistivity and local chloride/moisture contents. The average difference between OCP measurements taken from the SCE and MMO-Ti mesh was 5.0 mV_{SHE}.

Location dependencies of the OCP measurements are more clearly illustrated by contour maps showing exposure time on the y-axis, sensor location with respect to the crack on the x-axis and OCP indicated by the color scale (Figures 4.26 and 4.27). Ordinary linear kringing interpolation was used to estimate the OCP between measurement locations. Location information on the x-axis is shifted based on the actual location of the sensors relative to the primary crack as measured after removal of the concrete cover. A shift in the contour color from blue to red corresponds to the -200 mV_{SHE} isoline indicates

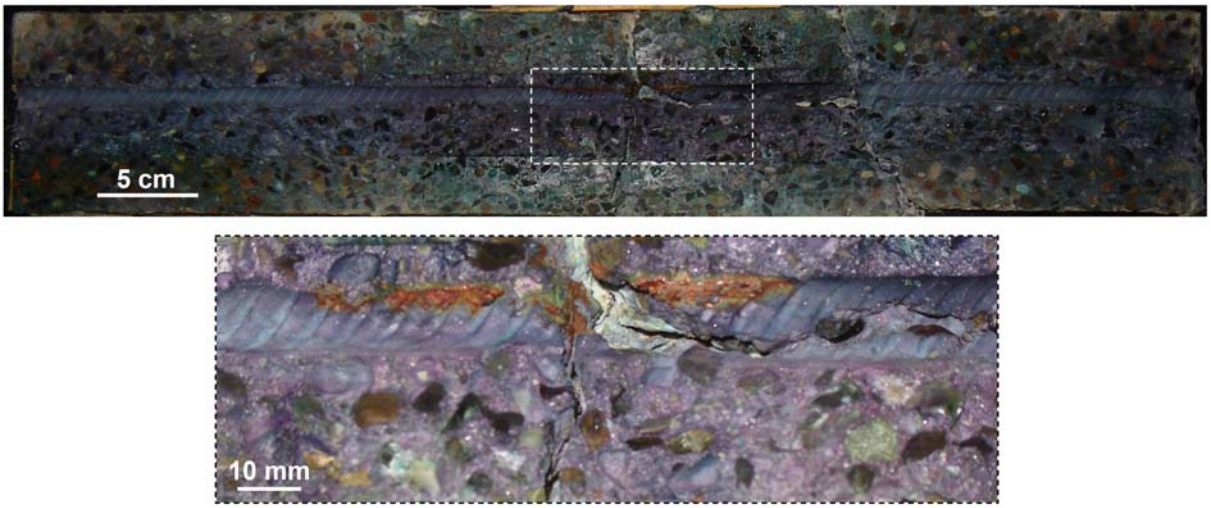

Figure 4.25 *Beam 4 with Rainbow Indicator applied. (Author's photos)*

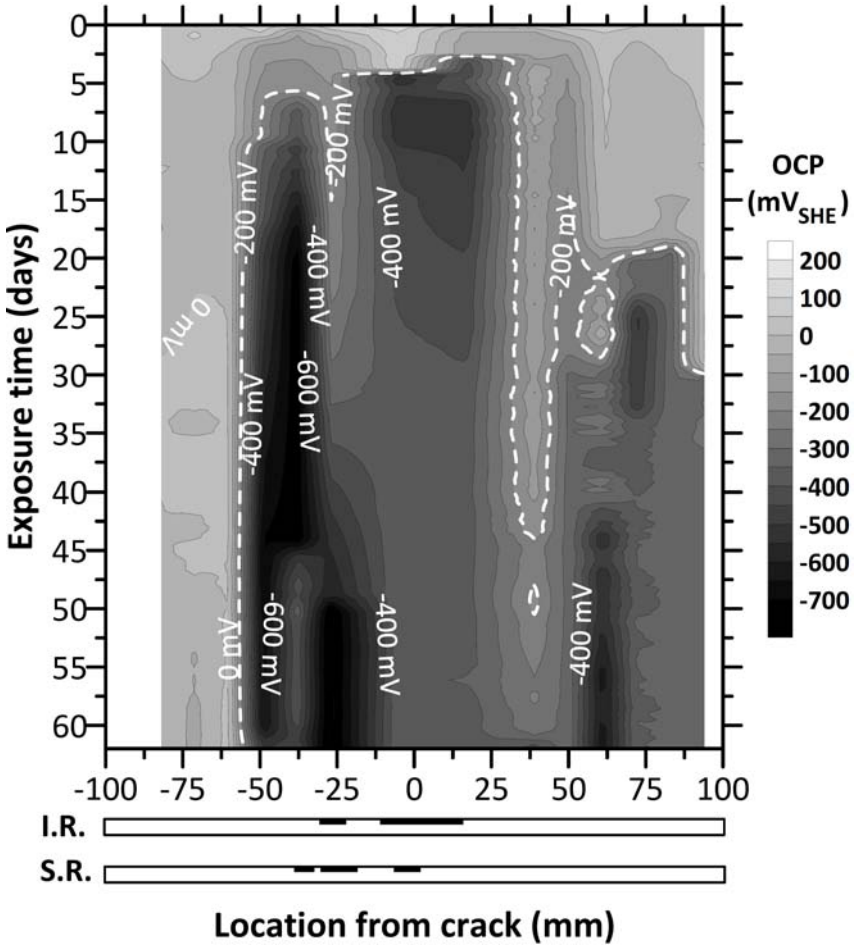

Figure 4.26 *Location and time dependent OCP of sensors in Beam 4 (0.7 mm crack width).*

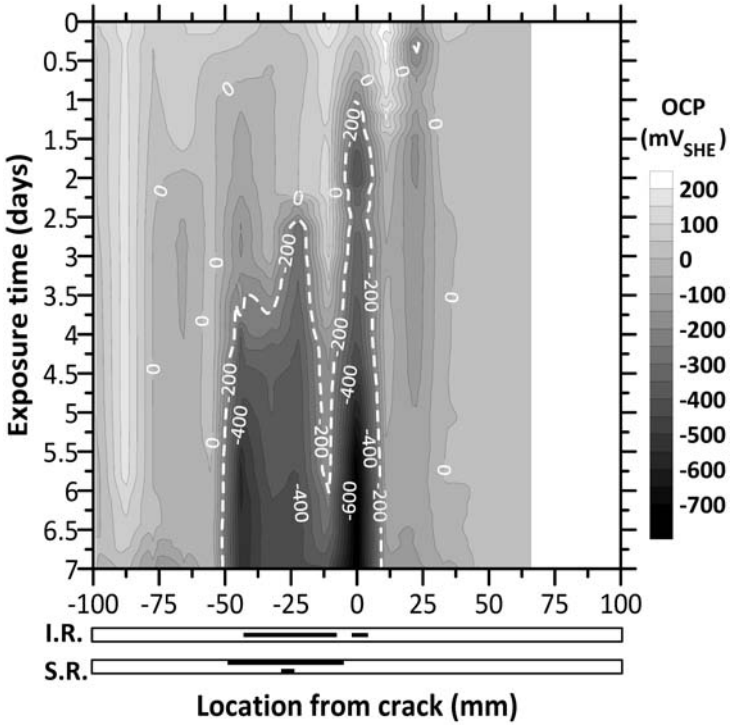

(a)

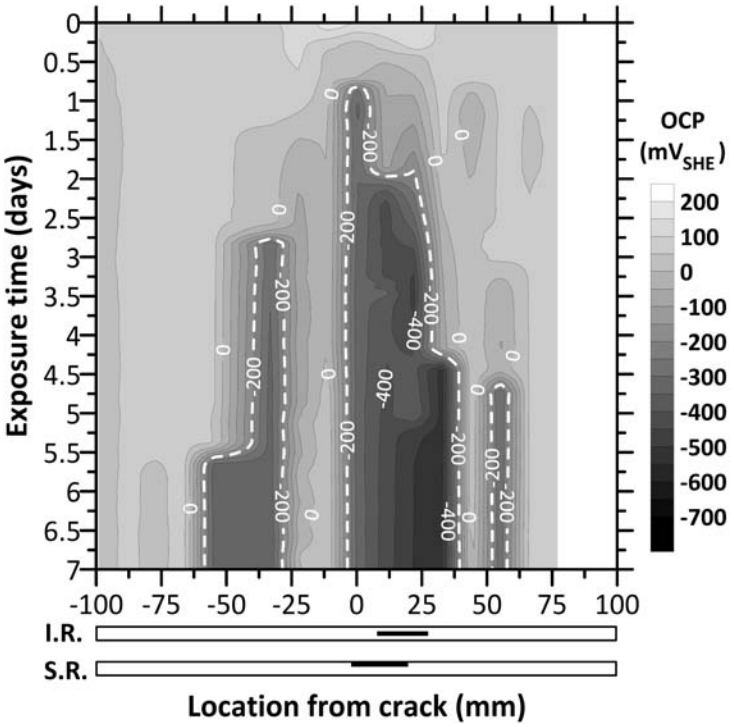

(b)

Figure 4.27 *Location and time dependent OCP of sensors in (a) Beam 1 (0.4 mm crack width) and (b) Beam 3 (0.6 mm crack width) during the first 7 days of exposure.*

where and when active corrosion becomes thermodynamically favored. Figure 4.26, which depicts the complete duration of Beam 4 testing, shows a typical measurement from a complete instrumented rebar. Initially, the OCP across the instrumented rebar has values between ∼0 to 200 mV_{SHE} with a distinctly higher OCP near the location of the crack. This might be explained by an initially higher oxygen content in the crack region. Drop in OCP below -200 mV_{SHE} tends to occur earliest nearby the primary crack, followed by more distant (from the primary crack) sensors. Table 4.7 lists the total length along the instrumented rebars where OCP dropped below -200 mV_{SHE} at the end of corrosion testing.

Figure 4.26 shows that at approximately 40 mm from the primary crack the drop in OCP takes significantly longer to occur than neighboring regions (both closer to and farther from the primary crack). Additionally, the OCP did not drop during testing for sensor below approximately -60 mm from crack for Beam 4. Similar behavior (i.e., delayed or no OCP drop at various locations) occurred in all beams and is likely attributable to the variations in the cracking behavior described in section 4.3.1.

Figures 4.27(a) and (b) illustrate the effect of varying crack width during the first 7 days of exposure for Beam 1 and 3, with 0.4 mm and 0.6 mm crack widths, respectively. In both cases, the -200 mV_{SHE} isoline initially appears at the location of the crack and extends further away from the crack location with increased time. The -200 mV_{SHE} isoline increases in length along the instrumented rebar for Beam 3 more rapidly than from Beam 1. After 7 days the isoline in Beam 3 reached a total length of approximately 77.5 mm, while Beam 1 reached a total length of 60 mm.

Figure 4.28 shows the OCP for all beams during the first 7 days of exposure to the chloride solution.

Visual observations of corrosion on rebars

Figure 4.29 shows the corrosion product immediately after the concrete cover was removed. A green colored corrosion product was seen for all beams at both the standard (Figure 4.29(a)) and instrumented rebars (Figure 4.29(b)). After a short period of time (approximately 30 minutes or once dried) the green product changed to black and after longer periods of time (approximately 24 hours) the black corrosion product was replace by typical 'red rust.'

Figure 4.30(a) and (b) show examples of the typical cross-sectional losses due to corrosion of the standard rebars. Multiple locations of pitting corrosion were seen for Beams 1 and 2 (2 mm mid-span deflection). Wider areas of corrosion were seen on standard rebars from Beams 3-6. Figure 4.30(a) shows a relatively deep corrosion pit in the standard reinforcement from Beam 2. Figure 4.30(b) shows corrosion took place over a wider area on the standard rebar from Beam 6. Deep corrosion pits were also observed on the instrumented rebars in Beams 1 and 2, with wider areas of corrosion seen on the instrumented rebars from Beams 3-6. Corrosion was observed on the tension-facing surface (i.e., steel surface facing beam's tension surface) of all standard rebars. One corrosion pit was found

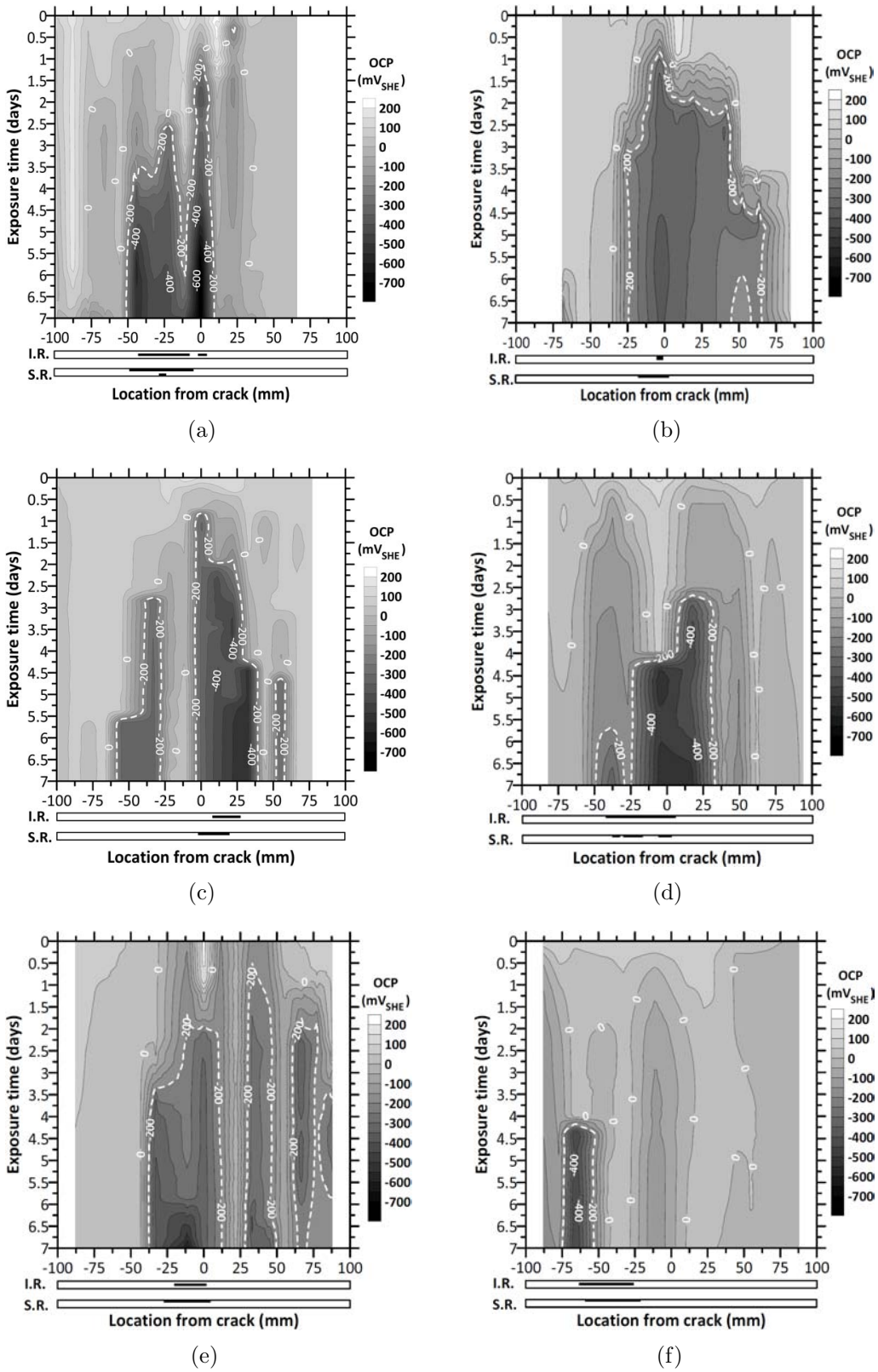

Figure 4.28 *Location and time dependent OCP of sensors in (a) Beam 1 (0.4 mm crack width), (b) Beam 2 (0.3 mm crack width), (c) Beam 3 (0.6 mm crack width), (d) Beam 4 (0.7 mm crack width), (e) Beam 5 (0.9 mm crack width), and (f) Beam 6 (1.2 mm crack width).*

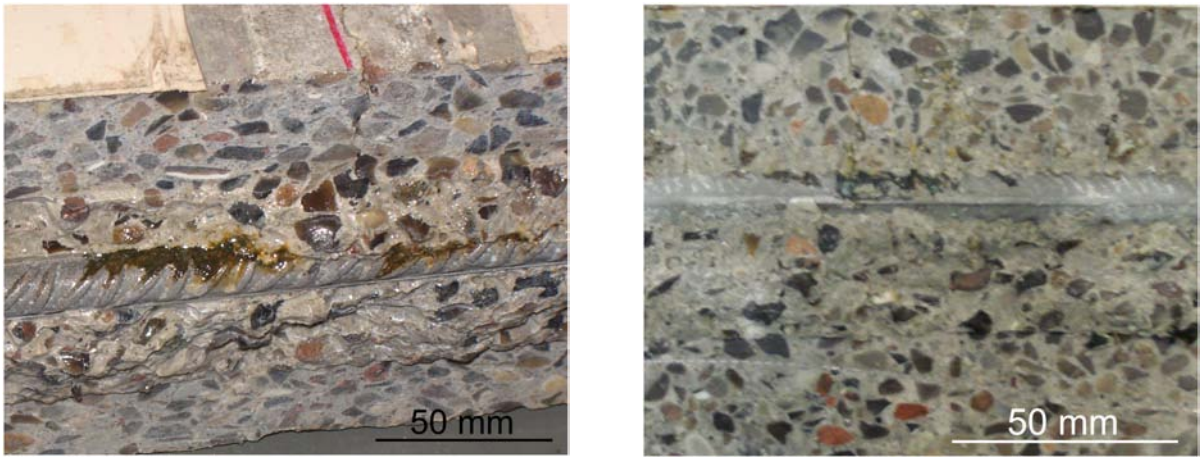

(a) (b)

Figure 4.29 *Images of corrosion product immediately after removal of cover concrete from (a) Beam 1, standard rebar and (b) Beam 6, instrumented rebar. (Author's photos)*

on the compression-facing surface of the standard rebar in Beam 1. Corrosion of the instrumented rebars was observed for Beams 1-3, 5-6 on the side surface of the rebars (i.e. steel surface towards side faces of beam). The total length, number, and location of anodic regions are listed in Table 4.7 for all beams.

Figures 4.26, 4.27(a), (b), and 4.28(a)-(f) compare the locations of anodes on both rebars to the measured OCP from the instrumented rebar. In some cases individual anode sites overlapped along the rebar length. For example, Beam 1 had 7 separate anode sites on the tension-facing surface of the standard rebar; however, all anodes overlapped giving the appearance of a singe anode in the sketch in Fig. 4.27(a). All anode sites were observed in regions where active corrosion was thermodynamically favored within the first week of exposure to chloride contaminated solution according to OCP measurements. As seen in Figure 4.28, similar results were seen for all beams.

During destructive removal of the rebars, corrosion products were seen on the surfaces of the reinforcement and the adjacent concrete. Corrosion products at a critical level can induce further cracking of the concrete [*Alonso et al.*, 1998], which could affect the OCP measurements of the sensors. However, the amount of corrosion product seen was unlikely to cause corrosion-induced cracking as the load-induced cracks likely provided ample space to accommodate the corrosion product. Additional time (and corrosion products) could result in corrosion-induced cracking for longer term testing utilizing the instrumented rebar.

4.3.3 Assessment of instrumented rebar and comparison of results

Results in section 4.3.1 indicated the instrumented rebar is capable of carrying loads and inducing similar cracking behaviors as standard rebars. The sensors from the instru-

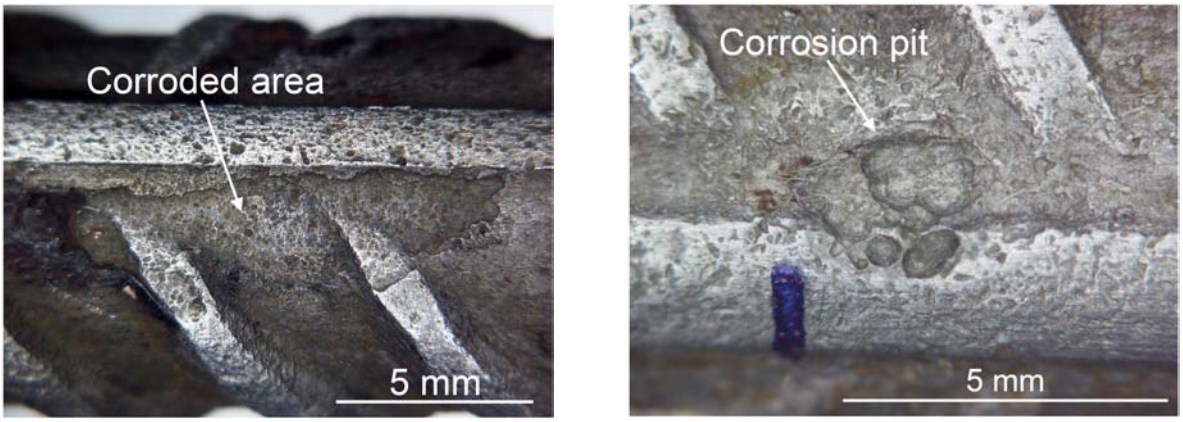

(a) (b)

Figure 4.30 *Images of corroding areas in the standard rebar from (a) Beam 2 (0.3 mm crack width) and (b) Beam 6 (1.2 mm crack width). (Author's photos)*

mented rebar, which protruded into the concrete, reduced slip, and separation to some extent.

Table 4.7 provides an overview of measurements including crack widths, lateral ingress of chloride ions, extent of length where active corrosion was thermodynamically favored at the end of testing (and after 7 days), and total length of the corroded regions for all beams. Lateral ingress of chloride ions increased with increasing exposure time and crack width. This is according to expectations as increased crack width causes increased slip and separation of the concrete-steel interface [*Pease et al.*, 2006; *Spangenberg*, 2009]; likely allowing for increased ingress along the rebar. The presence of defects or damage at the concrete-steel interface also decreases the critical chloride threshold required for initiation of active corrosion [Buenfeld et al, 2004; *Nygaard*, 2003; Nygaard and Geiker, 2005] and increases the likelihood of active corrosion [*Mohammed et al.*, 2002; *Yano et al.*, 2002]. Measurements of the OCP in Figures 4.27 and 4.28 indicated the length where the environmental conditions thermodynamically favor active corrosion (i.e., -200 mV_{SHE} isoline) typically increased more rapidly for beams with larger crack widths (and corresponding increased interfacial separation).

The extent of OCP drop after 7 days is given in parentheses in Table 4.7 under the 'extent of OCP drop' heading. Comparing the extent of OCP drop from Beams 1 and 2 after 7 days and the cracking behavior observed from Beam 0, all of which were loaded to 2 mm MSD resulting in similar average crack widths, indicate a direct relationship between damage at the concrete-steel interface and reinforcement corrosion may exist. The OCP drop extended 60 and 90 mm after 7 days for Beams 1 and 2, while the cracking was found to extend 36-44 mm in both directions from the primary crack (i.e., 72-88 mm in total). Further investigations are needed to verify the relationship between interface damage and risk/extent of reinforcement corrosion. Damage at the concrete-steel interface may therefore be an important factor influencing reinforcement corrosion (potentially a much more important factor than crack width). Rather than simply controlling surface

Table 4.7 *Overview of various measurement results, including lateral chloride ion ingress at the rebar, extent of OCP drop at termination of experiment (and at 7 days), extent and location of anodic regions (S.R. – standard rebar, I.R. – instrumented rebar).*

Crack width	Beam I.D.	Exposure duration	Max. length of Cl^- ingress	Length of OCP drop	S.R. Length of anode region	S.R. Location of anode*	I.R. Length of anode region	I.R. Location of anode*
—	mm	days	mm	mm	mm	—	mm	—
0.3	2	35	177	148† (90)	20.2 (2)‡	TS	3.9 (1)‡	TS & SS
0.4	1	62	310	113† (60)	44.3 (8)‡	7 TS & 1 CS	47.5 (3)‡	SS
0.6	3	14	235	115 (115)	22.2 (1)‡	TS	21.4 (1)‡	SS
0.7	4	62	323	151† (72)	41.0 (3)‡	TS	47.8 (4)‡	TS
0.9	5	35	281	187† (107)	32.1 (3)‡	TS	22.3 (1)‡	SS
1.2	6	62	367	113† (21)	38.3 (1)‡	TS	37.6 (1)‡	SS

* Locations of anodes: TS – rebar tension-facing surface, CS – rebar compression-facing surface, SS – rebar side-facing surface

† Extent of OCP drop reached a boundary of the instrumented rebar

‡ Number of corrosion sites

crack widths, which is the current norm [*AASHTO*, 2007; *ACI Committee 224*, 2001; EuroCode2, 2003], design considerations such as concrete cover depth and properties of the concrete and steel may be modified to optimize the corrosion resistance of reinforced concrete.

Comparing the lengths of chloride ion ingress and OCP drop, particularly Beam 3 where OCP drops did not exceed the measured length, indicated the critical chloride threshold required for active corrosion exceeded the threshold needed to cause the color change in $AgNO_3$ spraying. Comparison of the OCP measurements to the length of anodic regions on both the standard and instrumented rebar in Table 4.7 indicates the length where the local environmental conditions favor (thermodynamically) active corrosion is far greater than the area where actual active corrosion occurs. The presence of an anodic region on the surface of the rebar may protect other electrically connected regions of the rebar where active corrosion is thermodynamically favored due to the aggressivity of the environment. The instrumented rebar therefore only assess the thermodynamically favored corrosion state based on local environmental conditions, and is not able to consider the corrosion state of neighboring regions of the rebar.

As presented in Section 4.3.2, corrosion typically occurred at the tension surface of standard rebars (i.e. steel surface towards tension face of beam). For the instrumented rebars, however, corrosion occurred on the side surface in 5 of the 6 beams tested. Figure 4.22 showed interfacial separations occurred at the tension side of the standard rebar, but not the instrumented rebar. Instead only radial cracks, extending from the sides of the instrumented rebar, were observed. The lack of interfacial separation at the instrumented rebar provided additional protection against active corrosion, causing the tendency for corrosion to occur at the side surface. Therefore, it is concluded that in future investigations the sensors shall not protrude from the instrumented rebar, but shall be made flush to the rebar surface.

4.4 Summary and conclusions

This chapter provides a review of terms and principles related to corrosion and reinforcement corrosion. Special rebar configurations are presented and issues with the configurations are discussed. Various destructive and non-destructive measurement techniques are presented, including several special rebar configurations which have been developed to assess corrosion in cracked reinforced concrete. One major shortcoming of the special rebar configurations is a lack of information on the cracking behavior of the concrete surrounding the special configurations.

A study of the literature (Table 4.4) concludes that the probability of corrosion initiation increases with crack width. In addition, corrosion rate at initiation increases with crack width. Corrosion propagation is not so clearly related to crack width.

As part of the experimental investigations, an instrumented rebar was developed to assess corrosion as a function of the distance from a crack. Based on the limited preliminary investigation where cracked RC beams were ponded with a 10% chloride solution the following conclusions were made:

- Cracks in the concrete surrounding standard and instrumented rebars are largely similar in appearance; however, sensors protruding from the instrumented rebar appeared to reduce the separation between the steel and concrete. In future investigations, it is recommended to place the sensors flush to the rebar surface to avoid this affect. Crevice corrosion of the sensors was not found.

- Ruthenium/iridium mixed metal oxide activated titanium (MMO-Ti) embedded in concrete remained stable, indicating MMO-Ti may be used as an inexpensive reference electrode in concrete. Care should however be taken if large variations in pH are anticipated.

- For the investigated conditions, the length along the instrumented rebar where the local environment lead to thermodynamic favoring of active corrosion was significantly larger than the area where anodes formed on the standard rebars. Anodic regions on the standard rebar can protect electronically connected neighboring regions where the local environmental favors active corrosion. This is not considered by the instrumented rebar.

- For the investigated conditions, the open circuit potential of the sensors changes more rapidly with increased crack width, indicating a more rapid change in thermodynamic state. Corrosion of the standard rebar was found to occur in all beams. The length of the anode region did not relate to crack width; however, corrosion type varied based on crack width for this investigation. The 0.3 mm and 0.4 mm crack width specimens (Beams 1 and 2) exhibited pitting corrosion while larger crack widths (Beams 3-6 with crack widths of 0.6 to 1.2 mm) resulted in corrosion over a relatively larger area.

- Comparison of the cracking behavior and measurements from the instrumented rebar indicates that damage along the concrete-reinforcement interface may be related to an increased risk of corrosion initiation. While further work is needed to verify this relationship, interfacial damage is likely more important (and relevant) to reinforcement corrosion issues than the current practice of controlling surface crack width.

Chapter 5

Summary and conclusions

5.1 Summary

The purpose of this work was to complete an in depth investigate of the effect mechanical load-induced cracking has on the ingress and corrosion behaviors in reinforced concrete. To narrow the aim of the study it was decided to focus on partially saturated concrete. The work included extensive mechanical and moisture ingress testing of wedge splitting test specimens and a corrosion investigation utilizing an instrumented rebar developed through the project. Through the presented experimental efforts, the moisture ingress and corrosion behaviors have been linked to fracture properties and cracking behaviors.

5.2 Overview of findings and conclusions

Chapter 2 introduces fracture mechanics, applicability of fracture mechanics to concrete, the wedge splitting test method, and inverse analysis of the cracked hinge model completed to determine fracture parameters. Fracture parameters were documented for Mixtures 1 and 2 as determined by measuring the crack mouth opening displacement. However, fluorescent epoxy impregnation of wedge splitting test specimens indicated cracking occurred outside the region of assumed cracking in the cracked hinge model. Therefore, fracture parameters were also determined using photogrammetry, which provided a local measure of the crack opening displacement. Optimization and sensitivity analyses determined that a 3–slope cohesive laws, determined through inverse analysis of the cracked hinge model, provide the optimal number of degrees of freedom to accurately fit model curves to experimental data. The 3–slope cohesive laws were found to be repeatable and computation times were approximately 40 minutes. Investigation of the cracking behavior through plane and thin sections indicated cracks consisted of a coalesced and non-coalesced region, for Mixture 1. Comparison of the cracking behavior to results of the cracked hinge model indicated a crack coalesces after approximately 16.5 to 18.5 mm of crack length estimated by the cracked hinge model. Finally, plastic shims inserted into the notch of the wedge splitting test specimen were found to effectively reduce crack width recovery upon unloading cracked specimens. A cracked specimen with a 0.20 mm crack mouth opening displacement recovered 46% of the crack opening displacement at the edge of the notch, while the hard plastic shims reduced recovery to 9%.

Chapter 3 introduced the controlling transport mechanisms commonly associated with concrete and other cementitious materials. Literature on the effect cracking has on ingress behavior was reviewed, and experiments were described which investigated the effect of cracking on sorption in partially saturated concrete. Moisture and chloride ion ingress was measured by x-ray attenuation measurements and silver nitrate spraying, respectively. It was found that the use of an x-ray camera provides high resolution images of moisture ingress in concrete specimens. The images taken indicated moisture ingress proceeded rapidly through cracks and that a portion of the crack behaved as free surfaces for water sorption and chloride ion ingress. It was hypothesized that coalesced cracks likely behave as free surfaces for water sorption. Additionally, it was found that the ingress behavior of chloride ions was delayed compared to moisture ingress behavior. This delay was likely due to chloride binding and the effect NaCl has on solution surface tension and viscosity.

Chapter 4 introduces thermodynamics and kinetics of reinforcement corrosion, reviews previous research works on the impact concrete cracking has on reinforcement corrosion, and presents an experimental investigation utilizing an instrumented rebar. The instrumented rebar was designed to carry mechanical load, induce realistic cracks in the surrounding concrete, and to provide location-dependent measurements of the corrosivity of the local environment. For the investigated conditions, the length along the instrumented rebar where active corrosion was thermodynamically favored was significantly larger than the area where anodes formed in the standard rebars. Anodic regions 'protects' other regions where the risk of corrosion exists. Open circuit potential of the sensors in the instrumented rebar changes more rapidly with increased crack width, indicating a more rapid change in thermodynamic state. Corrosion of the standard rebar was found to occur in all beams. The length of the anode region did not relate to crack width, however corrosion type varied based on crack width. Smaller cracks (≤ 0.4 mm) resulted in relatively deep pitting corrosion while larger cracks resulted in less severe (i.e. deep) corrosion over a relatively larger area. Comparison of the cracking behavior and measurements from the instrumented rebar indicates that damage along the concrete-steel interface may be related to an increased the risk of corrosion initiation. Based on this work, it seems damage at the concrete-steel interface is likely more important (and relevant) to reinforcement corrosion issues than surface crack width.

The following two sections discuss the interaction and relationships between conclusions from the individual chapters of this thesis.

5.3 Importance of cracking on ingress, reinforcement corrosion, and service life

As discussed in Chapter 3, non-coalesced cracks appear to partially restrict the ingress of water and chloride ions. However, the resistance to ingress provided by non-coalesced cracks cause only relatively minor delays in the ingress of these aggressive substances (for partially saturated conditions) compared to a typical service life for a RC structure. For example, the coalesced crack from the Mixture 1 WST specimen loaded to peak load

reached an average depth of approximately 6.1 mm into the specimen; however, after only 6 hours the 75% ABS contour reached the bottom of the measurement area (37 mm below the notch bottom, see Figure 3.13(c)). Therefore, the resistance to water ingress (and based on Figure 3.25, chloride ion ingress) provided by the inhibiting cracks appears to be negligible when compared to a RC structure service lifetime. It should also be noted that the crack width at the crack edge for the peak load WST specimen, measured from a plane section, was approximately 0.02 mm. This crack opening correlates reasonably well with the estimated crack opening of 0.013 mm as shown in Figure 3.22(a). Both values are an order of magnitude lower than typical crack width restrictions [*ACI Committee 224*, 2001; *AASHTO*, 2007; EuroCode2, 2003]. Based on the results presented in Chapter 3, the presence of even minute cracks appear to significantly influence the ingress of moisture, chloride ions, and other aggressive substances. However, as discussed below, this accelerated ingress behavior may not directly affect reinforcement corrosion and service life of RC structures.

Chapter 4 and Papers II and IV indicate that when a transverse crack intersects reinforcement damage, including slip and separation, may occur at the concrete-steel interface (see Figures 4.10 and 4.21). Comparison of the cracking behavior and measurements from the instrumented rebar in Section 4.3.3 indicates that damage along the concrete-steel interface may be related to an increased risk of corrosion initiation. Previous work has also concluded that corrosion initiation is more likely to occur at gaps between the concrete and steel due to readily accessible supplies of oxygen, chloride ions and moisture [*Mohammed et al.*, 2002; *Yano et al.*, 2002; Buenfeld et al, 2004; *Nygaard*, 2003; Nygaard and Geiker, 2005]. While further work is needed to verify a relationship, interfacial damage is likely more important (and relevant) to reinforcement corrosion issues than the current practice of controlling surface crack width.

Based on this hypothesis, the author recommends future work on RC durability issues should focus on the determination of a relationship to estimate the extent of concrete-steel interfacial damage based on the controlling parameters which should include, but are not limited to, loading type (parallel or V-shaped cracks and static or dynamic load), concrete cover thickness, surface crack width, concrete materials properties, and reinforcement type (deformed or smooth bar). The extent of damage to the concrete-steel interface could therefore be designed by increasing cover thicknesses, reducing surface crack width, improving concrete properties, and/or changing the reinforcement type (smooth bars induce less damage [*Mohammed et al.*, 2001]). Furthermore, future studies should ascertain acceptance limits of concrete-steel interfacial damage to ensure a particular service life requirement.

5.4 Relating fracture properties to ingress and reinforcement corrosion behaviors

Chapter 2 provides a brief description of fracture mechanics, which simplify concrete's complex cracking behavior into a homogeneous fracture property – the cohesive law. The cohesive law, when implemented into a representative model (e.g., the cracked hinge

model), can accurately estimate the structural response and the crack profile of the material. However, details on the crack morphology (i.e., tortuosity, coalesced versus non-coalesced cracks, crack branching, microcracking, etc.) are lost in such estimates. Crack morphology has a major impact on ingress behavior, as shown by epoxy impregnation of cracked WST specimens. The crack networks were not completely impregnated though the crack mouth, indicating a portion of the crack was isolated. Moisture and chloride ingress experiments in Chapter 3 and Paper II verify the crack can partially resist ingress of these substances. Crack profiles, estimated by the cracked hinge model, can be subdivided into a coalesced and a non-coalesced portion, the latter of which had a relatively consistent length of 16.5 - 18.5 mm for Mixture 1. Therefore, results presented in this work indicate fracture mechanics/properties may be simply modified to estimate the length of a coalesced crack, which is a useful insight when considering ingress of moisture, etc.

While fracture modeling of RC was not completed as part of this work, experimental results highlighted potential links between cracking in RC, which is controlled by fracture mechanics, and reinforcement corrosion. First, the relationship between fracture properties and ingress discussed above can be directly related to reinforcement corrosion if the penetrating substance affects the thermodynamic state of the reinforcement. In addition, based on results in Chapter 4 and Paper IV, damage along the concrete-steel interface is related to the risk, extent, and location of reinforcement corrosion initiation. As concluded in Chapter 4, damage at the concrete-steel interface is likely more important than surface crack width. Therefore, relating fracture mechanics/properties of concrete and the concrete-steel interface may be a significant improvement to current durability design approaches for cracked RC. Specifically, an analytical model relating fracture mechanics/properties, geometry, and loading to both the damage along the interface and the surface crack width would be a useful tool in the design of future RC structures.

Bibliography

AASHTO, LRFD Bridge design specifications, SI units, 4th edition, *Tech. rep.*, American Association of State Highway and Transportation Officials, Washington, D.C., USA, 2007.

ASTM G 59, Standard test method for conducting potentiodynamic polarization resistance measurements, 2009.

ASTM G 102-89, Standard practice for calculation of corrosion rates and related information from electrochemical measurements, 1999.

ACI Committee 224 (2001), ACI 224.2R-92: Cracking of concrete members in direct tension, American Concrete Institute, Farmington Hills, MI, USA

ACI Committee 224 (2001), ACI 224R-01: Control of cracking in concrete structures, American Concrete Institute, Farmington Hills, MI, USA

ACI Committee 318, Building code requirements for structural concrete (*ACI 318-02*) and commentary (*ACI 318R-02*), American Concrete Institute, Farmington Hills, MI, USA, 2008.

ACI Committee 446, Fracture mechanics of concrete: Concepts, models and determination of material properties, *ACI 446.1R-91*, American Concrete Institute, Farmington Hills, MI, USA, 1991 (Reapproved 1999).

Ahmad, S., Reinforcement corrosion in concrete structures, its monitoring and service life prediction A review, *Cement and Concrete Composites*, *25*(4-5), 459–471, 2003.

Ahmed, S. F. U., M. Maalej, and H. Mihashi, Cover cracking of reinforced concrete beam due to corrosion of steel, *ACI Materials Journal*, *104*(2), 153–161, 2007.

Akita, H., and T. Fujiwara, Water and salt movement within mortar partially submerged in salty water, in *Proc. of CONSEC 95*, E & FN Spon, Sapparo, Japan, 1995.

Aldea, C.-M., S. Shah, and A. Karr, Permeability of cracked concrete, *Materials and Structures*, *32*(219), 370–376, 1999.

Aldea, C.-M., M. Ghandehari, S. P. Shah, and A. Karr, Estimation of water flow through cracked concrete under load, *ACI Materials Journal*, *97*(5), 567–575, 2000.

Alonso, C., C. Andrade, J. Rodriguez, and J. M. Diez, Factors controlling cracking of concrete affected by reinforcement corrosion, *Materials and Structures*, *31*(211), 435–441, 1998

Anderson, T. L., *Fracture Mechanics: Fundamentals and Applications*, CRC Press, 2005.

Aramis, *Aramis v5.4 User Manual*, GOM Optical Measuring Techniques, 2005.

Arya, A., and F. Ofori-Darko, Influence of crack frequency on reinforcement corrosion in concrete, *Cement and Concrete Research*, *26*(3), 345–353, 1996.

Arya, C., and L. A. Wood, The relevance of cracking in concrete to corrosion of reinforcement, *Tech. Rep. 44*, The Concrete Society, Slough, U.K., 1995.

Arya, C., N. Buenfeld, and J. Newman, Factors influencing chloride-binding in concrete, *Cement and Concrete Research*, *20*(2), 291–300, 1990.

Baker, P. H., D. Bailly, M. Campbell, G. H. Galbraith, R. C. McLean, N. Poffa, and C. H. Sanders, The application of x-ray absorption to building moisture transport studies, *Measurement*, *40*(9-10), 951–959, 2007.

Bardal, E., *Corrosion and Protection*, Springer-Verlag, London, 2004.

Barenblatt, G. I., On equilibrium cracks, formed in brittle fracture, *Doklady, USSR Academy of Sciences*, *127*(1), 47–50, in Russian, 1959.

Bazant, Z. P., *Fracture Mechanics of Concrete: Structural Application and Numerical Calculation*, Chapter 1 - Mechanics of Fracture and Progressive Cracking in Concrete Structures, pp. 1–9, Martinus-Nijhoff, Doordrecht-Boston, 1985.

Bentz, D., M. Geiker, and K. Hansen, Shrinkage-reducing admixtures and early-age desiccation in cement pastes and mortars, *Cement and Concrete Research*, *31*(7), 1075–1085, 2001.

Bentz, D., Influence of shrinkage-reducing admixtures on the early-age properties of cement paste, *Presentation at the ACI Fall Convention, Denver, CO, USA*, 2006.

Berke, N., M. Dallaire, M. Hicks, and R. Hoopes, Corrosion of steel in cracked concrete, *Corrosion Engineering*, *49*(11), 934–943, 1993.

Birnin-Yauri, U., and F. Glasser, Friedel's salt, $Ca_2Al(OH)_6(Cl,OH)\cdot 2H_2O$: Its solid solutions and their role in chloride binding, *Cement and Concrete Research*, *28*(12), 1713–1723, 1998.

Breysse, D., and B. Gérard, Cracking of concrete relevance and effects, tightness of concrete with respect to fluids, *TCF State-of-the-Art Report TC-146*, RILEM, 1997.

Brooks, R. A., and G. D. Chiro, Beam hardening in x-ray reconstructive tomography, *Physics in Medicine and Biology*, *21*(3), 390–398, 1976.

Brühwiler, E., and F. H. Wittman, The wedge splitting test, a new method of performing stable fracture mechanics tests, *Engineering Fracture Mechanics*, *35*, 117–125, 1990.

Buenfeld N, Glass G, Reddy B, Viles F (2004) Process for the Protection of Reinforcement in Reinforced Concrete. United States Patent # 6685822, Alexandria, VA, USA

Buenfeld, N., M.-T. Shurafa-Daoudi, and I. McLoughlin, Chloride transport due to wick action in concrete, in *RILEM International workshop on chloride penetration into concrete*, France, 1995.

Campbell, D., R. Sturm, and S. Kosmatka, Detecting carbonation, *Concrete Technology Today*, *12*(1), 1–5, 1991.

Castel, A., T. Vidal, R. Francois, and G. Arliguie, Influence of steel - concrete interface quality on reinforcement corrosion induced by chlorides, *Magazine of Concrete Research*, *55*(2), 151–159, 2003.

Castro, P., A. Sagues, E. Moreno, L. Maldonado, and J. Genesca, Characterization of activated titanium solid reference electrodes for corrosion testing of steel in concrete, *Corrosion*, *52*(8), 609–617, 1996.

Chen, Q., M. K. Gingras, and B. J. Balcom, A magnetic resonance study of pore filling processes during spontaneous imbibition in berea sandstone, *Journal of Chemical Physics*, *119*(18), 9609, 2003.

Clear, C. A., Effects of autogenous healing upon the leakage of water through cracks in concrete., *Technical Report - Cement and Concrete Association*, 1985.

Concrete Society Report, *Non-structural cracks in concrete*, Technical Report No. 22, 3rd ed., 48 pp., Concrete Society, London, 1992.

Couch, J., and J. Weiss, Experimental techniques for calibrating and processing x-ray data examining moisture ingress into cementitious materials, *In Preparation*, 2009.

Crank, J., *The mathematics of diffusion*, 2nd ed., Clarendon Press, Oxford, UK, 1986.

Curry, T., J. Dowdey, and R. Murry, *Christensens Physics of Diagnostic Radiology*, 522 pp., Lea and Febiger, London, 1990.

Darcy, H., Experience and application principles to follow and formulas to be used in the question of the distribution of water, *Tech. rep.*, The Public Fountains of the City of Dijon, Dalmont, Paris, 1856.

De Schutter, G., Quantification of the influence of cracks in concrete structures on carbonation and chloride penetration, *Magazine of Concrete Research*, *51*(6), 427–435, 1999.

DS-2426, Concrete - Materials - Rules for application EN 206-1 in Denmark, *Tech. rep.*, Danish Standards Association, 2004.

DSF 423.39 Danish test method, Testing of concrete, Hardened concrete: Production of fluorescense impregnated plane sections, 1998.

DSF 423.40 Danish test method, Testing of concrete, Hardened concrete: Production of fluorescense impregnated thin sections, 1998.

Dugdale, D. S., Yielding of steel sheets containing slits, *Journal of the Mechanics and Physics of Solids*, *8*, 100–104, 1960.

DuraCrete, General guidelines for durability design and redesign, *Tech. Rep. Report BE95-1347/R15*, European Union, Luxembourg, part of the Brite-EuRam III Project BE95-1347 Probabilistic Performance based Durability Design of Concrete Structures, 109 pp., 2000.

Dyson, N., *X-rays in atomic and nuclear physics*, 244 pp., Longman Scientifc & Technical, London, 1973.

Edvardsen, C., Water permeability and autogenous healing of cracks in concrete, *ACI Materials Journal*, *96*(4), 448–454, 1999.

Ehlen, M. A., M. D. A. Thomas, and E. C. Bentz, Life-365 service life prediction model version 2.0 - widely used software helps assess uncertainties in concrete service life and life-cycle costs, *Concrete International - the Magazine of the American Concrete Institute*, *31*(5), 41, 2009.

Elsener, B., C. Andrade, J. Gulikers, R. Polder, and M. Raupach, Half-cell potential measurements - potential mapping on reinforced concrete structures, *Materials and Structures/Materiaux et Constructions*, *36*(261), 461–471, 2003.

Eurocode 2: Design of concrete structures, 2003.

fib Bulletin 34, Model code for service life design, *Tech. Rep. fib Bulletin 34*, International Federation for Structural Concrete (fib), Lausanne, Switzerland, 126 pp., 2006.

Fick, A. E., *Poggendorff's Annalen der Physik*, 1855.

Fidjestol, P., and N. Nilson, Field test of reinforcement corrosion in concrete, in *ACI SP-65*, pp. 205–217, 1980.

Francois, R., and G. Arliguie, Influence of service cracking on reinforcement steel corrosion, *Journal of Materials in Civil Engineering*, *10*(1), 14–20, 1998.

Francois, R., and G. Arliguie, Effect of microcracking and cracking on the development of corrosion in reinforced concrete members, *Magazine of Concrete Research*, *51*(2), 143–150, 1999.

Francois, R., A. Castel, T. Vidal, and N.-A. Vu, Long term corrosion behavior of reinforced concrete structures in chloride environment, *Journal de Physique IV*, *136*, 258–293, 2006.

Frederiksen, J., and E. Poulsen, Hetek: Chloride penetration into concrete - manual, *Tech. Rep. Report No. 123*, Road Directorate, Danish Ministry of Transport, 1997.

Gautefall, O., and O. Vennesland, Effects of cracks on the corrosion of embedded steel in silica-concrete compared to ordinary concrete., *Nordic Concrete Research*, (2), 17–28, 1983.

Geiker, M. R., and P. Laugesen, On the effect of laboratory conditioning and freeze/thaw exposure on moisture profiles in HPC, *Cement and Concrete Research*, *31*(12), 1831–1836, 2001.

Glass, G., and N. Buenfeld, The influence of chloride binding on the chloride induced corrosion risk in reinforced concrete, *Corrosion Science*, *42*(2), 329–344, 2000.

Glass, G., B. Reddy, and N. Buenfeld, The participation of bound chloride in passive film breakdown on steel in concrete, *Corrosion Science*, *42*(11), 2013–2021, 2000.

GNI X-ray Absorption Systems, www.gni.dk, Purdue University, 2006.

GNI X-ray Absorption Systems, www.gni.dk, Denmark, 2008 (year of hardware/software updating).

Goto, Y., Cracks formed in concrete around deformed tension bars, *Journal of the American Concrete Institute*, *68*(4), 244–251, 1971.

Greiner, U., and W. Ramm, Air leakage characteristics in cracked concrete, *Nuclear Engineering and Design*, *156*, 167–172, 1995.

Griffith, A. A., The phenomena of rupture and flow in solids, *Philosophical transactions of the Royal Society of London, Series A, Physical sciences and engineering*, *221*, 163–198, 1920.

Gummerson, R., C. Hall, W. Hoff, R. Hawkes, G. Holland, and W. Moore, Unsaturated water flow with porous materials observed by NMR imaging, *Nature*, *281*(5726), 56–57, 1979.

Hall, C., Water sorptivity of mortars and concretes: a review, *Magazine of Concrete Research*, *41*(147), 51–61, 1989.

Hall, C., W. D. Hoff, and M. Skeldon, The sorptivity of brick: dependence on the initial water content, *Journal of Physics D: Applied Physics*, *16*(10), 1875–1880, 1983.

Halvorsen, U., Korrosion och kalkurlakning vid spricker i betongkonstruktioner, *Tech. Rep. Bulletin 1*, Institutionen for byggnadsteknik, LTH, Lund, 1966.

Hansen, K., S. Jensen, L. Gerward, and K. Singh, Dual-energy x-ray absorptiometry for the simultaneous determination of density and moisture content in porous structural materials, in *Proceedings of the 5th Symposium on Building Physics in the Nordic Countries*, vol. 1, pp. 281–288, Gothenburg, Sweden, 1999.

Hansen, K. B., Corrosion initiation in cracked reinforced concrete, *Bachelor exam project*, Technical University of Denmark, Department of Civil Engineering, Kgs. Lyngby, Denmark, 2009.

Hartl, G., Dauerhaftigkeit von beton - chloridkorrosion, *Mitteilungen aus dem Forschungsinstitut des Vereins der österreichischen Zementfabrikanten*, *37*.

Hasegawa, M., M. Imano, T. Yamamoto, T. Kida, K. Kato, T. Kondo, M. Sudo, N. Kato, and M. Takano, Neutralization mechanism of concrete under repetitive contact of environmental water, *Theoretical and Applied Mechanics Japan*, *55*, 41–50, 2006.

Hasegawa, Y., S. Miyazato, and T. Oyamoto, Proposal for corrosion rate analytical model of reinforced concrete, in *29th Conference on Our World in Concrete & Structures*, pp. 281–288, Singapore, 2004.

Hillemeier, B., and H. Hilsdorf, Fracture mechanics studies on concrete compounds, *Cement and Concrete Research*, *7*(5), 523–535, 1977.

Hillerborg, A., Analysis of fracture by means of the fictitious crack model, particularly for fibre reinforced concrete, *The International Journal of Cement Composites*, *2*, 177–184, 1980.

Hillerborg, A., M. Moder, and P. Petterson, Analysis of crack formation and crack growth in concrete by means of fracture mechanics and finite elements, *Cement and Concrete Research*, *6*, 773–781, 1976.

Hiraishi, Y., T. Honma, M. Hakoyama, and S. Miyazato, Steel corrosion at bending cracks in ductile fiber reinforced cementitious composites, in *28th Conference on Our World in Concrete & Structures*, pp. 333–340, Singapore, 2003.

Hiraishi, Y., S. Miyazato, and K. Yokozeki, Influence of unsteady external environment on corrosion rate in reinforced concrete, in *Concrete Repair, Rehabilitation and Retrofitting*, edited by Alexander, pp. 401–407, Taylor & Francis Group, 2006.

Hoff, W., M. Wilson, D. Benton, M. Hawkesworth, D. Parker, and P. Fowles, Use of positron emission tomography to monitor unsaturated water flow within porous construction materials, *Journal of Materials Science Letters*, *15*(13), 1101–1104, 1996.

Houston, J., E. Atimay, and P. Ferguson, Corrosion of reinforcing steel embedded in structural concrete, *Tech. Rep. Research Report 112-1F*, Center for Highway Research, Univerisity of Texas at Austin, 1972.

Hu, J., and P. Stroeven, X-ray absorption study of drying cement paste and mortar, *Cement and Concrete Research*, *33*(3), 397–403, 2003.

Hubbard, S. S., J. E. Peterson, J. Zhang, P. J. Monteiro, and Y. Rubin, Experimental detection of reinforcing bar corrosion using nondestructive geophysical techniques, *ACI Materials Journal*, *100*(6), 501–510, 2003.

Hubbell, J., and S. Seltzer, Tables of x-ray mass attenuation coefficients and mass energy-absorption coefficients, *Tech. Rep. NISTIR 5632*, National Institute of Standards and Technology, Maryland, USA, 2004.

Hwan Oh, B., K. Hyun Kim, and B. Seok Jang, Critical corrosion amount to cause cracking of reinforced concrete structures, *ACI Materials Journal*, *106*(4), 333–339, 2009.

ImageJ Image Processing and Analysis in Java, www.rsbweb.nih.gov/ij/, 2008.

Imamoto, K., K. Shimozawa, M. Nagayama, J. Yamazaki, and S. Nimura, A novel approach to evaluate the steel corrosion risk induced by transverse cracks in concrete, in *Transport mechanisms in cracked concrete*, edited by K. Audenaert, L. Marsavina, and G. De Schutter, pp. 77–86, Ghent, Belgium, 2007.

Germann Instruments, Deep purple and rainbow indicator.

Irwin, G. R., Analysis of stresses and strains near the end of a crack traversing a plate, *Journal of Applied Mechanics*, *24*, 361–364, 1957.

Isgor, O. B., and A. G. Razaqpur, Modelling steel corrosion in concrete structures, *Materials and Structures*, *39*(287), 259–270, 2006.

Jacobsen, S., J. Marchand, and L. Boisvert, Effect of cracking and healing on chloride transport in opc concrete, *Cement and Concrete Research*, *26*(6), 869–881, 1996.

Jaffer, S. J., and C. M. Hansson, Chloride-induced corrosion products of steel in cracked-concrete subjected to different loading conditions, *Cement and Concrete Research*, *39*, 116–125, 2009.

Kamiyama, H., Rust of steel bars in concrete, *Cement and Concrete*, *308*, 50–57, in Japanese, 1972.

Karihaloo, B. L., *Fracture Mechanics & Structural Concrete*, Concrete Design and Construction Series, Longman Scientifc & Technical, Essex, England, 1995.

Kashino, N., A durability investigation of existing buildings, in *International Symposium on Long-term Observations of Concrete Structures*, Budapest, 1984.

Katawaki, K., Corrosion of steel in the concrete exposed to seawater spray zone, in *Symposium proceedings on cracking of concrete structures*, pp. 133–136, 1977.

Kayyali, O. A., and M. N. Haque, Effect of carbonation on the chloride concentration in pore solution of mortars with and without flyash, *Cement and Concrete Research*, *18*(4), 636–648, 1988.

Kelham, S., Water adsorption test for concrete, *Magazine of Concrete Research*, *40*(143), 106–110, 1988.

Kitsutaka, Y., Fracture parameters by polylinear tension-softening analysis, *Journal of Engineering Mechanics - Proceedings of the ASCE*, *123*(5), 444–450, 1997.

Knoll, G., *Radiation Detection and Measurement*, J. Wiley, 1989.

Kumaran, M., and M. Bomberg, A gamma-spectrometer for determination of density distribution and moisture distribution in building materials, in *Proceedings of the International Sypmposium of Moisture and Humidity*, pp. 485–490, Washington, D. C., 1985.

Küter, A., Management of reinforcement corrosion: A thermodynamical approach, Ph.D. thesis, Technical University of Denmark, Kgs. Lyngby, Denmark, 2009.

Küter, A., M. Geiker, and P. Møller, Corrosion of steel in concrete - setup for conclusive testing of multiple specimens, *Submitted to ACI Materials Journal*, 2010.

Laugesen, P., Crack sampling, treatment and analysis, in *Proceedings of the Knud Højgaard Conference Advanced Cement-Based Materials Research and Teaching*, Lyngby, Denmark, 2005.

Li, C., Life-cycle modeling of corrosion-affected concrete structures: Propagation, *Journal of Structural Engineering*, *129*(6), 753–761, 2003.

Li, V., On engineered cementitous composites (ecc) - a review of the material and its applications, *Journal of Advanced Concrete Technology*, *1*(3), 215–230, 2003a.

Li, C.-Q., Y. Yang, and R. E. Melchers, Prediction of reinforcement corrosion in concrete and its effects on concrete cracking and strength reduction, *ACI Materials Journal*, *105*(1), 3–10, 2008.

Life-365 Consortium II, *Life-365 Service life prediction model and computer program for predicting the service life and life-cycle cost of reinforced concrete exposed to chlorides*, version 2.0.1 ed., 2010.

Linsbauer, H., and E. Tschegg, Fracture energey determination of concrete with cube shaped specimens (in german), *Zement und Beton*, *31*, 38–40, 1986.

Liu, Y., and R. Weyers, Modeling the time-to-corrosion cracking in chloride contaminated reinforced concrete, *ACI Materials Journal*, *95*(6), 675–681, 1998.0

Lorentz, T., and C. French, Corrosion of reinforcing steel in concrete: effects of materials, mix composition, and cracking, *ACI Materials Journal (American Concrete Institute)*, *92*(2), 181–190, 1995.

Luping, T., and L.-O. Nilsson, Chloride binding capacity and binding isotherms of OPC pastes and mortars, *Cement and Concrete Research*, *23*(2), 247–253, 1993.

Lura, P., D. P. Bentz, D. A. Lange, K. Kovler, and A. Bentur, Pumice aggregates for internal water curing, in *Concrete Science and Engineering: A Tribute to Arnon Bentur International RILEM Symposium*, pp. 137–151, 2004.

Löfgren, I., H. Stang, and J. F. Olesen, Fracture properties of frc determined through inverse analysis of wedge splitting and three-point bending tests, *Journal of Advanced Concrete Technology*, *3*(3), 423–434, 2005.

Makita, M., Y. Mori, and K. Katawaki, Marine corrosion behavior of reinforced concrete exposed at tokyo bay, in *ACI SP-65: Performance of Concrete in Marine Environment*, pp. 271–290, 1980.

Mangat, P., and B. Molloy, Factors influencing chloride-induced corrosion of reinforcement in concrete, *Materials and Structures*, *25*(151), 404–411, 1992.

Marchand, J., Modeling the behavior of unsaturated cement systems exposed to aggressive chemical environments, *Materials and Structures*, *34*, 195–200, 2001.

Marcotte, T., and C. Hansson, The influence of silica fume on the corrosion resistance of steel in high performance concrete exposed to simulated sea water, *Journal of Materials Science*, *28*, 4765–4776, 2003.

Mariscotti, M. A., F. Jalinoos, T. Frigerio, M. Ruffolo, and P. Thieberger, Gamma-ray imaging for void and corrosion assessment - safety and utility of the technology make it appropriate for field application, *Concrete International - the Magazine of the American Concrete Institute*, *31*(11), 48–53, 2009.

Masschaele, B., M. Dierick, V. Cnudde, L. V. Hoorebeke, S. Delputte, A. Gildemeister, R. Gaehler, and A. Hillenbach, High-speed thermal neutron tomography for the visualization of water repellents, consolidants and water uptake in sand and lime stones, *Radiation Physics and Chemistry*, *71*(3-4), 807–808, 2004.

Mastikhin, I. V., H. Mullally, B. MacMillan, and B. J. Balcom, Water content profiles with a 1D centric sprite acquisition, *Journal of Magnetic Resonance*, *156*(1), 122–130, 2002.

Meijers, S., J. Bijen, R. de Borst, and A. Fraaij, Computational results of a model for chloride ingress in concrete including convection, drying-wetting cycles and carbonation, *Materials and Structures*, *38*, 145–154, 2005.

Midgley, H., and J. Illston, The penetration of chlorides into hardened cement pastes, *Cement and Concrete Research*, *14*(4), 546–558, 1984.

Miller, T. H., T. Yanagita, T. Kundu, J. Grill, and W. Grill, Nondestructive inspection of reinforced concrete structures, *Proceedings of SPIE - The International Society for Optical Engineering*, *7295*(1), 1–12, 2009.

Mindess, S., J. F. Young, and D. Darwin, *Concrete*, second ed., Prentice Hall, 2003.

Miyazato, S., and Y. Hiraishi, Transport properties and steel corrosion in ductile fiber reinforced cement composites, in *Proceedings of the 11th International Conference on Fracture*, Turin, Italy, 2005.

Miyazato, S.-i., N. Otsuki, and H. Kimura, Steel corrosion induced by chloride ions and carbonation in mortar with bending cracks and joints, in *2nd International Conference on Engineering Materials*, pp. 531–542, California, USA, 2001.

Mohammed, T., N. Otsuki, M. Hisada, and T. Shibata, Effect of crack width and bar type on corrosion of steel in concrete, *Journal of Materials in Civil Engineering*, *13*(3), 194–201, 2001.

Mohammed, T. U., N. Otsuki, H. Hamada, and T. Yamaji, Chloride-induced corrosion of steel bars in concrete with presence of gap at steel-concrete interface, *ACI Materials Journal*, *99*(2), 149–156, 2002.

Moreno, M., W. Morris, M. Alvarez, and G. Duff, Corrosion of reinforcing steel in simulated concrete pore solutions effect of carbonation and chloride content, *Corrosion Science*, *46*, 2681–2699, 2004.

Mouri, K., and S. Miyazato, Investigation into chloride induced corrosion of existing reinforced concrete structures and discussion based on wind direction, in *1st International Concrete on Structural Condition Assessment, Monitoring and Improvement*, pp. 269–274, Perth, Australia, 2005.

Myrdal, R., The electrochemistry and characteristics of embeddable reference electrodes for concrete, *Tech. Rep. 43*, European Federation of Corrosion Publications, 2007.

Nagataki, S., N. Otsuki, M. Hisada, and S. Miyazato, The experimental study on corrosion mechanism of reinforced concrete at local repair part, *JSCE*, *32*(544), 109–119, 1996.

Nanakorn, P., and H. Horii, Back analysis of tension-softening relationship of concrete, *Journal of Materials, Concrete Structures, Pavements, JSCE*, *32*, 265–275, 1996.

Neithalath, N., B. J. Pease, J.-H. Moon, F. Rajabipour, and W. J. Weiss, Considering moisture gradients and time-dependent crack growth in restrained concrete elements subjected to drying, in *International Conference on Advances in Concrete Composites and Structures (ICACS)*, Chennai, India, 2005.

Neville, A., *Properties of Concrete*, fourth ed., John Wiley & Sons, 1996.

Nielsen, A., Gamma-ray-attenuation used for measuring the moisture content and homogeneity of porous concrete, *Building Science*, *7*(4), 257–263, 1972.

Nielsen, E., and M. Geiker, Chloride diffusion in partially saturated cementitious material, *Cement and Concrete Research*, *33*, 133–138, 2003.

Nilsson, L.-O., *Advanced Concrete Technology Book*, Butterworth Heinemann, 2002.

Nilsson, L.-O., E. Poulsen, P. Sandberg, H. E. Sørensen, and O. Klinghoffer, Hetek, chloride penetration into concrete state-of-the-art - transport processes, corrosion initiation, test methods and prediction models, *Tech. Rep. Report No. 53*, The Danish Road Directorate, 1996.

Nilsson, L.-O., P. Sandberg, E. Poulsen, L. Tang, A. Anderson, and J. M. Frederiksen, Hetek: A system for estimation of chloride ingress into concrete – theoretical background, *Tech. Rep. Report No. 83*, Road Directorate, Danish Ministry of Transport, 1997.

Nishiyama, H., Experiments on steel corrosion due to cracking, in *Proceedings of the 30th Annual Conference of the Japan Society of Civil Engineers*, vol. 5, pp. 258–259, 1975.

Nygaard, P. V., Effect of steel-concrete interface defects on the chloride threshold for reinforcement corrosion, Master's thesis, Technical University of Denmark, Kgs. Lyngby, Denmark, 2003.

Nygaard, P. V., Non-destructive electrochemical monitoring of reinforcement corrosion, Ph.D. thesis, Technical University of Denmark, Kgs. Lyngby, Denmark, 2008.

Nygaard P. V., Geiker M., A method for measuring the chloride threshold level required to initiate reinforcement corrosion in concrete. *Materials and Structures*, *38*(278), 489–494, 2005.

Ohtsu, M., and Y. Tomoda, Phenomenological model of corrosion process in reinforced concrete identified by acoustic emission, *ACI Materials Journal*, *105*(2), 194–199, 2008.

Olesen, J. F., Technical papers - fictitious crack propagation in fiber-reinforced concrete beams, *Journal of Engineering Mechanics - Proceedings of the ASCE*, *127*(3), 272–280, 2001.

O'Neil, E. F., Study of reinforced concrete beams exposed to marine environment, in *ACI SP-65: Performance of Concrete in Marine Environment*, pp. 113–132, 1980.

Otieno, M., Alexander, M., and Beushausen, H.-D., Corrosion in cracked and uncracked concrete - Influence of crack width, concrete quality and crack reopening, *Magazine of Concrete Research 62*(6), 393–404, 2010.

Pease, B., J. Couch, M. Geiker, H. Stang, and J. Weiss, Assessing the portion of the crack length contributing to water sorption using x-ray absorption measurements on concrete wedge splitting specimens, in *ConcreteLife'09: Second International RILEM Workshop on Concrete Durability and Service Life Planning*, Haifa, Israel, 2009.

Pease, B. J., M. R. Geiker, H. S. Stang, and W. J. Weiss, Photogrammetric assessment of flexure induced cracking of reinforced concrete beams under service loads, in *Proceedings of the Second International RILEM Symposium Advances in Concrete through Science and Engineering*, Qubec City, Qubec, Canada, 2006.

Perez, N., *Electrochemistry and Corrosion Science*, Kluwer Academic Publishers, 2004.

Philip, J. R., The theory of infiltration: 4. Sorptivity and algebraic infiltration equations, *Soil Science*, *84*(3), 257–264, 1957.

Poulsen, E., and L. Mejlbro, *Diffusion of Chloride in Concrete Theory and Application*, Taylor & Francis, 2006.

Pourbaix, M., *Atlas of Electrochemical Equilibria*, second ed., NACE, Houston, Texas, 1974.

Pour-Ghaz, M., F. Rajabipour, J. Couch, and W. J., Modeling fluid transport in cementitious systems with crack-like (notch) geometries, in *Proc. to ConcreteLife'09: Second International RILEM Workshop on Concrete Durability and Service Life Planning*, 2009.

Pour-Ghaz, M., F. Rajabipour, J. Couch, and W. J., Numerical and Experimental Assessment of Unsaturated Fluid Transport in Saw-Cut (Notched) Concrete Elements, in *ACI SP 266 - Modeling As a Solution to Concrete Problems*, 73–83, 2009a.

Poursaee, A., and C. M. Hansson, The influence of longitudinal cracks on the corrosion protection afforded reinforcing steel in high performance concrete, *Cement and Concrete Research*, *38*(8-9), 1098–1105, 2008.

Powers, T., and T. Brownyard, Studies of the physical properties of hardened portland cement paste, *Journal of the American Concrete Institute*, *18*(8), 1947.

Qi, C., W. J. Weiss, and J. Olek, Characterization of plastic shrinkage cracking in fiber reinforced concrete using semi-automated image analysis, *Concrete Science and Engineering*, *36*(260), 386–395, 2003.

Ramm, W., and M. Biscoping, Autogenous healing and reinforcement corrosion of water-penetrated separation cracks in reinforced concrete, *Nuclear Engineering and Design*, *179*(2), 191–200, 1998.

Raupach, M., Zur chloridinduzierten makroelementkorrosion von stahl in beton, *Deutscher Ausschuss fur Stahlbeton*, *433*, 7–106, 1992.

Reddy, B., G. Glass, P. Lim, and N. Buenfeld, On the corrosion risk presented by chloride bound in concrete, *Cement and Concrete Composites*, *24*(1), 1–5, 2002.

Rehm, G., and H. L. Moll, Versuche zum studium des einflusses der rissbreite auf die rostbilding an der bewehrung von stahlbeton-bauteilen, *Deutscher Ausschuss fur Stahlbeton*, *169*, 1964.

Roberts, E., Elastic crack-edge displacement for the compact tension specimen, *Materials Research and Standards*, *9*(2), 27, 1969.

Rodriguez, O., and R. Hooton, Influence of cracks on chloride ingress into concrete, *ACI Materials Journal*, *100*(2), 120–126, 2003.

Roels, S., and J. Carmeliet, Analysis of moisture flow in porous materials using microfocus x-ray radiography, *International Journal of Heat and Mass Transfer*, *49*, 4762–4772, 2006.

Roels, S., et al., A comparison of different techniques to quantify moisture content profiles in porous building materials, *Journal of Building Physics*, *27*(4), 261, 2004.

Roels, S., K. Vandersteen, and J. Carmeliet, Measuring and simulating moisture uptake in a fractured porous medium, *Advances in Water Resources*, *26*(3), 237–246, 2003.

Saetta, A., R. Scotta, and R. Vitaliani, Analysis of chloride diffusion into partially saturated concrete, *ACI Materials Journal*, *90*(5), 441–451, 1993.

Sagoe-Crentsil, K., and F. Glasser, "Green rust", Iron solubility and the role of chloride in the corrosion of steel at high pH, *Cement and Concrete Research*, *23*(4), 785–791, 1993.

Saito, M., and H. Ishimori, Chloride permeability of concrete under static and repeated compressive loading, *Cement and Concrete Research*, *25*(4), 803–808, 1995.

Sandberg, P., Critical evaluation of factors affecting chloride initiated reinforcement corrosion in concrete, *Tech. Rep. Report TVBM-3068*, University of Lund, Lund, Sweden, 1995.

Sant, G., and J. Weiss, Using x-ray absorption to assess moisture movement in cement-based materials, *Journal of ASTM International*, *6*(9), 2009.

Sant, G., Eberhardt, A., Bentz, D., and J. Weiss, Influence of shrinkage-reducing admixtures on moisture absorption in cementitious materials at early ages, *Journal of Materials in Civil Engineering, American Society of Civil Engineers*, *22*(3), 277–286, 2010.

Scheffler, G., B. Pease, and H. Janssen, Determination of optimal x-ray settings for moisture content measurement with x-ray attenuation, *In preparation*, 2010.

Schiessl, P., Zur frage der zulassigen rissbreite und der enforderlichen betondeckung im stahlbetonbau unter besonderer berucksichtigung der karbonatisierung des betons, *Deutscher Ausschuss fur Stahlbeton*, *255*, 1976.

Schiessl, P., Einfluss von rissen auf die dauerhaftigkeit von stahlbeton- und spannbetonbauteilen, *Deutscher Ausschuss fur Stahlbeton*, *370*, 9–52, 1986.

Schiessl, P., and M. Raupach, Laboruntersuchungen und berechnungen zum einfluss er rissbreite des betons auf die chloridinduzierte korrosion von stahl in beton, *Bauingenieur*, *69*(11), 439, in German, 1994.

Schiessl, P., and M. Raupach, Laboratory studies and calculations on the influence of crack width on chloride-induced corrosion of steel in concrete, *ACI Materials Journal*, *94*(1), 56–62, 1997.

Seki, H., Corrosion of steel bars at crack of reinforced concrete exposed to sea environments, *The Report of Port and Airport Research Institute*, *12*(3), 203–225, (In Japanese), 1973.

Shah, S. P., S. E. Swartz, and C. Ouyang, *Fracture Mechanics of Concrete*, John Wiley & Sons, Inc., 1995.

Shalon, R., and M. Raphael, Corrosion of reinforcing steel in hot countries, *RILEM Bulletin*, (24), 29–45, 1964.

SIMCO Technologies Inc., *Description of the STADIUM model*, 203 - 1400 boul. du Parc-Technologique, Quebec, Canada, available at www.simcotechnologies.com, 2009.

Skoček, J., Fracture propagation in cementitious materials - Multi-scale approach: measurements and modeling, Ph.D. thesis, Technical University of Denmark, Kgs. Lyngby, Denmark, 2010.

Skoček, J., and H. Stang, Inverse analysis of the wedge splitting test, *Engineering Fracture Mechanics*, *75*(10), 3173–3188, 2008.

Skoček, J., and H. Stang, Application of optical deformation analysis system on wedge splitting test and its inverse analysis, *Submitted to Materials and Structures*, 2009.

Spangenberg, J., Numerical modeling of crack propagation in reinforced concrete beams, Master's thesis, Technical University of Denmark, Kgs. Lynbgy, Denmark, 2009.

Spragg, R. P., Castro, J., Li, W., Pour-Ghaz, M., Huang, P.-T., Weiss, J. Wetting and drying of concrete in the presence of deicing salt solutions, *Submitted to Transportation Research Record Concrete Materials and Construction.*

Suzuki, K., Y. Ohno, S. Praparntanatorn, H. Ninomiya, and T. Hiroshi, Influence of flexural crack on corrosion of steel in concrete, *Journal of structural and construction engineering*, *397*, 1–11, (In Japanese), 1989.

Synder, K. A., *Validation and modification of the 4sight computer program*, National Institute of Standards and Technology (NIST), Gaithersburg, Maryland, 2001.

Tada, H., P. C. Paris, and G. R. Irwin, *The Stress Analysis of Cracks Handbook*, Paris Productions Incorporated, 226 Woodbourne Dr., St. Louis, Missouri, USA, 1985.

Tottori, S., S. Tsuchida, and T. Miyagawa, Deterioration prediction of concrete structures based in the exposure test results concerning cracking and rebar corrosion, *Concrete Research and Technology, Japan Concrete Institute*, *10*(3), 1–15, (In Japanese), 1999.

Tremper, B., The corrosion of reinforcing steel in cracked concrete, *Journal of the American Concrete Institute*, *18*(10), 1137–1144, 1947.

Tuutti, K., Corrosion of steel in concrete., in *EUROCOR '77, Eur Congr on Met Corros, 92nd Event of the Eur Fed of Corros*, pp. 655–661, Soc of Chem Ind, 1977.

Tuutti, K., Cracks and corrosion (the corrosion of steel in concrete - the effect of cracks in the concrete cover), *Tech. Rep. 6*, Swedish Cement and Concrete Research Institute at the Instituite of Technology, Stockholm (CBI), 1978.

Tuutti, K., Corrosion of steel in concrete, *Swedish Cement and Concrete Institute (CBI)*, *4-82*, 1982a.

Uchida, Y., and B. I. G. Barr, Tension softening curves of concrete determined from different test specimen geometries, in *Fracture Mechanics of Concrete Structures, FRAMCOS-3*, edited by H. Mihashi and K. Rokugo, pp. 387–398, Freiburg, Germany, 1998.

Ulfkjaer, J. P., S. Krenk, and R. Brincker, Analytical model for fictitious crack propagation in concrete beams, *Journal of Engineering Mechanics*, *121*(1), 7–15, 1995.

Van Geet, M., Optimisation of microfocus x-ray computer tomography for geological reserach with special emphasis on coal components (macerals) and fractures (cleats) characterisation, Ph.D. thesis, KU Leuven, Heverlee, 2001.

Van Geet, M., R. Swennen, and P. David, Quantitative coal characterisation by means of microfocus x-ray computer tomography, colour image analysis and back-scattered scanning electron microscopy, *International Journal of Coal Geology*, *46*, 11–25, 2001.

van Mier, J., and M. van Vliet, Uniaxial tension test for the determination of fracture parameters of concrete: state of the art, *Engineering Fracture Mechanics*, *69*(2), 235–247, 2002.

van Mier, J. G. M., *Fracture Processes in Concrete Assessment of Material Parameters for Fracture Models*, CRC Press, 1997.

Vidal, T., A. Castel, and R. Francois, Corrosion process and structural performance of a 17 year old reinforced concrete beam stored in chloride environment, *Cement and Concrete Research*, *37*, 1551–1561, 2007.

Voelmy, A., and B. Bernardi, Remarques sur l'adhrence et la formation des fissures dans le beton arm, in *RILEM - Symposium on Bond and Crack Formation in Reinforced Concrete*, vol. II, p. 347, Stockholm, 1957.

Volkwein, A., The capillary suction of water into concrete and the abnormal viscosity of the porewater, *Cement and Concrete Research*, *23*(4), 843–852, 1993.

Vu, K., M. Stewart, and J. Mullard, Corrosion-induced cracking: Experimental data and predictive models, *ACI Structural Journal*, *102*(5), 719–726, 2005.

Walter, R., L. Ostergaard, J. Olesen, and H. Stang, Wedge splitting test for a steel-concrete interface, *Engineering Fracture Mechanics*, *72*(17), 2565–2583, 2005.

Wang, K., D. Jansen, S. Shah, and A. Karr, Permeability study of cracked concrete, *Cement and Concrete Research*, *27*(3), 381–393, 1997.

Wang, K., W. Weiss, S. Yoon, and S. Shah, Combined effect of corrosion and stresses in reinforced concrete beams, in *American Society of Civil Engineers Engineering Mechanics Division*, Austin, TX, 2000.

Weiss, W. J., Prediction of Early-Age Shrinkage Cracking in Concrete Elements, Ph.D. thesis, Northwestern University, Evanston, IL, 1999, pp. 277.

Weiss, W. J., M. R. Geiker, and K. K. Hansen, Using x-ray absorption to detect fluid ingress in cracked concrete, *Report, Purdue University, West Lafayette, IN, USA*, pp. 15, 2004.

Win, P., Watanabe, M., and Machida, A., Penetration Profile of Chloride Ions in Cracked Reinforced Concrete, *Cement and Concrete Research*, *34*(7), 1073–1079, 2004.

Xray_Tiler v1.7, Purdue University, written in ImageJ, 2008.

Xi, Y., and Z. Bazant, Modeling chloride penetration in saturated concrete, *Journal of Materials in Civil Engineering*, *11*(1), 58–65, 1999.

Xu, H., Y. Liu, W. Chen, R.-G. Du, and C.-J. Lin, Corrosion behavior of reinforcing steel in simulated concrete pore solutions: A scanning micro-reference electrode study, *Electrochimica Acta*, *54*(16), 4067–4072, 2009.

Yachida, M., Cracking and reinforcement corrosion in reinforced concrete bridges, *Journal of Materials, Concrete Structures and Pavements*, *6*(378), 195–202, (In Japanese), 1987.

Yang, Z., Assessing cumulative damage in concrete and quantifying its influence on life cycle modeling, Ph.D. thesis, Purdue University, West Lafayette, IN, 2004.

Yano, M., T. Iida, K. Kawabata, and S. Miyazato, Steel corrosion induced by chloride and carbonation in concrete with defects, in *The Ninth East Asia-Pacific Conference on Structural Engineering and Construction*, pp. 62–68, 2002.

Yoon, D.-J., W. J. Weiss, and S. P. Shah, Assessing damage in corroded reinforced concrete using acoustic emission, *Journal of Engineering Mechanics*, *126*(3), 273–283, 2000a.

Yoon, S., K. Wang, W. Weiss, and S. Shah, Interaction between loading, corrosion, and serviceability of reinforced concrete, *ACI Materials Journal*, *97*(6), 637–644, 2000b.

You, J., and T. Ohno, Influence of crack and water cement ratio on corrosion of steel in carbonated concrete, *Journal of Structural and Construction Engineering*, *559*, 15–22, (In Japanese), 2002.

Østergaard, L., Early-age fracture mechanics and cracking of concrete - experiments and modeling, Ph.D. thesis, Technical University of Denmark, Lyngby, Denmark, 2003.

Part II

Appended papers

Paper I

The wedge splitting test: Influence of aggregate size and water-to-cement ratio

Pease, B.*, Skoček*, J., Geiker*, M., Stang*, H., Weiss, J.†

*Department of Civil Engineering, Technical University of Denmark (DTU Byg), 2800 Kgs. Lyngby, Denmark, e-mail: bjp@byg.dtu.dk

†School of Civil Engineering, Purdue University, West Lafayette, IN, USA 47907

Paper in the proceedings of: *RILEM workshop: Transport Mechanisms in Cracked Concrete, Ghent, Belgium, September, 2007*

THE WEDGE SPLITTING TEST: INFLUENCE OF AGGREGATE SIZE AND WATER-TO-CEMENT RATIO

Brad J. Pease (1), Jan Skoček (1), Mette R. Geiker (1), Henrik Stang (1), and Jason Weiss (2)

(1) Technical University of Denmark, Department of Civil Engineering, Lyngby, Denmark

(2) Purdue University School of Civil Engineering, West Lafayette, Indiana, USA

Abstract

Since the development of the wedge splitting test (WST), techniques have been used to extract material properties that can describe the fracture behavior of the tested materials. Inverse analysis approaches are commonly used to estimate the stress-crack width relationship; which is described by the elastic modulus, tensile strength, fracture energy, and the assumed softening behavior. The stress-crack width relation can be implemented in finite element models for computing the cracking behavior of cementitious systems.

While inverse analysis provides information about the material properties of various concrete mixtures there are limitations to the current analysis techniques. To date these techniques analyze the result of one WST specimen, thereby providing an estimate of material properties from single result. This paper utilizes a recent improvement to the inverse analysis technique, which enables the stress-crack width response to be determined simultaneously from multiple experimental tests. The effect of water-to-cement ratio and aggregate size are discussed. A comparison of epoxy-impregnated cracked WST specimen and material properties indicate a relationship between fracture properties and characteristics of load induced cracks.

Corresponding author's e-mail: bjp@byg.dtu.dk

Corresponding author's fax:+45 4588 3282

1. INTRODUCTION

The cohesive crack model is commonly applied to quasi-brittle materials such as concrete. The concept of the cohesive crack approach deviates from linear elastic fracture mechanics and considers that stresses can be transferred across the fractured surfaces. This transfer of stresses was first seen in steel in the form of plasticity [**1**,**2**] and was later applied to concrete with the concept of strain softening in [**3**]. The transfer of stresses in cracked concrete is illustrated in Figure 1a, and a generic cohesive law, or softening behavior (which can be readily applied in FEM programs) is shown in Figure 1b.

The wedge splitting test (WST) was created in [**4**] and further developed in [**5**] as a tool to determine the fracture of concrete or other cementitious materials. More recently, through the application of suitable analytical or finite element models, additional information including the estimated direct tensile strength, elastic modulus, and the cohesive law can be determined [**6**,**7**,**8**,**9**]. In [**9**] an analytical solution for the WST was determined using the hinge cracking model developed in [**10**]; however, several limitations existed. Included in these limitations are that only bi-linear cohesive laws could be determined and the inverse analysis could be conducted on a single test result. An iterative approach was developed in [**11**], which is described in greater detail in a following section. This iterative approach can be used to provide *N*-linear cohesive laws, however the inverse analysis is still conducted on a single experimental result.

The purpose of this paper is to investigate the effect to varying material parameters on the fracture behavior as determined by the WST and inverse analysis. A method to consider multiple experimental results in the inverse analysis approach is used. The effect of aggregate size, water-to-cement ratio, and cyclic loading is discussed. In addition, image analysis of cracked epoxy-impregnated specimens provides insight on the effect of changing fracture parameters on the characteristics of the cracks formed in concrete.

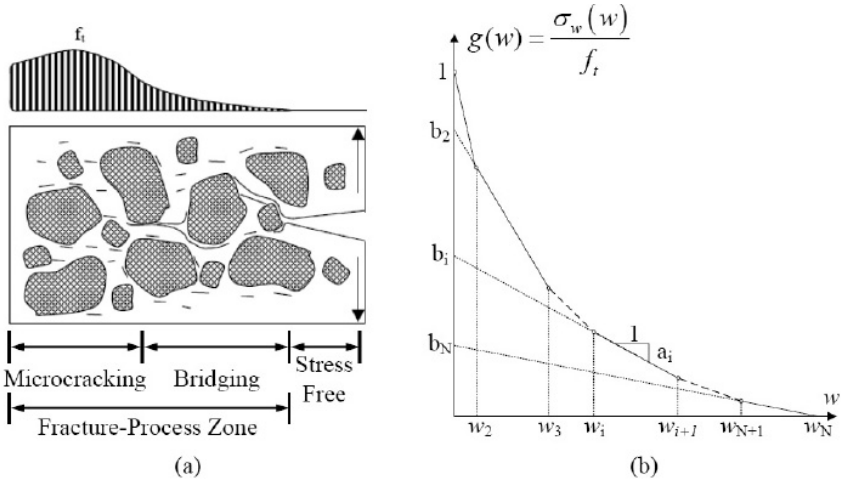

Figure 1. Illustrations of (a) concrete crack development with a fracture-process zone consisting of a bridging and microcracking regions (after [**12**]) and (b) the multi-linear softening behavior of cracked concrete.

Corresponding author's e-mail: bjp@byg.dtu.dk
Corresponding author's fax:+45 4588 3282

2. EXEPERIMENTAL DESCRIPTION

2.1 Mixture Proportioning and Specimen Preparation

Table 1 describes the mixture proportions used for testing, which included mixtures with varying maximum aggregate size and water-to-cement ratio (w/c). The concrete mixtures contained 65% aggregate by volume, with equal portions of graded sand and granite aggregate. The mortar mixture contained identical proportions of aggregate as the concrete mixtures, minus the coarse granite aggregate (i.e., 32.5% graded sand by volume). Aalborg Portland Basis© cement designated CEM II/A-LL 52.5 was used for all mixtures.

A conventional pan mixer was used for mixing 60 liter batches. The aggregate, half of the sand, water and cement were added to the mixer followed by the remaining sand. Mixing took place for 2 minutes, followed by a 2 minute rest period, and finally an additional minute of mixing. After mixing the concrete was placed and vibrated in 100 x 100 x 100 cube molds which contained a 20 mm x 30 mm plastic block to create a recess. The samples were cured in laboratory conditions, covered with plastic sheets for 24 hours. After this time the specimen we removed from the molds and were submerged in lime-saturated water at 20°C until testing at 1, 3, 5, 7, 14, and 21 days. Immediately prior to testing a 30 mm deep notch was cut into the specimen using a concrete saw. Figure 2 and 3 provide illustrations of the final specimen geometry after saw cutting. Additional information on the mixing procedure can be found in [**13**].

Table 1. Mixture Proportions and Descriptions

Mixture ID	w/c	Description	Max. Size Aggregate (mm)
A	0.42	Large Aggregate Concrete	16
B	0.42	Small Aggregate Concrete	8
C	0.42	Mortar	4
E	0.34	Paste	--
G	0.50	Large Aggregate Concrete	16
H	0.30	Large Aggregate Concrete	16

2.2 Wedge Splitting Test and Inverse Analysis

The WST experimental setup is shown in Figure 2. During testing, a splitting load is applied to a concrete specimen through a rigid wedge and bearing plates with low-friction rollers. The specimen consists of a 100 x 100 x 100 mm cube with a 20 mm deep by 30 mm wide recess, which allows for application of the splitting load.

The WST can be used, through inverse analysis (e.g., minimizing the difference between the model calculations and experimental results by altering mechanical parameters), to determine the cohesive law for cementitious composites. Figure 3 shows the implementation of the hinge model developed in [**14**,**10**] to the WST geometry. The hinge model simulates the area directly surrounding a propagating crack, which are attached to rigid boundaries. The rigid boundaries of the cracked hinge are allowed to translate and rotate as indicated in Figure 3b. The rigid boundaries seamlessly join the bulk (uncracked) specimen, where the behavior is controlled by the classical elastic theory (i.e. Hooke's Law).

Corresponding author's e-mail: bjp@byg.dtu.dk
Corresponding author's fax:+45 4588 3282

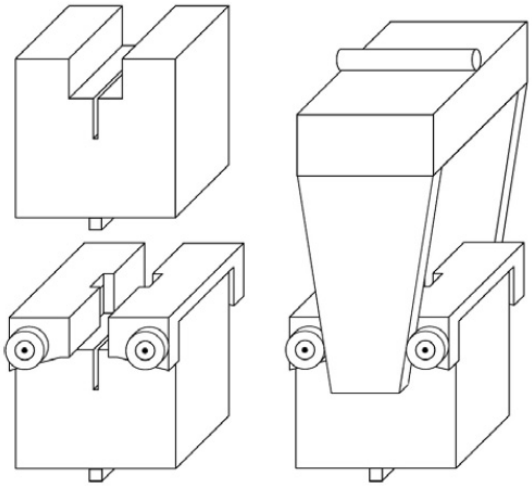

Figure 2. Schematic of WST geometry: Specimen is placed on line support, two roller bearing loading devices are mounted, and wedge applies splitting load [**9**].

The stresses transferred in the hinge model are controlled by Equation 1

$$\sigma = \begin{cases} \sigma(\varepsilon) = E\varepsilon & \text{Precracked State} \\ \sigma_w(w) = g(w) f_t & \text{Cracked State} \end{cases} \qquad \text{Equation 1}$$

where E is the elastic modulus, ε is the elastic strain, $\sigma_w(w)$ represents the cohesive law, and f_t is the uniaxial tensile strength. Figure 1b illustrates a general $g(w)$ curve, which mathematically is given by

$$g(w) = b_i - a_i w \text{ where } w_{i-1} < w < w_i \text{ and } i = 1 \to N . \qquad \text{Equation 2}$$

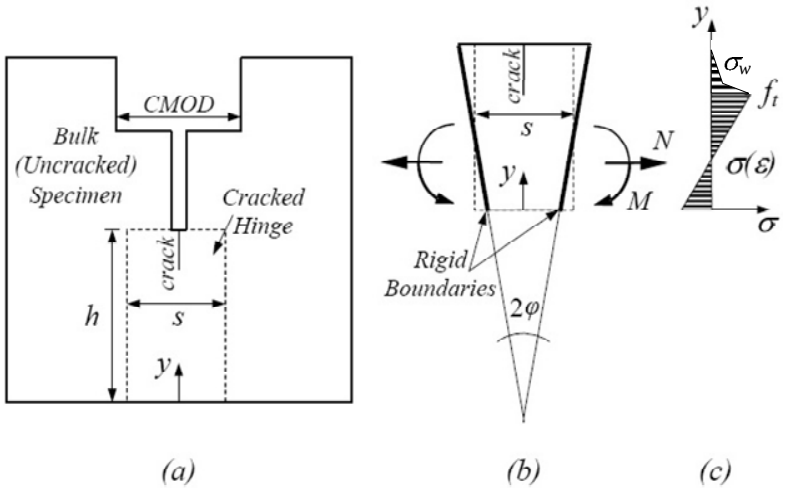

Figure 3. (a) The wedge split testing specimen with the hinge model applied, (b) Loading and deformation of the hinge (after [**10**]), and (c) the assumed stress distribution (after [**10**]).

Corresponding author's e-mail: bjp@byg.dtu.dk
Corresponding author's fax:+45 4588 3282

The term w_i is the intersection of two consecutive lines and is computed by

$$w_i = \frac{b_i - b_{i+1}}{a_i - a_{i+1}} \text{ where } i < N,$$

and the critical crack width (width at which $g(w) = 0$) is calculated by

$$w_c = w_N = \frac{b_N}{a_N}$$

where N is equal to the number of lines in the cohesive law. The deformation of the hinge is determined by the angular rotation, φ and the location of the neutral axis, y_0 (see Figure 3). The mean value of longitudinal strains, $\varepsilon^*(y)$ is calculated by Equation 3.

$$\varepsilon^*(y) = (y - y_0)2\varphi / s \qquad \text{Equation 3}$$

The deformation of an incremental strip of the hinge is then given by $u(y) = s \cdot \varepsilon^*(y)$, where s is the length of the hinge ($s = 0.5h$). Once cracking occurs, $u(y)$ can be computed as the sum of the elastic deformation and the crack opening, as shown in Equation 4.

$$u(y) = s \cdot \varepsilon^*(y) = s\frac{\sigma_w(w(y))}{E} + w(y) \qquad \text{Equation 4}$$

By combining Equation 3 and 4 the stress distribution as seen in Figure 3c is mathematically written as follows in Equation 5

$$\sigma_w(w(y)) = (2(y - y_0)\varphi - w(y))\frac{E}{s} \qquad \text{Equation 5}$$

and by introducing the cohesive law (Equation 1) and solving with respect to $w(y)$ and $\sigma_w(w(y))$ the following solutions are obtained:

$$\sigma_w(w(y)) = \frac{\zeta - 2\varphi(y - y_0)\beta_{i\,i}}{1 - \beta_i}\frac{E}{s} \qquad \text{Equation 6}$$

$$w(y) = \frac{2\varphi(y - y_0) - \zeta_i}{1 - \beta_i} \qquad \text{Equation 7}$$

where the dimensionless factors β_i and ζ_i are defined by

$$\beta_i = \frac{f_t a_i s}{E} \text{ and } \zeta_i = \frac{f_t b_i s}{E}. \qquad \text{Equation 7a}$$

Additional information on the development and implementation of the hinge model can be found in [**10**] and [**9**,**15**,**11**], respectively.

In [**9**] the hinge model was applied to the WST geometry and an analytical solution was utilized to determine a bilinear cohesive law. An iterative approach was developed in [**11**] which allows for determination of N-linear cohesive laws. The following section provides an

overview of the iterative inverse analysis technique for determination of *N*-linear cohesive laws.

The inverse analysis proceeds based upon the following two main equations:

$$M_{\exp} - M_{Hinge} = 0 \quad \text{and} \quad CMOD_{\exp} - CMOD_{Hinge} = 0 \qquad \text{Equation 8}$$

where M_{exp} is the bending moment applied during experimental testing, M_{Hinge} is the bending moment applied in the hinge model approach, $CMOD_{exp}$ is the observed CMOD from experiments, and $CMOD_{Hinge}$ is the CMOD computed from the hinge model. The experimental bending moment, M_{exp} is computed by

$$M_{\exp} = P_{sp}\left(d_2 - y_0\right) + \frac{1}{2}P_v d_1 + \frac{1}{2}mge \qquad \text{Equation 8a}$$

where

$$P_v = P_{sp}\frac{2\tan\alpha_w + \mu_c}{1 - \mu_c \tan\alpha_w} \qquad \text{Equation 8b}$$

which accounts for the wedge angle, α_w and the friction in the roller bearings, μ_c; m is the mass of the specimen and g is the acceleration of gravity. The bending moment applied in the hinge model, M_{Hinge} is computed by

$$M_{Hinge} = \int_0^h \sigma(y)(y - y_0)dy \qquad \text{Equation 8c}$$

where $\sigma(y)$ is the cohesive law from Equation 1. The CMOD calculated by the hinge model, $CMOD_{Hinge}$ is the sum of the elastic deformation, δ_e; the deformation caused by the crack, δ_w; and the deformation caused by geometrical amplification, δ_g. The calculation of the elastic deformation, δ_e is found in [**16**] as

$$\delta_e = \frac{P}{Et}\upsilon_2 . \qquad \text{Equation 8d}$$

Here t is the specimen thickness and υ_2 is computed by [**16**]:

$$\upsilon_2 = \frac{x}{(1-x)^2}\left[38.2 - 55.4x + 33.0x^2\right] \qquad \text{Equation 8e}$$

The deformation caused by the crack, δ_w can be directly calculated from Equation 7 at $y = h$. Finally, the deformation caused by geometrical amplification, δ_g is computed by

$$\delta_g = 2(b-h)\left(\frac{\delta_w}{2d} - \frac{\varphi_e}{1-\beta_i}\right) \qquad \text{Equation 8f}$$

where φ_e is defined as the maximum elastic angular deformation of the hinge and d is the depth to which the crack has propagated through the hinge.

An analytical solution to Equation 8 cannot be obtained and therefore an optimization process has been implemented using MatLab. This process minimizes the difference between the observed load applied in experiments, P_{exp} and the load predicted by the hinge model, P_{Hinge} using the following error normalization function:

$$\left\| P_{\exp} - P_{Hinge} \right\| = \sqrt{1 + \frac{\left(P_{\exp} - P_{Hinge}\right)^2}{2}} - 1 \qquad \text{Equation 9}$$

Corresponding author's e-mail: bjp@byg.dtu.dk
Corresponding author's fax:+45 4588 3282

This normalization function is applied to various stages of the load response curves, including the elastic portion for determination of E, the peak load for determination of f_t, and the softening branch for determination of a_i and b_i. Additional information on this optimization process, including a parametric study and method of implementation in Matlab can be found in [**11**].

Previously, this and similar inverse analysis approaches have been used to fit results from single experimental data [**9**,**15**,**11**], however experimental results tend to vary slightly from test to test. Therefore, in order to allow for fitting from multiple specimen the following modification has been made, which minimizes the difference between the hinge model curve and a multitude of experimental curves.

$$\min = \sum_{i=1}^{N_{\exp}} \left[\left(\sum_{j=1}^{N_p} \sqrt{1 + \frac{\left(P_{\exp}^{i,j} - P_{Hinge}^{i,j}\right)^2}{2}} - 1 \right) \Big/ N_p \right] \qquad \text{Equation 10}$$

for $i=1$ *to* N_{exp}, where N_{exp} is the number of experimental curves and for $j=1$ *to* N_p where N_p is the number of data points in the individual experimental curve. By dividing by the number of data points, N_p in the individual curves, the data is normalized by the number of points; therefore, not overemphasizing the effect of a single curve on the overall fitting of the hinge model. Figure 4a shows multiple experimental WST results from a single concrete batch along with the results of the inverse analysis. It can be seen that the inverse analysis is averaging the behavior of the multiple tests.

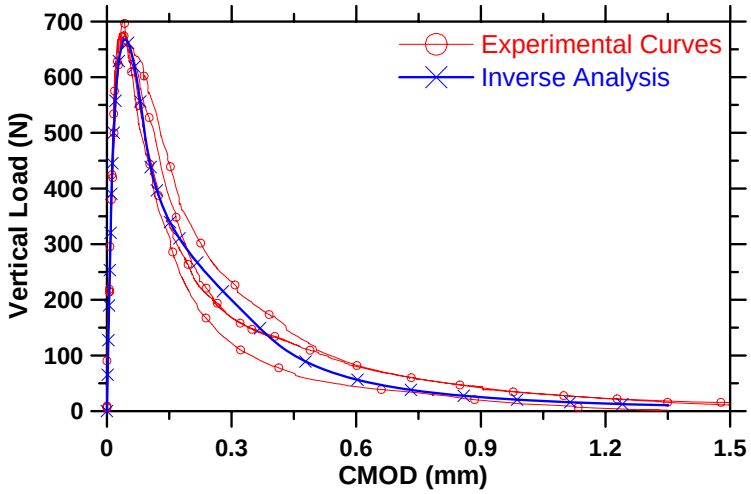

Figure 4. Results of inverse analysis of multiple WST specimen

2.3 Crack Impregnation and Image Analysis

A fluorescent dye epoxy was used for impregnation of cracked WST specimen at varying crack mouth opening displacements (CMOD). The WST specimens were loaded to a specific CMOD and then epoxy impregnated under vacuum. After hardening of the epoxy the samples were cut using a diamond saw. Images were taken of the impregnated samples under a UV-light source which causes the epoxy to illuminate, simplifying the image analysis

Corresponding author's e-mail: bjp@byg.dtu.dk
Corresponding author's fax:+45 4588 3282

process. A semi-automated image analysis technique was used to convert the images into black and white (solid concrete presented in black, crack(s) in white) and various masks were applied to determine geometrical characteristics of the cracks. Additional information on the epoxy impregnation and semi-automated image analysis techniques can be found in [**17**] and [**18**], respectively.

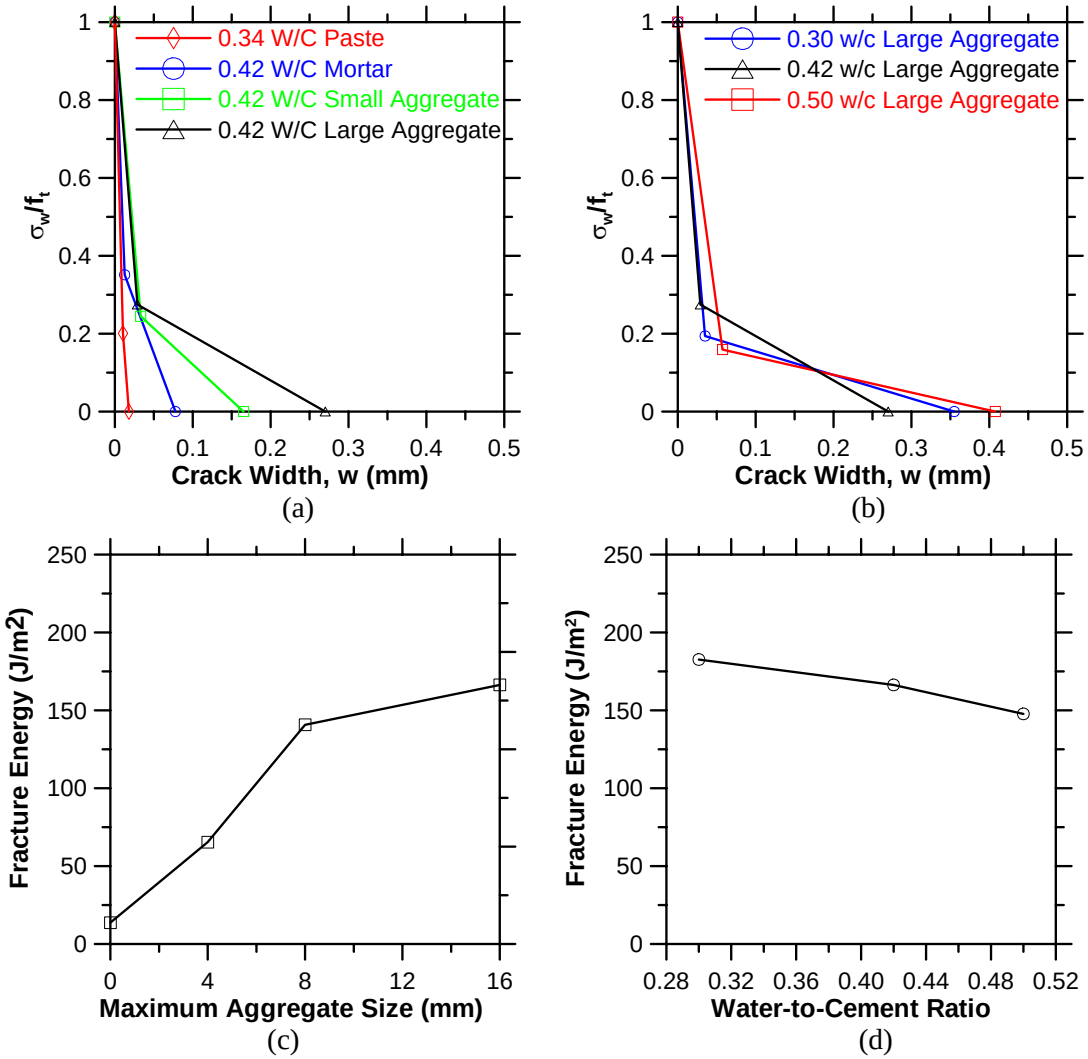

Figure 5. The effect of aggregate size on the (a) cohesive law and (c) fracture energy, and the effect of w/c on the (b) cohesive law and (d) fracture energy for all mixtures at age of 14 days.

3. RESULTS AND DISCUSSION

3.1 Inverse Analysis Results

The results of the inverse analysis of the various concrete mixtures are presented in Figure 5. In this case the results of a bi-linear cohesive law inverse analysis are presented. Figure 5a illustrates the effect of increasing the maximum aggregate size on the transfer of stresses

Corresponding author's e-mail: bjp@byg.dtu.dk
Corresponding author's fax:+45 4588 3282

across a crack. The paste mixture transfers only minimal stresses after cracking, while the stresses transferred across the crack increases with an increase in the size of the maximum aggregate. The effectiveness of the aggregate to transfer stresses can be quantified by the critical crack width, or the crack width where stress transfer ceases. The critical crack width of the paste is approximately 0.02 mm, while the concrete with 16 mm aggregate has a value of approximately 0.27 mm. The increase in stress transfer and critical crack width is typically attributed to aggregate interlock and friction between the fracture surfaces [**19**]. Figure 5c shows the effect of the maximum aggregate size on the fracture energy (paste is assumed to have maximum aggregate size of 0 mm). The effect of aggregate size on increasing the fracture energy is clearly illustrated. The fracture energy increases from 13.7 J/m^2 for the cement paste to 166 J/m^2 for the large aggregate concrete. It should be noted that the paste used in this investigation had a different w/c than the concrete and mortar mixtures. The 0.34 w/c paste was selected, based on the estimations in [**20**], to assess the properties of the paste if the effects of the interfacial transition zone were not considered. However, as presented below, the effect to of w/c is relatively minor; therefore it is reasonable to assume a similar result would be obtained from a 0.42 w/c paste.

The effect of w/c on the cohesive laws and fracture energy are shown in Figure 5b and d, respectively. Figure 5b shows that the w/c has a relatively minor effect on the cohesive law as compared aggregate size. The effect of w/c on the fracture energy is plotted in Figure 5d. The fracture energy increases 24% by decreasing w/c from 0.50 to 0.30. Similar results have been seen previously (for example [**6**,19]). The same reduction in w/c caused a 49% increase in stiffness and a 45% increase in tensile strength. Additionally, the effect of age was investigated. Results indicated increases in elastic modulus and tensile strength with time; however, fracture energy varied only slightly with time.

Figure 6 shows the results of the epoxy impregnation of the cracked WST specimens. The area of the crack was determined using image analysis software, and has been plotted versus the CMOD for the 0.42 w/c concrete with small and large aggregate (8 mm and 16 mm maximum size aggregate). Figure 6 shows that the small aggregate concrete developed cracks with a larger crack area for a particular crack width than the large aggregate cracks with a

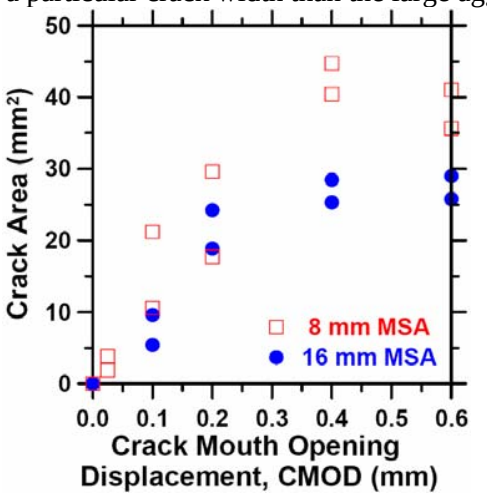

Figure 6. The resulting crack area from varying CMOD's for the 0.42 w/c concrete with 8 mm (small) and 16 mm (large) maximum sized aggregate (MSA) [**21**].

Corresponding author's e-mail: bjp@byg.dtu.dk
Corresponding author's fax:+45 4588 3282

larger crack area for a particular crack width than the large aggregate concrete. As shown in Figure 5a and c the stress transfer and fracture energy increase as the maximum aggregate size increases. The ability of the larger aggregate concrete to transfer stresses at larger crack widths allows this material to restrict the opening of the crack, and therefore maintaining a smaller crack area.

3.2 Unloading Stiffness of the Wedge Splitting Test

Figure 7 shows the result of cyclic load application to a single wedge splitting specimen of Mixture A. The specimen was unloading in both the pre- and post- peak portions of loading, and the load and CMOD have been normalized to the peak vertical load (1500 N) and the corresponding CMOD (0.042 mm). The slopes of the individual unloading responses converge on a common point, referred to as the focal point (σ_0,ε_0), which is shown in Figure 7a. As discussed at greater length in [**22**,**23**] the focal point allows for the determination of the stiffness at any point along the envelope of the load-CMOD response. Figure 7b shows the degrading effect of increasing crack width on the original stiffness, $E_{Original}$. A 1% reduction in stiffness occurred after loading to 47% of the peak load. The degradation of stiffness then increases rapidly, resulting in a 38% reduction in stiffness at peak loading (i.e., normalized CMOD equal to 1). The stiffness continues to degrade with increasing crack width.

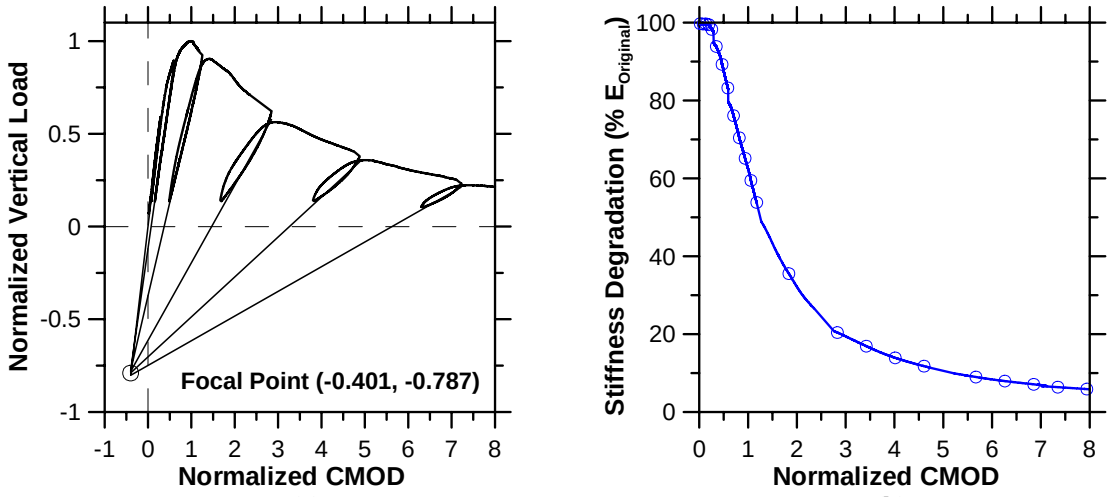

(a) (b)

Figure 7. (a) Cyclic loading of the WST indicates a focal point, and (b) the unloading stiffness degradation

4. SUMMARY

This paper has shown that the wedge splitting test specimen geometry can be used to determine material properties that can describe the fracture behavior of concrete. It has been shown that:

Corresponding author's e-mail: bjp@byg.dtu.dk
Corresponding author's fax:+45 4588 3282

- The use of the normalization function presented in Equation 10 makes it possible to perform a simultaneous inverse analysis on multiple test specimens.
- The inclusion of aggregate resulted in an order of magnitude increase in fracture energy. The critical crack width and the fracture energy increased with the maximum aggregate size. The fracture energy for the large aggregate concrete was 12 times higher than for cement paste. This increase is attributed to the increase in aggregate interlock and friction between fracture surfaces.
- While varying the water-to-cement is typically thought to have a major influence on mechanical properties, the fracture energy and cohesive laws are only slightly affected by such variations. The fracture energy varied only 24% for the water-to-cement ratios used.
- Epoxy impregnation of cracked WST specimen indicates links between the fracture properties and the geometric characteristics of the cracks. It was seen that increasing the fracture energy results in a less tortuous crack geometry.
- The slopes of the individual unloading responses from a cyclic wedge splitting test converge at a focal point, similarly to compression and direct tension results from previous investigations. The focal point allowed for the determination of the stiffness at any point along the vertical load-CMOD curve. The stiffness of the wedge split test specimen rapidly degraded after reaching approximately 47% of the peak load.

ACKNOWLEDGEMENTS

The authors gratefully acknowledge the support provided by the Knud Højgaard Foundation. Additionally, the last author acknowledges the National Science Foundation (Grant No. 0134272) for support. Any opinions, findings, and conclusions or recommendations expressed in this material are those of the author(s) and do not necessarily reflect the views of the research sponsors.

REFERENCES

[1] Dugdale, D. S. (1960) *Journal of the Mechanics and Physics of Solids***8**, 100–104.

[2] Barenblatt, G. I. (1962) *Advances in Applied Mechanics***7**, 55–129 Originally Published in Russian, See e.g. Karihaloo 1995.

[3] Hillerborg, A., Modéer, M., and Petterson, P. (1976) *Cement and Concrete Research***6**, 773–781.

[4] Linsbauer, H. and Tschegg, E. (1986) *Zement und Beton***31**, 38–40.

[5] Brühwiler, E. and Wittman, F. H. (1990) *Engineering Fracture Mechanics***35**, 117–125.

[6] Wittmann, F. H., Roelfstra, P. E., Mihashi, H., Huang, Y.-Y., Zhang, X.-H., and Nomura, N. (1987) *Materials and Structures***20(116)**, 103–110.

[7] Ulfkjær, J. and Brincker, R. (1993) In Fracture and Damage of Concrete and Rock – FCDR-2 : E & FN Spon pp. 135–144.

[8] Kitsutaka, Y. (1997) *Journal of Engineering Mechanics - Proceedings of the ASCE***123(5)**, 444–450.

[9] Østergaard, L. Early-Age Fracture Mechanics and Cracking of Concrete - Experiments and Modeling PhD thesis Technical University of Denmark Lyngby, Denmark (2003).

Corresponding author's e-mail: bjp@byg.dtu.dk

Corresponding author's fax:+45 4588 3282

[10] Olesen, J. F. (2001) *Journal of Engineering Mechanics - Proceedings of the ASCE***127(3)**, 272–280.

[11] Skocek, J. and Stang, H. (2007) *Submitted to Engineering Fracture Mechanics*.

[12] vanMier, J. G. M. (1997) Fracture Processes in Concrete Assessment of Material Parameters for Fracture Models, CRC Press, .

[13] Weiss, W. J., Geiker, M. R., and Hansen, K. K. (2007) *Submitted to Journal of Testing and Evaluation*.

[14] Ulfkj$æ$r, J. P., Krenk, S., and Brincker, R. (1995) *Journal of Engineering Mechanics***121(1)**, 7–15.

[15] Löfgren, I., Stang, H., and Olesen, J. F. (2005) *Journal of Advanced Concrete Technology***3(3)**, 423–434.

[16] Tada, H., Paris, P. C., and Irwin, G. R. (1985) The Stress Analysis of Cracks Handbook, Paris Productions Incorporated, 226 Woodbourne Dr., St. Louis, Missouri, USA.

[17] Laugesen, P. June 2005 In Proceedings of the Knud Højgaard Conference Advanced Cement-Based Materials – Research and Teaching Lyngby, Denmark: . .

[18] Qi, C., Weiss, W. J., and Olek, J. (2003) *Concrete Science and Engineering***36(260)**, 386–395.

[19] Shah, S. P., Swartz, S. E., and Ouyang, C. (1995) Fracture Mechanics of Concrete, John Wiley & Sons, Inc., .

[20] Bentz, D., Detwiler, R., Garboczi, E., Halamickova, P., and Schwartz, L. (1997) In L.O. Nilsson and J.P. Ollivier, (ed.), Proceedings of Chloride Penetration into Concrete, RILEM : .

[21] Weiss, J. and Geiker, M. The influence of cracks on concrete Presentation at ACI Spring Meeting April 24 2007.

[22] Puri, S. and Weiss, J. (2006) *Journal of Materials in Civil Engineering***18(3)**, 325–333.

[23] Yankelevsky, D. Z. and Reinhardt, H. W. (1987) *ACI Materials Journal***84(5)**, 365–373.

Corresponding author's e-mail: bjp@byg.dtu.dk

Corresponding author's fax:+45 4588 3282

Paper II

Photogrammetric assessment of flexure induced cracking of reinforced concrete beams under service loads

Pease, B.*, Geiker*, M., Stang*, H., Weiss, J.†

*Department of Civil Engineering, Technical University of Denmark (DTU Byg), 2800 Kgs. Lyngby, Denmark, e-mail: bjp@byg.dtu.dk

†School of Civil Engineering, Purdue University, West Lafayette, IN, USA 47907

Paper in the proceedings of: *Second International RILEM Symposium, Advances in Concrete through Science and Engineering, Qubec City, Canada, September 2006*

PHOTOGRAMMETRIC ASSESSMENT OF FLEXURE INDUCED CRACKING OF REINFORCED CONCRETE BEAMS UNDER SERVICE LOADS

Brad J. Pease (1), Mette R. Geiker (1), Henrik Stang (1), and W. Jason Weiss (2)

(1) Department of Civil Engineering, Technical University of Denmark, Denmark

(2) School of Civil Engineering, Purdue University, USA

Abstract

Reinforced concrete structures are known to crack due to restrained shrinkage, temperature gradients, application of load, and expansive reactions. Cracks provide paths for rapid ingress of moisture, chlorides, and other aggressive substances, which may affect the long-term durability of the structure. For example, concrete cracks which reach the reinforcing steel may contribute to rapid corrosion initiation and propagation. Previous research has shown that cracked reinforced concrete under static flexural loading may have an increased ingress of chloride ions along the reinforcement/concrete interface.

The aim of this paper is to provide a detailed description of the development of cracks in reinforced concrete under flexural load. Cracking at both realistic service load levels (1.0-1.8 times estimated cracking load) and unrealistically high service load levels (> 0.5 times beam capacity) has been investigated. These load levels result in relatively small cracks (< ~0.1 mm) and cracks larger than expected in field concrete, respectively. The investigation constitutes a preliminary study in a project aimed at describing the effect of cracking on the transport and corrosion behaviors of reinforced concrete.

Reinforced concrete beams were subjected to flexural load and the associated cracking behavior was monitored using three dimensional photogrammetry. The results indicate that minute surface cracks (~10 microns) may cause slip and separation at the reinforcement/concrete interface. This has direct implications on the ingress and corrosion behaviors in concrete subjected to flexural loading, e.g. samples prepared for laboratory studies.

1. INTRODUCTION

A U.S. Federal Highway Administration report estimates the total cost to repair or replace that nation's structurally deficient concrete bridges to be between $78 billion and $112 billion [1]. Furthermore, the estimated average cost to simply maintain a constant number and distribution of deficient bridges was placed at $5.2 billion annually between 2001 and 2011 [2]. These estimates only account for a single structural application of reinforced concrete in one country; however, they alone indicate necessity for control of corrosion in reinforced concrete.

Concrete frequently cracks under even minimal tensile loading (when compared to compressive loading causing crack formation), which may be induced via restrained hygral/thermal shrinkage or by mechanical load. Cracking allows for increased local ingress of substances contributing to corrosion (i.e., chlorides, carbon dioxide, oxygen) near the crack surfaces [3-10]. Permeability increases with crack width and appears to have a dependence on the material type, i.e. paste, mortar, or concrete [3,4]. Results from Aldea et al. [4] indicate that alterations in mixture proportions, such as aggregate content/size and water-to-cement ratio (w/c), may affect crack morphology and the permeability of the cracked material. Expressions for an influence factor of cracks on diffusion of chlorides were developed and showed reasonable correlation with field measurements; however, the investigations did only cover idealized and relatively large cracks (crack width, $w \geq 0.2$ mm) [5]. These expressions indicate diffusion is significantly influenced by cracks width less than 0.2 mm. Similarly, Rodriquez and Hooton [6] have shown that load induced cracks with widths greater than 80 µm act as free surfaces for diffusion of chloride ions. Under specific conditions autogenous (self) healing occurs, which may provide a reduction in chloride migration (28-35% of migration in newly cracked specimen) and improved (reduced) permeability, despite only a minor recovery of mechanical performance [7,8]. In contrast, cyclic loading resulting in the opening and closing of concrete cracks may result in increased chloride ingress [9]; although the importance of this type of loading in structural applications should be further assessed. Finally, results have shown a preferential ingress of chlorides along the reinforcement/concrete interface in cracked concrete [10]. This ingress behavior may affect reinforcement corrosion, specifically anode and cathode size, significantly.

The use of low water-to-cement ratios (w/c) and certain mineral admixtures, such as silica fume, in so-called high performance concrete has resulted in concretes with improved strength, low permeability, and increased electrical resistance. In optimum conditions (i.e., without cracks), such concretes provide a highly protective barrier to ingress. However, these concretes are especially susceptible to early-age cracking [11] due to increases in autogenous shrinkage, material stiffness, and brittleness in conjunction with reduced creep [12]. Field observations support these experimental conclusions as cracking has increased in reinforced concrete bridge decks in recent years [13].

If cracks in reinforced concrete intersect the reinforcement a local depassivation of the steel may occur, and due to the increased ingress behavior a localized corrosion may rapidly initiate. Several studies exist on the effect of cracks on reinforcement corrosion [14-18]. Investigations on uncracked and cracked (with widths between 0.1 mm and 0.7 mm) reinforced concrete showed that crack widths of 0.1 mm, dependent on the w/c and cover, may affect the time to corrosion initiation [14,15]. Concrete with crack widths greater than

0.1 mm allowed corrosion to initiate nearly immediately when exposed to chloride solution. The effect of crack width on the rate of corrosion was found to diminish over time [14]. This suggests that crack parameters effect corrosion initiation more than propagation.

Thus, previous studies [3-10,14-16] indicate that ingress and corrosion behaviors are strongly influenced by crack width and morphology; however, minimal work has been carried out to compare cracks in these experimental investigations with in-situ cracks. These investigations have utilized various methods including splitting tensile loading, direct tensile loading, flexural loading, freeze-thaw cycling, and the use of shims to produce cracks with widths varying between 0.08 mm to 0.70 mm. Limited information has been published concerning cracking of field concrete; however, an investigation of various pavements in Indiana indicates that in-situ cracks may be relatively small compared to the range used in these experiments (even after 25 years of traffic and environmental loading) [19]. Additionally, several studies have used segments of reinforcement to monitor the effect of cracks on corrosion [14-16]. While these studies have provided important insight into the effect of cracks on reinforcement corrosion, the segments are not mechanically accurate which may affect the cracking, ingress, and corrosion behaviors.

The aim of this paper is to investigate the cracking behavior of laboratory specimen which will be used in an investigation of the effect cracks have on ingress and corrosion. In particular emphasis has been placed on developing an experimental technique which allows detailed information about cracking patterns and geometry to be obtained. Such data is critical for development of models for the effect of cracking on transport, corrosion initiation, and corrosion development. Finally, this initial investigation will facilitate comparison with in-situ cracking in future work.

2. RESEARCH SIGNIFICANCE

Cracking in reinforced concrete allows for rapid ingress of chlorides and other deleterious substances which may initiate corrosion of reinforcement. In order to investigate the effect of cracks on ingress and corrosion in laboratory conditions, researchers often use flexural loading. The flexural load-induced cracks may not however accurately represent in-situ cracking. Variation in crack parameters (i.e., width, tortuosity) may result in varying ingress and corrosion behavior. Therefore, a comparison between cracking in a laboratory specimen, designed for a corrosion investigation, and in-situ cracking is needed. This paper presents results of photogrammetric analysis of cracks in laboratory specimen, which will be compared to petrographic analysis and in-situ cracks in subsequent work.

3. EXPERIMENTAL PROCEDURE

3.1 Specimen preparation and mixture design

Reinforced concrete beams with dimensions 150 mm x 150 mm x 600 mm were cast with two 8 mm diameter deformed bar reinforcement, as shown in Figure 1. The mixture designs used, described in Table 1, contained sea sand, and two naturally rounded coarse aggregates with maximum aggregate sizes of 8 mm and 16 mm, respectively. White Portland cement from Aalborg Portland, Denmark, was used in all mixtures. The beams were cast with the reinforcement near the bottom of the form to reduce the effect of bleeding on the transition zone. The specimen were cast in three layers, vibrated, and finished using a steel trowel. The beams remained in the forms for 24 hours at 20°C, were demolded and placed in water

saturated with lime at 20°C for an additional 55 days. Three cylinders for each mixture were cast and cured under identical conditions for 28 days for standard compressive strength measurements.

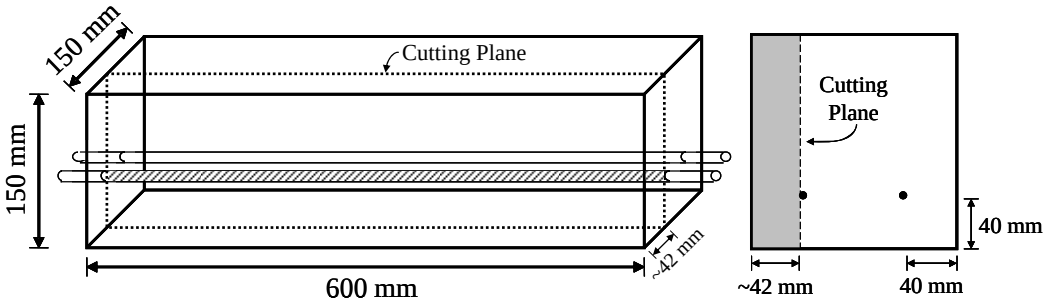

Figure 1: Specimen Geometry with Location of Saw Cutting Indicated.

After removal from the lime saturated water a concrete saw was used to cut the covering concrete from one side of the reinforced concrete beams (see Figure 1) to expose the reinforcement. Approximately 2 mm of the 8 mm diameter reinforcing bar was cut away to provide a view of the reinforcement. Figure 2(a) shows an example of one of the beams after saw cutting where it is possible to see both the concrete and reinforcing steel. Following saw cutting the surfaces of the concrete and steel were further prepared to allow for three dimensional (3-D) photogrammetry analysis of cracking at the interface. Further details on the surface preparation necessary for 3-D photogrammetry are provided in Section 3.2. After saw cutting and surface preparation for photogrammetry the samples were stored sealed in plastic until testing.

Table 1: Mixture Proportions, Compressive Strength, and Beam Failure Load

Mix Design	w/c	Cement Content	Sea Sand	4-8 mm	8-16 mm	f'c	Beam Failure Load
	-	kg/m^3 (lb/yd^3)	kg/m^3 (lb/yd^3)	kg/m^3 (lb/yd^3)	kg/m^3 (lb/yd^3)	MPa (psi)	kN (kips)
1	0.50	330 (556)	809 (1363)	1073 (1808)	-	43 (6200)	52.2 (11.7)
2	0.50	330 (556)	766 (1291)	150 (252)	953 (1606)	39 (5700)	54.9 (12.3)

3.2 Testing procedures

Two test series were preformed by applying varying loads in three point bending over a span length of 500 mm. 3-D photogrammetry measurements, which are discussed further in the following section, were taken for both test series. Series I involved testing of one specimen from each mixture. In the initial test series an increasing load level was applied to a single specimen to assess which loads were of interest for further analysis. The estimated cracking loads of the cut specimen, determined using the ACI Building Code, were found to be 13.6 kN and 13.0 kN for the 8 mm and 16 mm maximum aggregate size specimen, respectively. The specimen was loaded to multiples of the estimated cracking load including 1.0, 1.2, 1.4, 1.6, and 1.8. Additionally, the beams were loaded to 30.0 kN and 35.0 kN to investigate cracking under more extreme loading conditions. Load was applied at a constant rate for three minutes to the maximum load followed by unloading over the same amount of time. The beams used for the Series I were then loaded to failure, however photogrammetry measurements were not taken due to danger of damage to the equipment. It should be noted

that previous cracking of specimens caused stiffness reductions affecting the crack opening response, necessitating Series II testing on previously unloaded samples to determine the actual cracking response. Thus, based upon the Series I results additional measurements were taken for Series II, on uncracked samples, at load levels including 1.4 and 1.8 times the estimated cracking load and at 35.0 kN.

3.3 3-D photogrammetry setup

A commercially available 3-D photogrammetry system was utilized to provide quantitative and qualitative information on the cracking behavior in the specimen. In order to facilitate photogrammetry measurements adequate contrast in the grayscale of individual objects is required. This was achieved by using black and white spray paint to apply a stochastic spatter pattern as seen in Figure 2(b). The individual aggregates remained clearly visible through the black and white spatter pattern. The surface of the reinforcement was also painted white to eliminate reflection of light from the polished steel.

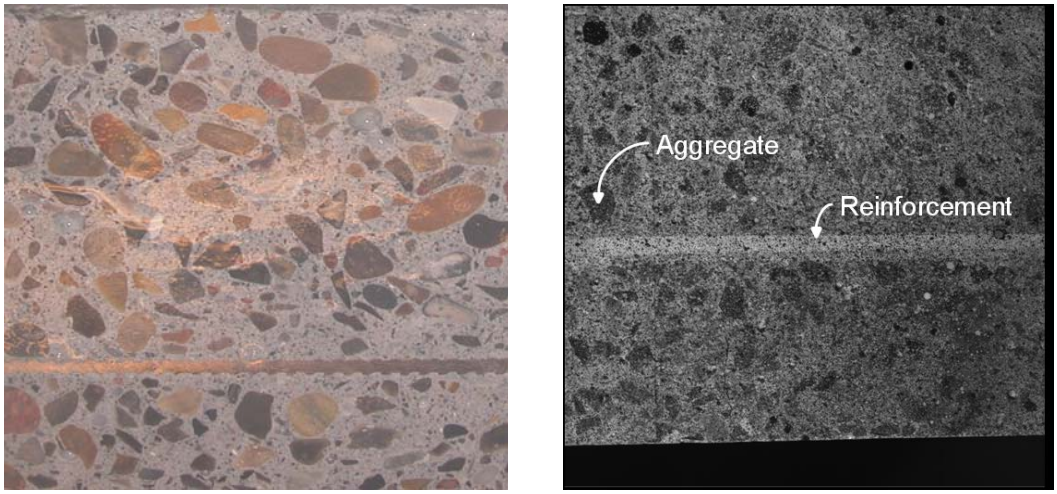

(a) (b)

Figure 2: Specimen Surface after Saw Cutting with Exposed Reinforcement (a) prior to and (b) after Application of Spatter Pattern.

The photogrammetry system uses two charged couple device (CCD) digital cameras to capture images at a predefined interval, once every second during testing in this case. The two CCD cameras were positioned at the same height and were focused on the same surface, but from different angles. The individual cameras will be referred to as camera right and camera left in the following explanation. A calibration is preformed prior to testing, using a calibration plate provided by the manufacturer, in order to insure accurate measurements. At each image capture interval, or stage an image from both cameras was taken. Figure 2(b) shows an image from one of the cameras, which were focused on a 100 mm x 100 mm area at the tension face directly opposite the applied load in order to monitor cracking. Based on the manufacture's specification an accurate of $1x10^{-5}$ times the image dimension (or 1 μm for the specimens used here) is possible for this equipment. A comparison of crack widths measured using the photogrammetry equipment and an extensiometer clip gage showed reasonable

accuracy (±5 μm). In order to calculate strain and displacement in the reinforced concrete beams a computational mask is applied by the provided software to the initial, non-deformed specimen surface image from camera left, see Figure 3(a). The mask consists of 15 x 15 pixel facets which overlap by two pixels, corresponding to length units of approximately 0.7 mm x 0.7 mm and 0.1 mm, respectively. The software then associates individual facets with the grayscale image contained within. Next, the software 'finds' the corresponding facets in the initial, non-deformed camera right image by searching for the same grayscale images. The software then tracks the deformation of the individual facets as load is applied. Figure 3(b) depicts the deformed computational mask after loading and cracking of a specimen. The discontinuity introduced by the crack in Figure 3(b) causes some facets to be lost as the software is unable to locate the appropriate grayscale images. The 2-D coordinates of the individual facets from the right and left camera images are determined and photogrammetric techniques are used to calculate 3-D movements. Using this, strain is calculated and visualized and point-point displacements are may be determined at any point on the measured surface. Additional information on the photogrammetry equipment, software, and the techniques employed therein can be found elsewhere [20].

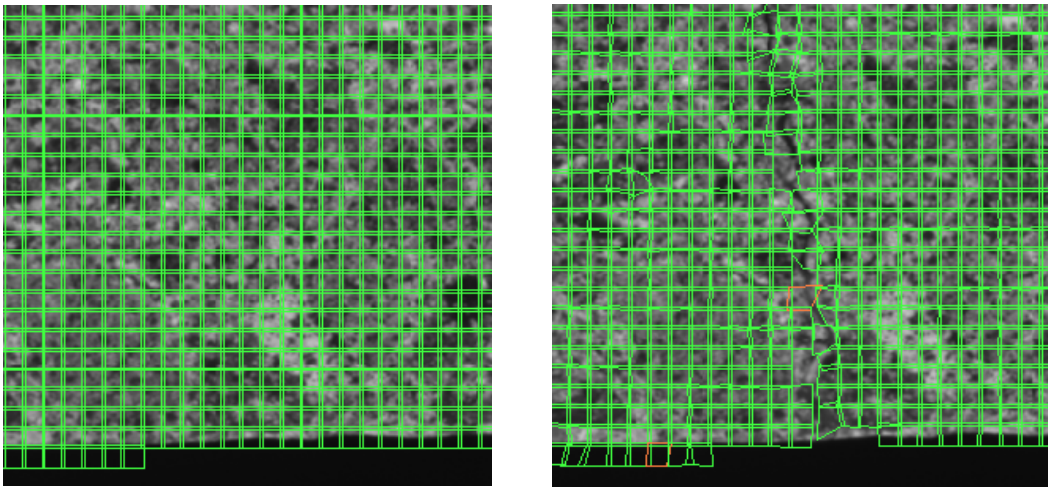

(a) (b)

Figure 3: Specimen Surface with Computational Mask Applied over the (a) Non-Deformed Specimen (Initial Stage) and (b) Deformed Specimen (Images are Zoomed).

4. RESULTS

A computational mask, as shown in Figure 3 is utilized to compute major strain in individual facets. This calculated strain is visualized using a color spectrum (similar to finite element analysis) and overlaid on an image of the specimen surface as shown in Figure 4. The strain overlay however contains holes where strain computations were not possible. These holes may be caused by inadequate contrast in grayscale, which is easily corrected by applying additional paint spatter before loading, or by inconsistent images from the two camera angles. The latter presents a problem for cut concrete surfaces due to the presence of large air voids. Voids, when viewed from different angles, vary visually due to changes in the line of sight. The larger voids were filled with paraffin wax to allow strain computations, however some

voids remained. The strain is computed based upon the deformation in the computational mask as opposed to strain in the actual material. Therefore, Figure 4 shows excessive strain at the crack surface, which is inaccurate in terms of actual material behavior as the presence of a crack would relieve strain locally. This erroneous representation is explained by Figure 3(b) which shows the facets directly next to the crack are substantially deformed after cracking of the concrete. However with this flaw, the computed strains provide useful qualitative information on the cracking behavior in reinforced concrete.

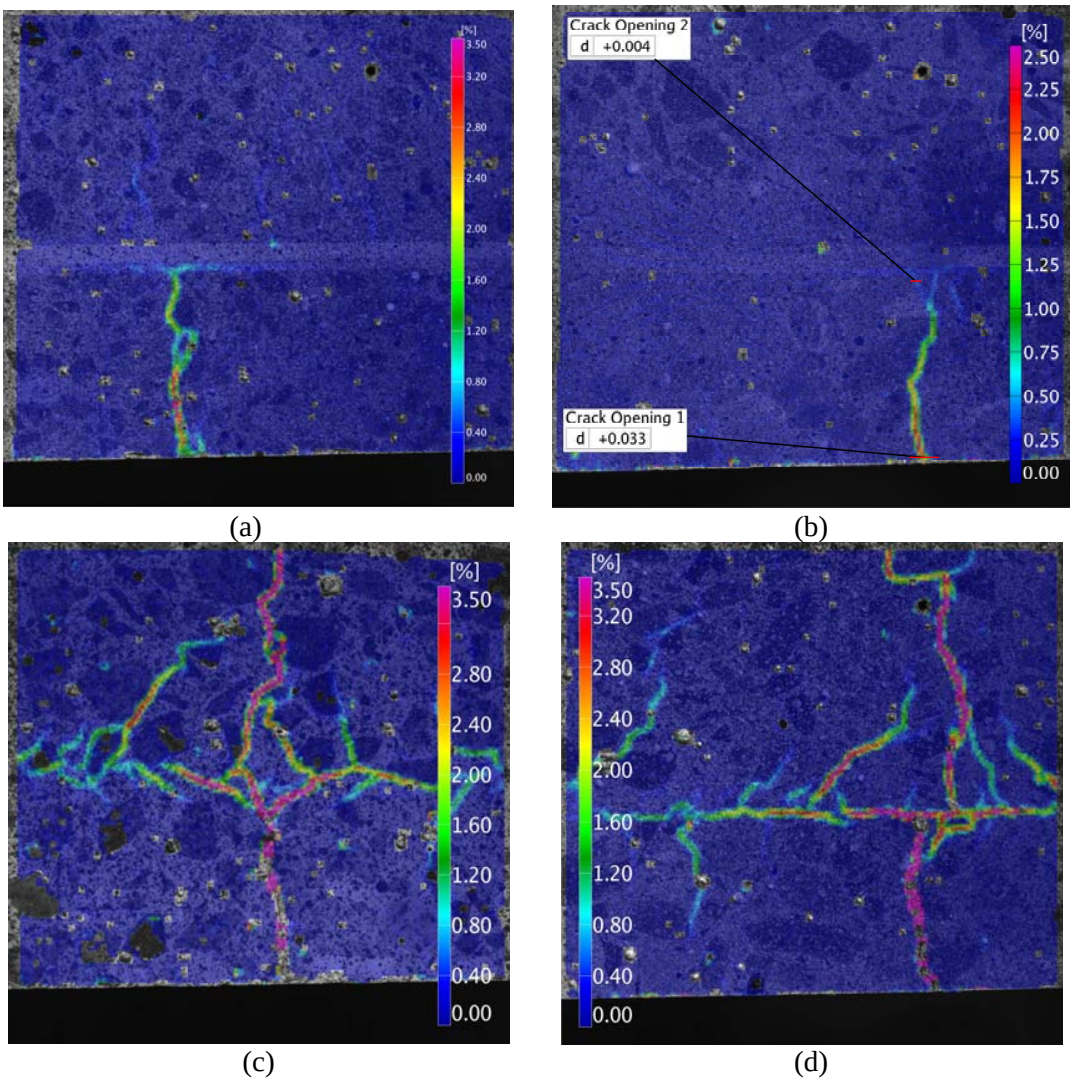

Figure 4: Computed Strain Overlay on Specimen with (a) 8 mm Maximum Aggregate Size under Estimated Cracking Load (14.0 kN) and with 16 mm Maximum Aggregate Size under (b) Estimated Cracking Load (13.0 kN), (c) 35.0 kN (single load), and (d) 35.0 kN (increasing cyclic load).

The computed strain in specimens with 8 mm and 16 mm maximum aggregate sizes while subjected to the estimated cracking load is shown in Figure 4(a) and 4(b), respectively. The transverse cracking propagates near aggregate interfaces and extends to the reinforcement; however, due to effect of the aggregate size the path of the cracks vary. The crack in the 8 mm maximum aggregate size specimen propagates completely around an aggregate and appears to be more tortuous than the crack in the larger aggregate size. In addition, the computed strain indicates that slight slip and/or separation occurs at the reinforcement/concrete interface even at these low load levels. Figure 4(c) shows the crack in a 16 mm maximum aggregate size specimen under 35.0 kN load. The transverse crack depth increases and extends past the reinforcement towards the neutral axis. The minimal slip and/or separation seen in Figures 4(a) and (b) has increased to extensive cracks which run parallel to the reinforcement. These cracks extend in both directions from the transverse crack in excess of 50 mm and beyond the measuring area. Figure 4(d) shows the cracking behavior in a 16 mm aggregate sample which was subjected to increasing cyclic loading (as discussed in Section 3.2). Although a non-uniform load level was applied, the effect of cyclic loading is still apparent when comparing Figure 4(c) with 4(d). After cyclic loading a continuous, nearly straight-line crack is seen at the reinforcement/concrete interface as opposed to the highly tortuous discontinuous cracking after a single load. The individual cracks seen in Figure 4(c) may therefore coalesce into a continuous crack under cyclic load, which would allow for a more rapid ingress of aggressive substances along the reinforcement. It should also be mentioned that the tortuous crack shown in Figure 4(a) had also coalesced after cyclic loading.

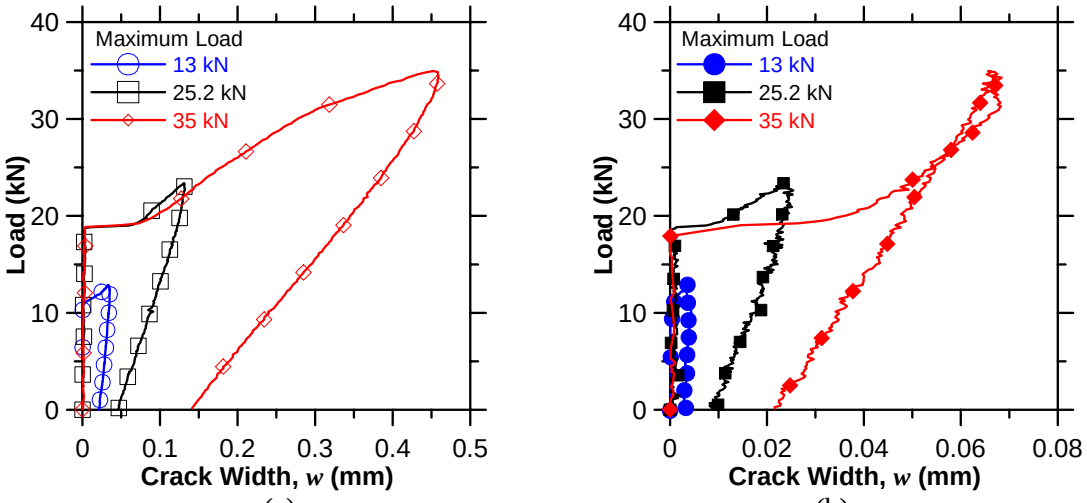

(a) (b)

Figure 5: Transverse Cracking Response at Varying Loads in 16 mm Maximum Aggregate Size Specimen (a) at the Tension Face and (b) next to the Reinforcement.

Figure 4(b) shows an example of a point-point displacement measurements near the tension surface (Crack Opening 1) and near the reinforcement (Crack Opening 2). Additional point-point displacement measurements show the response at the reinforcement/concrete interface approximately 5 mm to the side of the transverse crack. Figure 5 shows the

transverse crack width as determined by a point-point displacement measurement versus the applied load for the 16 mm aggregate size specimen at varying load levels. The cracking at the tension face is shown in Figure 5(a) while the crack width near the reinforcement is seen in Figure 5(b). The crack width at the tensile face initiates at approximately 11 kN for the specimen loaded to 13.0 kN. The crack then opens rapidly to a maximum of 35 µm (it should be noted this crack was too small for visual observation during testing). The specimens loaded to higher levels cracked at higher loads, possible due to the increased loading rate. The crack widths at the tension face were measured by Aramis to be 0.13 mm and 0.46 mm at a load of 23.4 kN (1.8 times the estimated cracking load) and 35.0 kN, respectively. Figure 5(b) shows that the crack immediately propagates to the reinforcement and that the width at the reinforcement is significantly reduced compared to the crack width at the tensile face. Upon complete unloading, the crack remains open even near the reinforcement.

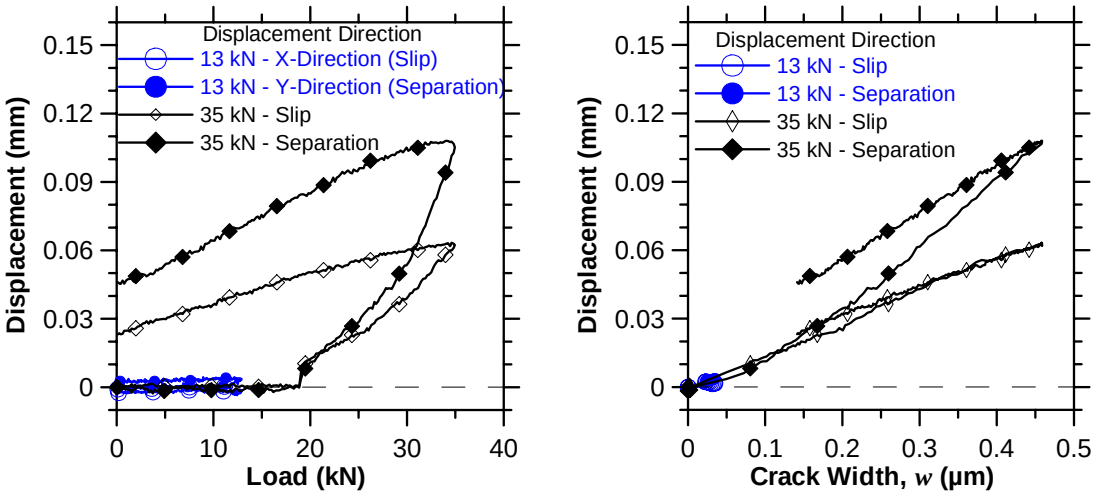

Figure 6: Cracking Response (i.e., Slip and Separation) at the Reinforcement/Concrete Interface versus (a) Load and (b) Crack Width at the Tension Face for 16 mm Maximum Aggregate Size Specimen.

Figure 4 showed that as the transverse crack reached the reinforcement cracking will continue parallel to the reinforcement. Therefore, point-point measurements were taken to determine the extent of this cracking. Figure 6 shows the corresponding slip and separation between the reinforcement and concrete due to increased flexural loading. Displacements were measured in the x-direction correspond to slip and the y-direction corresponding to separation. Figure 6(a) shows that separation between the reinforcement and concrete is effected more by the application of load resulting in a maximum separation of approximately 0.11 mm at 35.0 kN load. The slip is however also significant, reaching 0.06 mm at the extreme load level. At 13.0 kN, which resulted in a crack width at the tension face of only 36 µm, slip and separation also occurs, although to a minimal level (less the 5µm). Figure 6(b) shows the slip and separation as a function of the crack width at the tension face. Displacements at the reinforcement/concrete interface initiate and increase nearly immediately after cracking at the tensile face.

5. CONCLUSIONS

This paper has demonstrated that commercially available 3-D photogrammetry equipment may provide both qualitative and quantitative information on the cracking behavior of reinforced concrete. It has been shown that:

- While the strains shown by photogrammetric analysis are based upon deformation of facets in a computational mesh as opposed to actual material strain, the capability of visualizing cracks and measuring crack displacements prove quite useful.
- The strain data and point-point displacement measurements provide a means of creating a full field map of the cracking geometry and openings in reinforced concrete with a resolution of a few micrometer of crack opening. Such maps are essential for subsequent development of detailed models of cracking, ingress, and corrosion behavior. Furthermore, the effect of differences in material and loading characteristics on crack patterns may be visualized and quantified.
- Qualitative analysis of the computed strain overlay on a specimen image showed that the 8 mm aggregate specimens resulted in more tortuous cracks than the 16 mm aggregate specimen under single load applications, and that cracks coalesce into interconnected cracks under cyclic loading.
- Quantitative analysis of the cracking behavior showed that minimal cracking ($w \approx 35$ μm) at the tension face results in cracks near the reinforcement, which are not completely closed at unloading.
- Slip and separation between the reinforcement and concrete were found to develop and increase nearly immediately after transverse crack initiation at the tension face.
- Slip and separation along the reinforcement extend typically from approximately 10 mm to over 50 mm from the transverse crack depending on load level and number of load applications.

ACKNOWLEDGEMENTS

The authors gratefully acknowledge the support received from the Villam Kann Rasmussen Foundation to purchase the Aramis 3-D photogrammetry system. Additionally, the assistance of Lennart Østergaard with the Aramis system was instrumental to this work.

REFERENCES

[1] Virmani, Y.P. and Clemena, G.G., 'Corrosion Protection—Concrete Bridges,' *FHWA Report No. FHWA-RD-98-088* (September 1999).

[2] Koch, G.H., Brongers, M.P.H., Thompson, N.G., Virmani, Y.P., Payer, J.H., 'Corrosion Cost and Preventive Strategies in the United States,' *FHWA Report* (September 2001) (Available at www.corrosioncost.com).

[3] Wang, K., Jansen, D.C., Shah, S.P., and Karr, A.F., 'Permeability Study of Cracked Concrete,' *Cem. Concr. Res.* **27** (3) (1997) 381-393.

[4] Aldea, C.-M., Shah, S.P., and Karr, A., 'Permeability of Cracked Concrete,' Mater. Struct. **32** (June 1999) 370-376.

[5] De Schutter, G., 'Quantification of the Influence of Cracks in Concrete Structures on Carbonation and Chloride Penetration,' *Mag. Concr. Res.* **51** (6) (December 1999) 427-435.

[6] Rodriguez, O.G. and Hooton, R.D., 'Influence of Cracks on Chloride Ingress into Concrete,' *ACI Mater. J.* **100** (2) (March-April 2003) 120-126.
[7] Edvarson, C., 'Water Permeabiltiy and Autogenous Healing of Cracks in Concrete,' *ACI Mater. J.* **96** (4) (July-August 1999) 448-454.
[8] Jacobsen, S., Marchand, J., and Boisvert, L., 'Effect of Cracking and Healing on Chloride Transport in OPC Concrete,' *Cem. Concr. Res.* **26** (6) (1996) 869-881.
[9] Küter, A., Geiker, M.R., Olesen, J.F., Stang, H., Dauberschmidt, C., and Raupach, M., 'Chloride Ingress of Concrete Cracks under Cyclic Loading,' *Proc. ConMat'05* (Vancouver, BC, Canada) (August 22-24, 2005).
[10] Win, P.P, Watanabe, M., and Machida, A., 'Penetration Profile of Chloride Ions in Cracked Reinforced Concrete,' *Cem. Concr. Res.* **34** (2004) 1073-1079.
[11] Shah, S.P. and Weiss, W.J., 'High Strength Concrete: Strength, Permeability, and Cracking,' *Proc. PCI/FHWA Int. Symp. on HPC* (Orlando, Florida, 2000) 331-340.
[12] Weiss, W.J., Yang, W., and Shah, S.P., 'Factors Influencing Durability and Early-Age Cracking in High-Strength Concrete Structures,' *ACI SP-189 High Per. Concr.: Res. to Practice* (January 2000) 387-410.
[13] Darwin, D., Browning, J., and Lindquist, W.D., 'Control of Cracking in Bridge Decks: Observations from the Field,' *Cem. Concr. Agg.* **26** (2) (December 2004) 148-154.
[14] Schieβl, P., and Raupach, M., 'Laboratory Studies and Calculations on the Influence of Crack Width on Chloride-Induced Corrosion of Steel in Concrete,' *ACI Mater. J.* **94** (1) (January-February 1997) 56-62.
[15] Mohammed, T.U., Otsuki, N., Hisada, M., and Shibata, T., 'Effect of Crack Width and Bar Type on Corrosion of Steel in Concrete,' *J. Mater. Civil Engng.* **13** (3) (2001) 194-201.
[16] Marcotte, T.D. and Hansson, C.M., 'The Influence of Silica Fume on the Corrosion Resistance of Steel in High Performance Concrete Exposed to Simulated Sea Water,' *J. Mater. Sci.* **28** (2003) 4765-4776.
[17] Berke, N.S., Dallaire, M.C., Hicks, M.C., and Hoopes, R.J., 'Corrosion of Steel in Cracked Concrete,' *Corrosion Engineering* **49** (11) (1993) 934-943.
[18] Arya, A., and Ofori-Darko, F.K., 'Influence of Crack Frequency on Reinforcement Corrosion in Concrete,' *Cem. Concr. Res.* **26** (3) (1996) 345-353.
[19] Yang, Z., 'Assessing Cumulative Damage in Concrete and Quantifying its Influence on Life Cycle Performance Modeling,' *Ph.D. Thesis* (Purdue University, West Lafayette, IN) (2004).
[20] GOM Optical Measuring Techniques, 'Aramis v5.4 User Manual,' *GOM mbH* (2005) (www.gom.com).

Paper III

Assessing the portion of the crack length contributing to water sorption using X-ray absorption measurements on concrete wedge splitting specimens

Pease, B.*, Couch, J.†, Geiker*, M., Stang*, H., Weiss, J.†

*Department of Civil Engineering, Technical University of Denmark (DTU Byg), 2800 Kgs. Lyngby, Denmark, e-mail: bjp@byg.dtu.dk

†School of Civil Engineering, Purdue University, West Lafayette, IN, USA 47907

Paper in the proceedings of: *ConcreteLife '09: 2nd International RILEM Workshop on Concrete Durability and Service Life Planning, Haifa, Israel, 2009*

ASSESSING THE PORTION OF THE CRACK LENGTH CONTRIBUTING TO WATER SORPTION IN CONCRETE USING X-RAY ABSORPTION

Brad Pease[1], Jon Couch[2], Mette Geiker[1], Henrik Stang[1], and Jason Weiss[2]

(1) Department of Civil Engineering, Technical University of Denmark, Lyngby, Denmark

(2) School of Civil Engineering, Purdue University, West Lafayette, IN, USA

Abstract

While it is generally known that cracks accelerate fluid movements, there is a need to quantify how cracks influence the controlling transport mechanism(s) for more accurate service life modeling. This paper describes an experimental approach using x-ray absorption measurements to quantify the influence of cracks with varying width and length on water sorption in concrete. Concrete wedge splitting specimens, conditioned to 50% relative humidity, were loaded to varying crack openings. Water sorption was monitored for ponded specimens with varying crack widths and lengths by taking multiple x-ray absorption measurements over time. The effect cracks have on sorption is discussed and compared to the behavior of pristine concrete. In addition, the maximum water sorption depth after one hour of exposure is compared to crack lengths determined by the cracked hinge model.

1. INTRODUCTION AND MOTIVATION

It is generally accepted that the presence of cracks in concrete allow for a more rapid ingress of aggressive substances, possibly leading to durability issues and shortened service life. To date however, few quantitative results relate the controlling processes of cracking and ingress; namely linking fracture mechanics approaches with fluid or ion transport behavior in cementitious materials.

In this paper, concrete wedge splitting test (WST) specimens were used to measure fracture parameters and ingress behavior. Elastic modulus, tensile strength and the cohesive law for concrete fracture were estimated via inverse analysis. Water sorption was monitored in cracked, non-saturated specimens using an x-ray camera. The comparisons indicate that cracks consist of two portions, an 'apparent crack' – behaving approximately like a free surface for ingress – and an 'inhibited crack.'

2. EXPERIMENTAL APPROACH

This paper outlines initial results from an experimental study which intends to quantify the effect cracking has on the ingress of water and aggressive substances into concrete. In this research program concrete WST specimens were cast, cured, conditioned, and placed under mechanical loading to introduce cracks with varying lengths and widths. The cracked WST

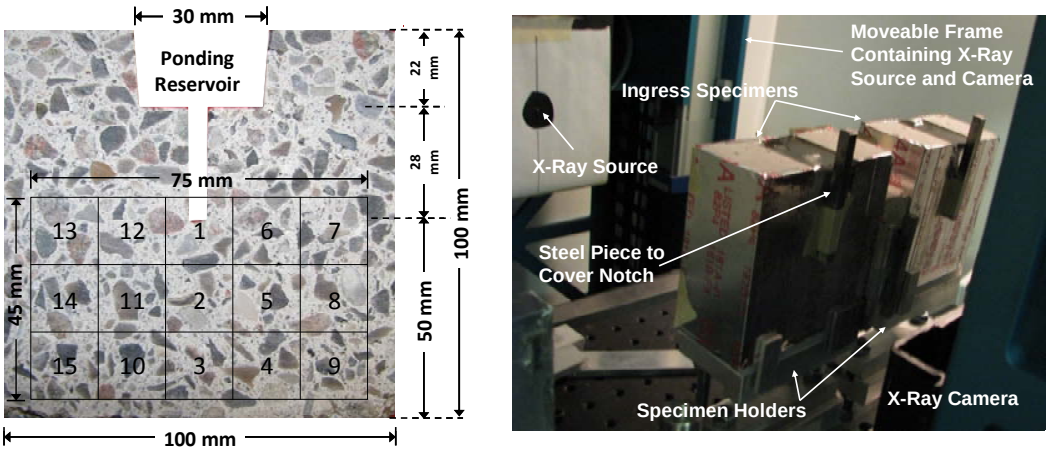

(a) *(b)*

Figure 1. *(a)* The WST specimen geometry and details on location of x-ray images and *(b)* x-ray system setup including moveable frame, x-ray source and camera, and specimen holders.

specimens were used to monitor water sorption via non-destructive x-ray measurements. Details on the experimental approach are given in the following sections.

2.1 Mixture Proportions and Specimen Preparation

Concrete WST specimens, with dimensions shown in Figure 1*(a)* and thickness of 100 mm, were prepared using a water-to-cement ratio of 0.50 and a cement content of 330 kg/m^3. Aalborg White© portland cement was used with chemical composition consisting of 78.8% C_3S, 10.5% C_2S, 4.9% C_3A, 1.0% C_4AF, 0.6% MgO, 2.1% SO_3, and an Na_2O equivalent alkali content of 0.19%. Aggregate consisted of washed Class E 0-4 mm sea-sand, and washed Class A 4-8 mm sea-gravel (in accordance with [1]). The concrete contained 72.5% aggregate by volume, 776 kg/m^3 fine aggregate and 1103 kg/m^3 coarse aggregate.

The concrete was mixed using a standard pan mixer with a 120 L capacity. The fine and coarse aggregate were first mixed dry for 1 minute, followed by 3 minutes mixing with one third of the mixing water. Mixing was stopped for 2 minutes prior to adding cement and mixing for 1 minute. The remaining water was then added and mixing continued for 3 minutes after addition of water. The mixer was then opened and the pan and blades were scraped, followed by 1 additional minute of mixing.

The concrete was placed and vibrated into molds and allowed to cure, covered by plastic, for 24 hours at ~20°C. WST specimens were cast in special molds to position the ponding reservoir vertically at the mold wall (i.e., the mold has cross-section shown in Figure 1*(a)* when viewed from above). Upon demolding, specimens were sealed with multiple layers of plastic, placed in sealed plastic storage containers, and stored at 20°C ±1°C for 6 days prior to storing in an oven at 45°C ±1°C until reaching a maturity age of ~1 year (using an activation energy 33.5 kJ/mol [2]). During the accelerated curing phase water was placed in the oven to minimize moisture loss in the sealed specimens. After curing, a 28 mm deep notch was cut using a wet saw, followed by halving the specimen perpendicular to the notch, resulting in two separate 50 mm thick specimens. The specimens were then allowed to dry in a 50% ±2% relative humidity, 23°C ±1°C chamber for 18 months prior to testing.

Load was applied to WST specimens via a rigid wedge and roller bearing to varying pre- and post-peak load conditions to induce crack growth. Additional information on the WST procedure is available in literature [3]. Three companion specimens were tested to failure for average fracture parameter determinations as described below. Water sorption was monitored for WST specimens that were unloaded, loaded to peak load and cracked with crack mouth opening displacements (CMOD's) of 0.10, 0.15, 0.20, and 0.40 mm. In order to maintain the induced crack openings in post-peak load specimen, loading was paused at the desired CMOD and 2 hard plastic shims were placed into the notch prior to load removal. Minimal CMOD recovery occurred in post-peak load specimens when using the wedges (~0.01 mm). Immediately after unloading, the specimens were sealed with aluminum tape on all sides, except the top, in order to create a reservoir for ponding. The tape was smoothed to insure a tight seal with the specimen surface (to avoid leakage). Specimens were then stored at 50% ±2% relative humidity and 23°C ±1°C until x-ray absorption testing.

2.2 Inverse Analysis of the Cracked Hinge Model

As previously mentioned, three WST specimens were used to determine fracture parameter. The WST can be used to determine the cohesive law, elastic modulus and tensile strength for a material through inverse analysis utilizing an appropriate model (e.g., minimizing difference between model calculations and experimental results by altering mechanical parameters). The inverse analysis procedure developed in [3] and further modified in [4] applies to the cracked hinge model [5,6] and was implemented on the WST geometry as shown in Figure 2. Figure 2*(a)* shows the crack hinge model (CHM) which simulates the area directly surrounding a propagating crack in the WST specimen using the stress profile shown in Figure 2*(c)*. The cracked hinge is joined to the remaining area via rigid boundaries which are allowed to translate and rotate as indicated in Figure 2*(b)*. The rigid boundaries seamlessly join the bulk (uncracked) specimen, where the behavior is controlled by Hooke's Law.

An inverse analysis procedure developed in [4] was used to estimate material properties (it was found that a cohesive law with three slopes provided the best fit). Additionally, the CHM provides an estimate of the crack profile at the various conditions considered for ingress testing. As show in [7] the angular deformation, φ (Figure 2*(b)*) of the crack hinge is determined during the inverse analysis, and can be used to calculate the crack profile for a particular load. Estimated profiles compared reasonable well to crack profiles determined using photogrammetry [7].

2.3 X-ray Absorption Measurement Technique

Several researchers have used x-ray absorption measurements to monitor fluid or moisture movements in cementitious materials in a non-destructive manner [8,9,10,11,12]. Here, x-ray absorption measurements in a GNI x-ray system located at Purdue University [13] were used to monitor water sorption in WST specimens. As shown in Figure 1*(b)*, the WST specimens were place between the x-ray source and camera, with 500 mm from the source to camera, and 392 mm from source to specimen. The x-ray source and camera are housed in a programmable, moveable frame (Figure 1*(b)*). Through trials, x-ray source energy levels of 75 keV and 100 μA were determined adequate for the specimen thickness used. X-ray absorption behavior varies with density changes caused by addition of water to the concrete. The x-ray absorption of the specimens was measured using a 25 mm x 25 mm x-ray camera.

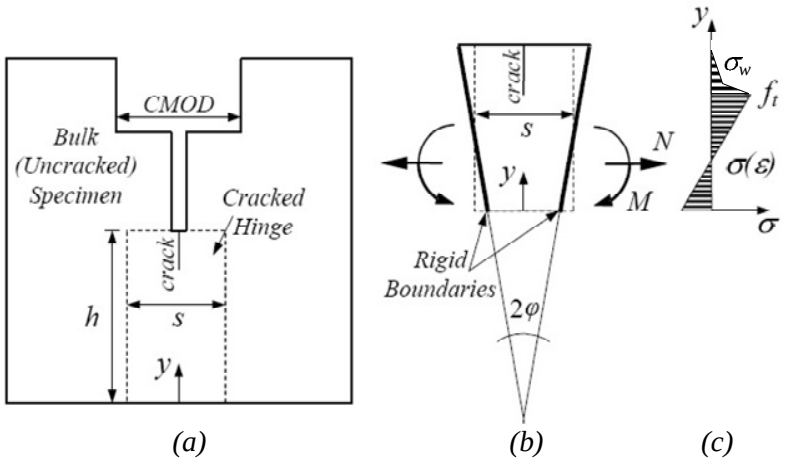

Figure 2. *(a)* The WST specimen with the cracked hinge model applied, *(b)* Loading and deformation of the hinge (after [8]), and *(c)* the assumed stress distribution (after [11]).

The camera consists of NaI crystals, which emit visible light when impacted by an x-ray photon; and a 252x256 pixel photomultiplier, which records the number of light events at each pixel over a set period of time (5 seconds used here). These light events are referred to as counts. Images from the x-ray camera were taken over the area of the specimen indicated in Figure 1*(a)* using 15 mm movements, proceeding in the order indicated. At each measurement location, 10 images were captured, cropped, de-speckled, averaged, tiled, shifted, and analyzed using a batch code written in ImageJ [14,15,16]. Reference measurements were initially taken on the dry specimens. After the reference measurements were taken the specimens were ponded with tap water. Additional x-ray measurements were taken immediately after the introduction of water (i.e., 1 minute) as well as 1, 2, 3, 4, 6 and 24 hours after water addition.

It is important to note the differences in data provided by an x-ray camera and an x-ray detector. In [8,9,10,11,12] x-ray detectors were used to measure x-ray absorption at a single point (or small area) in a specimen over a period of time. Spatial data was provided by repeating measurements at many locations, moving the x-ray source and detector relative to the specimen. In [12], an x-ray detector was used to observe water sorption in WST specimen over a comparable sized area using a grid of 91 measurement points (13x7 pixels). Here, using an x-ray camera at 15 measurement areas (Figure 1*(a)*) a grid of 695506 points were monitored (1057x658 pixels). The measurement process took approximately 28 minutes.

An empirical water absorption index (*ABS)* was computed using the x-ray images and the algorithm shown in Equation 1

$$ABS = \frac{\left(I_{x,y}\right)_{Dry} - \left(I_{x,y}\right)_{Wet,i}}{\left(I_{x,y}\right)_{Dry} - \left(I_{x,y}\right)_{Wet,n}} \cdot 100\% \qquad \text{Equation 1}$$

where $(I_{x,y})_{Dry}$ and $(I_{x,y})_{Wet,i}$ are the counts in each pixel of the dry image and wet image taken at each individual (i hours) and final measurement time (n = 6 hours). After 6 hours of ponding, the initial moisture front had passed through the measurement area. While the entire pore structure is not saturated after 6 hours, little change in x-ray absorption was seen after

this time. The normalization to the 6 hour measurement accounts for differences in counts that occur due to variations in paste content in the concrete [12].

3. EXPERIMENTAL RESULTS

3.1 Inverse Analysis and Crack Profile Estimation

Figure 3*(a)* shows the average cohesive law determined through inverse analysis of three WST specimens loaded to failure. The critical crack width (minimum width causing a stress-free crack) was found to be 0.66 mm. The elastic modulus and tensile strength were estimated at 31.4 GPa and 3.2 MPa, respectively.

Using these material parameters and the angular deformation of the cracked hinge, φ shown in Figure 2*(b)*, the crack profile can be calculated [6]. The estimated crack profiles for the CMOD's used in this study are shown in Figure 3*(b)*, with the crack length (in terms of depth into WST specimen) versus CMOD response shown in Figure 3*(c)*. At peak loading a crack length of 24.5 mm was estimated, although with narrow crack opening displacements (Figure 3*(b)*). Figures 3*(b)* and *(c)* show crack length increases with larger CMOD's to a length of 45.2 mm for the 0.40 mm CMOD specimen. Figure 3*(c)* indicates that initially crack length increases rapidly at smaller CMOD's (< 0.15 mm) followed by more stable crack growth. In addition, as the CMOD increases tractions reduce according to the cohesive law resulting in the slope change in crack profiles shown in Figure 3*(b)*.

Photogrammetry measurement of the crack profile at the WST specimen surface have been shown to agree well with estimated crack profiles, especially with post-peak loading [7]. It is important to note that the CHM uses the cohesive law (Figure 3*(a)*) to simplify fracture processes of concrete and assumes a single discrete crack with an idealized shape. However, in actuality the crack opening displacement at a particular depth of the concrete is likely comprised of coalesced cracks, crack branches, and/or isolated microcracks. As discussed in the following sections, the crack behavior (coalesced, branched, isolated) may have implications on ingress behavior.

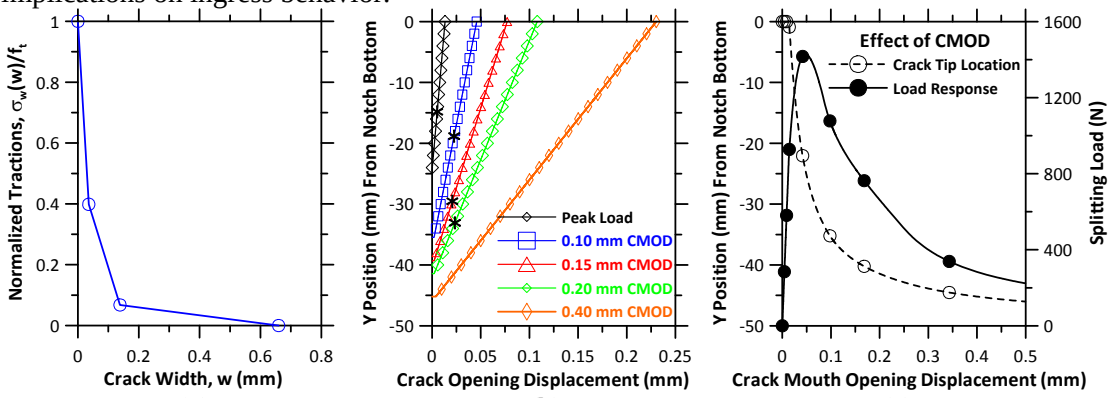

Figure 3. *(a)* The cohesive law from inverse analysis, *(b)* crack profiles from CHM with asterisks indicating maximum sorption depth after 1 hour of ponding, and *(c)* the effect of CMOD on crack length from the notch bottom (dash line) and load response (solid line).

3.2 Moisture Ingress Measurements

Figure 4*(a)* shows a contour plot of the moisture ingress (the *ABS* ratio) after 1 hour of water ponding for the 0.15 mm CMOD specimen, as calculated from Equation 1. The black rectangle indicates the location of the notch. Water traveled rapidly through cracks resulting in an accelerated ingress behavior into the depth of the WST specimens. Similar accelerated ingress behavior was seen for all cracked specimen after 1 hour of water exposure as illustrated in Figure 4*(b)*.

Using the 75% *ABS* ratio contour lines from the x-ray measurements taken 1 hour after water exposure, the lateral sorption was determined at varying depths in the specimens (Y-position). The *ABS* ratio contour lines were exported to AutoCAD and the total lateral sorption was measured at various depths (0.50 mm vertical steps used starting from 5 mm above notch). The lateral sorption was averaged at each depth and the results are shown as sorption profiles in Figure 4*(b)*. The 0.40 mm CMOD specimen was not included as rapid moisture ingress occurred in the vertical direction beyond the measurement area. The average lateral sorption from 0 to +5 mm (y position) indicates the sorption behavior from the sides of the notch.

The notch in the WST specimens may be considered a free surface for water sorption. Similar average lateral sorption distances were observed in the cracked specimens above and below the notch bottom to a given depth (Figure 4*(b)*). This indicates a free surface may exist below the notch bottom in the cracked WST specimens, possibly in the form of a coalesced crack. The maximum sorption depth into the cracked WST specimens after 1 hour of water exposure (from Figure 4*(b)*) is plotted over the corresponding crack profile in Figure 3*(b)* as asterisks (except for CMOD 0.4 mm). After 1 hour of exposure, water has yet to reach the full extent of the crack length. Therefore, Figures 3*(b)* and 4*(b)* indicate that although water traveled rapidly through cracks and free surface sorption behavior was observed below the notch bottom in cracked specimens, only a portion of the total crack length contributes as a free surface to water sorption while the remaining portion of the crack length inhibits sorption.

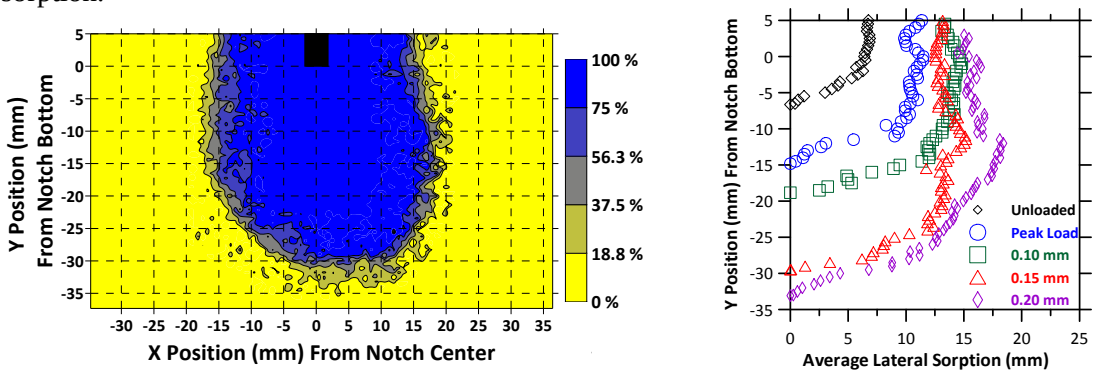

(a) *(b)*

Figure 4. *(a)* Absorption ratio contour plot for 0.15 mm CMOD specimen after 1 hour of ponding, and *(b)* Sorption profiles for WST specimen after 1 hour of ponding, under varying crack conditions

4. COMPARISON OF CRACK LENGTH AND SORPTION MEASUREMENTS

Figure 5*(a)* compares the CHM crack lengths to the maximum sorption depth after 1 hour of ponding in the cracked WST specimens. The broken line indicates equivalency. The single point which shows a higher maximum sorption depth than the crack length for the unloaded specimen (CHM crack length of 0 mm), while sorption in all cracked specimen has yet to reach the crack length after 1 hour of exposure to water.

As Figure 3*(b)* and 4*(b)* indicate a portion of the crack length behaves as a free surface while the remaining crack length inhibits water sorption. A possible source of this inhibition may be a lack of coalescence of the crack across a portion of the crack length. Figure 5*(b)* shows the difference between the CHM crack length and the maximum sorption depth for the specimens with varying crack lengths. For three of the cracked specimens tested (peak load, 0.15 mm CMOD, and 0.20 mm CMOD) this difference had a consistent range of 8 mm to 10 mm. Assuming the maximum sorption depth after 1 hour of exposure relates to the location of free surface behavior through the controlling sorption mechanisms, Figure 5*(b)* may indicate that a consistent length of the crack inhibits sorption. In other words, the results indicate the crack length consists of two portions, an apparent crack and an inhibiting crack. The apparent crack behaves approximately as a free surface in terms of sorption, while the inhibiting crack may have a consistent length and impedes sorption.

Further investigation is needed to determine if the sorption behavior in WST specimens with varying crack lengths can be directly related to fracture behavior using a constant inhibiting crack length. The 0.10 mm CMOD specimen results must also be investigated, although it is hypothesized that the rapidly increasing crack lengths at lower CMOD's (Figure 3*(c)*) may have affected this result. Additional testing will be undertaken to assess crack profiles and to verify the presence of coalesced cracks and isolated microcracks.

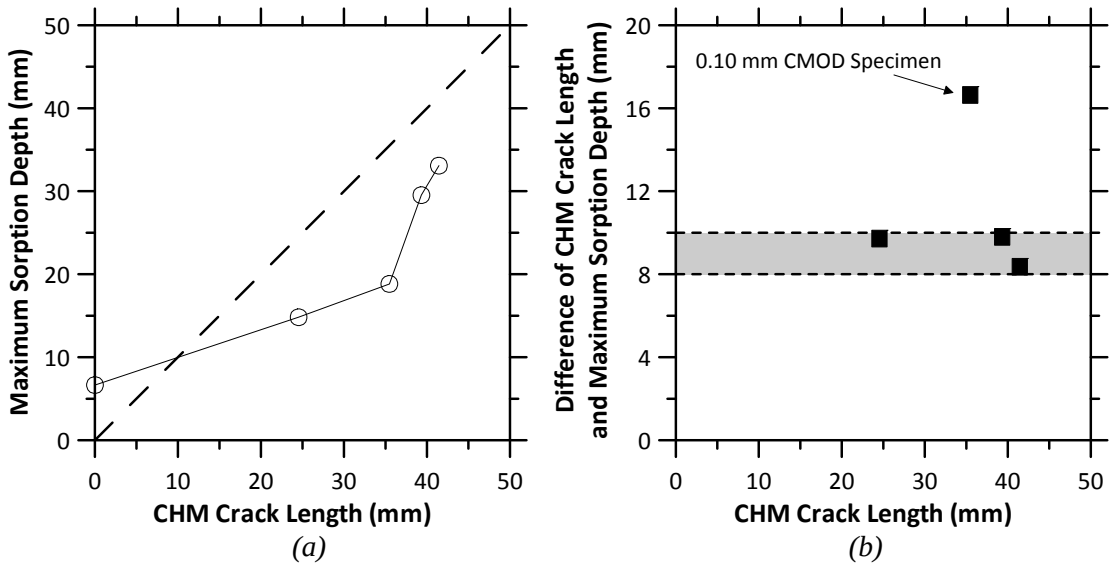

Figure 5. *(a)* Crack length from the CHM versus maximum sorption depth after 1 hour of water exposure, and *(b)* the difference in crack depth and maximum ingress depth for specimens with varying crack lengths.

5. SUMMARY

This paper presented results from x-ray absorption measurements of water sorption in WST specimens with varying crack lengths. The sorption behavior was used to quantify the impact of crack length on water sorption. It has been show that:

- As the crack mouth opening displacement increased the crack length increased and moisture reached deeper into the WST specimens after one hour of ponding.
- X-ray absorption measurements indicated that only a portion of the crack length has a free surface sorption behavior, while a consistent length of the total crack inhibits water sorption.

ACKNOWLEDGEMENTS

The first author gratefully acknowledges support received from the Otto Mønsted Fund and the Technical University of Denmark Department of Civil Engineering Travel Fund. The contents of this paper reflect the views of the authors, who are responsible for the accuracy of the data presented herein.

REFERENCES

[1] DS 2426, "Concrete – Materials – Rules for Application of EN 206-1 in Denmark"
[2] Comité Euro-International du Béton (CEB), "Durable Concrete Structures," Thomas Telford Services, Ltd. (1992)
[3] Østergaard, L., "Early-Age Fracture Mechanics and Cracking of Concrete - Experiments and Modeling," Ph.D Thesis, Technical University of Denmark, Lyngby, Denmark, 2003
[4] Skoček, J. & Stang, H., "Inverse Analysis of the Wedge Splitting Test," Engineering Fracture Mechanics, **75**(10) (2008) 3173-3188
[5] Ulfkjaer, J., Krenk, S. & Brincker, R., "Analytical Model for Fictitious Crack Propagation in Concrete Beams," Journal of Engineering Mechanics, **121**(1) (1995) 7-15
[6] Olesen, J., "Fictitious Crack Propagation in Fiber-Reinforced Concrete Beams," Journal of Engineering Mechanics, **127**(3) (2001) 272-280
[7] Skoček, J. & Stang, H., "Application of Optical Deformation Analysis System on Wedge Splitting Test and its Inverse Analysis, Submitted to Computational Materials Science (2008)
[8] Bentz, D., Geiker, M. & Hansen, K., "Shrinkage-reducing Admixtures and Early-age Desiccation in Cement Pastes and Mortars," Cement and Concrete Research, **31**(7) (2001) 1075-1085
[9] Hu, J. & Stroeven, P., "X-ray Absorption Study of Drying Cement Paste and Mortar," Cement and Concrete Research, **33**(3) (2003) 397-403
[10] Lura, P., Bentz, D., Lange, D., Kovler, K., Bentur, A. & Van Breugel, K., "Measurement of Water Transport from Saturated Pumice Aggregates to Hardening Cement Paste," Materials and Structures, **39**(293) (2006) 861-868
[11] Roels, S. & Carmeliet, J., "Analysis of Moisture Flow in Porous Materials using Microfocus X-Ray Radiography," Int. Journal of Heat and Mass Transfer, **49**(25-26) (2006) 4762-4772
[12] Weiss, J., Geiker, M. & Hansen, K., "Using X-Ray Absorption to Detect Fluid Ingress in Cracked Concrete," Submitted to Cement and Concrete Research (2008)
[13] GNI X-ray System, www.gni.dk (2006)
[14] ImageJ – Image Processing and Analysis in Java, www.rsbweb.nih.gov/ij/ (2008)
[15] Purdue Xray_Tiler ver 1.5, written in Image J, Compiling Date July 2008
[16] Couch, J. and Weiss, J., "Experimental Techniques for Calibrating and Processing x-ray Data Examining Moisture Ingress into Cementitious Materials," In Preparation

Paper IV

The design of an instrumented rebar for assessment of corrosion in cracked reinforced concrete

Pease, B.*, Geiker*, M., Stang*, H., Weiss, J.†

*Department of Civil Engineering, Technical University of Denmark (DTU Byg), 2800 Kgs. Lyngby, Denmark, e-mail: bjp@byg.dtu.dk

†School of Civil Engineering, Purdue University, West Lafayette, IN, USA 47907

Paper accepted by: *Materials and Structures*

Materials and Structures
DOI 10.1617/s11527-010-9698-1

ORIGINAL ARTICLE

The design of an instrumented rebar for assessment of corrosion in cracked reinforced concrete

Brad Pease · Mette Geiker · Henrik Stang · Jason Weiss

Received: 1 July 2010 / Accepted: 2 December 2010

Abstract An instrumented rebar is presented which was designed to have a realistic mechanical performance and to provide location dependent measurements to assess the environment with regards to reinforcement corrosion. The instrumented rebar was constructed from a hollowed 10 mm nominal diameter standard rebar with 17 electronically isolated corrosion sensors. Instrumented and standard rebars were cast into concrete beams and bending cracks were induced and held open using steel frames. Epoxy impregnation was used to assess and compare cracks in the concrete around the instrumented and standard rebar. As bending-induced cracks reached the reinforcement, slip and separation occurred along the concrete–reinforcement interface. Cracks in the concrete surrounding standard and instrumented rebars are largely similar in appearance; however, sensors protruding from the instrumented rebar reduced the separation between the steel and concrete. Cracked beams with cast-in instrumented and standard rebars were ponded with a 10% chloride solution and the open circuit corrosion potential (OCP) of the 17 sensors was measured for up to 62 days. Measurements from the individual sensors indicate when and where active corrosion may be thermodynamically favored based upon the local environmental conditions. Results indicated the length along the instrumented rebar where active corrosion was thermodynamically favored increased with exposure time due to the increased aggressivity of the local environmental conditions.

Keywords Reinforcement corrosion · Instrumented rebar · Cracked concrete · Crack width · Corrosion potential

B. Pease (✉) · M. Geiker · H. Stang
Department of Civil Engineering, Technical University of Denmark, Brovej Bygning 118, 2800 Kgs. Lyngby, Denmark
e-mail: bjp@byg.dtu.dk

J. Weiss
School of Civil Engineering, Purdue University, 550 Stadium Mall Dr., West Lafayette, IN, USA

Published online: 14 December 2010

1 Introduction

Concrete without cracks or damage protects the reinforcement from corrosion due to its high pH (~12–14) and the physical barrier it provides to resist the ingress of aggressive substances. Quality and thickness of concrete cover are the most influential material parameters affecting reinforcement corrosion. In practice however, concrete cracking can occur due to tensile strains induced by restrained hygral or thermal shrinkage and/or mechanical load.

Cracks facilitate local ingress of substances that increase the risk of reinforcement corrosion [1–11]. Laboratory studies also indicate that cracks may allow

more rapid initiation of reinforcement corrosion [12–23]. In-situ observations confirm this [24–29]. This has lead to attempts to correlate the width of the crack to the risk and/or extent of corrosion. Good correlations between crack width and corrosion behavior can be found after relatively short ($\leq \sim 3$ year) periods of exposure [17, 18, 23, 24, 28, 30]. However, improving cover quality (either through increased thickness, reduced water-to-binder ratio, or use of supplementary cementitious materials) alters the impact of crack width—delaying initiation and reducing corrosion rates for a constant crack width [17, 18, 31–33, 36]—meaning no single relationship can assess the impact cracks have on reinforcement corrosion during these early periods of exposure. Furthermore, with additional time the relationship between concrete crack width and extent of corrosion diminishes and other factors including concrete quality and cover thickness seem to dominate reinforcement corrosion behavior [17, 18, 23, 25, 34–36].

Many test methods exist to assess the influence of cracking on reinforcement corrosion in laboratory studies; however, as discussed in Sect. 1.1 many of these laboratory methods have drawbacks.

1.1 Review of laboratory test methods

Destructive techniques such as gravimetric or visual analysis (including microscopy/EDS) of reinforcement provide key information on extent of corrosion and corrosion products related to the location of a crack. However, as these methods are destructive, they are typically used to verify results of other test methods. Concrete crack mapping, which has been used in a series of investigations [37–39], is a time- and location-dependent assessment of reinforcement corrosion in cracked concrete; however, this is a measure of the impact of corrosion [40–42]. Electrochemical measurements on standard reinforcing bars provide time-dependent information, but requires the destructive removal of the reinforcement to ascertain location dependent information as anode size [13, 14]. Therefore, several specialized reinforcement configurations have been developed for use with electrochemical measurements to provide time- and location- dependent information on reinforcement corrosion.

Configurations include ‘rebar segments,’ consisting of mechanically and electrically discontinuous reinforcement section [32, 43], ‘segmented rebar,’ consisting of reinforcement sections connected mechanically with epoxy [23, 44], and partially epoxy coated rebar [17–19]. The ‘rebar segment’ configurations consists of segments of reinforcement that are fixed to an electrically isolated dummy rebar which carries loads and induces cracking [32–43]. While ‘segmented rebar’ configurations are mechanically joined using epoxy, a dummy rebar is also used to “prevent the breakdown of the specimens during cracking” [23]. In [17–19] a standard rebar is partially coated with epoxy to limit the possible anodic region to a 20 mm segment. Separate cathodic segments are cast in the concrete at various distances from the crack.

Photogrammetric investigations of flexural beams have shown bending cracks reaching the concrete–reinforcement interface develop an intricate cracking behavior including slip and separations [45, 46]. This slip and separation may facilitate chloride ingress along the reinforcement [7]. Therefore, realistic cracking behavior should be considered when testing the impact of cracks on reinforcement corrosion. The authors are unaware of any direct comparisons of the cracking behavior of concrete reinforced with standard reinforcement and the specialized reinforcement configurations discussed in the previous paragraph.

This paper describes an instrumented rebar which provides location dependent measurements of the aggressivity of the environment in terms of reinforcement corrosion. In addition, the instrumented rebar is capable of carrying and transferring loads and inducing realistic cracks. The cracking behavior of concrete around a standard rebar and an instrumented rebar was compared using fluorescent epoxy impregnated sections. Corrosion potential was measured by sensors mounted at 17 locations in the instrumented rebar. A preliminary study of the impact of cracks on reinforcement corrosion illustrates the applicability of the instrumented rebar.

2 Experimental investigation

2.1 Instrumented rebar configuration

The instrumented rebar consists of four sections of standard 10 mm diameter deformed rebar cut to lengths shown in Fig. 1. The central section of the rebar (i.e. the 340 mm instrumented part) was bored,

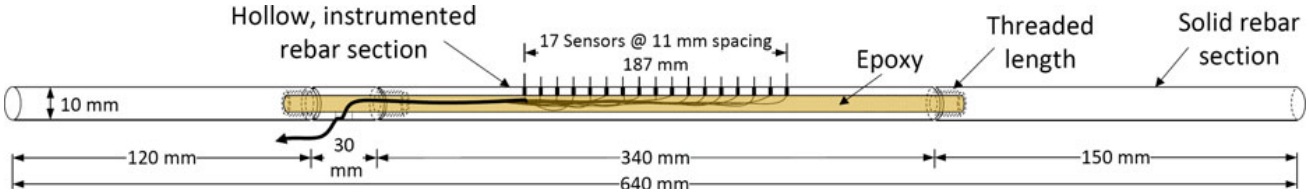

Fig. 1 Schematic of the instrumented reinforcement used for corrosion investigations (*Note*: Deformed reinforcement was used, ribs not shown in drawing)

providing a 4 mm diameter void along the center. Seventeen (17) 1.5 mm diameter holes were drilled through the outer surface into the inner void. The holes were spaced 11 mm apart and carefully located between reinforcement ribs. Sensors protruded 5 mm from the reinforcement at each hole. The sensors were constructed by soldering 1 mm diameter steel pins (~10 mm in length) to individual lead wires. Glue-coated heat-shrink tube encased each steel pin to protect the soldered connection and electronically disconnect the steel pins from the rebar. The 5 mm length protruding from the reinforcement was not covered by the heat-shrink tube. All 17 lead wires were bundled and sealed with heat-shrink tube. The bundle was passed through a hole in the 30 mm long hollowed section as shown in Fig. 1. Epoxy was then injected into the hollowed section to protect the wires, electrical connections, and sensors. To provide adequate length of the instrumented rebar, two end parts of solid rebar were attached using threaded connections. Teflon tape was used at all threaded connections of the instrumented rebar.

2.2 Materials and specimen preparation

Aalborg white portland cement was used with an estimated Bogue composition of 78.8% C_3S, 10.5% C_2S, 4.9% C_3A, 1.0% C_4AF, 0.6% MgO, 2.1% SO_3, and an Na_2O equivalent alkali content of 0.19%. The aggregate was washed. Class E 0-4 mm sea-sand was used along with washed Class A 4–8 mm sea-gravel (in accordance with [47]). A water-to-cement ratio of 0.50 was used with a cement content of 330, 776 kg/m^3 fine aggregate, and 1,103 kg/m^3 coarse aggregate (72.5% aggregate by volume).

The concrete was mixed using a standard pan mixer with a 120 l capacity. The fine and coarse aggregate were first mixed dry for 1 min, followed by 3 min mixing with one third of the mixing water. Mixing was stopped for 2 min prior to adding and mixing the cement for 1 min. The remaining water was then added and mixing continued for 3 min after addition of water. The mixer was then opened and the pan and blades were scraped, followed by 1 additional minute of mixing.

Table 1 Loading conditions, average crack width as measured from the tension surface of the concrete, and exposure durations for all beams

Beam I.D. (–)	Mid-span deflection (mm)	Avg. crack (mm)	Exposure duration (days)
0[a]	2	0.4	–
1	2	0.4	62
2	2	0.3	35
3	3	0.6	14
4	3	0.7	62
5	4	0.9	35
6	5	1.2	62

[a] Beam 0 used for fluorescent epoxy impregnation

A total of eight beams were cast, where two beams were utilized for initial testing presented in [48] and the remaining beams were utilized as described in Table 1 (Beam 0 was utilized in both studies). The concrete was placed and vibrated into 100 × 100 × 600 mm^3 molds and covered by plastic for 24 h at ambient conditions (i.e. 20°C). As shown in Fig. 2, the concrete beam specimens were cast with an instrumented rebar, a standard rebar, and a ruthenium/iridium mixed metal oxide activated titanium (MMO-Ti) mesh. The sensors in the instrumented rebar were cast to face the tension surface of the beam, while the MMO-Ti mesh was cast 10 mm from the compression surface, opposite the instrumented rebar. The casting direction was opposite of the orientation shown in Fig. 2 (i.e., reinforcement closer to bottom of molds) to minimize interfacial defects due to settlement and/or bleeding. Additional information on the use of MMO-Ti mesh as a counter electrode in concrete can be found in the literature

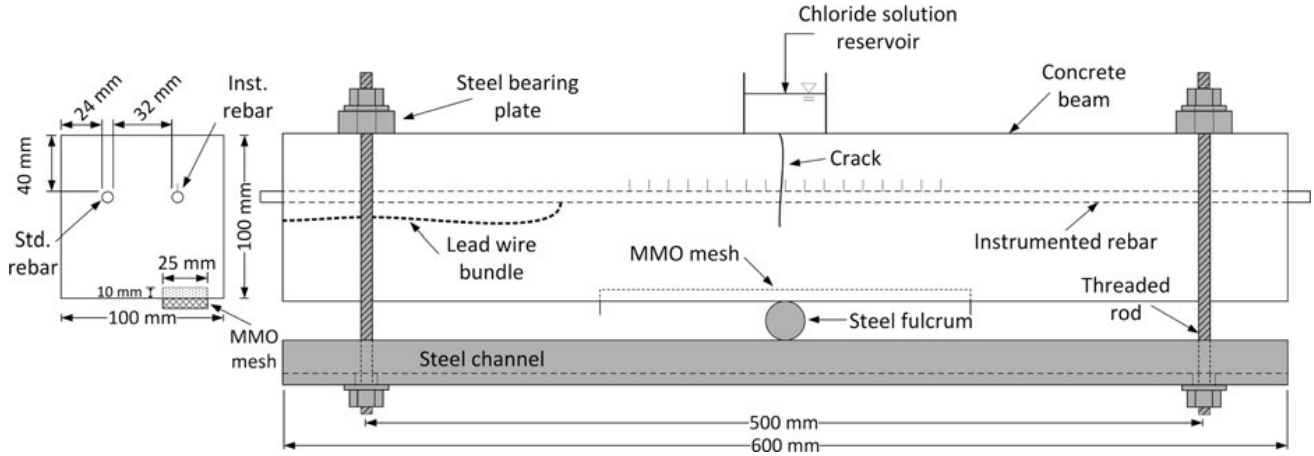

Fig. 2 Beam specimen design including instrumented rebar, MMO-Ti mesh, and reservoir for chloride solution. Cracking frame is shown in *gray*

[49, 50]. Upon demolding, the specimens were sealed with multiple layers of plastic followed by aluminum foil and packaging tape and were stored at 20 ± 1°C until testing.

2.3 Experimental methods

2.3.1 Mechanical loading and environmental exposure

Steel cracking frames, shown in Fig. 2 in gray, were used to load the beams to 2, 3, 4, and 5 mm mid-span deflection (MSD) to induce cracking (Table 1). Bolts were finger-tightened, then the defined MSD was applied by turning the bolts a required number of revolutions using a wrench.

Prior to application of mechanical load, the sides of the specimens (i.e., not the compression and tension surfaces) were sealed using silicone caulk. This was completed prior to loading as to not seal the induced crack(s). The hardened silicone did not rupture during loading of the beam specimens. After loading, a plastic ponding dike (40 × 80 mm^2) was placed over the crack and the tensile surface outside the ponding area was sealed with silicone caulk. In cases where multiple cracks occurred only the crack directly over the steel fulcrum (Fig. 2) was ponded. The compression surface was left unsealed. The ponding dike was then filled with a 10% chloride solution by weight (using NaCl). The ponding dike was refilled as necessary during testing.

2.3.2 Assessment of cracking behavior

To compare the cracking behavior of the concrete surrounding the instrumented rebar, epoxy impregnated plane and serial sections were investigated from Beam 0 (a 2 mm MSD beam used as part of an initial investigation presented in [48], corrosion data from this beam are not presented in this paper). The impregnated beam was kept loaded in a cracking frame during the impregnation process described below.

To impregnate the cracked beam the crack was rinsed with deionized water multiple times to minimize crystallization of NaCl, which may impede the flow of epoxy. The specimen was then allowed to dry for 7 days at 20 ± 1°C and 50 ± 2% relative humidity. The beam compression surface was coated using a thick layer (~5 mm) of silicone to seal the specimen (needed to draw a vacuum). A 5 mm thick cylindrical acrylic vacuum chamber with an inner diameter of 85 mm was placed over the crack. Channel-shaped rubber gaskets coated with vacuum grease placed on each end of the acrylic chamber provided an adequate seal. The chamber was then evacuated to a pressure of 10 mBar (1 kPa) and fluorescent epoxy was impregnated as described in accordance with the procedures in [51, 52]. After 24 h the epoxy hardened and the specimen was removed from the cracking frame and sectioned using a wet saw as shown in Fig. 3. The transverse and parallel sections were used to compare the cracking behavior of the concrete immediately surrounding the instrumented and standard rebars.

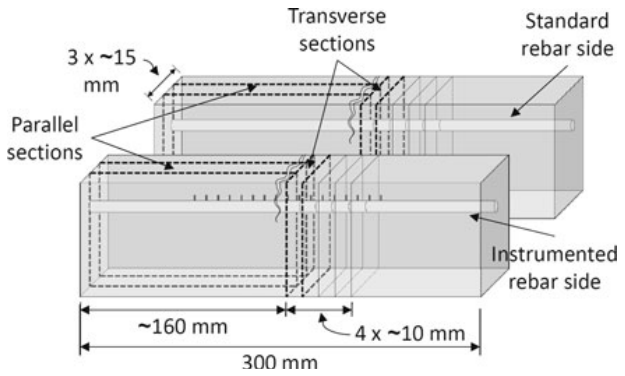

Fig. 3 Locations of the parallel and transverse epoxy impregnated sections. 150 mm was removed from each end of the beam prior to cutting sections

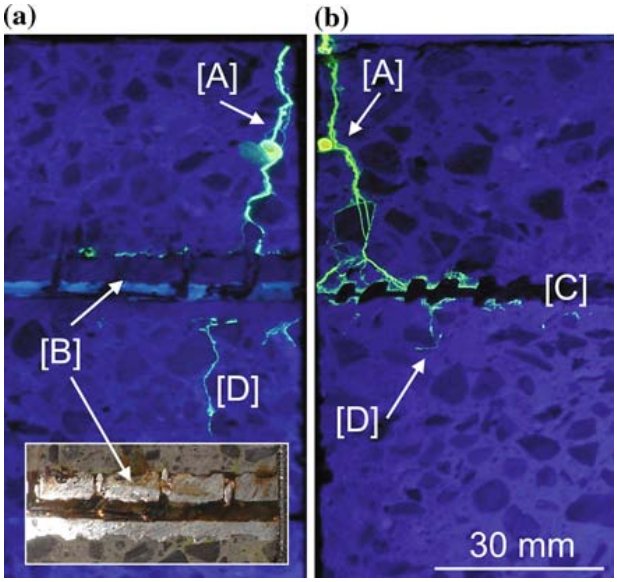

Fig. 4 Parallel sections showing the **a** instrumented rebar and **b** standard rebar, with the following details indicated [*A*]—primary crack, [*B*]—instrumented rebar, [*C*]—standard rebar, and [*D*]—reflected cracking. The *top* of the image was the tension surface of the beam

The location of transverse and parallel sections shown in Figs. 4 and 5, respectively are indicated in Fig. 3. Results are discussed in Sect. 3.1.2.

2.3.3 *Corrosion testing*

The open circuit corrosion potential (OCP) of each sensor was measured versus a standard calomel electrode (SCE) placed in the pond and versus the embedded MMO-Ti mesh. OCP of the MMO-Ti mesh was also measured against the SCE. OCP measurements were adjusted to the standard hydrogen

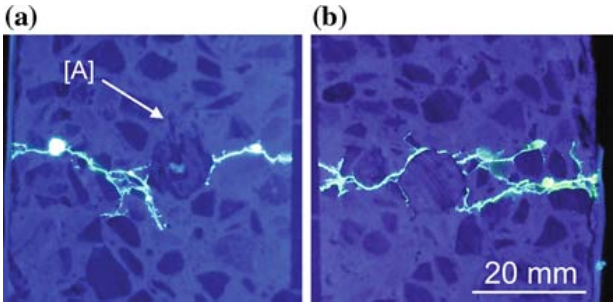

Fig. 5 Transverse sections from the **a** instrumented rebar and **b** standard rebar. Sections were located ~5 mm from primary crack. [*A*] indicates the location of a sensor

electron (SHE) using an offset of 244 mV (values range from 240 to 245 mV in the literature [49, 53–55]). Potential measurements were recorded every 2 h by a LabVIEW controlled corrosion measurement system which is described in [49]. The system, which utilizes switch cards to connect individual clusters of up to eight electrodes to a SCE, minimizes the required number of data acquisition channels. OCP measurements are conducted in sweeps wherein an electrical connection is initially established between a measurement card and a reference electrode. After establishing the electrical connection a delay period is set in the program (2 min) at which time the corrosion potential of the sensors is measured and recorded. The program automatically switches to the next card, establishes an electrical connection between the card and the reference electrode material, measures and records the corrosion potential of the sensors. Additional information on the measurement system is available in the literature [49].

At the conclusion of corrosion measurements the concrete covering the standard and instrumented rebar was removed from the side of the beam for inspection of the concrete and rebars. To facilitate this, 25 mm deep notches were cut above and below the rebars (standard and instrumented) and the concrete was removed by chisel and hammer. Silver nitrate, $AgNO_3$, and Rainbow Indicator were sprayed on opposite exposed surfaces to assess the ingress behavior of chloride ions and change in pH, respectively. Rainbow Indicator is an aqueous pH indicator that changes color based on the pH range of concrete pore solution [56, 57]. pH ranges include 5–7, 7–9, 9–11, and 11–13. Inspection of the rebars included removing selected sensors to assess their corrosion behaviors and assessment of corrosion (i.e., anode sites) on both rebars.

3 Results and discussion

3.1 Performance of instrumented rebar

Three potential problems with the instrumented rebar were investigated: (1) change in mechanical behavior in the rebar due to the hollow sections and sensor pin holes, (2) the cracking behavior of the concrete immediately surrounding the instrumented rebar, and (3) the corrosion behavior of the sensors. Basic structural analysis on the impact of hollowing the instrumented rebar and microscopic observations concerning impact of stress concentrations caused by sensor pin holes in the instrumented rebar are discussed in Sect. 3.1.1. Fluorescent epoxy impregnated cracks in the concrete immediately surrounding the instrumented and standard rebars are compared using the parallel and transverse sections in Sect. 3.1.2. The individual sensors consist of a steel pin sealed partly using glue-coated heat-shrink tube which creates a potential site of crevice corrosion. Upon completion of corrosion testing of each beam, randomly selected pins were removed to check for crevice corrosion as discussed in Sect. 3.1.3.

3.1.1 Mechanical behavior of hollow rebar with holes

Hollowing of the instrumented rebar results in a 2.56% reduction in bending stiffness (i.e., $E{\cdot}I$) and a 16% reduction in cross-sectional area of the rebar (using nominal diameter, 10 mm and considering the 4 mm diameter bore is centered). The axial stiffness (i.e., $E{\cdot}AI$) of the instrumented rebar is equivalent to a standard rebar with a 9.17 mm nominal diameter.

Stresses are known to concentrate at holes in steel, which can modify deformation and failure. However, visual and microscopic inspections of all instrumented rebar and sensor holes indicated no excessive deformations or diameter reductions due to yielding or rupture of the steel occurred.

3.1.2 Comparison of cracking behavior

Parallel and transverse sections from the instrumented and standard rebar sides of the impregnated beam (Beam 0) are shown in Figs. 4 and 5, respectively. Images were taken under ultraviolet light, causing the fluorescent epoxy to glow. Similar primary crack (indicated by [A] in Fig. 4) behaviors and widths were seen from both sides of the beam. Once the primary crack intersected the rebars additional tensile stresses are developed in the steel, which induces cracking in the concrete and slip and separation between the concrete–reinforcement interface [45, 46]. Separations are particularly visible at the concrete–reinforcement interface above both the instrumented [B] and standard [C] rebars (i.e. tension surface of rebars). The reflected crack [D] continued deeper towards the compression side of the beam on the instrumented rebar side. This is possibly caused by the reduced axial stiffness of the instrumented rebar described in Sect. 3.1.1, but may also be attributable to natural variabilities in concrete cracking. Direct comparison of cracking behaviors in Fig. 4 is hindered as the standard rebar [C] and the instrumented rebar [B] were unable to be sliced at identical locations, giving the appearance the standard rebar has a smaller diameter. Nevertheless, less separation appeared to occur at the interface of the instrumented rebar [B]. Additionally, the separations along the instrumented rebar interface vary along its length as a section is seen where no separations are evident from the impregnated section. Transverse sections in Fig. 5 provide additional details on cracking in the concrete and slip and separation at the concrete–reinforcement interface.

Figure 5 shows cracks extend from both rebars to the outer sides of the beams. Observation from additional transverse sections (see Fig. 3) showed epoxy impregnation of these cracks terminated between 36 and 44 mm from the primary crack (in both directions) along both rebars. On the standard rebar side (Fig. 5b), separation at the concrete–reinforcement interface is seen on the tension-facing side of the rebar. As indicated by [A] in Fig. 5a the sensor extends from the instrumented rebar into the concrete, likely causing the reduced and varying interfacial separation shown in Fig. 4a.

As discussed further in Sect. 3.3, the critical chloride threshold required to induce corrosion decreases due to the presence of flaws or damage at the interface. Therefore, for future investigations it is recommended to place the sensors flush with the reinforcement surface in an effort to eliminate the effect on interfacial separations. The reduced cross-section of the instrumented rebar appears to have only minor implications on the concrete crack

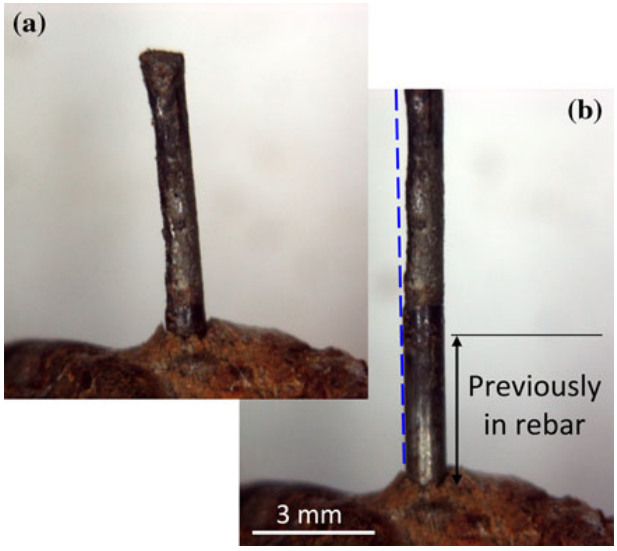

Fig. 6 **a** An individual sensor pin from Beam 1 after corrosion testing. **b** The sensor pin was partially removed to check for corrosion inside the instrumented rebar

behavior when compared to concrete cracking around the standard rebar for the beam investigated, with a 0.4 mm average crack width.

3.1.3 Corrosion behavior of sensors

Figure 6a shows a typical sensor after corrosion testing, still inside the instrumented rebar. In Fig. 6b the pin was partially removed to expose the portion of the pin which was inside the instrumented rebar. The broken line in Fig. 6b indicates a significant cross-sectional reduction in the portion of the sensor which was embedded in the concrete; however, cross-sectional reduction is not apparent from inside the glue-coated heat-shrink tube. Crevice corrosion was not observed on the sensors.

3.2 Influence of cracking on reinforcement corrosion

3.2.1 Ingress of chloride ions

Ingress of chloride ions, as indicated by $AgNO_3$, occurred through the primary crack on the tension side of the beam. Chloride ions reached the level of the MMO-Ti mesh in all beams during corrosion testing (due to ingress through the primary crack and the pore network in the uncracked concrete), causing variable moisture and chloride conditions at the MMO-Ti mesh surface. After chloride ions penetrated through the primary crack, chloride ions penetrated along the reinforcement, likely due to the interfacial separation and cracking shown in Figs. 4 and 5. Maximum lengths of lateral ingress for all beams are listed in Table 2.

3.2.2 Open circuit corrosion potential measurements

Figure 7 shows OCP's of the embedded MMO-Ti mesh during the exposure time of Beam 3. As shown in the figure, the OCP of MMO-Ti mesh embedded in concrete was stable under the varying chloride contents indicated in Sect. 3.2.1. The average OCP of the MMO-Ti mesh embedded in all beams was 183 mV_{SHE} with maximum fluctuations of mV_{SHE}. Based on these measurements, the MMO-Ti mesh is considered suitable for use as a second reference electrode. Similar OCP's were measured when using the SCE and MMO-Ti mesh as the reference electrode, as shown for the selected sensors in Fig. 7. It should be noted that, while the MMO-Ti mesh potential remained stable and correlated well with previous measurements in cementitious materials (180 $mV_{SHE} \pm \sim 22 mV_{SHE}$ in mortar [49]), a pH dependency has been observed [58]. The pH of the split concrete beams ranged between 11 and 13 after testing, as indicated by Rainbow Indicator [56, 57].

Figure 7 also shows typical OCP measurements of sensors in the instrumented rebars using both the SCE and MMO-Ti mesh as the reference electrodes. As can be seen, the OCP's all undergo a rapid drop, but at varying times. This rapid drop likely corresponds to a change in the thermodynamically favored corrosion state (i.e., passive to active) of the individual sensors. An OCP drop of -200 mV_{SHE} or larger typically indicates active corrosion [49]. While this value may be up to debate [54], corrosion was observed on 80% of sensors with a potential drop in excess of -200 mV_{SHE}. Gradual changes in OCP of sensors are likely due to variations in the concrete resistivity and local chloride contents and moisture contents. The average difference between OCP measurements taken from the SCE and MMO-Ti mesh was 5.0 mV_{SHE}.

Location dependencies of the OCP measurements are more clearly illustrated by contour maps showing exposure time on the *y*-axis, sensor location with respect to the crack on the *x*-axis and OCP indicated

Table 2 Overview of various measurement results, including lateral chloride ion ingress at the rebar, extent of OCP drop at termination of experiment (and at 7 days), extent and location of anodic regions

Crack width (mm)	Beam I.D. (–)	Exposure duration (days)	Lateral Cl^- ingress @ rebar (mm)	Extent of OCP drop (mm)	S.R. Extent of anode region (mm)	S.R. Location of anode[a] (–)	I.R. Extent of anode region (mm)	I.R. Location of anode[a] (–)
0.3	2	35	177	148[b] (90)	20.2 (2)[c]	TS	3.9 (1)[c]	TS & SS
0.4	1	62	310	113[b] (60)	44.3 (8)[c]	7 TS & 1 CS	47.5 (3)[c]	SS
0.6	3	14	235	115 (115)	22.2 (1)[c]	TS	21.4 (1)[c]	SS
0.7	4	62	323	151[b] (72)	41.0 (3)[c]	TS	47.8 (4)[c]	TS
0.9	5	35	281	187[b] (107)	32.1 (3)[c]	TS	22.3 (1)[c]	SS
1.2	6	62	367	113[b] (21)	38.3 (1)[c]	TS	37.6 (1)[c]	SS

S.R. standard rebar, *I.R.* instrumented rebar

[a] Locations of anodes: *TS* rebar tension-facing surface, *CS* rebar compression-facing surface, *SS* rebar side-facing surface

[b] Extent of OCP drop reached a boundary of the instrumented rebar

[c] Number of corrosion sites

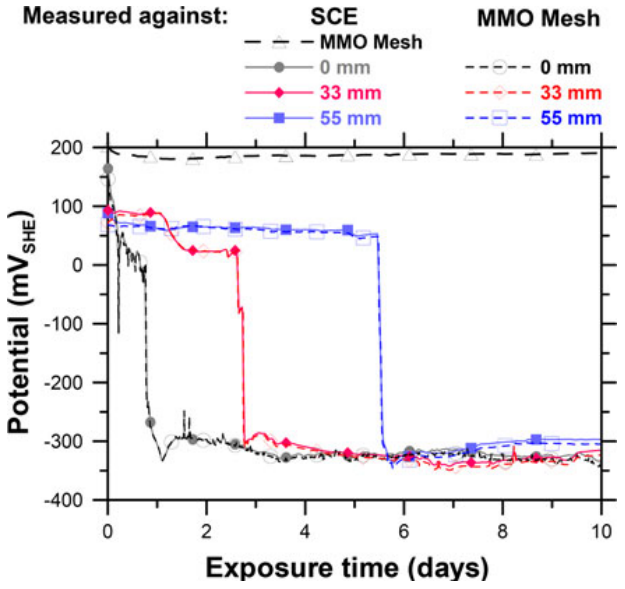

Fig. 7 OCP measurements of the MMO-Ti mesh and selected sensors in the instrumented rebar from Beam 3. OCP of the sensors were taken against both the SCE (*solid lines*) or MMO-Ti mesh (*broken lines*). Sensors are identified by their distance from the primary crack

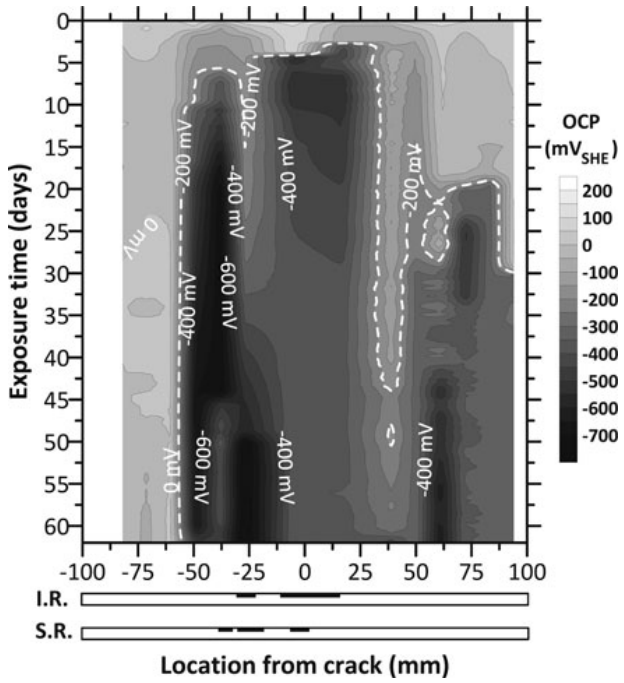

Fig. 8 Location and time dependent OCP of sensors in Beam 4 (0.7 mm crack width) instrumented rebar. Sketches of instrumented rebar (I.R.) and standard rebar (S.R.) indicate location and length of anode(s)

by the grayscale (Figs. 8, 9). Ordinary linear kringing interpolation was used to estimate the OCP between measurement locations. Location information on the *x*-axis is shifted based on the actual location of the sensors relative to the primary transverse crack (i.e. the ponded crack) as measured after removal of the concrete cover. Figure 8, which depicts the complete duration of Beam 4 testing, shows a typical measurement from an instrumented rebar. Initially, the OCP across the instrumented rebar has values between ~0 and 200 mV_{SHE} with a distinctly higher OCP near the location of the crack. This might be explained by an initially higher oxygen content in the crack region. Drop in OCP below −200 mV_{SHE}, indicated by the broken white line in the figures, tends to occur earliest nearby the primary crack

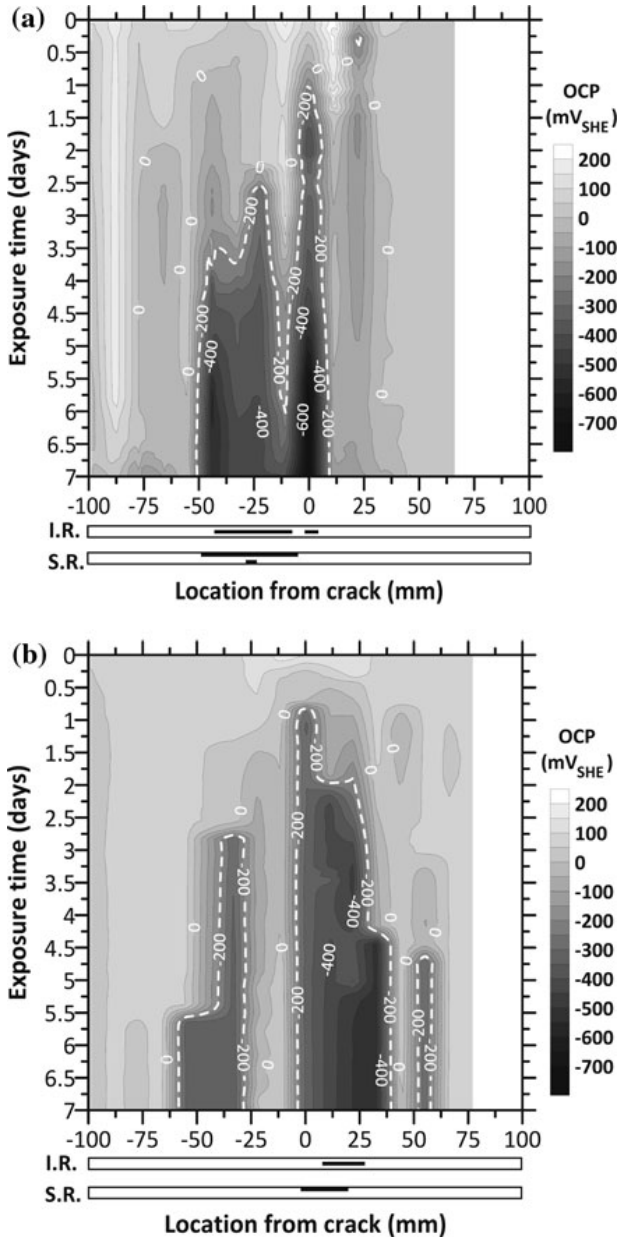

Fig. 9 Location and time dependent OCP of sensors in **a** Beam 1 (0.4 mm crack width) and **b** Beam 3 (0.6 mm crack width) during the first 7 days of exposure. Sketches of instrumented rebar (I.R.) and standard rebar (S.R.) indicate location and length of anode(s)

followed by more distant (from the primary transverse crack) sensors. Table 2 lists the total length along the instrumented rebars where OCP dropped below -200 mV_{SHE} at the end of corrosion testing.

Figure 8 shows that at approximately 40 mm from the primary crack the drop in OCP takes significantly longer to occur than neighboring regions (both closer to and farther from the primary crack). Additionally, the OCP did not drop during testing for sensor below approximately -60 mm from crack for Beam 4. Similar behavior (i.e., delayed or no OCP drop at various locations) occurred in all beams and is likely attributable to the variations in the cracking behavior described in Sect. 3.1.2.

Figures 9a and b illustrate the effect of varying crack width during the first 7 days of exposure for Beam 1 and 3, with 0.4 mm and 0.6 mm crack widths, respectively. In both cases, the -200 mV_{SHE} isoline initially appears at the location of the crack and extends further away from the crack location with increased time. The -200 mV_{SHE} isoline increases in length along the instrumented rebar for Beam 3 more rapidly than from Beam 1. After 7 days the -200 mV_{SHE} isoline in Beam 3 reached a total length of approximately 77 mm and an extent of approximately 115 mm, while Beam 1 reached a total length of 60 mm.

3.2.3 Visual observations of corrosion on rebars

Figure 10a and b show examples of the typical corrosion behaviors found on the standard rebars. Multiple locations of pitting corrosion were seen for Beams 1 and 2 (2 mm MSD). Wider areas of corrosion were seen on standard rebars from Beams 3–6. Figure 10a shows a relatively deep corrosion pit in the standard reinforcement from Beam 2. Figure 10b shows corrosion took place over a wider area on the standard rebar from Beam 6. Deep corrosion pits were also observed on the instrumented rebars in Beams 1 and 2, with wider areas of corrosion seen on the instrumented rebars from Beams 3–6. The majority of corrosion was observed on the tension-facing surface (i.e. steel surface towards tension face of beam) of the standard rebars. One corrosion pit was found on the compression surface of the standard rebar in Beam 1. Corrosion of the instrumented rebars was observed for Beams 1–3, 5–6 on the side surface of the rebars (i.e. steel surface towards side faces of beam). The extent of the length, number, and location of anodic regions are listed in Table 2 for all beams.

Figures 8, 9a and b compare the locations of anodes on both rebars to the measured OCP from the instrumented rebar for Beams 4, 1, and 3, respectively. In some cases individual anode sites overlapped along the rebar length. For example Beam 1 had 7 separate anode sites on the tension-facing surface of the

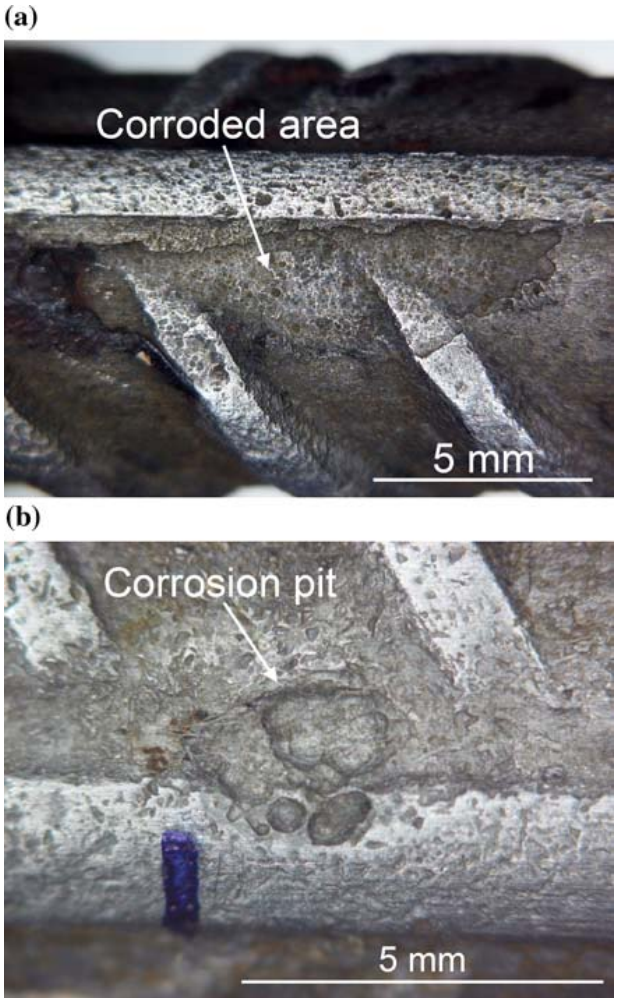

Fig. 10 Images of corroding areas in the standard rebar from **a** Beam 2 (0.3 mm crack width) and **b** Beam 6 (1.2 mm crack width)

standard rebar; however, all anodes overlapped giving the appearance of a singe anode in the sketch in Fig. 9a. All anode sites were observed in regions where active corrosion was thermodynamically favored within the first week of exposure to chloride contaminated solution according to OCP measurements. Similar results were seen for all beams.

During destructive removal of the rebars, corrosion products were seen on the surfaces of the reinforcement and the adjacent concrete. Corrosion products at a critical level can induce further cracking of the concrete [40], which could affect the OCP measurements of the sensors. However, the amount of corrosion product seen was unlikely to cause corrosion-induced cracking as the load-induced cracks likely provided ample space to accommodate the corrosion product. Additional time (and corrosion products) could result in corrosion-induced cracking for longer term testing utilizing the instrumented rebar.

3.3 Assessment of instrumented rebar and comparison of results

Results in Sect. 3.1 indicated the instrumented rebar is capable of carrying loads and inducing similar cracking behaviors as standard rebars. The sensors from the instrumented rebar, which protruded into the concrete, reduced slip and separation to some extent.

Table 2 provides an overview of measurements including crack widths, lateral ingress of chloride ions, extent of length where active corrosion was thermodynamically favored at the end of testing (and after 7 days), and total length of the corroded regions for all beams. Lateral ingress of chloride ions increased with increasing exposure time and crack width. This is according to expectations as increased crack width causes increased slip and separation of the concrete–reinforcement interface [45, 46]; likely allowing for increased ingress along the rebar. The presence of defects or damage at the concrete–reinforcement interface also increases the likelihood of active corrosion [59, 60] and decreases the critical chloride threshold required for initiation of active corrosion [61, 62]. OCP measurements in Fig. 9 indicated the length where the environmental conditions thermodynamically favor active corrosion (i.e., $-200\ mV_{SHE}$ isoline) typically increased more rapidly for beams with larger crack widths (and corresponding increased interfacial separation).

The extent of OCP drop after 7 days is given in parentheses in Table 2 under the 'extent of OCP drop' heading. Comparing the extent of OCP drop from Beams 1 and 2 after 7 days and the cracking behavior observed from Beam 0, all of which were loaded to 2 mm MSD resulting in similar average crack widths, indicate a direct relationship between damage at the concrete–reinforcement interface and reinforcement corrosion may exist. The OCP drop extended 60 and 90 mm after 7 days for Beams 1 and 2, while the cracking was found to extend 36–44 mm in both directions from the primary crack (i.e., 72–88 mm in total). Further investigations are needed to verify the relationship between interface damage

and risk/extent of reinforcement corrosion. Nevertheless, damage at the concrete–reinforcement interface may be an important factor influencing reinforcement corrosion, potentially a much more important factor than crack width. Rather than simply controlling surface crack widths, which is the current norm [63–65], designers may utilize other factors, such as concrete cover depth and properties of the concrete and steel, to minimize damage at the concrete–reinforcement interface due to cracking—thereby optimizing the corrosion resistance of reinforced concrete.

Comparing the lengths of chloride ion ingress and OCP drop, particularly Beam 3 where OCP drops did not exceed the measured length, indicated the critical chloride threshold required for active corrosion exceeded the threshold needed to cause the color change in $AgNO_3$ spraying. Comparison of the OCP measurements to the length of anodic regions on both the standard and instrumented rebar in Table 2 and Figs. 8 and 9 indicate the length where the local environmental conditions favor (thermodynamically) active corrosion is far greater than the area where actual active corrosion occurred. The presence of an anodic region on the surface of the rebar may protect other electrically connected regions of the rebar where active corrosion is thermodynamically favored due to the aggressivity of the environment. The instrumented rebar therefore only assess the thermodynamically favored corrosion state based on local environmental conditions, and is not able to consider the corrosion state of neighboring regions of the rebar.

As presented in Sect. 3.2.3, corrosion typically occurred at the tension surface of standard rebars (i.e. steel surface towards tension face of beam). For the instrumented rebars, however, corrosion occurred on the side surface in 5 of the 6 beams tested. Figure 5 showed interfacial separations occurred at the tension side of the standard rebar, but not the instrumented rebar. Instead only cracks extending from the sides of the instrumented rebar were observed. The lack of interfacial separation at the instrumented rebar provided additional protection against active corrosion, causing the tendency for corrosion to occur at the side surface. Therefore, it is concluded that in future investigations the sensors shall not protrude from the instrumented rebar, but shall be made flush to the rebar surface.

4 Conclusions

An instrumented rebar was developed to assess the aggressivity, with regard to reinforcement corrosion, of the local environment as a function of the distance from a transverse crack. Based on the limited preliminary investigation where cracked reinforced concrete beams were ponded with a 10% chloride solution the following conclusions were made:

- Cracks in the concrete surrounding standard nd instrumented rebars are largely similar in appearance; however, sensors protruding from the instrumented rebar appeared to reduce the separation between the steel and concrete. In future investigations, it is recommended to place the sensors flush to the rebar surface to avoid this affect. Crevice corrosion of the sensors was not found.
- Ruthenium/iridium mixed metal oxide activated titanium (MMO-Ti) embedded in concrete remained stable, indicating MMO-Ti may be used as an inexpensive reference electrode in concrete. Care should however be taken if large variations in pH are anticipated.
- For the investigated conditions, the length along the instrumented rebar where the local environment lead to thermodynamic favoring of active corrosion was significantly larger than the area where anodes formed on the standard rebars. Anodic regions on the standard rebar can protect electronically connected neighboring regions where the local environmental favors active corrosion. This is not considered by the instrumented rebar.
- For the investigated conditions, the OCP of the sensors changes more rapidly with increased crack width, indicating a more rapid change in thermodynamic state. Corrosion of the standard rebar was found to occur in all beams. The length of the anode region did not relate to crack width; however, corrosion type varied based on crack width for this investigation. The 0.3 and 0.4 mm crack width specimens (Beams 1 and 2) exhibited pitting corrosion while larger crack widths (Beams 3–6 with crack widths of 0.6–1.2 mm) resulted in corrosion over a relatively larger area.
- Comparison of the cracking behavior and measurements from the instrumented rebar indicates

that damage along the concrete–reinforcement interface may be related to an increased risk of corrosion initiation. While further work is needed to verify this relationship, interfacial damage is likely more important (and relevant) to reinforcement corrosion issues than the current practice of controlling surface crack width.

Acknowledgments The first author would like to thank Kim Beck Hansen for his assistance in the modification of an existing corrosion measurement system to facilitate measurements of the instrumented rebars used in this work. Additionally, our appreciation is extended to Peter Laugesen (Pelcon Materials & Testing ApS) for preparation of the fluorescent epoxy impregnated beam.

References

1. Jacobsen S, Marchand J, Boisvert L (1996) Effect of cracking and healing on chloride transport in OPC concrete. Cem Concr Res 26(6):869–881
2. Aldea CM, Shah S, Karr A (1999) Permeability of cracked concrete. Mater Struct 32(219):370–376
3. De Schutter G (1999) Quantification of the influence of cracks in concrete structures on carbonation and chloride penetration. Mag Concr Res 51(6):427–435
4. Edvardsen C (1999) Water permeability and autogenous healing of cracks in concrete. ACI Mater J 96(4):448–454
5. Gowripalan N, Sirivivatnanon V, Lim C (2000) Chloride diffusivity of concrete cracked in flexure. Cem Concr Res 30(5):725–730
6. Rodriguez O, Hooton R (2003) Influence of cracks on chloride ingress into concrete. ACI Mater J 100(2):120–126
7. Win P, Watanabe M, Machida A (2004) Penetration profile of chloride ions in cracked reinforced concrete. Cem Concr Res 34(7):1073–1079
8. Lindquist WD, Darwin D, Browning J, Miller GG (2006) Effect of cracking on chloride content in concrete bridge decks. ACI Mater J 103(6):467–473
9. Ismail M, Toumi A, Francois R, Gagne R (2008) Effect of crack opening on the local diffusion of chloride in cracked mortar samples. Cem Concr Res 38:1106–1111
10. Kanematsu M, Maruyama I, Noguchi T, Iikura H, Tsuchiya N (2009) Quantification of water penetration into concrete through cracks by neutron radiography. Nucl Inst Methods Phys Res A 605(1–2):154–158
11. Pease B, Couch J, Geiker M, Stang H, Weiss J (2009) Assessing the portion of the crack length contributing to water sorption using X-ray absorption measurements on concrete wedge splitting specimens. In: ConcreteLife'09: second international RILEM workshop on Concrete durability and service life planning, Haifa, Israel
12. Houston J, Atimay E, Ferguson P (1972) Corrosion of reinforcing steel embedded in structural concrete. Tech. Rep. Research Report 112-1F, Center for Highway Research, University of Texas at Austin
13. Gautefall O, Vennesland O (1983) Effects of cracks on the corrosion of embedded steel in silica-concrete compared to ordinary concrete. Nordic Concr Res 2:17–28
14. Berke N, Dallaire M, Hicks M, Hoopes R (1993) Corrosion of steel in cracked concrete. Corros Eng 49(11):934–943
15. Lorentz T, French C (1995) Corrosion of reinforcing steel in concrete: effects of materials, mix composition, and cracking. ACI Mater J 92(2):181–190
16. Arya A, Ofori-Darko F (1996) Influence of crack frequency on reinforcement corrosion in concrete. Cem Concr Res 26(3):345–353
17. Schieß l P, Raupach M (1994) Laboruntersuchungen und berechnungen zum einfluss er rissbreite des betons auf die chloridinduzierte korrosion von stahl in beton. Bauingenieur 69(11):439 (in German)
18. Schießl P, Raupach M (1997) Laboratory studies and calculations on the influence of crack width on chloride-induced corrosion of steel in concrete. ACI Mater J 94(1): 56–62
19. Ramm W, Biscoping M (1998) Autogenous healing and reinforcement corrosion of water-penetrated separation cracks in reinforced concrete. Nucl Eng Des 179(2): 191–200
20. Francois R, Arliguie G (1999) Effect of microcracking and cracking on the development of corrosion in reinforced concrete members. Mag Concr Res 51(2):143–150
21. Wang K, Weiss W, Yoon S, Shah S (2000) Combined effect of corrosion and stresses in reinforced concrete beams. In: American Society of Civil Engineers – Engineering Mechanics Division, Austin, TX
22. Yoon S, Wang K, Weiss W, Shah S (2000) Interaction between loading, corrosion, and serviceability of reinforced concrete.. ACI Mater J 97(6):637–644
23. Mohammed T, Otsuki N, Hisada M, Shibata T (2001) Effect of crack width and bar type on corrosion of steel in concrete. J Mater Civ Eng 13(3):194–201
24. Rehm G, Moll HL (1964) Versuche zum studium des einflußes der rissbreite auf die rostbilding an der bewehrung von stahlbeton-bauteilen. Deutscher Ausschuss für Stahlbeton 169
25. Schießl P (1976) Zur frage der zulassigen rissbreite und der enforderlichen betondeckung im stahlbetonbau unter besonderer berucksichtigung der karbonatisierung des betons. Deutscher Ausschuss für Stahlbeton 255
26. Kamiyama H (1972) Rust of steel bars in concrete. Cem Concr 308:50–57 (in Japanese)
27. Fidjestol P, Nilson N (1980) Field test of reinforcement corrosion in concrete. In: ACI SP-65, pp 205–217
28. Katawaki K (1977) Corrosion of steel in the concrete exposed to seawater spray zone. In: Symposium proceedings on cracking of concrete structures, pp 133–136
29. O'Neil EF (1980) Study of reinforced concrete beams exposed to marine environment. In: ACI SP-65: performance of concrete in marine environment, pp 113–132
30. Makita M, Mori Y, Katawaki K (1980) Marine corrosion behavior of reinforced concrete exposed at tokyo bay. In: ACI SP-65: performance of concrete in marine environment, pp 271–290
31. Scott A, Alexander M (2007) The influence of binder type, cracking and cover on corrosion rates of steel in chloride-contaminated concrete. Mag Concr Res 59(7):495–505

32. Poursaee A, Hansson CM (2008) The influence of longitudinal cracks on the corrosion protection afforded reinforcing steel in high performance concrete. Cem Concr Res 38(8–9):1098–1105
33. Otieno M, Alexander M, Beushausen H-D (2010) Corrosion in cracked and uncracked concrete - Influence of crack width, concrete quality and crack reopening. Mag Concr Res 62(6):393–404
34. Tottori S, Tsuchida S, Miyagawa T (1999) Deterioration prediction of concrete structures based in the exposure test results concerning cracking and rebar corrosion. Concr Res Technol Jpn Concr Inst 10(3):1–15 (in Japanese)
35. Yachida M (1987) Cracking and reinforcement corrosion in reinforced concrete bridges. J Mater Concr Struct Pavements 6(378):195–202 (in Japanese)
36. Schiessl P (1986) Einfluss von rissen auf die dauerhaftigkeit von stahlbeton- und spannbetonbauteilen. Deutscher Ausschuss für Stahlbeton 370:9–52
37. Francois R, Arliguie G (1998) Influence of service cracking on reinforcement steel corrosion. J Mater Civil Eng 10(1):14–20
38. Francois R, Castel A, Vidal T, Vu NA (2006) Long term corrosion behavior of reinforced concrete structures in chloride environment. J Phys IV 136:258–293
39. Vidal T, Castel A, Francois R (2007) Corrosion process and structural performance of a 17 year old reinforced concrete beam stored in chloride environment. Cem Concr Res 37:1551–1561
40. Alonso C, Andrade C, Rodriguez J, Diez JM (1998) Factors controlling cracking of concrete affected by reinforcement corrosion. Mater Struct 31(211):435–441
41. Vu K, Stewart M, Mullard J (2005) Corrosion-induced cracking: experimental data and predictive models. ACI Struct J 102(5):719–726
42. Ahmed SFU, Maalej M, Mihashi H (2007) Cover cracking of reinforced concrete beam due to corrosion of steel.. ACI Mater J 104(2):153–161
43. Marcotte T, Hansson C (2003) The influence of silica fume on the corrosion resistance of steel in high performance concrete exposed to simulated sea water. J Mater Sci 28: 4765–4776
44. Miyazato S, Hiraishi Y (2005) Transport properties and steel corrosion in ductile fiber reinforced cement composites. In: Proceedings of the 11th international conference on Fracture, Turin, Italy
45. Pease B, Geiker M, Stang H, Weiss J (2006) Photogrammetric assessment of flexure induced cracking of reinforced concrete beams under service loads. In: Proceedings of the second international RILEM symposium—advances in concrete through science and engineering, Québec City, QC, Canada
46. Spangenberg J (2009) Numerical modeling of crack propagation in reinforced concrete beams. Master's thesis, Technical University of Denmark, Kgs. Lynbgy, Denmark
47. DS-2426 (2004) Concrete—materials—rules for application en 206-1 in Denmark. Tech. rep., Danish Standards Association
48. Hansen K (2009) Corrosion initiation in cracked reinforced concrete. Bachelor exam project report. Technical University of Denmark, Kgs. Lyngby, Denmark
49. Küter A (2009) Management of reinforcement corrosion: a thermodynamical approach. PhD thesis, Technical University of Denmark, Kgs. Lyngby, Denmark
50. Nygaard PV (2008) Non-destructive electrochemical monitoring of reinforcement corrosion. PhD thesis, Technical University of Denmark, Kgs. Lyngby, Denmark
51. Danish test method DSF 423.39 (1998) Testing of concrete, Hardened concrete: production of fluorescense impregnated plane sections
52. Laugesen P (2005) Crack sampling, treatment and analysis. In: Proceedings of the Knud Højgaard conference advanced cement-based materials—research and teaching
53. Bardal E (2004) Corrosion and protection. Springer, London
54. Elsener B, Andrade C, Gulikers J, Polder R, Raupach M (2003) Half-cell potential measurements - potential mapping on reinforced concrete structures. Mater Struct 36(261):461–471
55. Myrdal R (2007) The electrochemistry and characteristics of embeddable reference electrodes for concrete. Tech. Rep. 43, European Federation of Corrosion Publications
56. Germann Instruments (2010) Deep purple and rainbow indicator. www.germann.org
57. Campbell D, Sturm R, Kosmatka S (1991) Detecting carbonation. Concr Technol Today Portland Cem Assoc 12(1):1–5
58. Castro P, Sagues A, Moreno E, Maldonado L, Genesca J (1996) Characterization of activated titanium solid reference electrodes for corrosion testing of steel in concrete. Corrosion 52(8):609–617
59. Mohammed TU, Otsuki N, Hamada H, Yamaji T (2002) Chloride-induced corrosion of steel bars in concrete with presence of gap at steel-concrete interface. ACI Mater J 99(2):149–156
60. Yano M, Iida T, Kawabata K, Miyazato S (2002) Steel corrosion induced by chloride and carbonation in concrete with defects. In: The ninth East Asia-Pacific conference on Structural engineering and construction, pp 62–68
61. Nygaard P (2004) Effect of steel-concrete interface defects on the chloride threshold for reinforcement corrosion. Master's thesis, Technical University of Denmark, Kgs. Lyngby, Denmark
62. Buenfeld N, Glass G, Reddy B, Viles F (2004) Process for the protection of reinforcement in reinforced concrete. United States Patent # 6685822, Alexandria, VA, USA
63. AASHTO (2007) LRFD Bridge design specifications, SI units, 4th edn. American Association of State Highway and Transportation Officials, Washington, DC, USA
64. ACI Committee 224 (2001) ACI 224R-01: control of cracking in concrete structures. American Concrete Institute, Farmington Hills, MI, USA, 2008, 22 pp
65. Eurocode 2: Design of concrete structures, 2003

Part III

Appendices

Appendix A

Questionnaire and report

This appendix includes a questionnaire, which was sent to numerous experts around the world, and the resulting report. The questionnaire was intended to collect the input and opinions of experts to help focus the research project on the most relevant aspects of concrete cracking and durability issues faced by RC structures. The original questionnaire and the follow-up report, which was returned to all participants, follow (in the original formatting).

Questionnaire
Effect of Cracks on Durability of Reinforced Concrete Structures

We Need Your Input
We would appreciate your input and opinions in order to focus our research on the most relevant aspects that cracks have on the durability of reinforced concrete structures.

Who Are We
A joint research project was initiated in August 2005 between the Technical University of Denmark (DTU) and Purdue University consisting of the following Ph.D. project:

Title:	Corrosion Behavior in Cracked Reinforced Concrete Structures
Ph.D. Student:	Brad Pease, DTU
Advisors:	Mette Geiker (Lead) and Henrik Stang, DTU and Jason Weiss, Purdue University
Funding:	DTU Ph.D. Scholarship

In addition to the above-mentioned project there are currently several related projects that will benefit from your input:

- *Non-destructive Electrochemical Methods for Monitoring of Reinforcement Corrosion*, Peter Vagn Nygaard, FORCE Institute and DTU
- *Management of Reinforcement Corrosion*, André Küter, DTU
- *Constitutive Modeling of Cracks in Reinforced Concrete Structures During Repeated Loading*, Peter Bernth, DTU
- *Using In-situ Monitoring to Predict the Life Cycle Performance of Concrete Structures*, Farshad Rajabipour, Purdue University
- *Water Transport in Cracked Concrete*, Jason Weiss, Purdue University

We hope that the proper focus and cooperation between these projects will lead to a significant step forward in the service life modeling and in the improved durability of reinforced concrete structures.

To facilitate the use of your opinions please complete the questionnaire and return it by **November 4, 2005** to:

> Brad Pease, Technical University of Denmark, bjp@byg.dtu.dk, or
> Mette Geiker, Technical University of Denmark, mge@byg.dtu.dk

Please feel free to forward this questionnaire to any interested third-parties having experience in design/maintenance/repair of reinforced concrete structures, corrosion of reinforcing steel, or other related fields.

An anonymous summary of the results of this questionnaire will be completed by December 31, 2005 and will be distributed to those who completed the questionnaire.

Thank you for your participation and insight on the complex issues of concrete cracking and durability.

General Information

Name:
Email:
Position Description (Check all that apply):

Owner	☐
Designer	☐
Construction Contractor	☐
Inspection and Assessment	☐
Repair	☐
Other (Please Specify):	☐

Years Experience:
Company:
Country:

When and how often, in your experience, do inspections for cracks in reinforced concrete structures take place?

During Construction and Handover	☐
Regularly in Connection with Maintenance	☐
Only Once Problems Arise	☐
Never	☐
Other (Please Specify):	☐

Questionnaire

In the questions 1 and 2 please rate the importance of the choices from 1, being of the least importance to 5, being of the most importance.

1. Rate the importance of the following factors affecting the durability of reinforced concrete structures exposed to harsh environments (i.e. marine environments and deicing salts).

	1	2	3	4	5
a) Quality of Concrete Cover	☐	☐	☐	☐	☐
b) Location of Reinforcing Steel	☐	☐	☐	☐	☐
c) Cracking of Concrete	☐	☐	☐	☐	☐
d) Chloride Loading	☐	☐	☐	☐	☐
e) Other (Please Specify):	☐	☐	☐	☐	☐

2. Rate the importance of the following factors on the durability of cracked concrete

	1	2	3	4	5
a) Harsh environments (i.e. splash zones of marine structures, or roadways)	☐	☐	☐	☐	☐
b) Maximum crack width	☐	☐	☐	☐	☐
c) Crack Orientation					
c1) Parallel to rebar	☐	☐	☐	☐	☐
c2) Perpendicular to rebar	☐	☐	☐	☐	☐
d) Crack type, indicating the morphology					
d1) Plastic cracking	☐	☐	☐	☐	☐
d2) Shrinkage cracking	☐	☐	☐	☐	☐
d3) Load induced cracking	☐	☐	☐	☐	☐
d4) Other (Please Specify):	☐	☐	☐	☐	☐
e) Other (Please specify):	☐	☐	☐	☐	☐

3. A table with several applications of reinforced concrete is shown below. It is assumed that the concrete contains cracks of two depths. The first crack considered has reached the depth of the reinforcing steel (i.e. crack depth/cover ≥ 1.0). The second crack has only reach half the depth of the reinforcing steel (i.e., crack depth/cover = 0.5). Two separate tables are provided, one for transverse cracks (considered perpendicular to rebar) and longitudinal cracks (considered parallel to rebar). For each structural application, crack orientation, and crack depth please indicate a crack width that would be of concern as related to the *durability* of the given structure.

Transverse Cracking (Perpendicular to rebar)

Structural Application	**Crack Width (mm)**	
	Depth/Cover ≥ 1.0	**Depth/Cover = 0.5**
Submerged Marine Structure		
Marine Structure in Splash Zone		
Bridge Deck		
Beam in Building		

Longitudinal Cracking (Parallel to rebar)

Structural Application	**Crack Width (mm)**	
	Depth/Cover ≥ 1.0	**Depth/Cover = 0.5**
Submerged Marine Structure		
Marine Structure in Splash Zone		
Bridge Deck		
Beam in Building		

4. Are you familiar with Service Life Models and their application towards estimating service life of reinforced concrete structures (□**Yes/**□**No**)? If **No** then skip to Question 6, if **Yes** please continue. In the following chart please indicate the applications you have used for various Service Life Model's, and please indicate the accuracy of service life predictions of each model in percentage based on past experience (if unknown for Service Life Model's you have used please type NA).

Service Life Model Title	Comparison of Mixtures and Cover	Evaluation of Service Life of Existing Structures	Design of New Structures	Accuracy (%)
Duracrete	□	□	□	
Hetek	□	□	□	
Life-365	□	□	□	
Stadium	□	□	□	
Others:				
	□	□	□	
	□	□	□	

5. Based on your experience with Service Life Model's, please rank which improvements are most needed to improve service life estimations provided by current Service Life Model's for reinforced concrete structures (1 being least important, 5 being most important).

	1	2	3	4	5
a) Improved environmental condition information (i.e. regional temperature data)	□	□	□	□	□
b) Improved material parameters	□	□	□	□	□
c) Treating concrete as a heterogeneous material	□	□	□	□	□
d) Including effect of cracks on life cycle estimation	□	□	□	□	□
e) Considering the moisture state of concrete (i.e. saturated, dry, cyclic wet and dry)	□	□	□	□	□
f) Other (Please specify):	□	□	□	□	□

6. Describe your opinion of what research work is most needed and which issues should be addressed to improve our knowledge on and control of the effect of cracks on durability of reinforced concrete structures.

7. What, in your opinion, is the most relevant direction research in service life modeling should proceed in the future?

Other Comments:

Once again thank you for your contribution.

Please email completed forms to Brad Pease at bjp@byg.dtu.dk or Mette Geiker at mge@byg.dtu.dk before November 4, 2005.

Report: Results of Questionnaire on the Effect of Cracks on Durability of Reinforced Concrete Structures

Brad Pease, Mette Geiker, Jason Weiss, and Henrik Stang

1. Introduction

This short report presents the results of a questionnaire entitled "Effect of Cracks on Durability of Reinforced Concrete Structures," which was sent to specialists involved in concrete durability throughout Europe and North America. The purpose of the questionnaire was to assist in the focusing of research on the durability, monitoring, and service life modeling of reinforced concrete structures. The results of the questionnaire were used to shape the Ph.D. study entitled "Transport and Corrosion Initiation in Cracked Reinforced Concrete," being performed at the Technical University of Denmark by Brad Pease. Additionally, the results will be utilized by other researchers at the Technical University of Denmark and Purdue University involved in the following projects:

- *Non-destructive Electrochemical Methods for Monitoring of Reinforcement Corrosion*, Peter Vagn Nygaard, FORCE Institute and DTU
- *Management of Reinforcement Corrosion*, André Küter, DTU
- *Using In-situ Monitoring to Predict the Life Cycle Performance of Concrete Structures*, Farshad Rajabipour, Purdue University
- *Water Transport in Cracked Concrete*, Jason Weiss, Purdue University

2. Demographics of Respondents

A total of 15 responses have been received from participants in Denmark, The United States of America, Germany, The Netherlands, and Canada with a range of 10 to 40 years experience. A total of eleven responses came from European nations and four from North America. Respondents' position descriptions included owners, designers, researchers, inspectors, repair contractors, materials engineers, producers, and consultants. Those surveyed had approximately 24 years of experience on average and came from a wide range of job descriptions and geographic locations, providing information from varying perspectives and leading to a more accurate view of the concrete society's opinions on current needs in research.

3. Results of Questionnaire

In this section the responses to the individual questions are presented as an average reply of all respondents. Additionally, the average response from North America and Europe has been provided to assess any trends based on geographic location. In this section, the questions are given followed by the response.

General / Question 0:
When and how often, in your experience, do inspections for cracks in reinforced concrete structures take place?

The results for this question can be seen below in the Table 1. The case of never inspecting for cracks was not indicated by any participant (i.e. 0%).

Table 1: Frequency of Crack Inspection

During Construction			Regularly with Maintenance			Once Problems Arise		
Overall	**North America**	**Europe**	**Overall**	**North America**	**Europe**	**Overall**	**North America**	**Europe**
73%	75%	73%	60%	75%	45%	33%	0%	45%

Question 1 and 2 within the Questionnaire section required the participant to rate the importance of various factors, where a 1 would be of little importance and 5 would be of great importance.

Question 1:
Rate the importance of the following factors affecting the durability of reinforced concrete structures exposed to harsh environments.

Table 2 shows the average rating for question 1 including the overall, European, and North American outlook. Additional factors were suggested (and ranked) by individuals including moisture (5), type of structure (4), drying and wetting cycles (5), availability of moisture and oxygen (5), and exposure conditions (5).

Table 2: Ranking of Factors Effecting Durability of Reinforced Concrete Structures

	Overall	**North America**	**Europe**
Quality of Concrete	4.5	4.3	4.6
Location of Reinforcing Steel	4.2	4.3	4.1
Cracking of Concrete	3.6	4.0	3.4
Chloride Loading	3.4	2.8	3.8

Question 2:
Rate the importance of the following factors on the durability of cracked concrete.

Table 3 provides the overall, European, and North American rankings for question 2. An additional crack type was suggested to be chloride induced cracking and was assigned a rank of 3 out of 5. Other suggested factors on the durability of cracked concrete were the type of loading, location and depth of cracks, cover depth, water-to-cement ratio, and reinforcement type.

Table 3: Ranking of Factors Effecting Durability of Cracked, Reinforced Concrete

	Overall	North America	Europe
Harsh Environments	4.5	4.8	4.4
Maximum Crack Width	4.0	3.8	4.0
Crack Orientation			
Longitudinal	3.8	3.3	4.1
Transverse	3.1	2.8	3.3
Crack Type			
Plastic Cracking	3.6	2.7	4.0
Shrinkage Cracking	3.7	3.0	4.0
Load Induced Cracking	3.6	3.3	3.7

Question 3:
For each structural application, crack orientation, and crack depth please indicate a crack width that would be of concern as related to the durability of the given structure.

Question 3 was a survey of crack widths concerning the durability of reinforced concrete structures. Various structural applications including marine structures in the submerged and splash zones, bridge decks, and a beam in a building were listed along with varying crack depth to cover ratios. The ranges of values given for crack widths are shown in Table 4.

Table 4: Results of Question 3 for (a) Transverse Cracking (Perpendicular to rebar) and (b) Longitudinal Cracking (Parallel to rebar)

(a)

Structural Application	Crack Width (mm)	
	Depth/Cover ≥ 1.0	Depth/Cover = 0.5
Submerged Marine Structure	0.2 - 0.5	0.3 - 1.0
Marine Structure in Splash Zone	0.1 - 0.3	0.1 - 0.5
Bridge Deck	0.15 - 0.3	0.15 - 0.3
Beam in Building	0.15 - 0.5	0.15 - 0.5

(b)

Structural Application	Crack Width (mm)	
	Depth/Cover ≥ 1.0	Depth/Cover = 0.5
Submerged Marine Structure	0.1 - 0.5	0.2 - 1.0
Marine Structure in Splash Zone	0.0 - 0.2	0.1 - 0.5
Bridge Deck	0.0 - 0.2	0.0 - 0.5
Beam in Building	0.1 - 0.5	0.2 - 0.5

Question 4:
Are you familiar with service life models and if so indicate the applications you have used various models for.

Of the 15 responses, 12 had experience with service life models. Duracrete, Life-365, HETEK, Stadium, and an in-house program were reported upon. Service life models have been used to compare and evaluate various mixtures and as a design tool, however on average these models were rated to be accurate only 45% of the time. It should be noted that several respondents indicated that too little information is available to assess the accuracy of these models currently.

Question 5:
Based on your experience with service life models, please rank which improvements are most needed to improve service life estimations provided by current service life models for reinforced concrete structures.

Table 5 provides the results on what is perceived as the most needed improvements to current service life models. Additional improvements suggested by participants included considerations of traffic loading, other factors affecting durability (i.e. alkali-silica reaction, sulfate attack, and freeze-thaw), and other variables such as workmanship and as-built material properties.

Table 5: Ranking of Possible Improvements to Current Life Cycle Models

	Overall	North America	Europe
Improved Environmental Condition Information	3.3	3.0	3.4
Improved Material Parameters	3.8	3.3	4.0
Treating Concrete as a Heterogeneous Material	2.3	2.5	2.3
Including Effect of Cracks on Life Cycle Estimation	4.3	4.7	4.1
Considering Moisture State of Concrete	4.0	3.7	4.1

4. Summary

Through a questionnaire on the effect of cracking on durability of reinforced concrete structures, the general opinions of professionals involved in design, execution, and operation has been examined. Based upon the results of the survey the following conclusions have been made.

- Longitudinal cracks were viewed as slightly more detrimental to the durability of reinforced concrete when compared to transverse cracks. Longitudinal cracks were ranked 3.8, compared to transverse cracks which were ranked 3.0.
- The varying causes of the cracking were considered to be less influential on the durability of concrete.

- Control of longitudinal crack width was considered more important than transverse crack width. The occurrence of any cracking, longitudinal to the reinforcement, caused concern; however, a less strict minimum crack width of 0.1 mm caused concern for transverse cracking.
- General opinion concluded that including the effect of cracking on durability of reinforced concrete structures is the most needed improvement to current service life models.

5. Acknowledgements

The authors would like to thank each person who participated in the questionnaire for their time and effort. Your contributions are appreciated and the results of this survey have been utilized in the refinement of a Ph.D. study entitled “Transport and Corrosion in Cracked Reinforced Concrete.”

Appendix B

Constituent materials

This appendix provides extensive information on the constituent materials used in the concrete mixtures described in Table 2.1 and shown in Figure B.1. Portions of this information was prepared in [*Nygaard*, 2008].

Cement

"Aalborg White©" portland cement type CEM I 52.5 R from Aalborg Portland in Denmark was used. All concrete mixtures were made with cement from the same batch (TUN no. 8919599). Table B.1 shows the results of an analysis of a sample of the cement performed at Aalborg portland.

Aggregates

Table B.2 shows the test methods used to determine the essential material properties for the aggregates used in this investigation. Table B.3 provides the results of these tests. The fine aggregate used was a Class E sea-sand (in accordance with [*DS-2426*, 2004]) from RN Sten og Grus in Denmark. The fine aggregate size varied between 0–4 mm and was graded as shown in Figure B.2. The coarse aggregate used was a Class A sea-gravel (in accordance with [*DS-2426*, 2004] from RN Sten og Grus in Denmark. The coarse aggregate size varied from 4–8 mm and was graded as shown in Figure B.2.

Commercially available packing software (4C-Packing) was used to determine the optimum combination of the coarse and fine aggregates. The result of the packing calculation is shown in Figure B.3. The optimum ratio of fine to coarse aggregate, 43% fine to 57% coarse aggregate, is indicated in the figure by the broken line. Additional information on the development of this concrete mixture can be found in the literature [*Nygaard*, 2008].

Water

Ordinary tap water was used during the mixing process. No analysis of the water was conducted.

Figure B.1 *Constituent materials for mixtures 1 and 2. (Author's photos)*

Table B.1 *Test Results from Cement Composition Testing*

Property		Value
		mass%
Oxides:	SiO_2	24.39
	Al_2O_3	2.06
	Fe_2O_3	0.34
	CaO	68.42
	MgO	0.59
	SO_3	2.09
Loss on Ignition		0.71
Cl^-		0.009
Alkalies:	K_2O	0.022
	Na_2O	0.176
	Eqv. Na_2O	0.191

Table B.2 *Physical Property Test Methods Used for Fine and Course Aggregates*

Property	Method
Absorption and Density	DS/EN 1097-6
Grading	DS/EN 933-1
Eigen Packing	APM 506

Table B.3 *Essential properties for the aggregates used in the concrete.*

Properties of aggregates		Fine aggregate 0-4 mm	Coarse aggregate 4-8 mm	
Sieve analysis	Sieve size [mm]	Percentage passing		
	31.5	100	100	% - mass
	16	100	100	% - mass
	8	100	100	% - mass
	4	98.4	4.4	% - mass
	2	88.0	0.4	% - mass
	1	71.9	0.2	% - mass
	0.5	49.5	0.2	% - mass
	0.25	19.8	0.2	% - mass
	0.125	1.8	0.2	% - mass
	0.075	0.4	0.2	% - mass
Density, saturated surface dry		2643	2623	kg/m^3
Absorption		0.36	1.0	% - mass
Eigen-packing		0.70	0.62	-
Cl^- content		0.012	0.007	% - mass
Equivalent Na_2O		0.011	0.006	% - mass

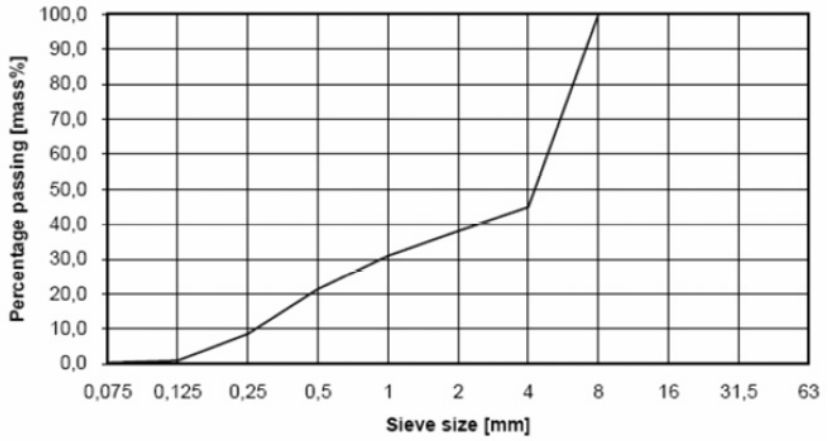

Figure B.2 *Coarse and Fine Aggregate Gradation Curve*

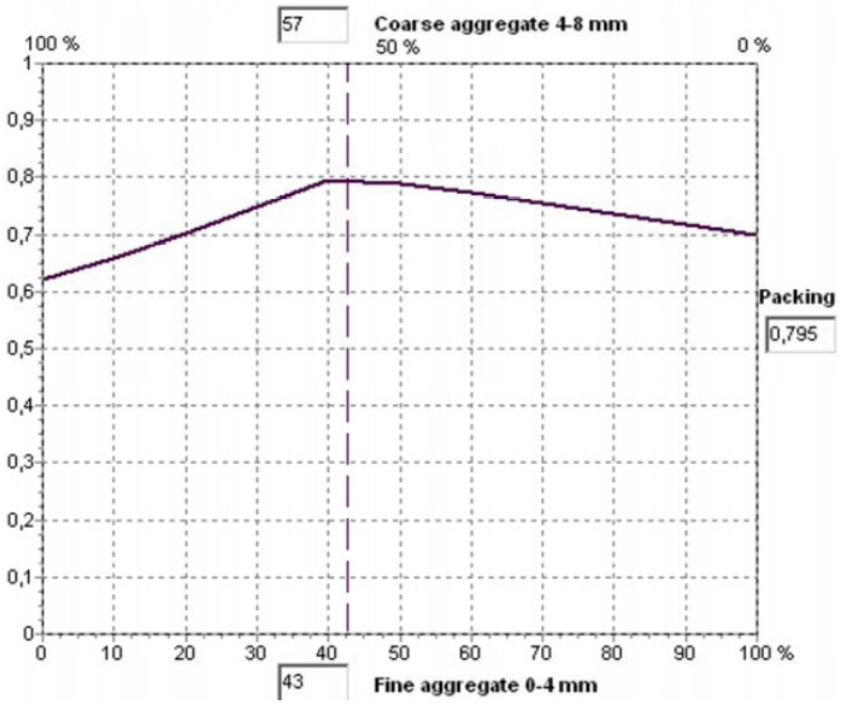

Figure B.3 *Results of 4C-Packing Theoretical Packing Calculation*

Fiber

The fiber used for this investigation was a Densit steel fiber with a tensile strength of 1300 MPa. The fiber was smooth, straight and round steel fiber with 0.4 mm diameter and 12.5 mm length. Figure B.4 shows the fibers used.

Figure B.4 *Steel fiber used for Mixture 2. (Author's photos)*

Appendix C

Practical guide - 2M and 4M Aramis photogrammetry systems

Scope

This appendix provides a practical user manual for the use of the Aramis three dimensional photogrammetry equipment (both 2M and 4M equipment). A description of placing and calibrating the digital cameras and collecting data is presented, which applies for all possible uses of the Aramis equipment. The data analysis section explicitly describes how to measure crack mouth openings using the collected data, and therefore applies to the investigation of cracking in materials such as concrete or other composites. For further details the reader should consult the references.

Field of application

Aramis is photogrammetry equipment, which is useful to measure deformations in various materials. The system can be used for either two or three dimensional photogrammetry depending upon the number of cameras used. The system captures images during testing and then computes the deformation of the measuring surface using a post-processing technique. The equipment can be utilized to measure, among others, crack widths, local and global deformations, and strain.

References

1. GOM Optical Measuring Techniques. *Aramis v5.4 User Manual*. GOM mbH, 2005 (www.gom.com)

Definitions

CCD (Charged-Coupled Device) - A semiconductor technology used to build light-sensitive electronic devices such as cameras and image scanners. Such devices may detect either color or black-and-white. Each CCD chip consists of an array of light-sensitive photocells.

Figure C.1 *Samples with spatter pattern applied. (Author's photos)*

The photocell is sensitized by giving it an electrical charge prior to exposure.

Facet - An individual grid section of the computational mask applied by Aramis to the image of the specimen surface.

Test method

Specimen preparation

In order to facilitate measurements with Aramis adequate contrast in the grayscale of the specimen surface is required. This is most easily achieved using black and white spray paint to apply a random spatter pattern. Fig. C.1 shows two examples of adequately varying grayscales for measurement.

The spatter marks applied should be of adequately small size such that multiple grayscales are contained within each facet of the computational mask. The spatter marks should be between 1/3 and 1/2 the size of a facet to track deformations in the specimen surface. A rule of thumb is that the spatter size should be approximately the measurement length divided by 200.

Aramis setup

Camera setup

Fig. C.2 shows the necessary hardware for measurements, two CCD digital cameras on an aluminum mounting bracket and a solid tripod. After affixing the camera assembly to the tripod the cameras must be placed at approximately the proper measuring distance, base distance, and camera angle as specified in [*Aramis*, 2005] in Section 3.2.1 (2M) or 3.2.2 (4M) or in Tables C.1 or C.2.

Next, the cameras must be connected to the computer. The exact procedure for the 2M and 4M machines varies slightly, however it is important to match the labels on the 'Right'

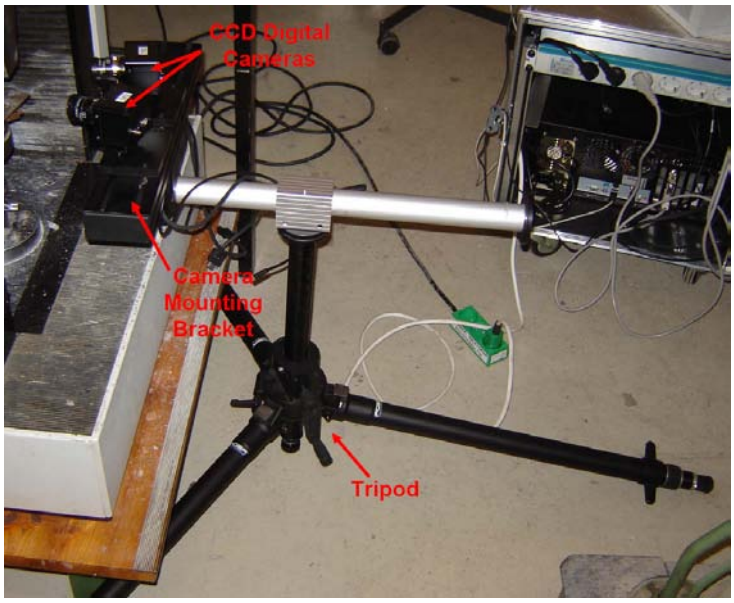

Figure C.2 *Tripod mount with affixed cameras. (Author's photos)*

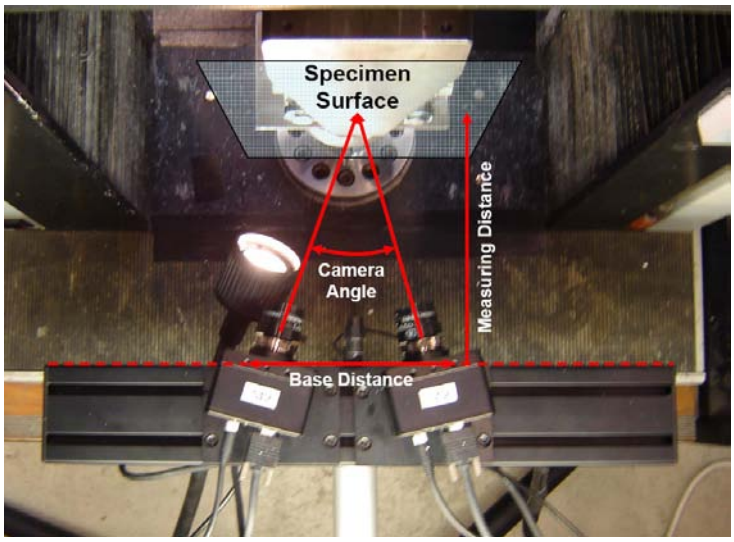

Figure C.3 *Placing cameras at proper base distance. (Author's photos)*

and 'Left' camera with the proper cables. Next, place a beam level on top of the cameras as shown in Fig. C.4 and adjust until the air bubble indicates the cameras are on a level plane.

The following tables provide the configurations for the cameras with the lenses currently available at the department for the 2M (Table C.1) and 4M (Table C.2) systems. There are additional configurations for other lenses shown in [*Aramis*, 2005].

Figure C.4 *Insuring cameras are on level plane. (Author's photos)*

Table C.1 *Camera configuration for Aramis 2M*

Focal Length of Lenses	Measuring Volume (L x W x H)	Calibration Object	Base	Min. Length of Camera Support	Measuring Distance	Camera Angle
50 mm Macro Aperture 16	200 x 160 x 160 mm^3	Panel	560 mm	800 mm	1300 mm	25°
	175 x 140 x 140 mm^3	Panel	530 mm	800 mm	1210 mm	
	135 x 108 x 108 mm^3	Panel	400 mm	600 mm	960 mm	
	100 x 80 x 80 mm^3	Panel	300 mm	500 mm	700 mm	
	65 x 52 x 52 mm^3	Panel	240 mm	500 mm	510 mm	
	50 x 40 x 40 mm^3	Panel	180 mm	500 mm	430 mm	
	35 x 28 x 28 mm^3	Panel	130 mm	500 mm	305 mm	
	25 x 20 x 14 mm^3	Panel	110 mm	500 mm	240 mm	
	15 x 12 x 8 mm^3	Panel	110 mm	500 mm	200 mm	30°
	10 x 8 x 4 mm^3	Panel	110 mm	500 mm	180 mm	35°
8 mm Aperture 11	1700 x 1360 x 1000 mm^3	Cross	800 mm	1000 mm	1700 mm	25°
	1200 x 960 x 700 mm^3	Cross	600 mm	800 mm	1200 mm	
	800 x 640 x 500 mm^3	Cross	400 mm	600 mm	800 mm	
	550 x 440 x 400 mm^3	Cross	280 mm	500 mm	570 mm	
	350 x 280 x 280 mm^3	Panel	190 mm	500 mm	400 mm	
	250 x 200 x 200 mm^3	Panel	140 mm	500 mm	290 mm	
	200 x 160 x 120 mm^3	Panel	110 mm	500 mm	235 mm	28°

Lighting

Adequate lighting must be provided to insure reliable measurements from the Aramis system. Many lighting option exist, although, based on the author's experience fluorescent tube lights are optimal. This type of light can remain on for long periods of time without creating excessive heat. *Warning: Lights which do generate excessive heat (fx. halogen lights) may cause expansion of the aluminum mounting bracket and possibly damage to the cameras if placed near the cameras!*

Creating a project in Aramis (software setup)

After starting up the Aramis computer a login screen will appear. *Note: There are power switches located on front and back on the computer, both of which need to be turned on.* The password for both systems is demo. Fig. C.5 shows the screen as it should appear after logging in. *Note: The operating system used on the Aramis computers is Linux, which is very similar in functionality to Windows. One key difference however is that when using an external hard drive it must be formatted as FAT32, not the standard NTFS format used on PC's. Once the external drive is properly formatted it will operate on both*

Table C.2 *Camera configuration for Aramis 4M*

Focal Length of Lenses	Measuring Volume (L x W x H)	Calibration Object	Base	Min. Length of Camera Support	Measuring Distance	Camera Angle
Titanar 20mm	1700 x 1700 x 1700 mm^3	Cross	980 mm	1200 mm	2200 mm	25°
	1200 x 1200 x 1200 mm^3	Cross	730 mm	1000 mm	1700 mm	
	800 x 800 x 800 mm^3	Cross	470 mm	600 mm	1100 mm	
	550 x 550 x 550 mm^3	Cross	370 mm	500 mm	850 mm	
	350 x 350 x 350 mm^3	Panel	240 mm	500 mm	550 mm	
	250 x 250 x 250 mm^3	Panel	190 mm	400 mm	410 mm	
	200 x 200 x 200 mm^3	Panel	160 mm	400 mm	330 mm	
	175 x 175 x 175 mm^3	Panel	150 mm	400 mm	310 mm	
	135 x 135 x 135 mm^3	Panel	120 mm	400 mm	250 mm	
	100 x 100 x 80 mm^3	Panel	100 mm	400 mm	200 mm	
	65 x 65 x 52 mm^3	Panel	110 mm	400 mm	150 mm	35°
50 mm Macro Aperture 2.8 – 16	1700 x 1700 x 1700 mm^3	Cross	2400 mm	Special Version	5650 mm	25°
	1200 x 1200 x 1200 mm^3	Cross	1590 mm	Special Version	3750 mm	
	800 x 800 x 800 mm^3	Cross	1160 mm	Special Version	2690 mm	
	550 x 550 x 550 mm^3	Cross	860 mm	1000 mm	2000 mm	
	350 x 350 x 350 mm^3	Panel	560 mm	800 mm	1310 mm	
	250 x 250 x 250 mm^3	Panel	380 mm	600 mm	960 mm	
	200 x 200 x 200 mm^3	Panel	350 mm	500 mm	775 mm	
	175 x 175 x 160 mm^3	Panel	325 mm	500 mm	660 mm	
	135 x 135 x 130 mm^3	Panel	255 mm	400 mm	535 mm	
	100 x 100 x 100 mm^3	Panel	210 mm	400 mm	340 mm	
	65 x 65 x 50 mm^3	Panel	155 mm	400 mm	325 mm	
	35 x 35 x 12 mm^3	Panel	100 mm	400 mm	220 mm	
	25 x 25 x 5 mm^3	Panel	100 mm	400 mm	195 mm	27°

Figure C.5 *Startup screen.*

Windows and Linux machines.

To start a new project in Aramis, first open the software by single clicking on the icon in the desktop or in the quick-start menu. Proceed by clicking on File ⇒ New Project and the New Project dialogue box will open as seen in Fig. C.6a. Create a filename and path for the project and click Next. The following two dialogue boxes, shown in Fig. C.6b and c, allow the user to adjust specific parameters. Typically, the default settings

are sufficient (additional information on these settings can be found in [*Aramis*, 2005]). Input a unique Label Name in the final dialogue box (Fig. C.6d) and click Finish.

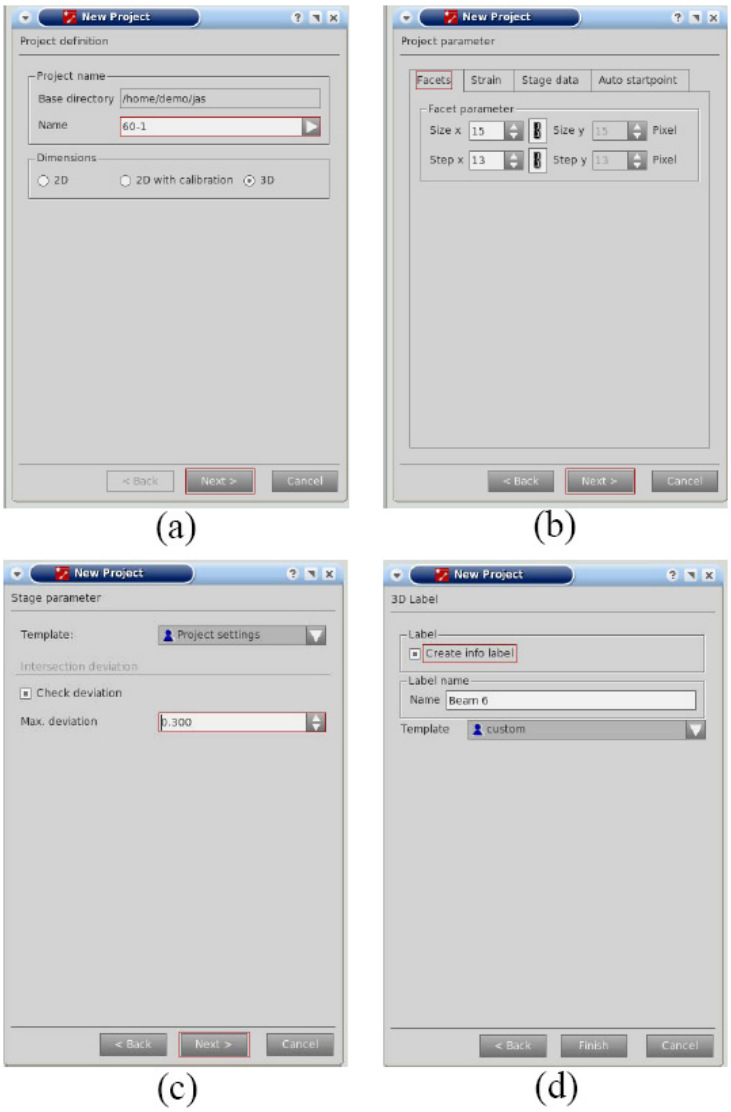

Figure C.6 *Starting a project in Aramis.*

Focusing cameras

The cameras must always be focused prior to calibration and collecting data. To focus the cameras first click on the Start/Stop Measurement icon (see Fig. C.7), which displays the live images from both cameras. Open the apertures on the cameras by loosening the locking screw and rotate the adjusting ring to the smallest number. Two options exist to easily focus the cameras:

- Place an object with text (i.e. business or credit card) at the proper distance away from the camera, or
- Using a calibration object, change the view to Overexposed and increase the shutter time such that the white points on the calibration item are overexposed.

Adjust the focus of each camera until the either the text is clear, or until the white objects are completely overexposed. To insure the best possible focus it is recommended to zoom in on the image from each camera while adjusting the focus. To do this rotate the scroll wheel on the mouse while the pointer is inside the image viewport. Tighten the locking screws to lock the focus and do not adjust during testing.

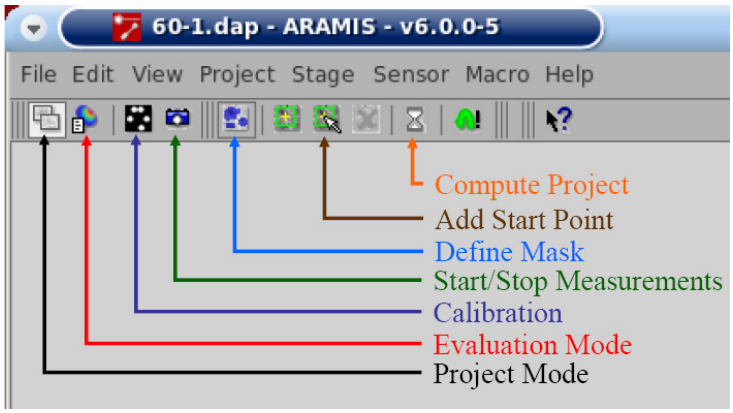

Figure C.7 *Aramis icon guide.*

Calibration

Prior to performing tests using Aramis, the sensors (cameras) must be calibrated. This is achieved by clicking on the Calibration icon (Fig. C.7), which opens the series of windows shown in Fig. C.8. First the correct Calibration object must be selected based upon the measuring volume (Fig. C.8a). See Appendix III or Section 3.2.1 or 3.2.2 of [*Aramis*, 2005] for details on selection of calibration objects. As shown in Fig. C.8b the focal length for the lenses and ambient temperature are input next. The focal length of the camera lenses can be found printed on the lenses. Finally, an overview of the calibration settings appears (Fig. C.8c) as a check, click Finish.

Fig. C.9 shows the next screen that appears after inputting the calibration parameters. During the next steps the lighting used for testing must be on. Adjust the shutter time such that the white points of the calibration object are not overexposed. Follow the on-screen instructions, changing the orientation of the calibration object, and click the snap button or use the external trigger option with trigger plugged into the Sensor plug-in (see Fig. C.14). If points on the calibration object are not recognized click undo and try again. Further adjustments to the shutter time may be necessary during the calibration for all

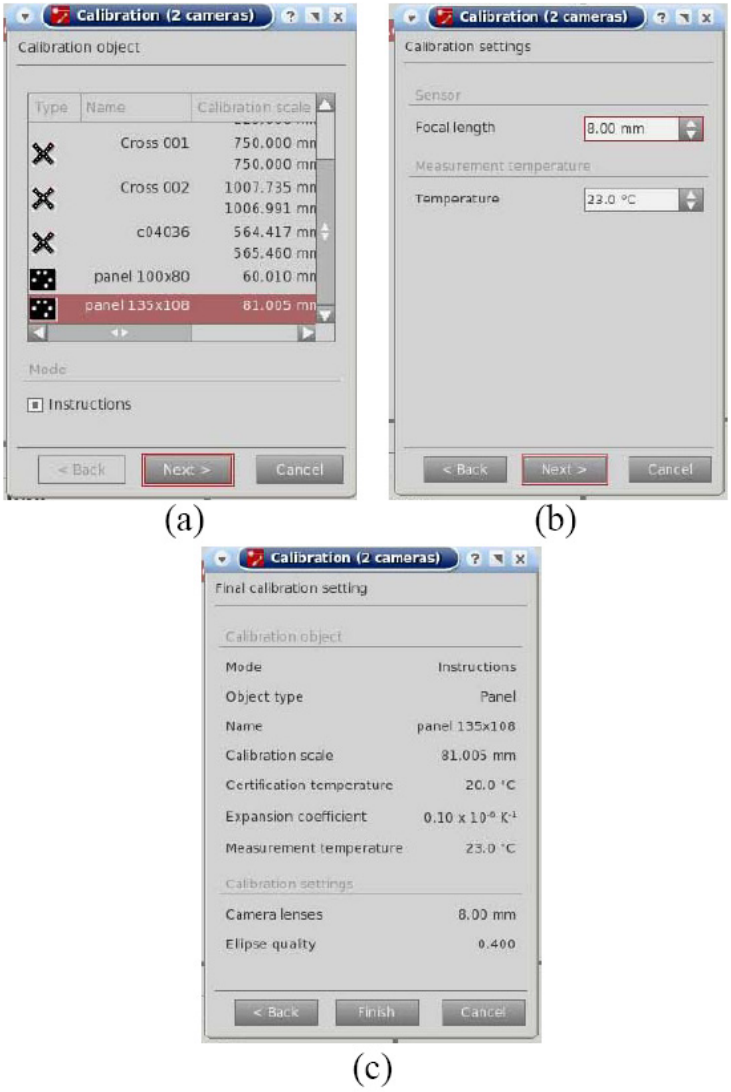

Figure C.8 *Calibration parameters dialogue boxes.*

points to be recognized. After the final calibration image has been captured click Compute and the Calibration Result will appear as seen in Fig. C.10. The Calibration Deviation should be less than 0.04 pixels. *Note: The positioning of the calibration panel during the calibration is important only for the first step. Subsequent steps in the calibration are less important and do not need to be precise. For calibration with a panel it is important that all five large dots and at least 30 small dots are detected.*

Data collection and processing

Before capturing images during an actual test it is advisable to check that the specimen surface is computable. The following section discusses a procedure to do this.

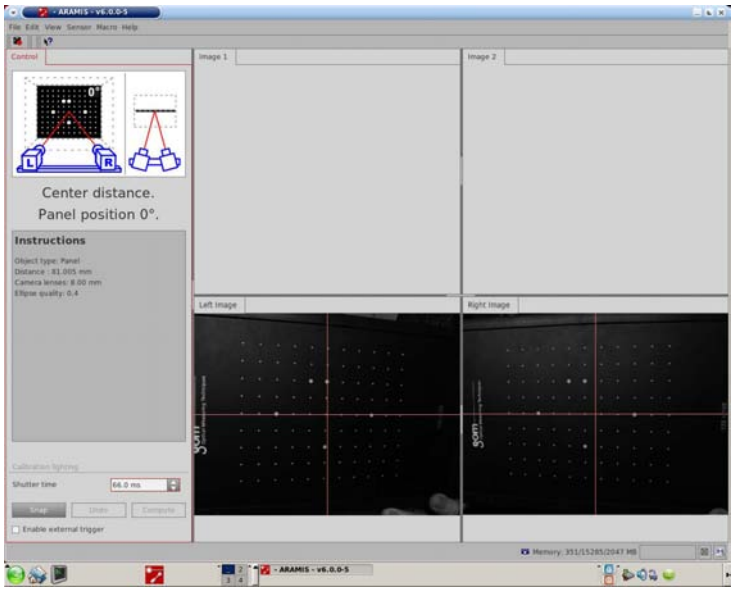

Figure C.9 *Calibrating cameras with calibration object.*

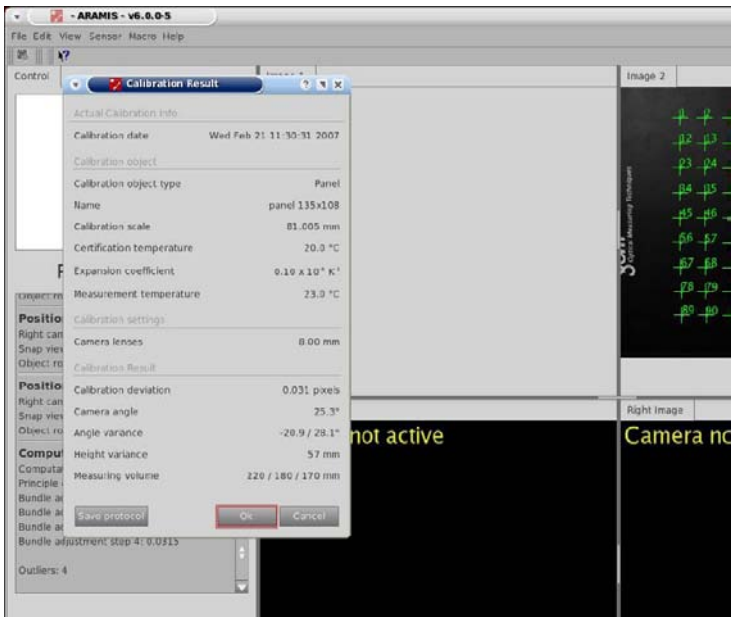

Figure C.10 *Final calibration information.*

Checking computability of the specimen surface

In order to check that the specimen surface will be computed in Aramis click the Start/Stop Measurement icon (see Fig. C.7).Set the mode to Simple, deactivate the Use timer option, and click the camera icon at the bottom of the screen to collect a single stage (See Fig.

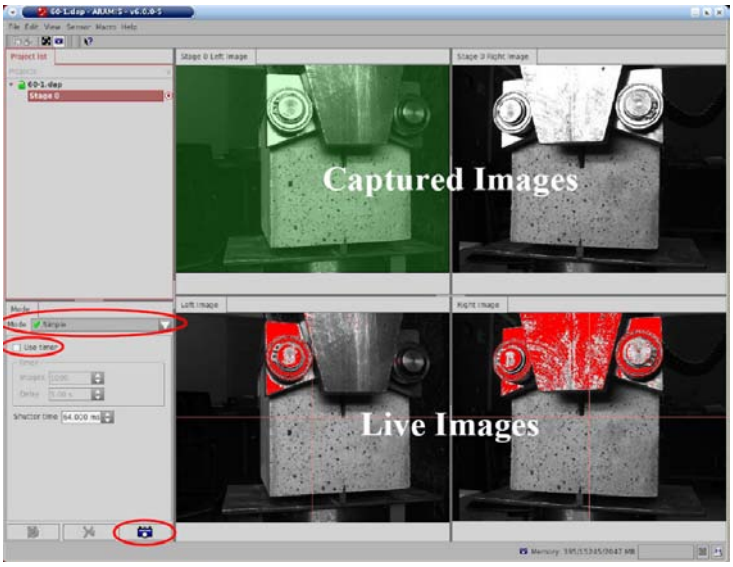

Figure C.11 *Capturing an image to check computability of specimen surface.*

C.11). As shown in Fig. C.11 the captured images from each camera will be shown above the corresponding live images.

Now, to check if the specimen surface is computable click again on the Start/Stop measurement icon followed by the Define Mask icon (See Fig. C.7). As can be seen in Fig. C.12 the Define Mask window will appear. Click the Mask Area icon and, in the left image viewport, define the mask area by left-clicking at the desired locations. When the mask has been defined right-click to mask the selected area. Next, click the Invert Mask icon followed by OK.

Next, a start point is added by first clicking on the Add Start Point icon (See Fig. C.7), which opens the Add Start Point window as shown in Fig. C.13. Pick a point in the Left Image viewport by holding down the 'Control' key and left-clicking with the mouse. The same point should be automatically recognized in the Right Image by Aramis; however, occasionally an incorrect point is selected. In this case the user may override the selection by holding the Control key and left-clicking in the Right Image near the correct point. Once the correct start point is selected in the Right Image click Create and close the Add Start Point window.

Next, click on the Compute icon (see Fig. C.7), which will compute the project and automatically change modes from the Project Mode to the Evaluation Mode. The computed area of the specimen surface will be shown in the top portion of screen in the Evaluation Mode as shown in Fig. C.16. If excessive holes appear in the computed area there is either not adequate contrast in grayscales on the specimen surface or the size of the spatter pattern applied is inappropriate. After altering the spatter pattern the previous proce-

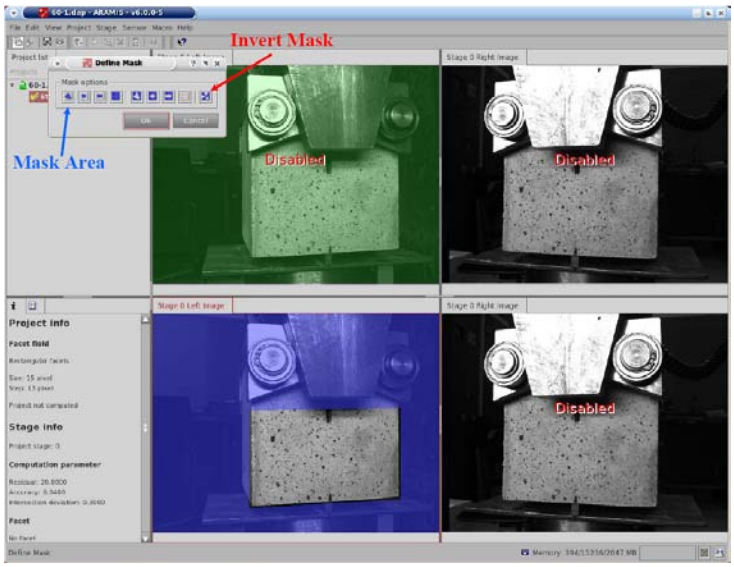

Figure C.12 *Defining a computational mask.*

dure should be repeated. *Note: Some materials may contain voids (i.e. a cut surface of concrete) that will typically not be computed as a void, when viewed from two angles, will not appear alike.* After checking that the specimen surface is computable by Aramis click on the Project Mode icon (see Fig. C.7), delete the stage by right clicking over the stage name and clicking on delete, and proceed with the data collection process.

Collecting data

The data collection process is very similar to the procedure for checking the computability of the specimen surface. Click the Start/Stop Measurement icon to again see the live images from the cameras (Fig. C.11). Several Mode options exist for data collection, with the two most commonly used being 'Simple' and 'Simple with Triggerbox,' that latter of which allows for collection of external signals from, for example, load cells. Fig. C.14 shows the triggerbox for external signal sources, which is located on the back of the Aramis computer case. Standard co-axial cables can be placed in channels 'A in 0' or 'A in 1' if desired. Additional modes include External Trigger, External Trigger with Triggerbox, Fast Measurement, Triggerlist, and Slave Mode. The Fast Measurement mode allows for collection of images up to 12 times a second for the 2M system or 7 times a second for the 4M system.

When using the Simple or Simple with Triggerbox modes check the Use Timer box and set the required number of Images and Delay and finally click the camera icon to start capturing images. If the set number of Images are not needed hit the Escape key and click OK of the dialogue box to stop the image capturing process.

After capturing images two options exist to compute the project. A computational mask

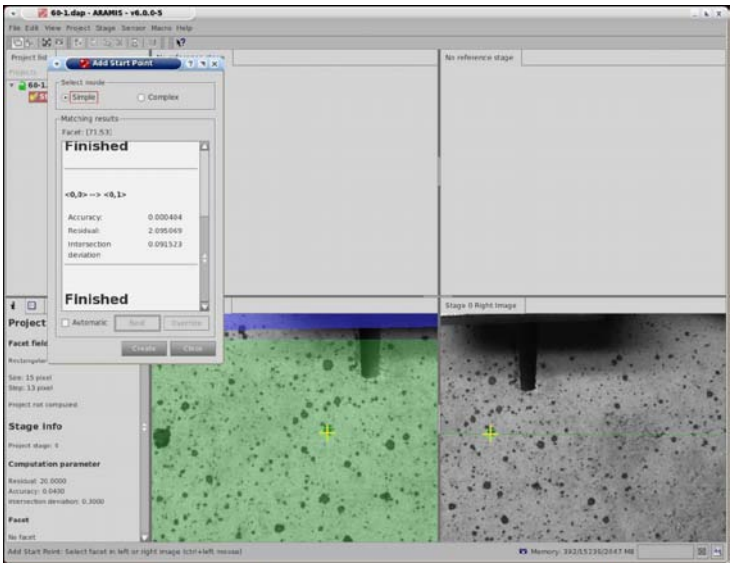

Figure C.13 *Adding a start point.*

can be defined as described in Section C, or the computed area can be restrained by changing the project parameters. To change the project parameters click Project ⇒ Project Parameter. As seen in Fig. C.15 a dialogue box will appear to set the project area. Click to deselect the Use Complete Image, change to the Quadrangle Mode, and define the area to be computed by left clicking on the bottom-left and top-right corners. After defining these points the other corners can be adjusted. Currently, only 4-sided objects can be used. *Note: If possible, it is always better to restrain the computed area as it will limit the area containing facets. This results in faster computation times and smaller files after computation.*

Next, a start point must be added as described before in section C. When multiple stages exist the procedure for adding a start point varies slightly. After picking a point in the Left Image viewport, check the Automatic box and click next. After a few moments, once the computer has located the start point in all stages click Create. *Note: If the specimen cracked during testing be sure to pick a start point away from the cracking zone as the appearance of the chosen starting point may change drastically during the testing. In addition, if the specimen has cracked across the entire measuring area it may be necessary to define multiple starting points in order to compute strains and deformations in the disconnected portions of the sample.* Again, after adding a start point click the Compute icon.

Data analysis

The data analysis sections are aimed towards cracking in concrete, however some of the techniques discussed may be useful for other materials. Additional information on analyzing data with the Aramis software can be found in the literature [*Aramis*, 2005].

Figure C.14 *Channels for input of external signal sources. (Author's photos)*

The analysis of data takes place in the Evaluation Mode screen (see Fig. C.16). The top portion of the Evaluation Mode screen shows the three dimensional 'strain' calculated by Aramis. The bottom portions of the screen show the left and right camera images. The strain can be overlayed on these images by right clicking and choosing Strain from the Visualization menu. These images are useful for videos which highlight the location of the crack. In addition, the right camera image viewport shows reports, which can be created and exported by the user.

Due to the cracking of the concrete the facets overlapping the crack become erroneous (the facets are measuring strain at a crack, which by definition would be strain free) and cannot technically be used. Therefore, additional facets can be added, either in the Project Mode or Evaluation Mode. In both cases, the following procedure is used. Click on Stage ⇒ Additional Points ⇒ Facet Point. As seen in Fig. C.17 a dialogue box will open. In the dialogue box specify Reverse Order, Simple Mode, Image Point Selection,

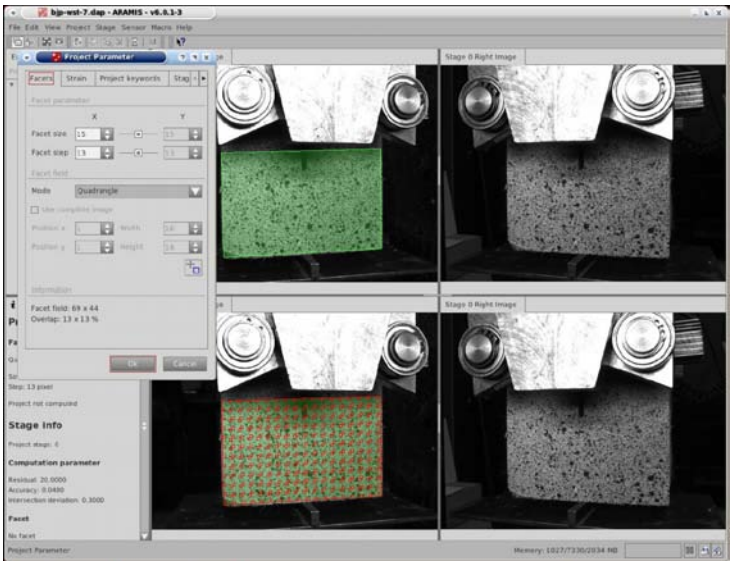

Figure C.15 *Changing the project parameters to reduce calculation time and space.*

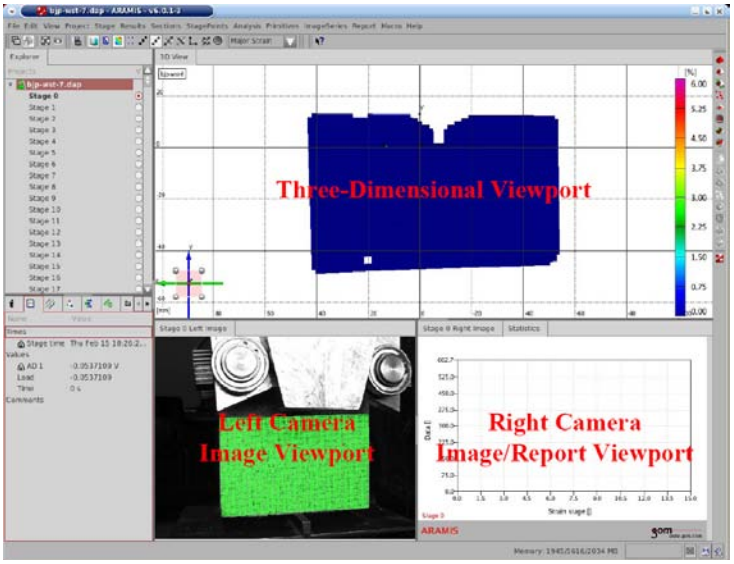

Figure C.16 *Evaluation mode screen.*

and then hold the Control key and left click to display an adjustable facet. The four corners of the facet as well as the crosshairs, which specify the calculated point, can be adjusted. Place the crosshairs near the crack, as shown in Fig. C.17. Right click on the new facet to lock the location. Check the Automatic box and then click Next and Aramis will determine the location of the new facet in reserve order (i.e. from last stage to first stage); after several moments click Create to add the new facet. More than one of these

additional facets could be added, for instance one each on opposite sides of a crack, and the crack width can then be accurately measured using the Point-Point Distance analysis option described in the following paragraph.

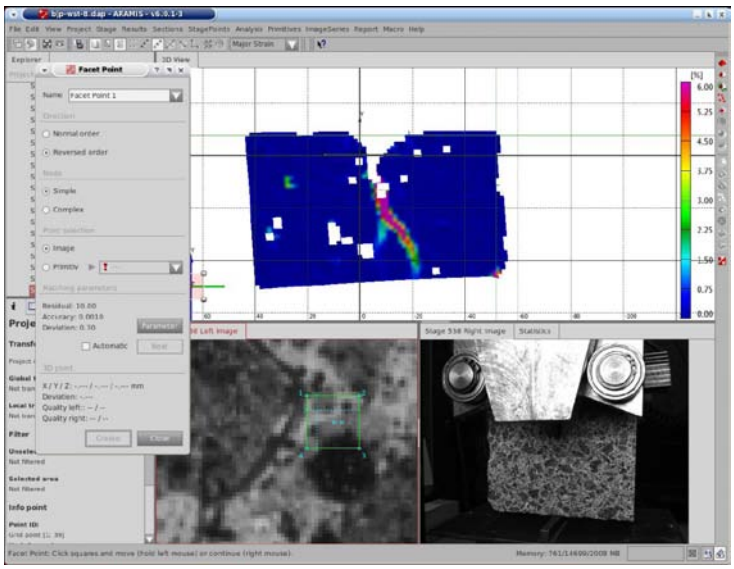

Figure C.17 *Adding individual facets.*

The distance, or change in distance between any two points can be computed by Aramis using the Point-Point Distance function. To add a Point-Point Distance measurement, first click Analysis ⇒ Point-Point Distance. As shown in Fig. C.18 a dialogue box will appear. Pick the two desired points by holding the Control key and clicking in the left camera image or the three dimensional result portion. Additionally, if new facets were added these facet can be selected directly in the Point 1 or Point 2 drop-down menus. The change in distance between the points can be plotted in a statistical report and the data exported for use in Excel, Matlab, etc.

To plot data from Point-Point Measurements in Aramis click on the Statistics report tab in the right camera image/report viewport (see Fig. C.16). Double click on the graph to open the Edit Element menu, and click the Data tab (see Fig. C.19). Choose the Line needed from the Measurements section and pick the required measurement(s), click OK. Next, to export the data, right-click on the Statistics report in the Report list (see Fig. C.19) and click Export Diagram Data. The data will be exported as a .txt file which can be opened in Excel as a space delimited file.

The Aramis equipment is capable of many other analysis options. Please refer to [*Aramis*, 2005] for additional details.

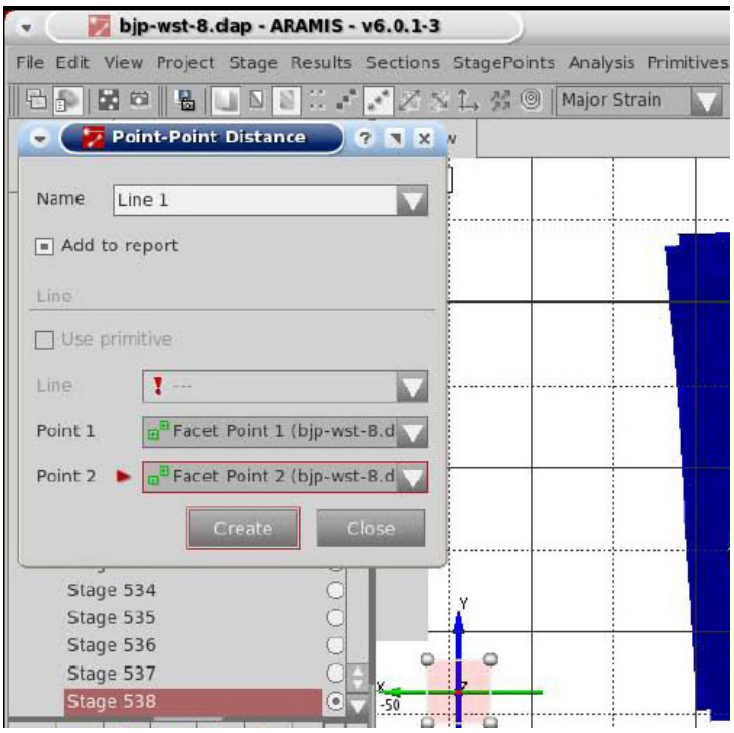

Figure C.18 *Measuring the change in distance between two points.*

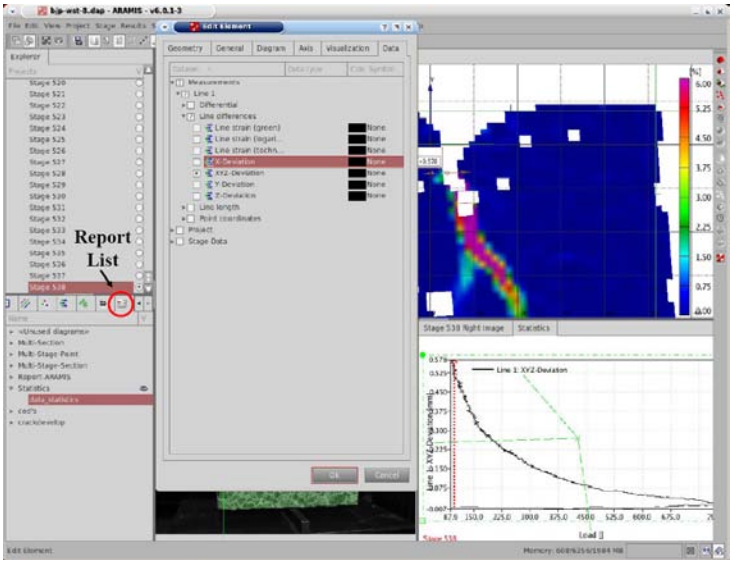

Figure C.19 *Creating and exporting data from graphs in Aramis.*

Appendix D

Practical guide - GNI X-Ray system at DTU

Scope

This appendix provides a practical guide for the operation and use of the GNI X-Ray system at the Department of Civil Engineering at the Technical University of Denmark (DTU Byg). This document is meant as a companion to the GNI X-Ray (CT) System User Manual. The system manual must be read prior to use of the system as additional necessary information and warnings are provided there. This practical guide provides descriptions and suggestions based on the author's experience, which may be useful to future inexperienced users. Description of basic operations include procedural details of the XRAS software, advanced operations include the calibration process of the X-ray camera, and an introduction to the use of ImageJ for analysis of X-ray images are found in this guide. The theory and details of the various components of the X-ray system are not detailed in this manual. For further details and information the reader should consult the references.

Field of application

The GNI X-ray System at DTU consists of an X-ray tube and an X-ray camera integrated into an X,Y,Z programmable axes system, which is all housed in an temperature controlled X-ray shielding chamber. This system is used for measuring the X-ray absorption (or attenuation) of materials. The system lends itself to the monitoring of moisture movements in porous materials due to the change in density (which effects X-ray absorption) with changing moisture conditions.

References

1. Gorm Groot Nielsen et al., X-Ray (CT) System - Purdue User Manual, (www.gni.dk)

2. ImageJ - Image Processing and Analysis in Java, (http://rsbweb.nih.gov/ij/)

Definitions

X-Ray Camera (referred to as camera throughout) – A device for detecting the presence and location of X-ray photons, which consists of NaI crystals, which emit visible light when impacted by an X-ray photon; and a 252x256 pixel photomultiplier, which records the number of light events at each pixel over a set period of time.

Integration time – The period of time the X-ray camera records the number of light events.

Dark current – The image recorded by an X-ray camera while no X-rays are being produced by the X-ray tube.

Basic operation

The following sections provide instruction on the procedures for basic operation of the GNI X-Ray System at DTU, including the startup and shutdown process and use of the controlling XRAS software package. The individual systems, including the X-ray source and camera and the moveable frame are shown in Figure D.1. *Notes* and **Warnings** are included throughout based upon the authors experience with the system.

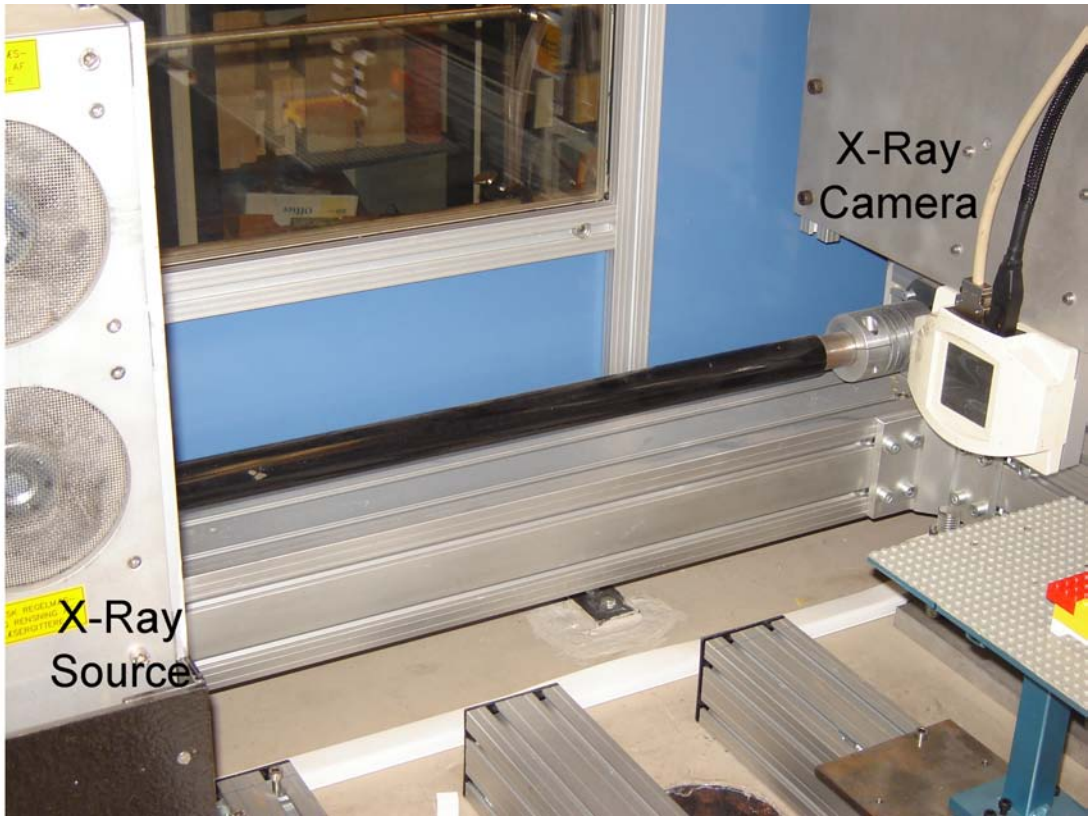

Figure D.1 *The X-ray system consists of an X-ray source and an X-ray camera, housed in a moveable frame. (Author's photos)*

Startup and shutdown procedure

Warning: Any use of the X-Ray System must first be approved by the responsible party (currently Kurt Kielsgaard Hansen). Failure to procure the proper allowance to use the system will likely result in lack of future access to the equipment.

Upon being granted access and approval of use of the X-ray System, a key will be provided to the user. Figure D.2 depicts the main control panel. This key is used to startup the system through the following procedure.

1. Place the key in the 'Nøgle til maskine' locking switch and turn to the on position.
2. Turn the large grey switch labeled 'Hovedafbryder' to the on position.
3. Press the 'Start' button.
4. Turn on the controlling computer.
5. Press the 'Aktivering af sikkerhedssytem' button upon startup and after opening of the door to reset the security system.

The large red buttons located on the control panel and on the outside and inside of the X-ray chamber are emergency shut-offs that remove power going to all systems (including the computer). For basic operations, the XRAS icon should be double-clicked to initialize all the systems as outlined below (Section D). For advanced operations, such as calibration of the X-ray camera, details on these procedures are provided in Section D.

After completing use of the X-Ray System, shutting down the system should follow this procedure.

1. Return the axes to the zero (0) positions. This will speed up the initialization process for the following user (further details on controlling the axes movements is located in the following section).

Figure D.2 *X-ray system control panel. (Author's photos)*

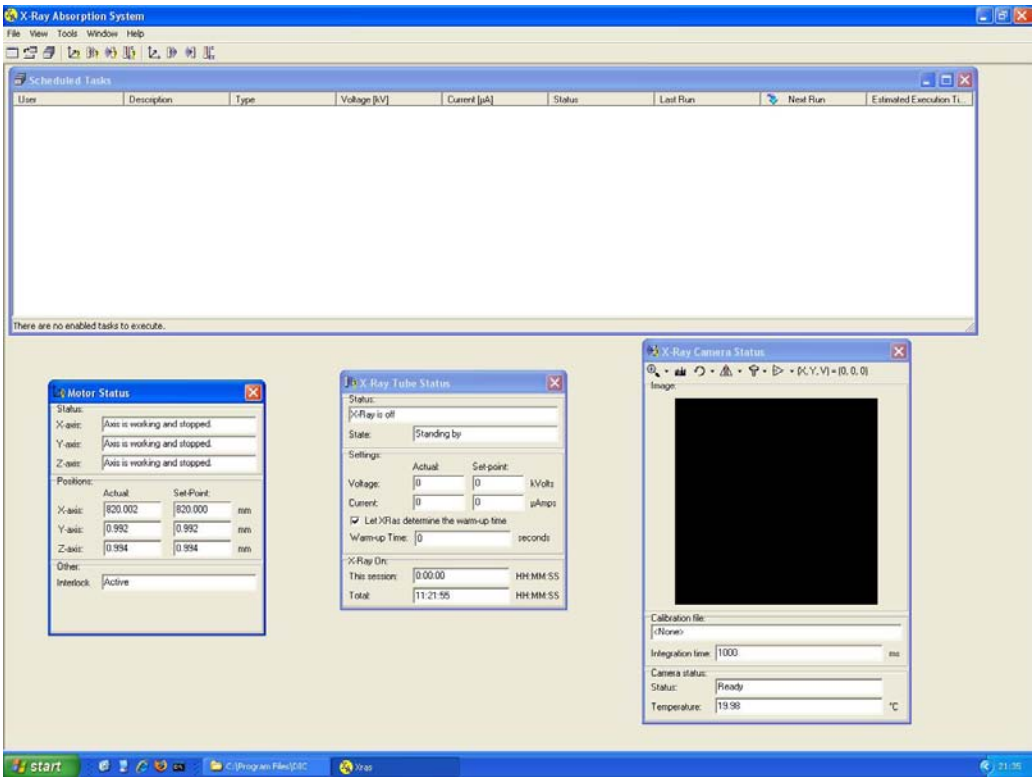

Figure D.3 *XRAS software window showing the status of all systems.*

2. Close the XRAS software.
3. Shutdown the computer.
4. Turn the large grey switch followed by the locking switch to the off positions.
5. The key must be removed from the control panel and replaced to the specified storage location.

Note: The user must leave the key in the storage location, failure to do so may result in the need for a special trip to the university to return said key and possible other actions.

XRAS software

The XRAS software controls all the systems used in the X-ray system during measurements, including the motor (which controls the X,Y,Z movements), X-ray tube, and X-ray camera. Start the XRAS software by double-clicking the icon on the desktop and then selecting the 'Yes, initialize all' button. The XRAS software has windows for each of the systems which operate in two modes: Status and Tool modes. Figure D.3 shows the XRAS software window. Initially all systems are in the status mode. The status mode is simply for monitoring the systems while the tool mode is used for operating the systems. There are several options for changing from the status to tool mode for each system. The

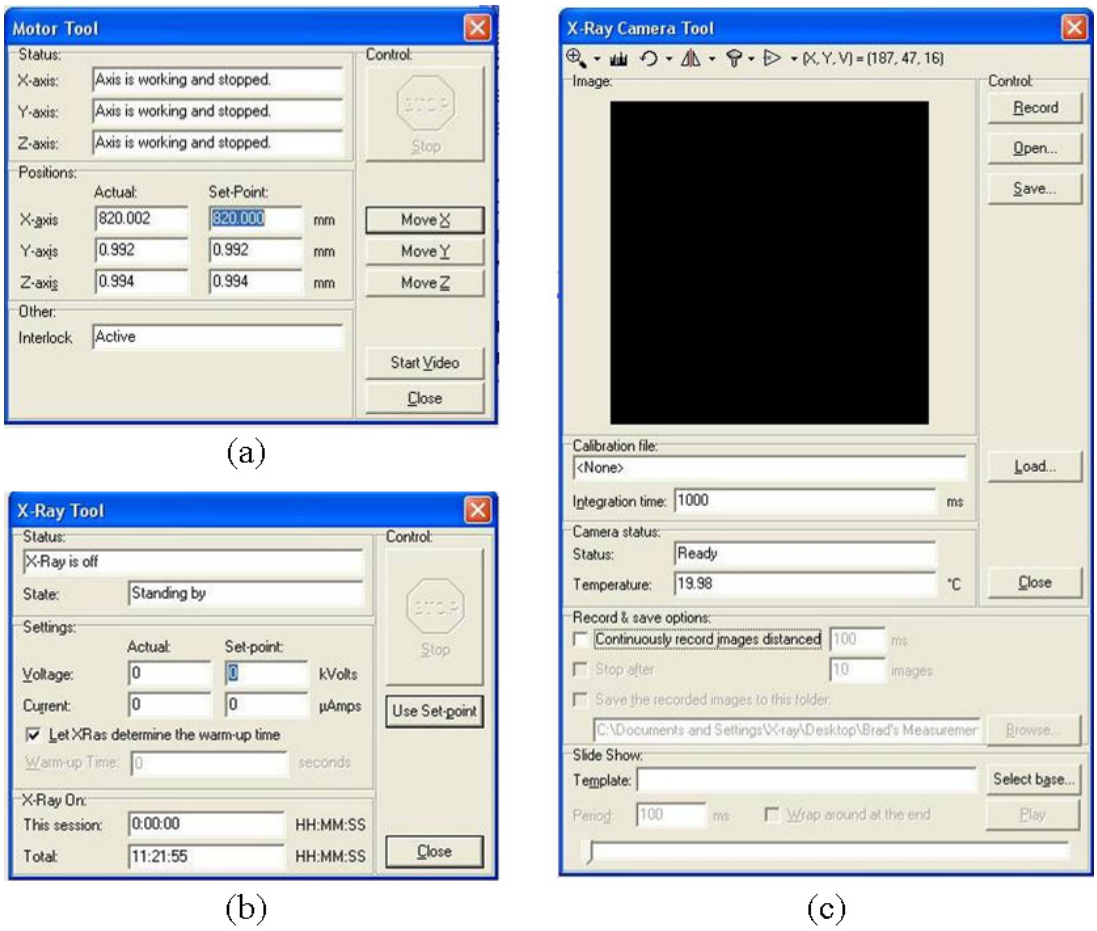

Figure D.4 *XRAS system tools consist of the (a) Motor Tool ($Shift + F2$), (b) X-Ray Tool ($Shift + F3$), and (c) X-Ray Camera Tool ($Shift + F5$)*

'Tools' dropdown menu, toolbar icons, and shortcut keys may be used (shortcut keys for each tool are shown in the respective sections below). The 'Close' button, or pressing 'Esc' exits the tool and reopens the status window. *Note: Only one Tool can be used at a time.* The use of the system tools, which are shown in Figure D.4 is outlined in the following sections.

Motor tool

The Motor Tool shown in Figure D.4(a) controls the movements of the X,Y,Z axes. The shortcut key for switching to the Motor Tool is $Shift + F2$. To move an axis simply type in the Set-point and click the 'Move *Axis*' button (*Axis being X, Y, or Z.* The movement of the axis is shown by the Actual position indicator. *Note: All Set-Points must be a positive value. The positive direction of the X-axis is to the right when facing the chamber, Y-axis is upward, and Z-axis moves the camera towards the front of the chamber. Only one axis may be moved at a time.*

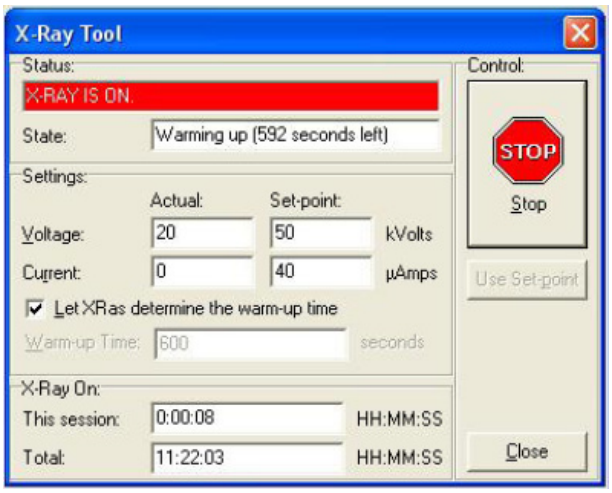

Figure D.5 *X-Ray Tool while in operation*

X-Ray tool

The Motor Tool shown in Figure D.4(a) controls the movements of the X,Y,Z axes. The shortcut key for switching to the Motor Tool is $Shift + F2$. To move an axis simply type in the Set-point and click the 'Move *Axis*' button (*Axis being X, Y, or Z*. The movement of the axis is shown by the Actual position indicator. *Note: All Set-Points must be a positive value. The positive direction of the X-axis is to the right when facing the chamber, Y-axis is upward, and Z-axis moves the camera towards the front of the chamber. Only one axis may be moved at a time.*

X-Ray camera tool

The X-Ray Camera Tool shown in Figure D.4(c) controls the X-ray image acquisition system. Images can be captured here, or using the Scheduled Tasks Tool described in the following section. To capture an image using the X-Ray Camera Tool simply press the 'Record' button after adjusting 'Integration time' to the desired period. The 'Record & save options' allow for continuous recording of a specified number of images, which may either be simply monitored in the Image window or saved to a folder for further analysis. Images will be saved as *.raw files with size 252x256 pixels, using little-endian byte order, and without a header. Further details on one option for using these image files is found in Section D.

Figure D.6 *X-Ray warning sign appears and blinks at the top of the screen when X-rays are being produced*

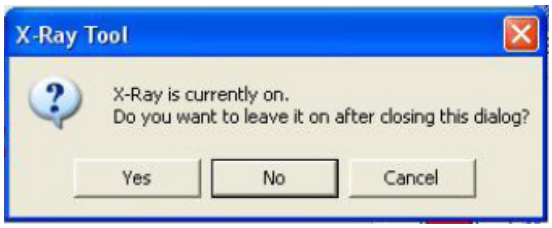

Figure D.7 *X-ray tool can be closed by clicking 'Yes' without turning off the X-ray tube*

Scheduled tasks and movement files

Scheduled tasks are used to complete more complicated measurements which may involve movements to capture images at various locations of a specimen. Figure D.8 shows the Scheduled Task window with the drop-down menu used to create, edit, and run tasks. This drop-down menu is accessed by simply right-clicking inside the Scheduled Task window. As measurements are often repeated at the same locations at different times, once a task has been created the 'Export Task To File...' button can be used to save the task and then recall it by using 'Import Task From File...'. By pressing the 'Enable Task' button a disabled task is enabled and can be run immediately by pressing the 'Run Now!' button. The process of creating a task is outlined in Figure D.9 and in the following paragraph.

After right-clicking to show the drop-down menu and selecting 'New Task...' Figure D.9(a) appears and general information is input, including the user's initials and a description of the task. The 'Disabled' box should typically be checked. Figure D.9(c) shows that a specific time and date may be set for measurements; however, typically it is better to set that time to a future date then enable and run the task as previously described. Reasons for not using the 'Date & Time' tab to start the task include: measurements must start at least one minute after the current time and if multiple tasks are scheduled there is a danger of overlapping times. If the user would rather allow the 'Date & Time' tab to initiate tasks, the 'Disabled' box must NOT be checked.

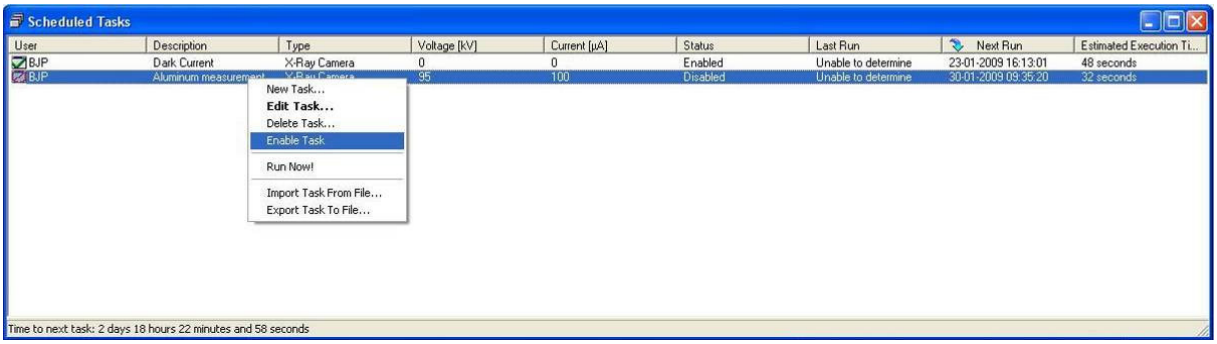

Figure D.8 *Scheduled Tasks window with drop-down menu which is accessed by right-clicking inside the window.*

Folders are specified for storage of images and a log file in the 'Files' tab shown in Figure D.9(b). A base folder is selected for the images; however, images from individual measurements will be stored in a separate subfolder named based on the measurement time. The logfile should be stored in the same base folder with a *.log file suffix.

As previously mentioned the start time and date may be specified in the 'Date & Time' tab (Figure D.4(c)); however, it is recommended to set this time to a future date and initiate measurements manually.

The 'Measurement Points' tab shown in Figure D.9(d) is used to specify the locations at which images are taken during the task. Typically, the 'Import of File' option is used to control movements. This file must first specify the total number of images taken followed by the relative movement from the 'Start Point' for each image. An example movement file, properly formatted, in which 5 images are recorded at each of two locations is given as follows:

```
10
(0.0,0.0)
(0.0,0.0)
(0.0,0.0)
(0.0,0.0)
(0.0,0.0)
(10.0,0.0)
(10.0,0.0)
(10.0,0.0)
(10.0,0.0)
(10.0,0.0)
```

Scripts appear in Section D for creating movement files which serpentine from top to bottom or side to side. *Note: It should be considered during the creation of movement files that movements in the X-direction are 10 times more rapid than the Y (i.e., minimize movements up and down).* Most typically movements in the Z-axis are not used, therefore check the box labeled 'Do not use Z-axis.' If Z-movements are used, the movement file must include a third column specifying such movements. **Warning: When using movement files during X-ray generation, it must be insured that AT ALL TIMES either the specimen or adequate shielding is placed between the X-ray source and camera to prevent damage to the camera.**

The X-ray settings are entered in the 'X-Ray' tab shown in Figure D.9(e). For dark current measurements simply enter 0 for voltage and current. As previously discussed, it is recommended to 'Let XRas determine the warm-up time' for the X-ray.

Finally, the X-ray camera settings are entered in the 'X-Ray Camera' tab shown in Figure D.9(f). The only setting to be changed here is the integration time. The 'Use already loaded calibration (if any)' box should remain checked.

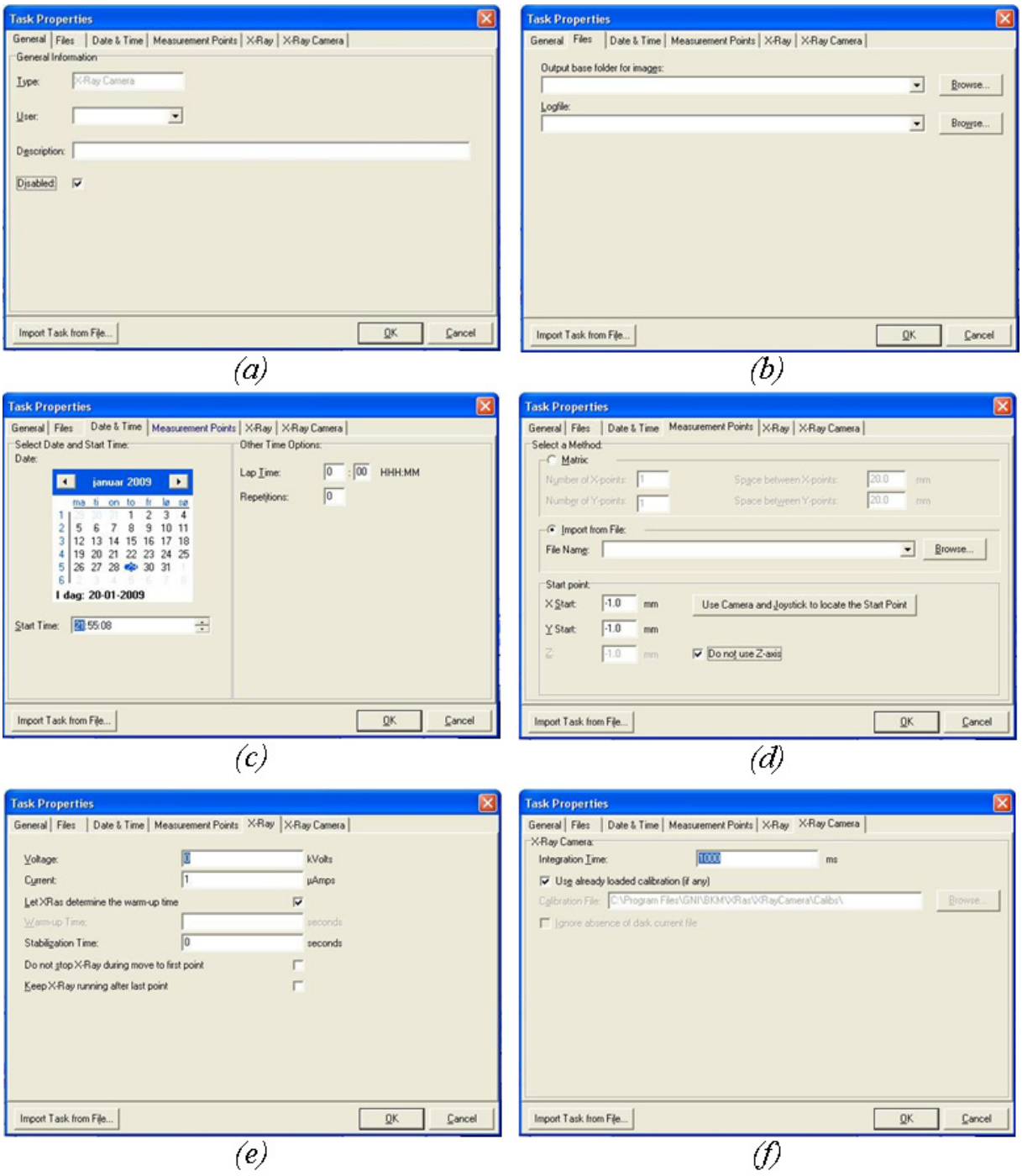

Figure D.9 *The process to create a new task includes (a) 'General Information', (b) specification of locations of 'Files', (c) starting 'Date & Time', (d) 'Measurement Points', (e) 'X-Ray' settings, and (f) 'X-Ray Camera' settings.*

Advanced operation

Warning: The term 'Advanced' indicates that the user is very familiar with the basic operation of the system, is aware of possible dangers during the

calibration process, and has taken the appropriate initial measurements for re-calibration of the camera.

Camera calibration

Calibration of the camera helps to provide more accurate measurements as it is possible to remove the dark current, allowing for longer integration times. Calibration should be completed at the voltage used for actual measurements and across a range of currents including the current used for actual measurements. In order to ascertain these values initial measurements must be taken to determine settings that provide a maximal contrast in the measured states (e.g., wet versus dry) while minimizing variability in these measurements. One possible way to assess the contrast in measurements caused by condition variation (e.g., wet condition versus dry condition) without sacrificing a specimen is to place a reasonable thickness of water or wedge of water between the specimen and the X-ray source such that the X-ray beam intersects both the water and the specimen as a composite.

If the specimen material to be measured is homogenous, then calibration may proceed using this material. However, if the specimen material is heterogenous (i.e., concrete or mortar), a stand-in homogenous material (i.e., aluminum) must be selected which has a similar X-ray absorption behavior. The thickness of the stand-in material should result in an average X-ray intensity similar to that of the specimen material. Calibrations should then be conducted with this stand-in material. **Warning: The stand-in material should be tested using XRAS to insure the X-ray intensity reaching the camera at the highest energy settings will not damage the camera. During calibration, X-rays will be produced for upwards of 3 minutes at each energy setting, which may cause damage to the camera if care is not taken.**

Calibration of the camera is completed outside of the XRAS software, using the AJAT X-Ray Imaging software (AJAT). This software is not capable of controlling the motors which move the X,Y,Z axes, therefore these locations must be set using XRAS prior to opening AJAT. Open XRAS as normal, move to the desired location, and close XRAS without moving the axes back to 0. *Note: Both XRAS and AJAT communicate with the camera, therefore it is not possible to run both programs at the same time.*

After all initial measurements and proper placement of the camera and X-ray source the calibration procedure is as follows.

1. In the AJAT software shown in Figure D.10 select Tools → Calibration.
2. The window shown in Figure D.12 appears and the settings shown in the figure should be selected, except for the voltage, minimum and maximum current, which must be selected by the user based on initial measurements.
3. Before calibration, the control of the X-ray system must be switched. Figure D.11 shows the control panel for the X-ray. For calibration the 'X-Ray Control' must be

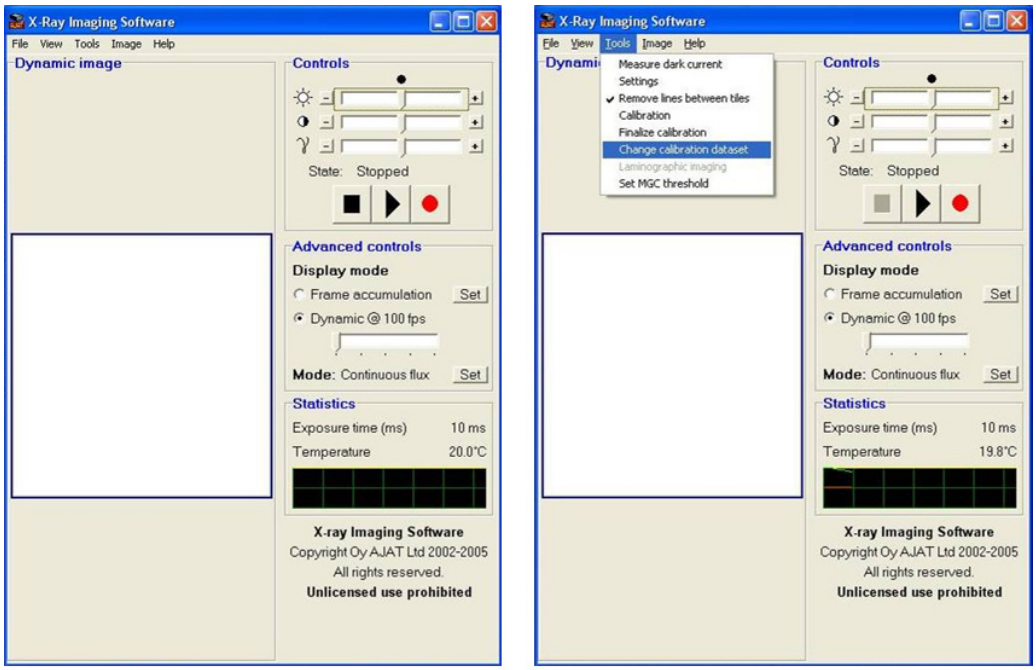

Figure D.10 *(a) AJAT software window, (b) use Tools → Calibrate to calibrate camera.*

set to 'Local' (rather than remote which is required for the XRAS software).

4. The target voltage and current are then set using the dials. The voltage should be set at 40 kV initially (pressing the 'kV Preset' button will show the current level in the digital gage). The voltage dial calibration is slightly off; therefore 40 kV is typically reached when the top number of the dial reads 3 and bottom 2. Initially, the current should be set to 50 μA (*Note: the units on the control panel are mA, 50μA = 0.05 mA*. The maximum current of the system if 500 μA (0.50 mA), and the current dial is calibrated such that one complete turn of the dial is 10% of the maximum (1 complete turn of the dial equals 0.50 μA).

5. Upon reaching these settings, press the black 'X-RAY ON' button. The voltage is then increased to the required setting in kV steps by slowly turning the dial such that the voltage increases 5 kV per 15 seconds, and then waiting 10 seconds.

6. After reaching the desired voltage set the current back to 0 and begin the calibration by clicking 'Calibrate' in the calibration window (Figure D.12).

Note: It is vital to the quality of the calibration that low currents are used during calibration. Therefore the minimum current must be zero. Additionally, the X-ray should not be 'cold' during calibration, in other words the X-ray should be used for approximately 1 hour immediately before calibrating.

Figure D.11 *Control panel for manual operation of the X-ray system. (Author's photos)*

To perform the calibration, follow the on-screen instructions, which will ask you to change the current settings prior to the software automatically capturing a series of images. Allow time for the current and voltage to stabilize before proceeding to the image capturing. After images are captured at all current settings the software will automatically proceed to a calibration finalization, which requires a mask file. Use the file entitled darkX_00000190.dat located at C:\Program Files\DIC for the finalization.

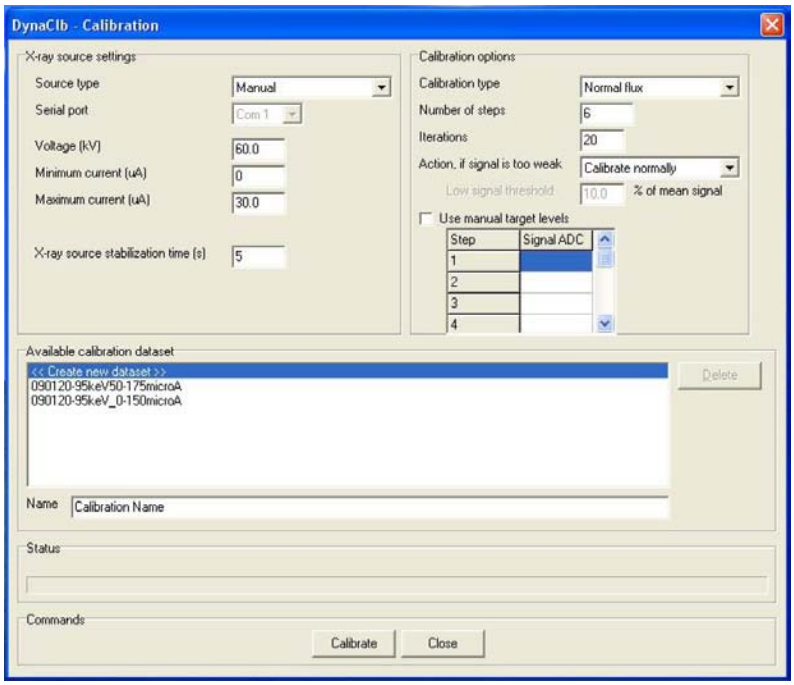

Figure D.12 *Calibration performed in this window with settings and options shown with the desired voltage and current settings.*

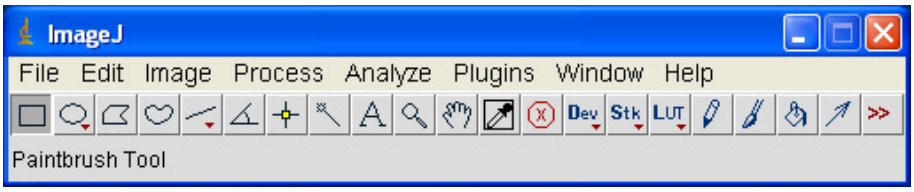

Figure D.13 *ImageJ main window.*

Analysis with ImageJ

ImageJ is a powerful open script image analysis program, available for free download at rsb.info.nih.gov/ij/, which has been used for analysis of images captured in the X-ray system. ImageJ utilizes Java, and therefore may take some more time to open on PC's than most programs. Typically after opening ImageJ once it will open much faster subsequently. The following section provide instruction for many operations commonly used for manipulating images.

Figure D.13 shows the main ImageJ window. Images captured with the X-ray system will be saved as a *.raw file, which is imported into ImageJ. If images were captured at a single location, the easiest way to import and average the images is through the following procedure (also shown in Figure D.14):

1. Click 'File' → 'Import' → 'Raw...' to open the window shown in Figure D.14(a).
2. Select a single image from the desired folder.
3. The 'Import...' window shown in Figure D.14(b) will open. Insure the width is 252, height is 256, offset and gap is 0, and number of images is 1. These values should appear automatically.
4. Check the box entitled 'Open All Files in Folder' in this window and click 'OK.'
5. The images will be imported as a stack as shown in Figure D.14(c). The scroll bar at the bottom of the image is used to view all images.

Typically, the stack of images are several images captured at the same location; therefore, they should be averaged into a single image. To do this the following procedure is used:

1. Click 'Image' → 'Stacks' → 'Z Project' to open the window shown in Figure D.15(b).
2. Select the start and stop slice (default is the first and last image, respectively) and select the 'Projection Type' desired. In this case 'Average Intensity' is selected although many options are available.
3. Click 'OK'

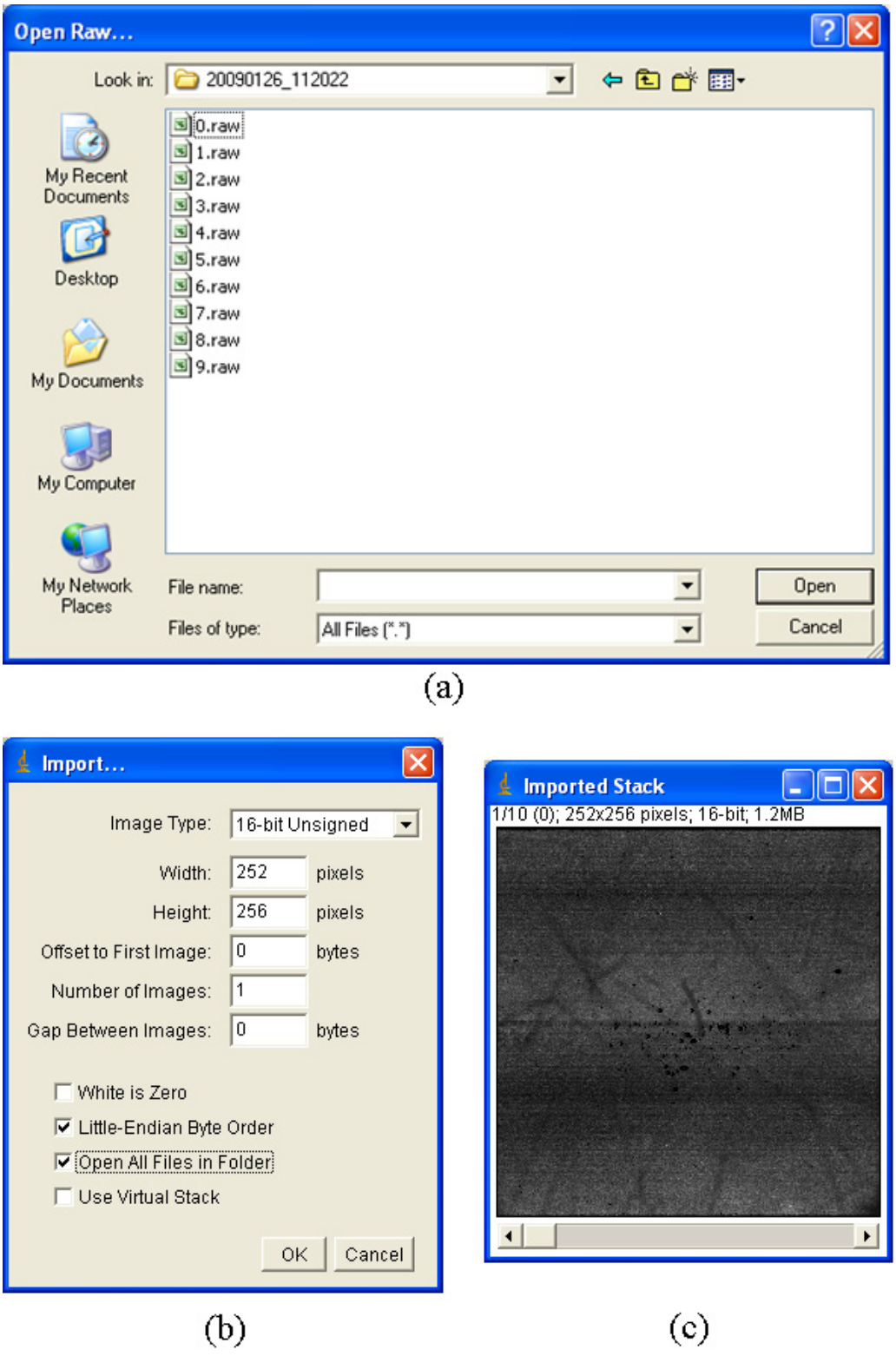

Figure D.14 *To import *.raw images into ImageJ click 'File' → 'Import' → 'Raw...' then (a) select a single *.raw image from the desired folder, (b) provide details on the images and check the 'Open All Files in Folder' option, (c) the stack of images is imported in a new window.*

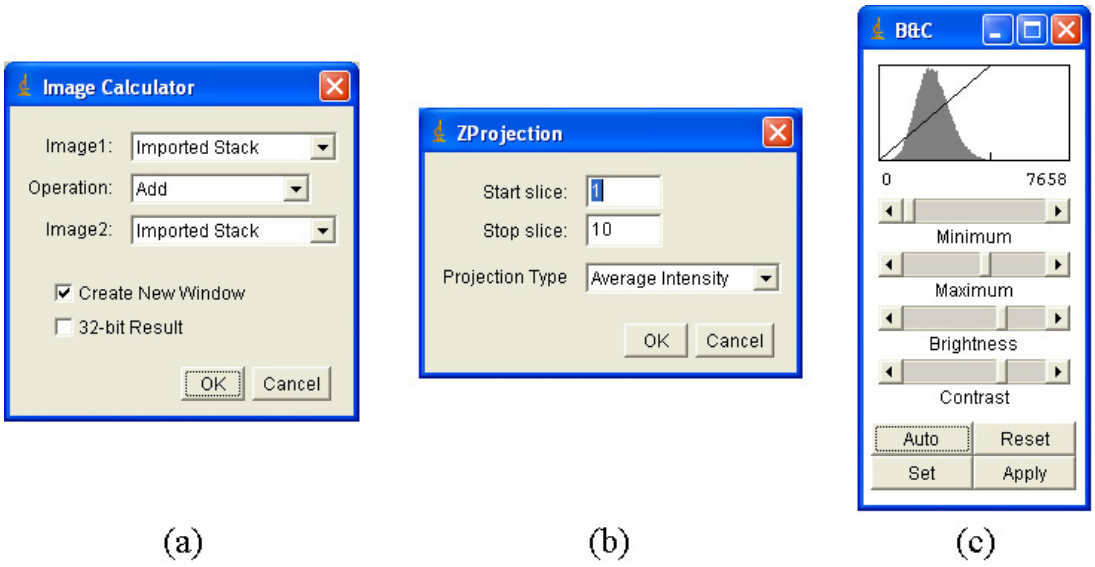

Figure D.15 *Other commonly used tools are (a) the 'Image Calculator' accessed through 'Process' → 'Image Calculator...', (b) 'ZProjection' accessed through 'Image' → 'Stacks' → 'Z Project...', and (c) 'B& C' accessed through 'Image' → 'Adjust' → 'Brightness\Constrast...' or simply* $Ctrl + Shift + C$.

An picture of the average intensity of all images appears in a new window.

Other commonly use tools in ImageJ are shown in Figure D.15. The 'Image Calculator' is shown in Figure D.15(a) which is accessed by clicking 'Process' → 'Image Calculator...'. This tool is used to perform arithmetic on two images (e.g., determining the difference in images from a wet and a dry specimen). Figure D.15(b) shows the 'ZProjection' tool, which was previously described. The 'B&C' window shown in Figure D.15(c) controls the brightness and contrast of the image. This tool is most easily access by pressing '$Ctrl + Shift + C$' however it is also located at 'Image' → 'Adjust' → 'Brightness\Constrast...' in the main ImageJ menu. Finally, measurements can be taken of entire images or selected sections of images by pressing '$Ctrl + m$.' To set the desired measurements click 'Analyze' → 'Set Measurements...' to open the window shown in Figure D.16 and check the boxes next to the desired measurements.

If more complex measurements are taken with the X-ray system, which involve movements, there are several programs which have been created to facilitate reconstructing these individual images into a clear picture in ImageJ. These programs are stored in the X-ray system computer at 'C:\Documents and Settings\X-ray\Desktop\Matlab and ImageJ files'. They are compiled Java programs (*.class files) which may be added to ImageJ by placing them into the plugins folder. The next time ImageJ is open the programs can be accessed in the 'Plugins' menu. To use these programs follow the on-screen commands. *Note: The movement file used for these programs is formatted the same was as the X-ray system. The Y-movements however must have the opposite sign for use with ImageJ.*

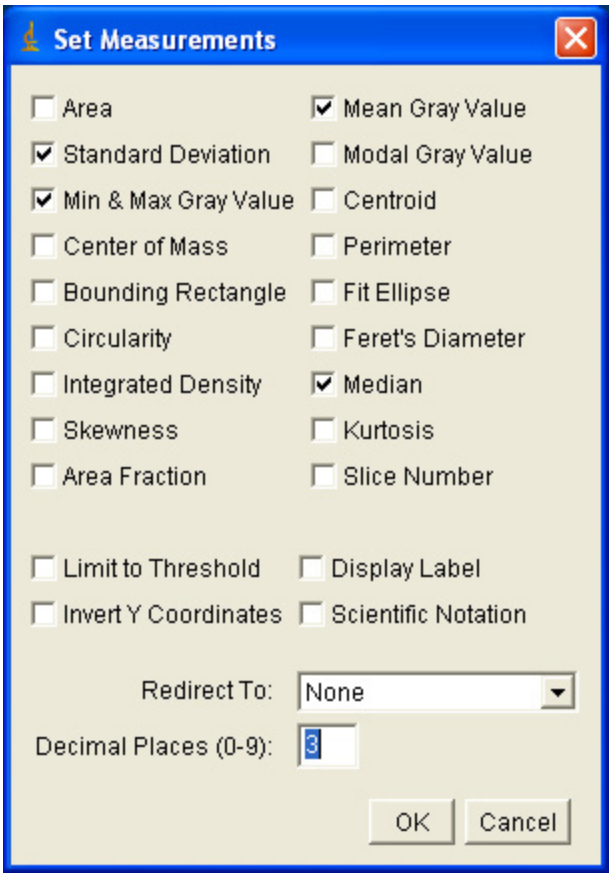

Figure D.16 *To set measurement options click 'Analyze' → 'Set Measurements...' and press Ctrl + m to complete measurements.*

Matlab and Java scripts

In this section user defined programs used in Matlab and ImageJ are presented. The first section includes programs for creation of simple movement files, followed by programs used for analysis with ImageJ.

Programs for movement file creation

The following script creates a movement file entitled 'exp.txt' which serpentine's from side to side.

```
function ss_xray_movement(P,X,Y,dx,dy)
% Function to create a side to side serpentine rectangular movement file
% for the X-ray system
% Script Author:  Brad Pease
%
%       P = Number of pictures to be taken at each location
%       X = Number of Rows
%       Y = Number of Columns
%       dx = Height Movement
%       dy = Longitudinal Movement

fid = fopen('exp.txt', 'wt');
NmrOfPics = P*X*Y;
fprintf(fid,'%.0f\n',NmrOfPics);
```

```
x_axis = 0;
y_axis = 0;

for j=1:Y
    for k=1:X
        for l=1:P
            if mod(j,2)==1
               x = (k-1)*dx;
            elseif mod(j,2)==0
               x = ((X-1)*dx)-(k-1)*dx;
            end
            y = y_axis;
            fprintf(fid,'(%.1f,%.1f)\n',x,y); % Creates XRAS movement file
            %fprintf(fid,'%.1f\t%.1f\n',x,y); % Creates tab delimited file
        end
    end
    k = 1;
    y_axis = j*dy;
end

fclose(fid);
```

The following script creates a movement file entitled 'exp.txt' which serpentine's from top to bottom.

```
function tb_xray_movement(P,X,Y,dx,dy)
% Function to create a top to bottom serpentine rectangular movement file
% for the X-ray system
% Script Author:  Brad Pease
%
%        P = Number of pictures to be taken at each location
%        X = Number of Rows
%        Y = Number of Columns
%        dx = Height Movement
%        dy = Longitudinal Movement

fid = fopen('exp.txt', 'wt');
NmrOfPics = P*X*Y;
fprintf(fid,'%.0f\n',NmrOfPics);

x_axis = 0;
y_axis = 0;

for j=1:X
    for k=1:Y
        for l=1:P
            if mod(j,2)==1
               y = (k-1)*dy;
            elseif mod(j,2)==0
               y = ((X-1)*dy)-(k-1)*dy;
            end
            x = x_axis;
            fprintf(fid,'(%.1f,%.1f)\n',x,y); % Creates XRAS movement file
            %fprintf(fid,'%.1f\t%.1f\n',x,y); % Creates tab delimited file
        end
    end
    k = 1;
    x_axis = j*dx;
end

fclose(fid);
```

Programs for analysis

The X,Y-coordinates in ImageJ are simply pixel numbers; however, scaling and translating the coordinates to actual distances is necessary for analysis. The following Matlab program scales the pixels numbers to distances and set the origin to a user specified location.

```
function scale_axes(File,NoPix,Dist,Xcenter,Ycenter)
% ScriptAuthor:  Brad Pease
% Function to scale and shift the x and y axes data in .txt files created
% using ImageJ's Save XY Coordinates tool.  Use this program scale the
% pixel numbers to actual distances.  The data must be arrange in the
% following order will automatically be if using ImageJ:

%    X-Position    Y-Position    Pixel Value
%             0             0            100
%             0             1            250
%             0             2            120
%             :             :              :
%             :             :              :
%             m             n              z

scale = Dist / NoPix; % x mm / pixel
Xzero = Xcenter;
Yzero = Ycenter;

% Creates an output file for scaled data
fid = fopen('output.txt', 'wt');

% Opens input data file
data_source = fopen(File, 'r');

% Loop to read, convert and write data to output file
while ~feof(data_source)
     line = fgetl( data_source );
     [Xpix, Ypix, Z] = strread( line );

     NewX = (Xpix - Xzero) * scale;
     NewY = (Ypix - Yzero) * scale;
     fprintf(fid,'%g\t%g\t%g\n',NewX, NewY, Z);
end

fclose all;
beep
beep
end
```

Reinforced concrete is known to crack due to restrained hygral/thermal shrinkage, various expansive reactions, and the application of mechanical load. Cracks provide a path of least resistance for ingress of aggressive substances that may cause rapid reinforcement corrosion initiation.

This study focused on establishing possible links between concrete fracture mechanics and ingress and reinforcement corrosion behaviors. Experimental observations from epoxy impregnated concrete cracks, x-ray attenuation measurements, a specially designed instrumented rebar, and other techniques are reported. Results indicate ingress and corrosion initiation may be linked to concrete fracture mechanics.

DTU Civil Engineering
Department of Civil Engineering
Technical University of Denmark

Brovej, Building 118
2800 Kgs. Lyngby
Telephone 45 25 17 00

www.byg.dtu.dk

ISBN: 9788778773128
ISSN: 1601-2917